DOPPLER BEAM SHARPENING FOR SUB-THZ MARINE RADAR IMAGERY AND SMALL TARGET DETECTION

By

Dillon Kumar

A thesis submitted to the University of Birmingham for the degree of

DOCTOR OF PHILOSOPHY

Electronic, Electrical and Systems Engineering

University of Birmingham

August 2024

Abstract

This thesis studies the use of Doppler Beam Sharpening (DBS) as a method of obtaining high resolution sub-THz radar imagery in the maritime environment for the purposes of detecting small, extended targets. The application of DBS in the maritime environment from a small vessel with radars at Sub-THz frequencies is a novel concept. The aim is to develop a radar system that enables radar measurements in the DBS modality, where the complete dataset enables automatic DBS processing for high resolution image production. This thesis presents the DBS technique from basic radar principles and discusses the limitations of using it in the context of maritime radar data. A simulation strategy was devised using Ansys' HFSS software, which was used to simulate the scattering off target models, including models of the ocean. The simulated data was then processed to understand DBS on a deeper level, where the limitations and optimisations of processing are discussed. A 150 GHz FMCW radar was upgraded by installing a new Direct Digital Synthesiser (DDS) and local oscillator to make it suitable for DBS measurements. The radar was then integrated into a novel sensing system which provides all the required time-synchronised data for DBS processing, including kinematics and optical ground truth. Alongside this work, a review of potential anomaly detection techniques is discussed in the context of sub-THz radar, which will form the next stage of the research on this topic.

Dedications

I thank Prof. Marina Gashinova for her unwavering patience and her ability to convey her expertise in radar in a way that progressed my research and taught me valuable lessons about the topic. Her willingness to send feedback on paper writing and presentations and her guidance during meetings made this PhD possible. I thank Prof. Mikhail Cherniakov who's calm demeanour, yet sharp focus kept my PhD on track.

I also thank Prof. Andy Stove for his massive contributions during meetings and trials, his deeply insightful and useful comments on any piece of academic writing and his keen attention to detail. His knowledge on radar has no bounds.

I thank Dr. Liam Daniel, who acted as both a supervisor and a good friend. His guidance unleashed my passion for radio-frequency hardware and taking measurements on field trials. Truly, the giant of who's shoulders I stand on. I thank Dr. Edward Hoare who provided in depth lessons on the radar hardware and was ready to provide a helping hand in the laboratory when needed as well as a good laugh.

I thank Dr. Anum Pirkani who provided endless conversation throughout the PhD. Her optimistic outlook on life made any activity a fun one, a true 'bright light' on this earth.

I thank Alan Yates, who guided all students as a single cohesive unit that looks after one another.

I thank all my friends and staff from the University of Birmingham during my PhD, Samuel Harris, Muge Bekar, Jared Taylor, Pamandeep Kaur, Elijah Uche, Emidio Marchetti, Dr. Fatemah Norouzian, to mention just a few!

I thank the STREAM project partners from the University of St.Andrews, Dr. Duncan A. Robertson, Dr. Saimur Rahman and Aleksanteri Vattulainen, who prepared joint meetings and trials immaculately, and provided good company during our travels.

I finally thank my friends and family, for all their support.

Acknowledgements

This PhD study is part of the project ‘Sub-THz Radar sensing of the Environment for future Autonomous Marine platforms - STREAM’ which is funded by EPSRC UK grant EP/S033238/1.

Contents

List of Abbreviations

ADAS	Advanced Driver Assistance System
ADC	Analogue to Digital Converter
BPF	Band Pass Filter
CPA	Closest Point of Approach
CW	Continuous Wave
DAC	Digital to Analogue Converter
DBS	Doppler Beam Sharpening
DDS	Direct Digital Synthesiser
DSP	Digital Signal Processor
FFT	Fast Fourier Transform
FMCW	Frequency Modulated Continuous Wave
FOG	Fibre Optic Gyroscope
FOV	Field Of View
FWHM	Full Width Half Maximum
GNSS	Global Navigation System Satellites
IF	Intermediate Frequency
IFFT	Inverse Fast Fourier Transform
IMU	Inertial Measuring Unit
ITRF	International Terrestrial Reference Frame
ITU	International Telecommunications Union
ISAR	Inverse Synthetic Aperture Radar
LNA	Low Noise Amplifier
LPF	Low Pass Filter

MGAD	Multi-variate Gaussian Anomaly Detection
MIMO	Multiple Input Multiple Output
PM	Pierson-Moskowitz
PMCW	Phase Modulated Continuous Wave
PSF	Point Spread Function
RCS	Radar Cross Section
SAR	Synthetic Aperture Radar
SSB	Single Side Band
UDP	User Datagram Protocol
USB	Upper Side Band

1 Introduction

Solutions for the autonomy of maritime platforms is a popular research area, where significant progress has been made for large vessels such as merchant ships. The challenge of providing autonomy to small maritime platforms will require a suitable sensor that can provide all the information required for path planning and obstacle evasion, where the obstacles will be much smaller and potentially closer than the significant obstacles for larger ships. The sensor must be robust in all environmental conditions to ensure the data collected is reliable and provides the intelligence to facilitate the autonomous operation of the platform with sensing and processing capabilities far greater than that of a human.

Sub-THz radar (0.1 – 1 THz) systems are currently being considered as an ideal sensor to provide the small autonomous marine platforms with the situational awareness for path planning and obstacle avoidance. The research into increasing the carrier frequency of radars for platform autonomy is quite mature in the automotive industry, where it began in 1960's at 10 GHz for research purposes and settled around 79 GHz where it was used for safety features [1], although not yet reaching the sub-THz band as this is still experimental. The move to sub-THz frequencies and its application in the marine environment, however, is rarely studied and only recently becoming feasible with advancements in technology. The marine environment, in which we would like these sensors to work, provides challenges not posed by the automotive environment in which they have previously been shown to work. The main challenge is the dynamic background which may constrain processing intervals according to correlation times in the environment, as well as the potential for targets to appear and disappear under the water surface and be periodically shadowed from view by waves on the surface. Hence, this thesis will draw from many ideas that have been used for automotive sensing and adapt them for the context of marine sensing. The latest generation of Sub-THz sensors have proven capabilities of producing high resolution radar imagery that can be processed to detect and classify targets against the background returns from the environment [2].

Firstly, it is important to determine the effective ranges of the target detection system. The vessel stopping distance can be estimated as one ship length for every three knots as a rule, where the engine is set to full astern, causing the vessel to slow down and turn off to one side [3]. Of course, in shallow waters the stopping force is less, and the rule may change to be up to six ship lengths per three knots. This does not dictate the minimum required detection distance as evasive manoeuvres do not always require the boat to stop and instead may only require a slight alteration of the vessel trajectory to avoid the obstacle, which also depends on the size of the obstacle and ship. The closest point of approach (CPA) is the smallest range between a vessel and a target, before it should manoeuvre to avoid collision due to the trajectory of both the target and vessel. It is usually slightly larger than double of the stopping distance to ensure ship safety. The calculation of CPA and the likelihood of collision is a complex topic beyond the scope of the thesis which uses manoeuvring guidelines from the Convention on the International Regulations for Preventing Collisions at Sea, (COLREGs), as well as target tracking, vessel kinematic data and sea dynamic information to determine safe distances [4], however representative values of CPA will determine the ranges at which the radar sensor will need to work. For large ships such as tankers and cruise ships, typical CPA values are around 1 mile [5]. Assuming the length of the small vessel is around ten meters, and the typical maximum speeds of these vessels are up to 30 kn, and assuming the safe CPA for this vessel is twice the stopping distance, this brings the CPA and thus the required detection ranges for the vessel to be two hundred meters.

Figure 1.1-1 maritime targets that present themselves as potential obstacles for the autonomous marine craft. Pictures taken from: Flotsam and Jetsam in (a) [6], Seal in (b) [7], Concurrent users (c) taken from ZED data at Coniston trial described in section 6.2, Large dangerous waves (d) [8].

Flotsam and Jetsam in Figure 1.1-1 (a) provide extended regions that cannot be traversed on the water's surface. Objects such as driftwood and rope may be quite small but be troublesome. Rope, in particular, can be become entangled in propellers and so the sensor must be sensitive to these fine textures where the rope breaks the water's surface, to be able to detect them. The safety of sea creatures, Figure 1.1-1 (b), that inhabit the same maritime environment as the vessel defines an ethical requirement for the ability to detect and avoid them. Sea mammals are at risk due to their requirement to surface for air and proximity to coastal areas which have higher vessel traffic [9]. Such targets may have different dynamics to the boat and environment and can submerge and emerge from the surface, so that the sensing system need to be capable of detection based on the behavioural pattern of the target. People who are swimming are also targets of interest, specifically for search and rescue applications.

Concurrent users of the maritime environment, Figure 1.1-1 (c), include vessels such as boats, kayaks and paddleboarders must be detected and avoided to ensure the users remain safe and prevent damage to the vessels.

For smaller platforms, the size of incoming waves, Figure 1.1-1 (d), also poses a credible threat to the platform, as it may cause it to capsize or drift into other objects in the scene, as well as the shock of impact causing long term damage to the vessel, so the ability to distinguish safe waves from dangerous ones is also necessary. Instances of rogue waves, defined as having an amplitude twice as much as the surrounding significant wave height, have been known to damage and capsize even large vessels [10]. These events need to be detected at a safe distance away from the platform to provide enough time for the platform to execute evasive manoeuvres. Specifically, the direction of the incoming wave, its orientation with respect to the boat hosting the radar, as well as its height and amplitude are the parameters which will inform the control system on whether avoidance manoeuvre is needed.

All of the above outline challenges and requirements for the radar system to be fit for purpose of providing information to the sensing system for small and medium sized marine vessels. Where a pure detection or image is required is not a matter of choice but a necessity, as the shape outline and sensitivity to texture would potentially be the only descriptors for the detection of anomalies on the surface to detect the target, e.g. when the target is floating. Most marine radar sensors operate with a rotating physical beam fixed in azimuth and elevation which defines the coarse range-dependant cross-range resolution of the radar map, not suitable for the imagery. At sub-THz frequencies, compact antenna can provide high gain and directivity with the beamwidth of ~1° [11], however even with such a beam at two-hundred meters, the cross-range resolution would be close to three and a half meters. As such objects of interest described above will appear to be beam filling in cross-range.

This is where Doppler Beam Sharpening (DBS) is introduced as the topic of this thesis. DBS is rarely studied as a mode of radar image formation and even more rarely researched for use in the dynamic marine environment as the motion of the platform and background can cause image defocussing. As it will be explained in Chapter 3, DBS is a radar modality that is used to form a synthetic aperture which refines the physical beam into smaller synthetic beams. The method has several advantages over traditional mechanically scanned radar and other radar imaging techniques. For example, DBS can yield azimuth resolutions much smaller than those defined by the physical azimuth beamwidths produced by antenna designed for imaging, allowing for high resolution imagery at much larger ranges, yet be much less computationally demanding as synthetical aperture back-projection technique [1]. However, the use of range-Doppler processing as an imaging method may lead to ambiguities, especially in the forward-looking direction, and so hardware must be optimised to mitigate the effect of Doppler ambiguity. Unlike SAR, Doppler Beam Sharpening does not use phase to focus on targets, which means the cross-range resolution may be poorer, however the method is more resilient to non-linear platform motion, i.e. the image does not defocus as easily as SAR might.

Therefore, the goal of the research is to investigate the suitability of DBS imaging technique to provide small autonomous marine craft with the sensing capabilities to detect targets that threaten the safety of the platform and concurrent users of the marine environment, including sea life. The research into the DBS processing technique and imaging modality will provide the high-resolution radar imagery data that will be further processed to do scene segmentation. As the input imagery is of a higher resolution, this should provide a more intricate segmentation map as well as imagery more akin to optical imagery where well-established optical image and video processing can be adapted to aid the image segmentation process.

1.1 Aims

The aims of the thesis are outlined below:

- Identify the DBS signal processing technique and develop the mathematics to analyse the performance on targets moving on the sea surface.
- Simulate DBS measurements on a dynamic maritime scene to analyse the performance of DBS.
- Prepare the sub-THz radar hardware on a system level, so it can take DBS measurements when used synchronously with video and kinematic measuring devices.

---

[1] M. Bekar, A. Bekar, C. Baker, M. Gashinova "Imaging Automotive Radar based on Burg-Aided MIMO-DBS and Burg-Aided MIMO-SAR in Automotive Scenario" , submitted to IEEE Trans. On Aerospace and Electronic Systems

- Take real measurements of the maritime scene with the upgraded system hardware, process the raw data into imagery using the DBS signal processing technique, and analysing the data according to the theory and simulations from the previous aims.

1.2 Novel contributions and publications

This PhD covered a wide range of topics, and the research produced some novel contributions. The publications that arose from the thesis are detailed in appendix A. The main contribution was identifying DBS as an optimal method of forming synthetic apertures at sub-THz frequencies for small marine platforms, which resulted in [100]. Extensive work in forming the methodology for simulating large dynamic scenes for DBS measurements were done, which is novel at sub-THz frequencies. This also includes the simulation of physically rough surface models, which adds to the novelty of the work. The comparison of the simulation work and repeatable real wave data also resulted in publications [102] and [128].

1.3 Thesis structure

The rest of the following chapters are organised as follows:

- Chapter 2 – Principles of Radar

  This chapter provides a brief discussion on the history of radar, including the applications of radar and radar principles required to understand and process radar signals.

- Chapter 3 – Doppler Beam Sharpening

  This chapter provides a detailed description of the DBS processing of the radar signals and how the dynamic maritime environment may affect the resulting imagery.

- Chapter 4 – Maritime Sub-THz Scattering Simulations

  This chapter details the process of simulating the returns from the sea surface and maritime targets for data analysis and testing DBS methodology. It starts by describing the design process of the sea surface, using empirically constructed sea spectra and time evolution to model the dynamic surface.

- Chapter 5 – 150 GHz Radar Development

  This chapter details the upgrade of the 150 GHz radar hardware which was used in data collection trials, so that the measured data is suitable for DBS processing. It details how the insertion of a new DDS and local oscillator in conjunction with an up-conversion mixer and frequency multiplier achieves operation suitable for gathering data for DBS at the Sub-THz frequencies. It also describes the macroscopic design of the system, and how it uses an IMU to account for a radar motion, as well as methodology to time synchronise data between devices.

- Chapter 6 – Maritime Sub-THz Measurement Campaign

  This chapter describes the physical measurement campaigns for maritime radar data collection and DBS measurements. It describes the setup of the wave tank experiment which enables repeatable wave measurements with the goal of testing anomaly detection techniques. The measurement campaigns for DBS at Coniston Water and Gosport Marina are also presented and analysed.

- Chapter 8 – Conclusion and Future Work

  A final discussion of the results presented throughout the thesis. This is followed by a discussion of how future work can be done to build on the results presented in this thesis and how future projects could be directed.

2 Applications and Principles of Radar

This chapter delivers a general overview of the applications of radar technology, and the principles of radar, discussing the most relevant principles for the topic of DBS for this thesis. Following this, an extended analysis is undertaken of the expected Doppler frequencies from targets in the marine environment, which is required to produce focused DBS imagery, which is further explained in chapter 3.

Most of the principles in this chapter can be found in standard radar textbooks [12], and their application to microwave radars is well understood but they are reproduced here so they can be discussed in the context for Sub-THz radars. This chapter found that the current state of the art architecture for marine radar could not provide small autonomous marine craft with optimal data required for situational awareness, and so the proposal of using experimental sub-THz radar was explored and how

2.1 A brief history on radar

The roots of the development of the radar, named as an acronym for **Ra**dio **D**etection **A**nd **R**anging, can be traced back to the early 20th century when scientists explored the properties of electromagnetic waves. The theoretical groundwork laid by Maxwell and experimental confirmations by Hertz in 1886 set the stage for the development of radar where it was demonstrated that radio waves are reflected by dielectric and metallic objects. In 1904, Christian Huelsmeyer invented the Telemobiloscope, which was used to detect passing ships by transmitting radio waves, and receiving the reflected signal, and is often noted as the first radar [13]. The true emergence of radar occurred during World War II, exemplified by the pioneering work of Sir Robert Watson-Watt and the creation of Chain Home, the first fully operational radar system [14][15].

Post-World War II witnessed rapid advancements in radar, into other applications. Civilian developments (aircraft weather radar and marine navigation radars were driven by exploiting wartime inventions. In particular the cavity magnetrons gave civil radars compact, affordable and reliable transmitters. During the Cold War, military radar was at first also reliant on magnetrons but later exploited coherent transmitter-amplifier chains using klystrons and travelling wave tubes which allowed a wider range of waveforms and processing techniques. During this period, radar became crucial in both military and civilian applications. The era also witnessed radar's diversification into civilian sectors, including aviation, meteorology, and navigation.

In the latter half of the 20th century and into the 21st, radar technology continued evolving. Advances in signal processing, digital technology, and materials science led to sophisticated radar systems and processing like synthetic aperture radar (SAR) and electronically steerable phased-array radar. The history of radar, from wartime necessity to its omnipresence in modern society, highlights its transformative impact.

2.2 Sub-THz Radar

The choice of moving to the Sub-THz band for the purpose of radar imaging is due to the many advantages that is discussed throughout this chapter in the context of marine sensing for small autonomous platforms. The capability of imaging at these frequencies was not attainable until the technology was developed and demonstrated in the 21st century. While being perceived initially as a sensing system for very short-range applications, such as security systems [16], non-destructive testing systems, finally the use of sub-THz frequencies was proposed for automotive sensing research [17][18]. The higher carrier frequency accommodates larger bandwidths and thus a finer range resolution [2]. The physical antenna aperture size is also much smaller for a given beamwidth as will be discussed in section 2.10. Having physically smaller sensing systems increases portability, allowing the freedom of installation around the vessel, including regions closer to the water. It also makes the possibility of installing distributed systems more realisable as multiple sensors can be installed close to each other due to the smaller hardware size [19]. The smaller wavelengths have shown higher sensitivity to surface textures due to diffuse scattering, which leads to the ability to classify regions with small texture deviations such as grass and asphalt as seen in [20][21].

2.3 Automotive radars

As the radar system proposed in this thesis is derived from experimental automotive radar systems, it is important to discuss the history of automotive radars and envisage how small vessel maritime radars could operate similarly modern automotive radars today. The first designs of automotive radar originate from the 1960s to 1970s from the U.S department of transportation and Japanese [22] automobile companies. At this time the motivation to equip automobiles with portable radar technology was to provide vehicles with the capability of pre-collision target detection for obstacle avoidance, providing the user with enhanced situational awareness when operating the vehicle [23]. Since then, the motivations for developing automotive radars have been towards the production of advanced driver assistance systems (ADAS) with partial and full automation [24], which take advantage recent technological advancement. The SAF86XX from NXP is an example of a recent automotive radar chip design used to form part of ADAS and provides some level of autonomy in adaptive cruise control, autonomous emergency breaking, and park assist [25].

Due to the inherent advantages of using Sub-THz frequencies for remote sensing, these radars have been applied for use in automotive applications. Currently the 76 – 77 GHz band has been regulated for automotive applications and standardised in Europe (ETSI EN 301 091) in the 90s. Since then, the band was allocated for the Intelligent Transport Services (ITS) [26]. In modern times, automotive radar is a standard in most new vehicles and is paving the way to the commercialisation of autonomous vehicles with many different types of system being considered, which usually involves a degree of sensor fusion [27]. For future systems, research into increasingly higher carrier frequencies beyond 100 GHz are being explored [1], for the enhancement of angular resolution and imaging capabilities [28].

2.4 Maritime Radar

This review sub-section covers the vast amount of sensing networks available for monitoring the maritime environment, to see if they are ideal for providing small maritime vessels with the data required for situational awareness needed for autonomous operations.

Like automotive radar, maritime radar has an extensive history. In World War II, the ability to position radar on the sea, for sea to air detection, was highly desirable. The early radar systems that operated at low frequencies were cumbersome and impractical to install on most maritime platforms, however moving up the spectrum to S and X-band radar in the following decade found practical use for maritime radar [29], such as surveillance and vessel tracking.

Historically, maritime surveillance has been done using a large variety of sensing equipment including air and spaceborne radar, coastal radar and vessel-mounted radar [30]. Maritime patrol radars are airborne radars that are usually located in the nose of the aircraft, downward facing which are optimised to conduct a wide area surface search [31]. These radars benefit from higher altitudes as they achieve wider fields of view, however this also increases the grazing angle and therefore the sea clutter returns, making target detection more difficult.

Many satellite-based radars for maritime surveillance produce Synthetic Aperture Radar (SAR) imagery, which is used to detect oil spills and large vessels on a large swath of ocean [32]. SAR is a technique which is explored in chapter 3, which exploits the motion of the radar – in this case the satellite, to refine the azimuth resolution, forming high resolution imagery. SAR based tools are currently deployed by the European Maritime Safety Agency (EMSA) [33]. Spaceborne SAR has also shown the capability of imaging relatively small slow-moving co-operative targets such as 10m yachts [34]. Some applications of the Space-borne illuminators of opportunity such as GNSS satellites have also been used in passive bistatic radar systems to measure large maritime targets, which also has the capability to detect sea clutter after some non-coherent integration in the Doppler domain [35]. However, the ability to detect smaller targets that are still dangerous to small vessels remains not well researched, which is likely due to satellite mounted radars not having the appropriate sensitivity to detect them.

Coastal radars that survey regions of the ocean from the shore have many applications. The typical grazing angles are much lower than that of airborne and spaceborne radars and so the RCS of the sea clutter will be less, however much larger transmit powers are available hence clutter can still be resolved. For the detection of small targets at sea, the limited resolution of ground-based coastal radars can make target detection difficult [36]. These systems could provide co-operative vessels information on the location of targets within the coastal region, however as soon as the vessel leaves the region within the field of view (FOV) of the radar network, no more information can be supplied to aid the navigation of the vessel. Forward scatter radar has been demonstrated as a potential method for maritime surveillance with the capability of tracking targets at sea, as the radars can be mounted on buoys and coastal areas forming a network of radars. It acts as an ‘electromagnetic fence’ where targets that pass through the baseline can be detected [37], which could be useful for marine traffic control in pre-defined regions, but likely not useful to provide any one vessel with full situational awareness due to its static nature.

Most vessels are equipped with some form of onboard radar to assist in navigation in real time as per the rules outlined in COLREGS. As the sensor is installed on the vessel, it provides data to the vessel regardless of the location, assuming the radar system does not require a connection to external components for function. Unlike the airborne, spaceborne and coastal radars, the radar will be set much closer to the water if it is mounted on a small vessel, and so grazing angles are much smaller, which means the effects of shadowing in radar imaging will be stronger. Companies like Raymarine currently offer a wide selection of radars, including their ‘Quantum’ models which transmit at X-band, around 9.4 GHz, and PRFs up to 6 KHz [38]. Even at these frequencies, the physical dimensions of these radars are around 50 cm, which is rather cumbersome to place anywhere other than the top of the boat.

2.5 Monostatic and Bistatic Radar configurations

Monostatic radar is a geometry the radar transmitter and receiver antenna are co-located in space, e.g. use the same antenna. The specific radar configuration considered in this thesis is quasi-monostatic, where the radar transmitter and receiver antennas are very close in space, such that the baseline is far smaller than the typical detection ranges. As a result, in most cases, monostatic approximations hold for quasi-monostatic radars, and so most principles defined in this chapter will be for the monostatic configuration. The bistatic radar configuration occurs when the transmitter and receiver antenna are not co-located and separated by a large baseline which is comparable to the range to the target.

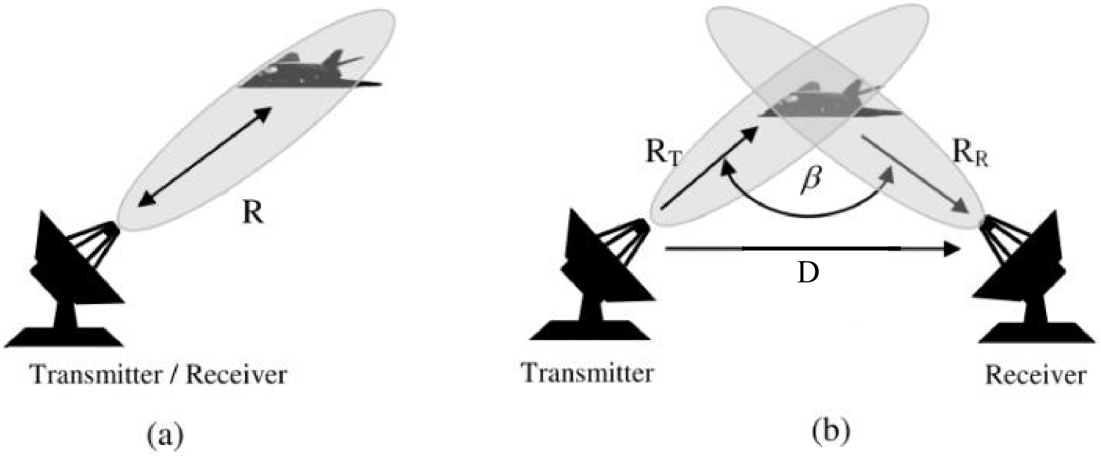

Figure 2.5-1 Monostatic configuration (a) and the bistatic configuration (b) taken from [39].

The bistatic configuration is defined by the baseline, which is the distance that separates the transmitter from the receiver, and the bistatic angle which is the angle formed between the transmitter to target range vector R_T and the receiver to target range vector R_R. The plane at which these vectors exist is known as the bistatic plane. The monostatic situation can be seen as a special case in the bistatic system where the bistatic angle $\beta = 0$, the baseline $D = 0$ m and the range to the target can be expressed as R where $R = R_T = R_R$.

2.6 Antenna

One of the key components of the radar is the antenna, which is defined by its radiation pattern. In this work, electrically large aperture antennae are considered, and the ray optics may be used to understand the resulting antenna patterns. Here, aperture antenna refers to antennae, that emit electromagnetic radiation through an opening. The radiation patterns for aperture antenna can be calculated via the field equivalence principle, which is simplified when calculated in the far field region [40]. For non-infinite planes, diffraction at the edges need to be considered however, at small angles around the boresight, the antenna pattern can be approximated using the Fourier transform of the aperture function [41]. . The far field region of the antenna is defined as the region at which the angular field distribution is independent of the range. The region before this is known as the Fresnel region, where the beam is noticeably curved across the aperture.

$$d_{Farfield} \geq \frac{2D^2}{\lambda} \qquad (2.6\text{-}1)$$

Here, $d_{Farfield}$ is the far field distance (also known as the Fraunhofer distance) and D is the aperture dimension. The factor of 2 derives from the maximum allowable phase error for the antenna [42], of which many radar designers use two which ensures a maximum phase error of $\pi/8$ [43].

2.6.1 Antenna Beam Pattern

The antenna beam pattern is determined by the shape of the antenna. It is known that the beamwidth of the antenna pattern is directly proportional to the wavelength, and inversely proportional to the size of the antenna [44].

$$\theta_{BW} \approx \frac{\varepsilon\lambda}{D_{ant}} \tag{2.6-2}$$

Here D_{ant} is the antenna aperture dimension in metres in the same plane as the antenna beamwidth, θ_{BW} (representing all planes including horizontal and vertical). Depending on the shape of the aperture, ε is a measured co-efficient, which accounts for resistive loses, impedance mismatches at the boundaries and the power that is distributed to the sidelobes. The benefit of using sub-THz sensors is shown here as the small-wavelengths enable the use of smaller antenna apertures whilst keeping the antenna beamwidth fine. Smaller apertures allow the radar systems to be more portable and therefore easier to mount to small vessels.

Radar antennae are specifically designed to produce well defined beam patterns. For instance, 'fan-beam imaging antenna' typically have an asymmetrical beam pattern, where the azimuth beamwidth is much narrower than the elevation beamwidth.

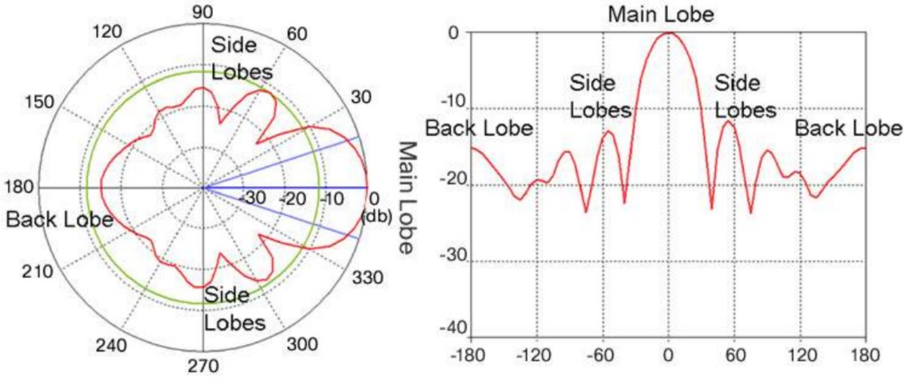

(a) Pattern in Polar Coordinates

(b) Pattern in Cartesian Coordinates

Figure 2.6-1 Relative radiation intensity vs elevation angle expressed in polar co-ordinates (a) and cartesian co-ordinates (b) for an antenna taken from [45].

The main lobe is the region that has the highest relative radiation intensity The width of the main lobe is usually characterised by the Full Width Half Maxmimum (FWHM), i.e. the width over which the power density is within -3 dB of the maximum. For a practical antenna there are other, smaller peaks in the antenna pattern known as side lobes. For most applications it is desirable to minimise the relative intensity of the sidelobes to avoid ambiguity between large targets seen in the sidelobes and small targets seen in the main lobe. Side lobe reduction can be accomplished by weighting the antenna aperture, which is part of the antenna design process, where the field distribution is non-uniform across the aperture.

The directivity (directive gain) of the antenna is defined as the ratio of the radiation intensity of the antenna in a particular direction and the average radiation intensity over the 4π steradians surrounding the antenna.

$$D(\theta,\phi) = \frac{U(\theta,\phi)}{U_{av}} = \frac{4\pi U(\theta,\phi)}{P_{rad}} \qquad (2.6\text{-}3)$$

Here $U(\theta,\phi)$ is the radiation intensity of the antenna facing a particular direction determined by the azimuth θ, and elevation ϕ, look angle. The average radiation intensity can be found by dividing the total radiated power by 4π. The total radiated power can be found by integrating the entire volume that encompasses the 3D radiation pattern.

The antenna gain measures how much power is directed into the main lobe and is normalised to the antenna input power rather than the total radiated power, which accounts for losses in the antenna.

$$G(\theta,\phi) = \frac{4\pi}{P_{tx}} U(\theta,\phi) = \eta D(\theta,\phi) \qquad (2.6\text{-}4)$$

The efficiency of the antenna is η and determines how much of the transmitter power gets radiated from the antenna. The above definitions for antenna gain are accurate, however for most scenarios where exact accuracy is not necessary, the maximum antenna gain can be estimated.

$$G = \frac{4\pi A_{eff}}{\lambda^2}\eta \tag{2.6-5}$$

Here G is the gain of the antenna, and λ is the wavelength of the transmitted signal. A_{eff} is the effective area of the antenna which is used in radar equation in section 2.9. The definition of gain can also be expressed as the ratio between 4π and the antenna beam widths in steradians, a function of the azimuth and elevation beam widths (in radians) in (2.6-6) [46].

$$G \approx \frac{4\pi}{\theta_{az}\phi_{el}} \tag{2.6-6}$$

Where θ_{az} is the azimuth beam width and $\emptyset_{el}$ is the elevation beam width, expressed in radians.

In CW radar and more specifically FMCW, the transmitting and receiving occurs simultaneously, and so a leakage from the transmitter to the receiver will reduce the dynamic range. To alleviate this problem, a quasi-monostatic system, where the transmit and receive antennas are separated by a small distance such that the antenna gain patterns of the receiver and transmitter are minimised at the relevant angle facing the antenna.

2.6.2 Rectangular aperture antenna

In this thesis, the antenna types used were rectangular aperture antennas, which, in general, produce antenna beam patterns with a different elevation beam width compared to the azimuth beam width.

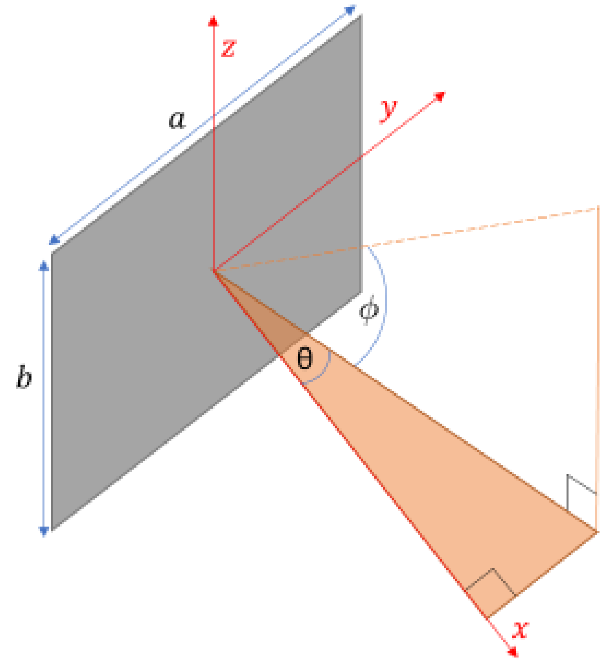

Figure 2.6-2 Rectangular aperture schematic diagram.

Here, θ refers to the azimuth angle and $\emptyset$ is the elevation angle. The physical antenna dimensions are a, which refers to the length and b which refers width. Assuming that the aperture has a uniform aperture field intensity distribution, the radiation intensity can be found by taking the Fourier transform across the aperture, which has been calculated in (2.6-7).

$$I(\theta,\emptyset) = \left(\mathrm{sinc}\left(\frac{ka}{2}\sin(\theta)\right)\right)^2 \left(sinc\left(\frac{kb}{2}\sin(\emptyset)\right)\right)^2 \tag{2.6-7}$$

Where *sinc*(*x*) is equivalent to *sin*(*x*)/*x*. The term k refers to the wave number which is equivalent to $2\pi/\lambda$, where λ is the radar signal. We can analyse the azimuth plane by looking at the plane where $\emptyset = 0$. In this case the radiation intensity reduces to:

$$I(\theta, \emptyset = 0) = \left(\operatorname{sinc}\left(\frac{ka}{2}\sin(\theta)\right)\right)^2 \qquad (2.6\text{-}8)$$

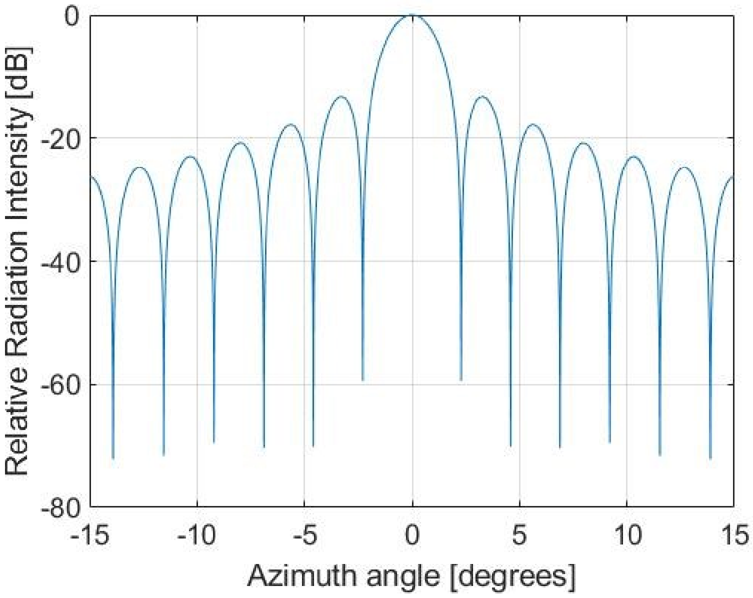

Figure 2.6-3 Azimuth beamwidth, using a wavelength of 2 mm and an aperture dimension of 5 cm.

The half power beam width can be found by finding the angle where the relative radiation intensity of the main lobe reaches -3 dB on either side of the lobe. This value is reached when the sinc function in (2.6-8) is set to $1/\sqrt{2}$. It is also assumed that the main lobe is symmetrical about 0 degrees, hence the angle at which the radiation intensity is -3 dB is also half of the beam width.

$$\frac{1}{\sqrt{2}} = \operatorname{sinc}\left(\frac{ka}{2}\sin(\theta)\right) \qquad (2.6\text{-}9)$$

$$\frac{ka}{2}\sin(\theta_{3dB}) = \frac{\pi a}{\lambda}\sin\left(\frac{\theta_{BW}}{2}\right) \approx 1.39 \qquad (2.6\text{-}10)$$

Assuming that the beam width is a small angle, we can approximate the antenna beam width for a rectangular aperture.

$$\theta_{BW} = \frac{0.88\lambda}{a} \tag{2.6-11}$$

The co-efficient seen in (2.6-2) has a value of 0.88 for rectangular antenna. In practice there will be power losses in the antenna which have not been considered in the analysis. Here we see that using higher frequencies enables the use of smaller aperture dimensions to obtain the similar beamwidth, hence the sub-THz radar front ends are more portable and easier to install on smaller vehicles.

2.6.3 Cross-Range Resolution and Angular Resolution

The antenna beamwidth is an important parameter to understand, especially in the context of DBS where it can help define the FOV of the image as well the performance of cross-range resolution improvement. Without any processing, the cross-range resolution is depicted in Figure 2.6-4 and is defined as,

$$\Delta R_{cr} = 2R \times tan\left(\frac{\theta_{az}}{2}\right) \tag{2.6-12}$$

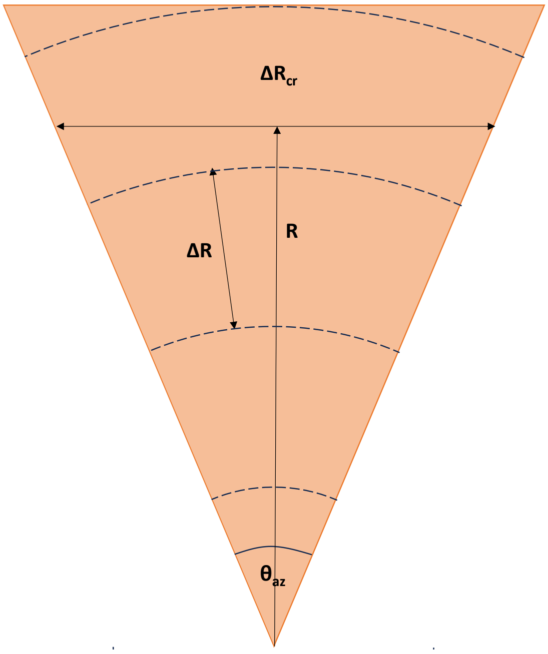

Figure 2.6-4 Geometry schematic of the region (shaded) within the azimuth beamwidth.

Here R is the range, and ΔR is the range resolution. The cross-range resolution is denoted ΔR_{cr} and the azimuth beamwidth is θ_{az}. Here, the cross-range resolution dependence on range is shown clearly. At target detection ranges of 100 m, to achieve the cross-range resolutions required to resolve the small features of targets of interest (~10 cm apart), an azimuth beam width of 0.05° will be required, which is an unrealistically small beamwidth. To pass safely between two targets, the range resolution is required to be at least the width of the vessel.

2.7 Radar wave propagation at Sub-THz frequencies

From the antenna, the electromagnetic wave is transmitted into the environment. As the EM wave travels through the environment, atmospheric attenuation reduces the energy of the wave by absorbing and scattering the signal before it reaches the target. The attenuation spectrum of the EM wave needs to be considered when selecting the frequency of the radar as specific frequencies will suffer heavy atmospheric attenuation and will therefore result in a very low SNR. The model recommended by the International Telecommunication Union (ITU) demonstrates how attenuation (here measured in dB/km) is affected by temperature, air pressure, and water vapour [47].

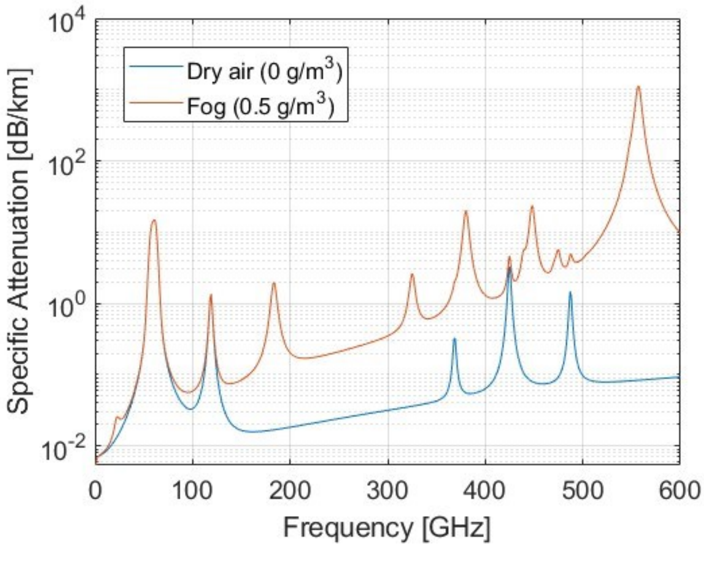

Figure 2.7-1 Atmospheric attenuation for EM wave frequencies from 10 GHz to 1 THz with different water vapour densities produce on MATLAB [48] which refers to the model in [47].

The two plots show the attenuation in dry air, and in foggy weather with the water vapour density of 0.5 gm^{-3} which corresponds to a less than 50 m visibility [49]. It can be seen for the lower sub-THz frequencies, the difference in attenuation over paths of less than 1km is small, but as the frequency increases, and the wavelength approaches the size of the condensed airborne water droplets, the attenuation in fog significantly increases. The attenuation in dry air is dominated by resonant absorption by the different gases in the atmosphere. There are distinct bands in the spectrum where the wave will have less attenuation and these are good candidates for radar frequency, such as 77 GHz, 150 GHz and the band between 210 GHz and 310 GHz. As the water vapour density increases, the frequencies having minimum attenuation change slightly and so it is important to pick a frequency that has relatively low attenuation for both conditions. It is important to note that the effect of sea spray can provide significant attenuation by way of adhesion to the radome/antenna covers, and its presence in the atmosphere, however this is dependent on its distribution in the environment, and in many cases it may not be significant enough to significantly decrease the sensitivity of the radars [50].

In free space, at large scale, EM waves travel in straight lines, however the waves may travel to geometrically shadowed regions by way of diffraction. The angle through which an EM wave is diffracted is dependent on the size and shape of the object relative to the EM wavelength, where objects that have sizes close to the wavelength have significant diffraction effects. At Sub-THz frequencies, the presence of shadows can be significant, and regions in the produced radar imagery need to be segmented as such [51]. The presence of shadows can be used to detect the presence of a target casting the shadow, providing the background provides enough clutter to contrast the shadow; however, they may also conceal the presence of other targets that exist in the shadowed regions. Therefore, the approach towards shadowed regions should be met with caution.

2.8 Radar cross section

The targets radar cross section (RCS), σ, is a measure of how the target scatters the incident radar signal around the surrounding three-dimensional space, in particular it describes how much of the transmitted signal is reflected back towards receiver. It is a function of many parameters such as, aspect angle, the target shape, and the dielectric material properties of the target. For monostatic radar, the RCS is a measure of how much of the transmitted radar signal is reflected at the radar and is therefore defined similarly to antenna gain. This assumes that the incident power is absorbed over an area equal to the RCS and re-radiated isotropically.

$$\sigma = \lim_{R\to\infty} 4\pi R^2 \frac{P_R}{P_D} \qquad (2.8\text{-}1)$$

R is the range from the target to the radar, where the target is assumed to be in the far field to ignore any near field effects. P_R is the radiation intensity at the receive antenna and P_D is the power density of the signal incident on the target. The RCS has dimensions of square-meters, which when converted to decibels, is commonly denoted as dBsm. A 10 cm reflector designed to reflect the signal directly back toward the receiver may have an RCS much larger than a large stealth aircraft designed to reflect the radar signal away from the receiver, and so RCS should not be thought of too literally as the physical surface area.

It should be noted that the monostatic RCS is dependent on the aspect angle of the target, which should not be confused with the bistatic angle, as the transmit and receive antenna are still co-located. The RCS is defined over all possible 4π steradians of aspect angles, in a sphere around the target. The aspect of a target can dramatically affect the RCS of the target, except for high symmetry targets such as a sphere.

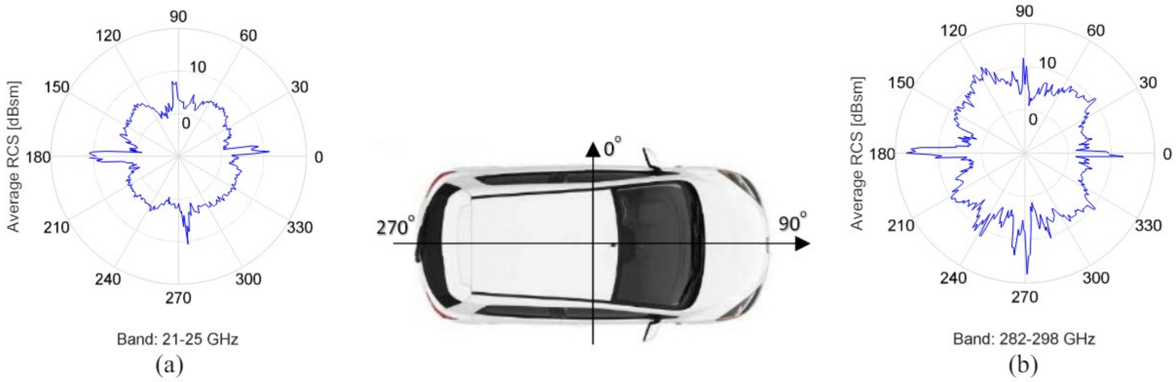

(a)

(b)

Figure 2.8-1 RCS of car at the 21-25 GHz band (a) and 282-298 band (b) taken from [52].

Polarisation is another parameter that can affect the RCS, and so the RCS can be represented as a scattering matrix,

$$\sigma = \begin{bmatrix} \sigma_{HH} & \sigma_{VH} \\ \sigma_{HV} & \sigma_{VV} \end{bmatrix} \qquad (2.8\text{-}2)$$

where the first subscript is the transmit polarisation, and the second subscript is the receive polarisation, so HV refers to a horizontal polarization of the transmitted wave and vertical polarization of the receive antenna.

RCS analysis can be complicated, and for non-isotropic targets it is usually measured or simulated rather than mathematically modelled. Simulation software such as Microwave Studio CST [53] and Ansys HFSS [54] can be good tools to estimate the RCS. The object Solvers that use ray tracing (Shooting bouncing rays) can be employed to obtain S parameters at different look angles around the target, hence retrieving the RCS information in both monostatic and bistatic radar.

2.8.1 RCS of a sphere

There are some relatively simple shapes for which RCS can be expressed using closed-form mathematical equations, and these targets are usually used when standard targets are required for radar calibration. One of these reference targets is the sphere, where the RCS is defined by Mie series, of which the result is well reported [55]. The three regimes into which the RCS of the sphere is usefully divided are the Rayleigh, resonance (which is also known as Mie) and optical regions [56].

- Rayleigh region is when $\lambda >> r_{sph}$, and the phase difference between the signals scattered from different parts of the sphere are negligible. Here the Mie series reduces to a single $(\lambda/d)^4$ dependence. This is typical of rain at microwave frequencies and fog at mmW/sub-THz [55].
- Resonance where $\lambda \sim r_{sph}$, where phase variations are significant due to the constructive and destructive interference of reflected signals at the targets surface, which leads an RCS dependency on the sphere diameter that oscillates with increasing sphere size.
- Optical region occurs when $\lambda << r_{sph}$, where the targets surface is many wavelengths wide, and so the backscatter largely depends on the angle of incidence for non-symmetrical targets as specular scattering dominates, of course for a sphere the RCS is independent of the angle of incidence. The Mie series reaches a limit such that the RCS is independent of wavelength and equal to the area of a circle with the same radius as the sphere The RCS for optical region will be the most common for the typical targets in the marine environment that will be measured with the Sub-THz radars, as the wavelengths will be on the order of a few millimetres, whereas the targets of interest will be on the order of tens of centimetres. This impacts the choice of modelling tools and measurement techniques which are most useful for obtaining radar cross section values.

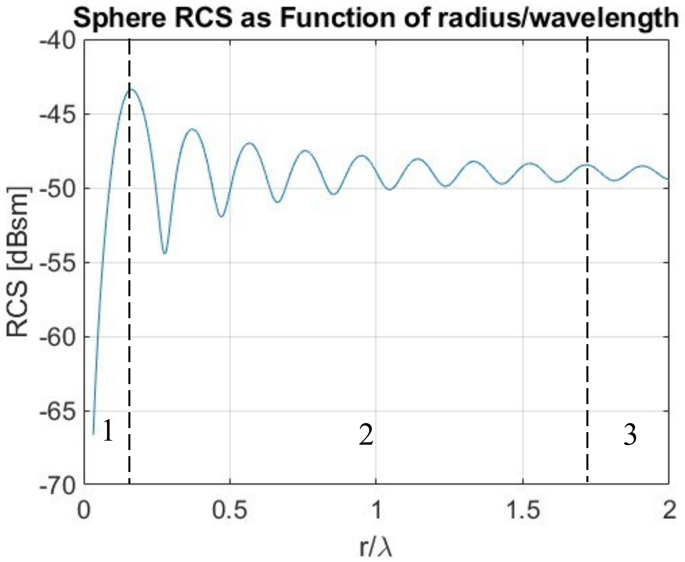

Figure 2.8-2 Sphere RCS regions, (1) Rayleigh, (2) Resonance/MIE, (3) Optical, produced on MATLAB [57][58].

2.8.2 RCS of Corner Reflector

Corner reflectors are targets with a very large RCS despite their small physical size. They are usually formed from three electrically conductive plates at three orthogonal planes, which reflects most of the incident radiation back towards the source. The monostatic RCS pattern also has quite a large directivity towards the line of symmetry that runs through the corner, as seen in Figure 2.8-3.

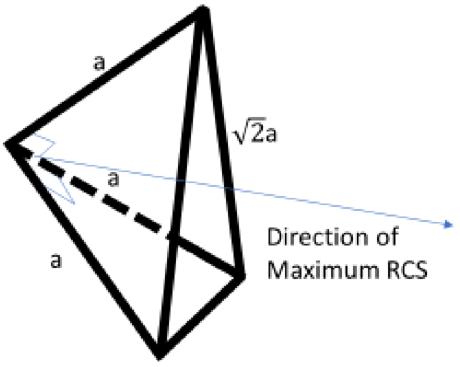

Figure 2.8-3 – Trihedral corner reflector formed with three right angle triangle plates with side length (base and height) of a and direction of maximum RCS, approximately 45 degrees to each plane occupied by a triangle plate.

$$\sigma = \frac{4\pi a^4}{3\lambda^2} \tag{2.8-3}$$

The maximum RCS of the trihedral corner reflector is expressed in (2.8-3), within 10° of the direction of maximum RCS [59]. The RCS of the trihedral corner reflector is inversely proportional to the square of the wavelength, so as the radar carrier frequency increases, the model predicts an increase of RCS of and ideal trihedral corner, i.e. smooth and flat.

Many man-made structures are constructed with right angles and therefore form corner reflector like regions, as well as intentionally built corner reflectors that are placed on top of objects such as buoys to inform passing vessels of their location, as the high RCS achieves a large SNR, hence the target is easier to detect [59].

2.9 The Monostatic Radar Equation

The radar equation defines the power budget for the radar system and can be used to find the signal to noise ratio (SNR) at the output channels for processing. The SNR can be used to find the sensitivity of the radar which indicates the radar’s ability to image targets of known RCS at specified ranges. It is also necessary to use when calibrating a radar system as it provides a comparison between the theoretical power received from a target and the measured power.

Initially the radar transmits a signal with a power denoted P_{tx}, which is assumed to be isotropic. Hence the power, P_{tx} is uniformly distributed around a hypothetical sphere of radius R_1, which means the power density can be found by dividing the total transmit power by the surface of the sphere, equivalent to the range of a target for example.

$$S_u = \frac{P_{tx}}{4\pi R_1^2} \tag{2.9-1}$$

The transmitter antenna directs most of the radiated power towards the boresight and defines the radiation pattern which is explored later in section 2.10. Therefore, the directional power density equation can be found by including a term for antenna gain denoted G.

$$S_g = \frac{P_{tx}}{4\pi R_1^2} G \tag{2.9-2}$$

Now we consider how the power of the incident signal is reflected towards the receiver. A property of the target known as the monostatic Radar Cross Section (RCS) determines how much of the incident power is reflected toward the receiver and can be a function of azimuth and elevation of the target relative to the transmitter and receiver. Hence the RCS of a target is different for monostatic configurations where it is just a function of relative azimuth and elevation angle to the antenna $\sigma(\theta_{ant,}\phi_{ant})$, and bistatic configurations, $\sigma(\theta_{tx,}\theta_{rx,}\phi_{tx,}\phi_{rx})$, where the azimuth and elevation angles are different for the transmitter and receiver. The units are in square-meters and it can be thought of as an effective target area that reflects all incident power in an isotopic manner.

$$P_r = \frac{P_{tx} G}{4\pi R_1^2} \sigma \tag{2.9-3}$$

Therefore, the power density at the receiver can be found by as the reflected power from the target is isotropic and equally spread on a sphere of radius R_2, which is the distance between the target and the receiver.

$$S_e = \frac{P_{tx} G \sigma}{(4\pi R_1^2)(4\pi R_2^2)} \tag{2.9-4}$$

Finally, the received power can be found by multiplying the radiation power density at the receive antenna by the affective area of the antenna.

The monostatic radar equation is used to calculate the expected received power from the reflection of the transmitted wave off a point scatterer with a defined RCS and range.

$$P_{rx} = \frac{P_{tx}\sigma G^2 \lambda^2}{64\pi^3 R^4 L} \qquad (2.9\text{-}5)$$

Where:

- P_{tx} is the peak power transmitted through the transmitter antenna.
- P_{rx} is the peak power received through the receiver antenna.
- σ is the monostatic RCS of the target.
- G is the gain of the antenna, assuming both transmit and receive antenna are the same.
- λ is the carrier wavelength of the propagating signal.
- R is the range between the antenna and the target/region.
- L is a general loss term, which includes atmospheric losses.

It is important to recognise that this equation assumes that the radar transmit and receive antennas are co-located and have the same beam patterns. This approximation holds in the quasi-monostatic case where $R \gg D$, where D is the baseline.

If we know the minimum detectable power (see next subsection), the maximum detection range can be found.

$$P_{rx} = P_{MIN} = \frac{P_{tx}\sigma G^2 \lambda^2}{64\pi^3 R_{MAX}^4 L} \qquad (2.9\text{-}6)$$

Therefore, by rearranging, the maximum detection range is given.

$$R_{MAX} = \sqrt[4]{\frac{P_{tx}\sigma G^2\lambda^2}{P_{MIN}64\pi^3 L}} \tag{2.9-7}$$

2.9.1 Detection of Signals in Noise

Noise is an unwanted electromagnetic signal with random phase and amplitude. The noise power at the receiver end of the radar comes from many sources, it could be solar, atmospheric, manmade to name a few examples, however at sub-THz frequencies the low sensitivity of the receivers means that atmospheric, extra-terrestrial and manmade interference can be ignored. However, even in the presence of no external noise sources, and assuming the receiver does not generate any excess noise, there is still a thermal noise, with energy related to the temperature of the system and frequency response of the receiver [60].

$$N = kB_n T_s N_F \tag{2.9-8}$$

Where:

- N is the mean noise power at the output of the receiver.
- B_n is the noise bandwidth of the receiver.
- k is Boltzmann's constant.
- T_s is the systems noise temperature.
- N_F is the noise factor

The noise factor accounts for the general increase of the noise level that occurs when a component of the receiver generates noise greater than the thermal noise. The noise factor of the receiver can be calculated using the Friis noise equation, however due to the additional gains, the noise factor can be approximated by the low noise amplifier (LNA) noise factor [61]. The receiver noise bandwidth is controlled by the IF frequency response, an integrated bandwidth which can be found by integrating the frequency response of the IF amplifier, rather than the conventional -3 dB bandwidth [60].

$$B_n = \frac{\int_{-\infty}^{\infty} |H(f)|^2 df}{|H(f_0)|^2} \qquad (2.9\text{-}1)$$

Here, $H(f)$ is the frequency response characteristic of the IF amplifier on the receiver end of the radar. The maximum of the frequency response occurs at f_0.

The signal to noise ratio is an important metric to consider the visibility of a target in the presence of noise. The signal to noise ratio (SNR) is defined as the received target power in (2.9-6) divided by the noise power in (2.9-8). An SNR of 0 dB or less indicates that a discrete target will have a similar amplitude to the noise and could therefore be difficult to distinguish in radar imagery without the use of detection processing.

$$SNR = \frac{P_{rx}}{N} = \frac{P_{tx}\sigma G^2 \lambda^2}{64\pi^3 R^4 L k B_n T_s} \qquad (2.9\text{-}9)$$

2.10 The Matched Filter

The matched filter is a term used in signal processing, where it’s output can be found by correlating a known delayed signal, i.e. the transmitted signal, with an unknown signal, i.e. the received signal, to detect the presence of the template signal. In the case for radar, the unknown received signal is a time-delayed, attenuated version of the transmitted signal with added noise. The matched filter is the optimal linear filter that can be used to maximise the

SNR in the presence of additive stochastic white noise added to the received waveform. Hence the impulse response *h*(*t*) maximises the SNR at the output when using an input signal of *s*(*t*) with added noise *n*(*t*).

$$SNR = \frac{|s_{out}(t)|^2_{max}}{N} \qquad (2.10\text{-}1)$$

Here, $s_{out}(t)$ is the voltage of the output signal from the filter and N is the average noise power. The Schawrtz inequality is used to solve the maximisation of *SNR* [62], which occurs when the frequency response of the matched filter is,

$$H(f) = G_a S^*(f) e^{-i2\pi f t_1} \qquad (2.10\text{-}2)$$

Here G_a is the gain of the matched filter, $S^*(f)$ is the complex conjugate of the spectrum of the received signal, and t_1 is the time when the voltage of the output signal is at its maximum. Hence, using Parseval's theorem, the signal energy E is equivalent to the sum of the square of the spectrum of the received signal.

$$SNR_{max} = \frac{2E}{N_0} \qquad (2.10\text{-}3)$$

Here N_0 is the power spectral density of the noise measured in W Hz^{-1}.

2.10.1 Matched Filter for Frequency Dependant Noise

The above examples are valid for the case where the noise at the input of the matched filter is white. However, the noise spectrum may be frequency dependent. In which case the response takes a different form.

$$H(f) = \frac{G_a S^*(f)^{-i2\pi f t_1}}{|N_{in}(f)|^2} = \frac{1}{N_{in}(f)} G_a \left(\frac{S(f)}{N_{in(f)}}\right)^* e^{-i2\pi f t_1} \qquad (2.10\text{-}4)$$

The expression is presented in a form where there are two filters. The first filter is the reciprocal of the frequency dependant noise input, which is known as a whitening filter, which converts the frequency dependant noise into a white noise spectrum. The second term is a variation of the matched filter.

A filter with an impulse response of $h(t)$ has an output $s_{out}(t)$ that is defined by the convolution of the impulse response with the input signal $s_{in}(t)$, where the signal contains returns off the target and noise.

$$s_{out}(t) = \int_{-\infty}^{\infty} s_{in}(t')h(t-t')\,dt' \qquad (2.10\text{-}5)$$

The impulse response of the matched filter is the Fourier transform of the frequency response, which is the same as the time reversed signal received from the target without the presence of noise.

$$h(t) = G_a s(t_1 - t) \qquad (2.10\text{-}6)$$

Here, t_1 again refers to the time where the filter output signal is at a maximum, hence (2.10-5) can be expressed as,

$$s_{out}(t) = G_a \int_{-\infty}^{\infty} s_{in}(t')s(t_1 - t' + t')dt' \qquad (2.10\text{-}7)$$

From this it is seen that the output of the matched filter is proportional to the cross correlation of the received signal with added noise and the time reversed, delayed complex conjugate of the transmitted signal.

$$s_{out}(t) = G_a X(t - t_1) \tag{2.10-8}$$

Here $X(t\text{-}t1)$ is the cross-correlation function and so the matched filter output is proportional to the cross correlation of the time reversed conjugate of the transmitted signal after some delay.

2.11 Linear FMCW radar

FMCW radars rely on the frequency modulation of the transmitted CW to construct a range profile of the scene. Specifically, linear FMCW radar signals take the form of a ‘chirp’, where the frequency increases or decreases directly proportional with time. The derivation of the chirp waveform processing is demonstrated in [63], which is supported by information from [64] which shows that the homodyne Rx is equivalent to the matched filter. The goal is to process the received waveform into a signal of Intermediate Frequency (IF) which can be processed to obtain range and Doppler data. The instantaneous transmitted frequency is shown in (2.11-1).

$$f(t) = f_0 + \alpha t \tag{2.11-1}$$

Here, f is the instantaneous frequency, f_0 is the initial starting frequency of the chirp, α is the rate of change of frequency know as the chirp rate, and t is the time. Hence the phase of the transmitted waveform can be expressed as,

$$\emptyset(t) = 2\pi\int_0^t f(t)dt = 2\pi\left[f_0 t + \frac{1}{2}\alpha t^2\right] \tag{2.11-2}$$

Where $\emptyset$ is the phase of the signal at time t. In fact, the most general expression also includes an arbitrary start phase, a detail which Stove neglected, but as this is subtracted in the homodyne receiver it may be ignored. The transmitted linear FMCW waveform can then be expressed as a sinusoid with amplitude A_{tx}.

$$s_{tx}(t) = A_{tx} sin\left(2\pi\left[f_0 t + \frac{1}{2}\alpha t^2\right]\right) \tag{2.11-3}$$

Here $s_{tx}(t)$ is the transmitted signal. Assuming the signal reflects off a point scatterer at a range of $R = \tau c/2$ meters, the received waveform after the time delay of τ is expressed as,

$$s_{Rx}(t) = A_{Rx}\ sin\left(2\pi\left[f_0(t-\tau) + \frac{1}{2}\alpha(t-\tau)^2\right]\right) \tag{2.11-4}$$

Here, $s_{Rx}(t)$ is the received signal, which is seen as the time-delayed transmit waveform. By mixing the received signal with the transmitted signal in real time, which is equivalent to multiplying the two signals, a new signal is produced where the IF signal may be extracted.

$$s_{Rx}(t)s_{tx}(t) = A_m sin\left(2\pi\left[f_0 t + \frac{1}{2}\alpha t^2\right]\right) sin\left(2\pi\left[f_0(t-\tau) + \frac{1}{2}\alpha(t-\tau)^2\right]\right) \tag{2.11-5}$$

Here A_m is the amplitude of the mixed signal. Using the 'product-to-sum' trigonometric identities, (2.11-5) can be expressed as the difference of two cosine functions in (2.11-6), where the first term refers to the signal with the IF.

$$s_{Rx}(t)s_{tx}(t) = A_m \left[\frac{cos\left(2\pi \left[f_0\tau - \frac{1}{2}\alpha\tau^2 + \alpha t\tau\right]\right)}{2} - \frac{cos\left(2\pi \left[\frac{1}{2}\alpha\tau^2 - f_0\tau + (2f_0 - \alpha\tau)t + \alpha t^2\right]\right)}{2} \right] \quad (\ 2.11\text{-}6\ )$$

The first term in the square brackets is a signal containing the beat frequency, which is constant and is related to the chirp parameters and the receive time delay, but is independent of the carrier signal (f_0t). The second term in the brackets contains no additional information and can be rejected using a low pass filter (LPF).

$$S_{IF}(t) = A_{IF}\cos\left(2\pi\left[f_0\tau - \frac{1}{2}\alpha\tau^2 + \alpha\tau t\right]\right) \quad (\ 2.11\text{-}7\ )$$

Here, A_{IF} is the amplitude of the intermediate signal. The first two terms in the square parenthesis are time independent and only depend on the delay and just set the initial phase of the intermediate signal at t=0. The third term is time dependent. Hence by taking the time derivative of the phase, and dividing it by 2π, the beat frequency, f_{beat}, is found as

$$f_{beat} = \alpha\tau = \frac{2\alpha R}{c} \quad (\ 2.11\text{-}8\ )$$

The above relation shows how the beat frequency is related to the range of the target. Therefore, by taking the Fourier transform of (2.11-7), the resulting spectrum is defined as a range profile, where the frequency can be related to range through (2.11-8).

In general, the point scatterer will have some radial velocity relative to the radar antenna, hence the range is dependent on time, and so is the time delay.

$$r(t) = r_1 + vt$$

$$\tau = \frac{2r(t)}{c} = \frac{2(r_1 + vt)}{c} \qquad (\ 2.11\text{-}9\ )$$

Hence by direct substitution the IF becomes,

$$S_{IF}(t) =$$

$$A_{IF} \cos \left(2 \left[\frac{2r_1}{c} \left[f_0 - \frac{\alpha r_1}{c} \right] + \frac{2 f_0 v t}{c} + \frac{2 r_1 \alpha t}{c} \left[1 - \frac{2v}{c} \right] + \frac{2 \alpha v t^2}{c} \left[1 - \frac{v}{c} \right] \right] \right) \qquad (\ 2.11\text{-}10\ )$$

It is now apparent that as well as the range dependent term discussed in (2.11-7), there is now a frequency term dependent on velocity, $2f_0vt/c$, which is the well-known Doppler shift. Another cross term appears, which can be interpreted as the effect of the ramping transmitter frequency on the Doppler shift, or a chirp on the beat frequency due to the changing range of the point scatterer.

2.12 Range Resolution

Range Resolution can be described as the radar's ability to distinguish the returns off two separate point targets in terms of their range from the antenna, or, equivalently, the time delay before receiving the returned signals from the two targets. Assuming the pulse is rectangular, the minimum separation in time between returns is usually used to quantify the range resolution, where the returns have a pulse width of τ_p at the output of the matched filter. This pulse width is usually defined at the FWHM of the maximum pulse power, i.e., the -3dB pulse width [65], although this is an approximation.

$$\Delta f_{3dB} \approx \frac{1}{\tau_p} \tag{2.12-1}$$

For monostatic radars, the example of two-point targets separated in range from the antenna is illustrated in Figure 2.12-1.

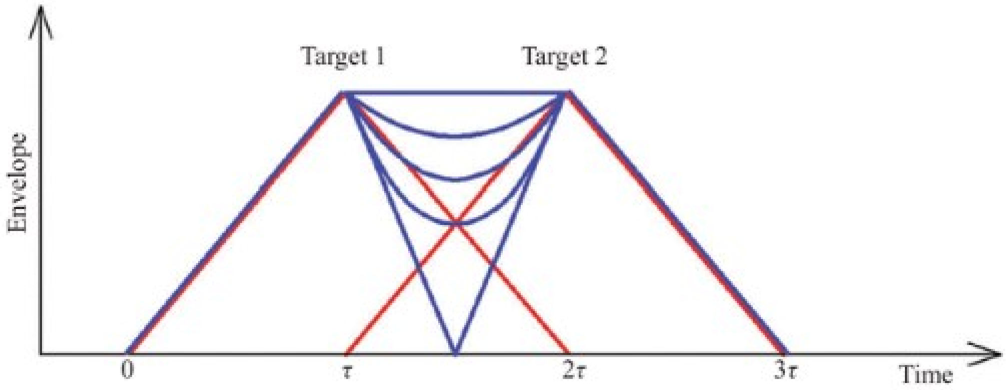

Figure 2.12-1 Matched filter output for two closely spaced targets, red shows matched filter output for each individual target, blue shows the potential output of the matched filter for two closely spaced targets depending the relative phases of each target. Image taken from [65].

In Figure 2.12-1, target 1 is separated from target 2 by a range of *ΔR* which is used to denote the range resolution. Hence target 1 can be resolved from target 2 in a range profile.

As the targets are separated in range from the antenna by *ΔR*, hence the extra round-trip distance the pulse travels between the two targets is 2*ΔR*. As discussed before, the required signal delay for the two targets to be resolved is τ_p, and so the minimum spatial distance *2ΔR* can be is $c\tau_p$, hence,

$$\Delta R \approx \frac{c\Delta t}{2} = \frac{c\tau_p}{2} \tag{2.12-2}$$

The generic time resolution term Δt is used here, which in pulse radar is the same as the pulse width. The above derivation assumes that the targets are point like and effectively demonstrates the best-case scenario. In practice, to be confident we can separate the returns of two point targets in range, we need them to be separated by twice the range resolution. For example, using a strong windowing function, as discussed in section 2.14.2, may result in the decrease of the range resolution (poorer range resolution), to the point where the targets become indistinguishable, even though separated by ΔR.

For Linear FMCW radar, the time resolution that corresponds to the frequency resolution in (2.12-1) is defined by the chirp rate, α, which is the FMCW bandwidth, B, divided by the pulse width.

$$\Delta t = \frac{1/\tau_p}{B/\tau_p} = \frac{1}{B} \qquad (\ 2.12\text{-}3\ )$$

Substituting (2.12-3) into (2.12-2) shows that the FMCW range resolution is inversely proportional to the bandwidth.

$$\Delta R \approx \frac{c}{2B} \qquad (\ 2.12\text{-}4\ )$$

2.13 Forming an Image Pixel using range and cross-range resolution

The previous subsection discussed the radar's ability to resolve point targets in range, however the range alone is only part of that describe the targets spatial position. To find the targets spatial position, the position in angular azimuth and elevation directions must also be known, which when combined with range, forms a set of polar co-ordinates.

Like the range resolution, the angular resolution is an estimate of the spatial separation between two point-like targets, so that they may be resolved in angle. For monostatic radar, the angular resolution is defined as the -3 dB (one way) beamwidth of the antenna pattern, θ_{BW}, illustrated in Figure 2.6-4 and show in (2.6-12). From this, the area of a pixel within the radar image can be formulated.

$$A_{pixel} \approx R\theta_{BW}\Delta R \tag{2.13-1}$$

2.14 The Doppler shift and Doppler resolution

The Doppler shift occurs when there is relative non-zero velocity between the radar antenna and the reflector, where the received radar signal changes in frequency relative to the transmitted signal, by the amount of Doppler shift.

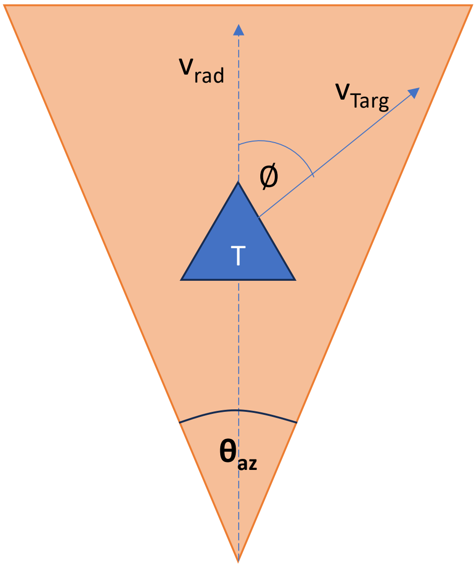

Figure 2.14-1 Field of View encompassed by -3 dB azimuth beam width, with the target having a velocity v_{Targ} directed at an angle of ∅ from the radial vector.

For a monostatic radar, for the case illustrated in Figure 2.14-1, the Doppler frequency is given by,

$$f_D = \frac{2v_{rad}}{\lambda} = -\frac{2v}{\lambda}\cos(\emptyset) \tag{2.14-1}$$

Here, v is the velocity of the target, $\emptyset$ is the angle between the velocity vector and the radial vector, and λ is the carrier signal wavelength. Following this, the Doppler frequency, f_D, as measured by the radar can then be used to find the velocity of the target, v_{rad}, by rearranging (2.14-1). To resolve two separate Doppler frequencies within the received signal, the required separation in Doppler frequency is defined as,

$$\Delta f_D \approx \frac{1}{\tau} \tag{2.14-2}$$

where τ is the coherent integration time of the received radar signal. Hence the velocity resolution is also determined as,

$$\Delta v_{rad} \approx \frac{\lambda}{2\tau} \tag{2.14-3}$$

The separation in (2.14-2) is usually defined by the -3dB bandwidth of the spectra, which is approximately the inverse of the integration time. In the case the reflector is accelerating, this will lead to a change in Doppler frequency over time, and if this is comparable to the Doppler resolution it will lead to significant spectral smearing. The higher the integration time, the better (smaller) the Doppler resolution is. Longer integration times may lead to more smearing between the finer Doppler resolution cells as the change in Doppler frequency required to smear is smaller and there is more time for the target to accelerate to higher/lower velocities. Much like the case with the range resolution, any windowing applied to the signal may broaden the spectral response, and as a result it will reduce the Doppler frequency resolution and therefore the velocity resolution for point targets.

2.14.1 Digital processing of FMCW signals

For Sub-THz radar, the front end signal processing occurs through the hardware components due to the high frequency of the signals, which are much higher than the sampling rates of the analogue to digital converter (ADC). The IF signal, however, may easily have a bandwidth lower than half the ADC sampling rate, and can therefore be formed into a digital signal that can be processed on a computer. Limitations therefore arise from the ADC sampling rate S_{ADC}. The number of samples recorded from the ADC is,

$$n_{fast} = S_{ADC} \times T_{chirp} \qquad (\ 2.14\text{-}4\ )$$

The number of samples n_{fast}, is named as such as it records each sample in 'fast time', i.e, the samples that form one chirp. Therefore, the frequency resolution is the inverse of the chirp duration, the maximum unambiguous frequency is the half of the ADC sampling rate, according to the Nyquist frequency [66]. As for general purpose surveillance, targets need to be detected at any range, the bandwidth is equal to the maximum IF. Therefore, generally, S_{ADC} should be twice the maximum IF.

From a digital point of view, the range resolution can also be derived from the frequency resolution of the FFT and the frequency to range conversion equation. As the frequency resolution is the inverse of the chirp duration, and the rate of change of frequency of the chirp is defined,

$$R_{res} = \frac{c\Delta f}{2\alpha} = \frac{c}{2\alpha T_{chirp}} = \frac{c}{2B} \qquad (\ 2.14\text{-}11\ )$$

The maximum unambiguous range is the furthest distance the radar can measure a targets range, before the range data becomes ambiguous, i.e, confused for another chirp. For the maximum unambiguous range, the Nyquist frequency from the sampling rate is used in the frequency to range conversion equation.

$$R_{max} = \frac{S_{ADC}T_{chirp}}{2} \times \frac{c}{2B} = \frac{cS_{ADC}}{4\alpha} \qquad (2.14\text{-}12)$$

Therefore, to improve the maximum unambiguous range, a higher ADC sampling rate is required. At the cost of having a poorer range resolution, a slower sweep may also be used to increase the maximum unambiguous range. It is also important to realise that the unambiguous range is directly proportional to the chirp duration. Therefore, by increasing the PRF for Doppler measurements (Increasing the maximum unambiguous Doppler), the maximum allowed chirp duration is decreased, and therefore the maximum possible unambiguous range is also decreased. Therefore, it is important to use the an adequate sampling rate for the ADC to obtain radar data that achieves reasonable maximum unambiguous range to detect targets at the required ranges. The maximum speed of the antenna platform is limited by the need to have a high enough PRF to avoid aliasing in the Doppler profiles.

2.14.2 Windowing

As described in the previous sub-section, the FFT of the IF signal results in the range profile. Window functions can be multiplied with the time domain IF signal data before the FFT to reduce the amplitude of the discontinuities that are found at the edges of the finite time domain data. By reducing the amplitude at the edges, the appearance of side-lobes related to the discontinuity are reduced after the FFT. As the windowing process reduces the information in the time domain, the effective resolution after the FFT is also reduced.

$$B_{Res} = \frac{B_{win}^{N}}{T} \tag{2.14-13}$$

Where B_{Res} is the resolution bandwidth after the application of the window. B_{win}^{N} is the effective number of data samples after windowing divided by the chirp period, T. Choosing an appropriate windowing function is an important task which involves a trade-off between resolution and sidelobe level. Note that when this is performed in the digital domain, as in the range and Doppler processing, some options become possible which are physically unrealisable for the equivalent task of defining the antenna pattern. An obvious example is the family of Dolph-Chebychev windows [67].

Window functions such as the Blackman-Harris window drastically reduce the sidelobes but essentially half the range resolution. In this thesis the N-point symmetric four-term window is used during Range and Doppler processing, which can have a sidelobe reduction level of 90 dB [68]. This window was used to ensure the processed radar imagery had no visible sidelobes, making the image clear and easy to understand. The radar parameters which will be discussed in chapter 5 and 6 were selected to provide range resolutions of 3 cm, hence the reduction in resolution when using the Blackman-Harris window was deemed an acceptable trade off.

2.15 Electromagnetic scattering in the maritime environment

As explained in section 2.6, the RCS of a target is important to understand how the signal reflects off a single target. However, in the maritime scene, there are many scatterers that will affect the observed RCS in a region of the radar image. For example, flotsam and jetsam may lead to differences in texture on the surface, and breaking waves may lead to small microstructures that scatter the incident radar signal much more than a swell wave which is a distinctive feature of radars above 60 GHz [69], where at low grazing angles, the returns come from the breaking wave crests [70]. Models that describe the expected distributions from the backscatter from literature are presented in this section.

2.15.1 Specular reflections

Specular reflections occur when the angle of incidence from the incoming radar signal is equal to the angle of reflection, so the scattering surface appears as a mirror. When the reflector is smooth in texture, i.e. the surface variation is much smaller than the wavelength of the radar signal, specular reflections dominate.

Hence the strongest returns from a specular surface in monostatic radar occur when the angle of incidence, and hence the angle of reflection, is equal to zero as the radar signal is reflected directly back toward the receiver.

Periodic surface gravity waves created by the circular flow of water particles on the surface leads to the formation of a set of trochoidal waves, with a smooth edge. In practice the waves will have a detailed surface texture, however the trochoidal wave is useful in modelling the specular reflection component from the waves.

2.15.2 Diffuse scattering

As the standard deviation in surface height normal to the radar signal, i.e. the texture, becomes comparable to the wavelength of the incident radar signal, diffuse scattering begins to become more significant in terms of the mechanism that scatters the most energy.

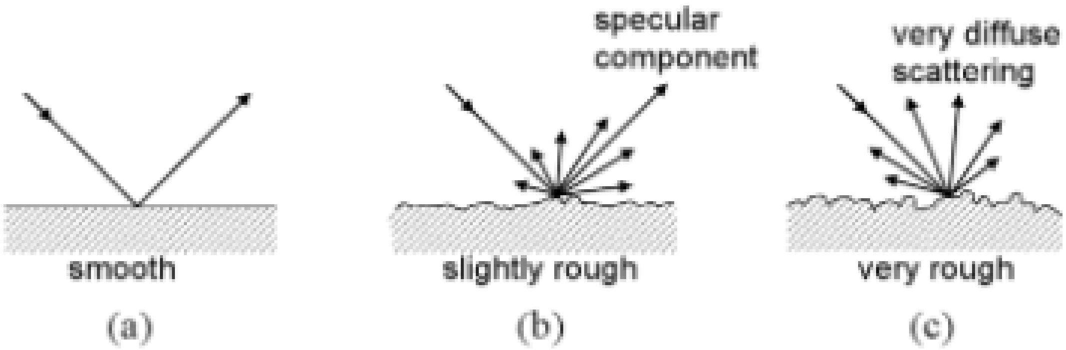

Figure 2.15-1 The occurrence of diffuse scattering as surface roughness increases [71].

Diffuse scattering occurs as the reflected waves off the surface begin to interfere with varying phase differences, creating a unique scattering pattern. The Rayliegh Roughness Criterion is used to define the limit for which the surface is considered “rough” [72].

$$h > \frac{\lambda}{8\cos(\theta)} \tag{2.15-1}$$

As the surface roughness approaches the wavelength of the incident radiation, the mechanisms which cause specular scattering in well-defined directions break down and the scattering becomes diffuse, over many directions. This is analogous to Lambertian scattering in optics and often follows a similar angular distribution.

2.15.3 Bragg scattering

Illuminated surfaces that are locally periodic lead to Bragg scattering. The microscopic scattering is similar to specular scattering except that the scattered signal is spatially modulated by the periodicity of the reflector so the directions in which the scattered signals add up coherently are changed, depending on the wavelength of the signal, the periodic spacing of the reflectors and the angle of incidence.

$$n\lambda = 2dsin(\theta) \tag{2.15-2}$$

Here, *d* is the average distance between two of the scatterers in the periodic structure known as the grating constant, n is the order, θ is the glancing angle (which is 90 degrees minus the angle of incidence).

2.16 Sea Clutter

An important topic to cover in this thesis is the presence of background clutter, specifically sea clutter, which is defined as backscattering associated from the sea waves, ripples and spray. It is usually defined under the context of unwanted backscattering off the sea surface, however as outlined in the introduction, some of the backscattered returns from the surface may indicate the presence of dangerous waves, or shadowed targets that change the dynamic of the local surface. Such phenomena can lead to "cluttered" radar imagery, where regions dominated with sea clutter may reduce the contrast of targets, and result in the reduction in performance of target detection techniques, where improvement of the signal to clutter ration (SCR) needs to be considered. Detection techniques must also be able to differentiate regions of clutter (which may be safe for the marine craft to pass) from unsafe regions. Hence, an understanding of the sea clutter statistics will be required to configure the anomaly detector to be able to classify the returns from the surrounding sea clutter and differentiate targets as anomalies by their distribution which will be inherently different from that of the sea clutter feature distributions. The appearance of sea clutter will also depend on the image processing algorithm used to form imagery and this will need to be considered during the detection process.

2.16.1 Sea wave mechanics

Waves on the sea surface are a result of many different physical mechanisms that define the dynamic and shape [73]. Swell defines waves that are driven by the wind, and tend to appear sinusoidal, with large wavelengths, and wide crestlines. Furthermore, the period of swell waves can be from six seconds to sixteen. When the depth of the sea is more than half a wavelength, the waves can be assumed to be deep water waves, where the sea floor has no effect on the dynamic of the waves. Waves where the significant restoring force on the perturbed mass of water is the weight of the water in the wave itself are referred to as gravity waves and have wavelengths greater than 1.7 cm. Waves with wavelengths smaller than 1.7 cm have surface tension as the significant restoring force and are referred to as capillary waves. The principle mechanism is Bragg scattering, at High Frequency radar it originates from the whole wave, at uW it comes from the gravity waves, so for sub-THz frequencies, Bragg scattering may originate from capillary waves.

2.16.2 Sea states

The sea state is a measure of the surface roughness of the sea, which is defined by the significant wave height. The significant wave height, denoted H1/3, is defined as the mean peak to trough height of the highest 1/3 of the waves present on the surface. In literature there are a few models that are used, for example Douglas Sea state, and the WMO sea state.

Table 2.16-1 Douglas sea state parameters [74].

Douglas Sea State	Wave Height, $H_{1/3}$ [m]	Wind Speed [kn]	Description
1	0 to 0.305	0 to 3.087	Smooth
2	0.305 to 0.914	3.087 to 6.173	Slight
3	0.914 to 1.524	6.173 to 7.717	Moderate
4	1.524 to 2.438	7.717 to 10.289	Rough
5	2.438 to 3.658	10.289 to 12.861	Very Rough
6	3.658 to 6.096	12.861 to 15.433	High
7	6.096 to 12.192	15.433 to 25.722	Very High

The Douglas Sea state is used in this thesis as work from Nathanson on sea clutter reflectivities is based on the Douglas sea state [75].

2.16.3 Sea clutter RCS

Much like the RCS of a target, an area of illuminated sea surface can have an RCS which is dependent on the shape of the surface at a given time, and hence the environmental parameters such as sea state and wind speed which will define the surface wavelengths and amplitude. For small grazing angles and narrow beamwidths, the area of an illuminated patch of sea, in a single range resolution cell is given as,

$$A_{cell} = R\theta_{az}\Delta R \tag{2.16-1}$$

Where A cell is the area illuminated in a range cell, R is the range of the cell from the antenna, θ_{az} is the azimuth one-way beamwidth of the antenna and ΔR is the range resolution for a single cell as defined in (2.12-2). As the normalised backscatter coefficient is defined by the RCS divided by the area of the cell,

$$\sigma_{clutter} = R\theta_{az}\Delta R\sigma_0 \tag{2.16-2}$$

2.16.4 Sea clutter Empirical models for Low grazing angles

The work done in Nathanson presents empirical models for the backscatter off the sea surface for 'low' Grazing angles at different frequency bands. The values of the normalised mean backscatter have been determined for frequencies up to 35 GHz (Ka band), for various grazing angles. This serves as a reference to see if the measured normalised backscatter coefficients at sub-THz frequencies fit the model and can also be used to estimate the performance of sub-THz radar for sea clutter measurements. For frequencies greater than Ka band, sea clutter data is limited in literature.

2.16.5 Sea Clutter spikes

The sea clutter will present itself as a mixture of smooth modulations and clutter spikes, which together result in the non-Gaussian distribution of the clutter [76]. Wave-like modulation which likely arises from Bragg scattering off the surface contributes to the spikiness, although the return itself is not formed of spikes, due to the high intensity of the reflected signal. The clutter spikes appear in two classes which are easy to identify with how they evolve in time. Short spikes, often referred as *bursts*, typically last around 200 ms, with a low amount of fluctuation. Burst scattering appears to originate from the specular reflection that occurs in the short moment a wave crest begins to spill. Longer spikes, referred to as *whitecaps*, last over a second and fluctuate like noise, which decorrelate within a few milliseconds. They also have a wider Doppler spectrum. The name whitecap is also a visual descriptor of the type of phenomena on the surface that causes these scattering events.

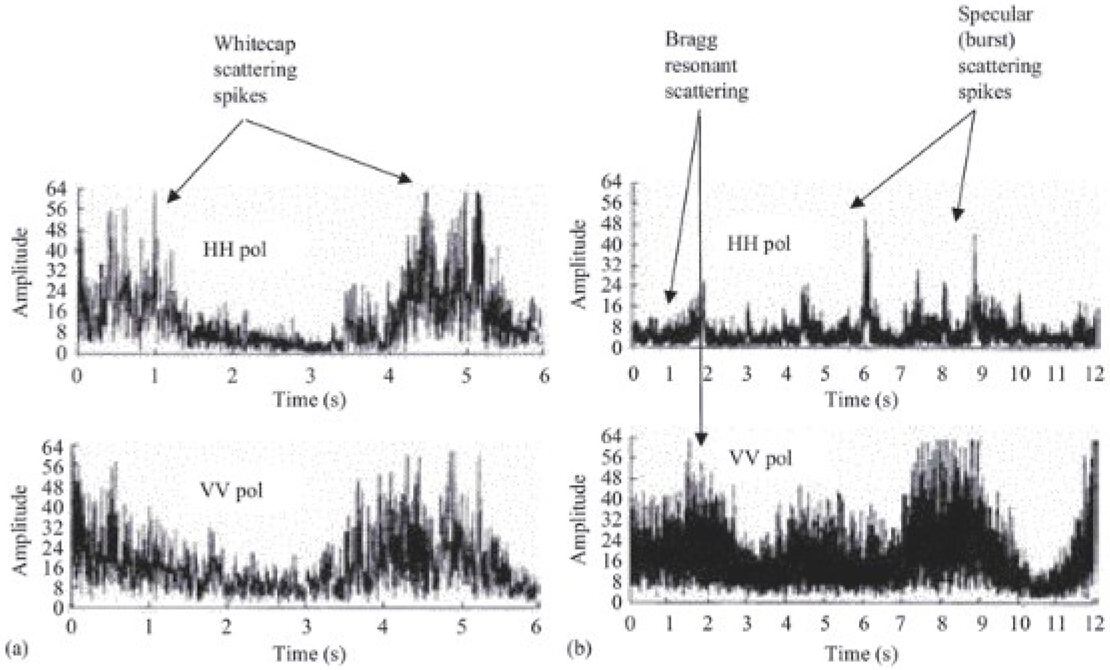

Figure 2.16-1 Simultaneous pulse-by-pulse histories of a single range clutter cell at HH and VV taken from [76].

3 Doppler Beam Sharpening

This chapter describes the DBS methodology, the required measurements for DBS processing and how the parameters affect the resulting image quality using various models. It also explains how DBS processing is affected in the dynamic marine environment and how target motion may defocus the image.

Using the DBS/SAR modality and DBS processing it is expected that the data collected from the radars, as they move along a track, can be used to form high resolution in the range and cross range directions, by forming synthetic apertures by using the range-Doppler domain to refine the beam. A result from Figure 2.15 shows the capability of DBS in lab conditions.

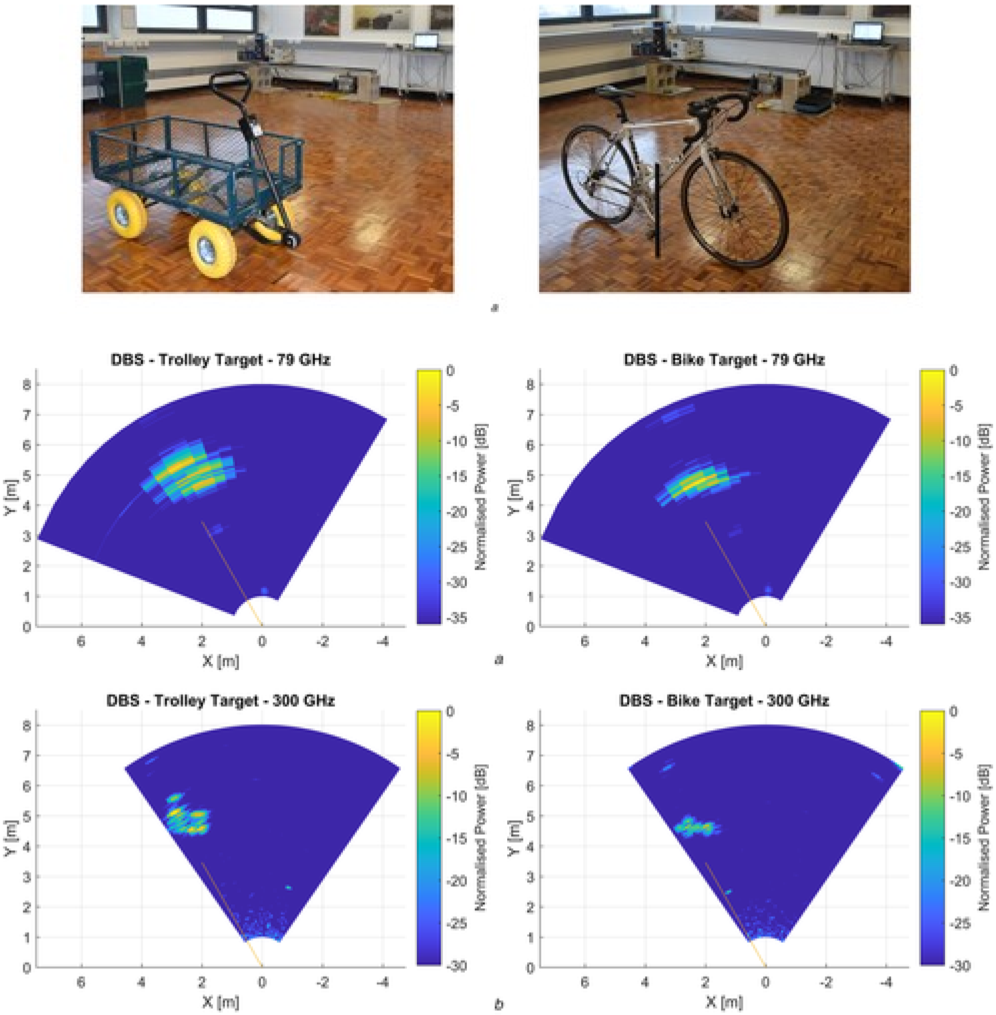

Figure 2.16-1 DBS experiment in lab conditions using 79 GHz and 300 GHz radars, measuring returns from a trolley and bike, taken from [77].

3.1 Doppler Beam Sharpening Literature Review

DBS was first introduced along with the advancements of the methodology of SAR by Carl A. Wiley in a 1951 Goodyear aircraft report [78]. The original motivation was to improve the resolution of the radar for airborne platforms, whilst using relatively small antenna. The idea was conceived by analysing the data collected in the SAR modality, utilising the motion of the antenna to form a synthetic aperture, through the frequency domain (DBS) rather than the time domain (SAR).

The methodology of DBS is explained later in this chapter; however, it may be summarised as the use of the platform's motion to link the Doppler signature of a stationary target within the radar beam with a specific azimuth angle, hence partitioning the physical beam into smaller synthetic beams, and therefore improving the cross-range resolution and imaging capability of the radar system. DBS has already been well established for airborne radar [79] where it has been described as a form of unfocused strip map SAR.

In modern times, the motivation to use high resolution in radar, particularly in the cross-range dimension(s) has been strengthened by the demands of autonomous systems to produce high resolution radar imagery that can be used for many different applications. In the context of automotive radar, the benefits of using Sub-THz radars to provide high resolution imagery, along with its practical advantages are well known [80]. The high resolution radar imagery from Sub-THz radar has been used for scene segmentation which can lead to viable path planning [81].

Doppler Beam Sharpening has already been proven to be an effective method to refine the azimuth resolution for Sub-THz radar in controlled conditions [77]. It was found that the combination of low-THz carrier frequencies and DBS processing achieved cross range resolutions on the same order of the achievable range resolution after range compression, on the order of centimetres. At these resolutions it becomes feasible to image targets and classify them according to their shape in the image.

The Doppler centroid gives the targets position, and so efforts to extract the target location have been implemented on DBS imagery. For example, the use of morphological edge detection coupled with DBS processing has shown promise that target position can be accurately measured from DBS processing [82].

Modern applications of maritime DBS have been demonstrated from remote platforms such as satellites or aircraft, where the variation in platform motion is less problematic for the DBS processing. It has been shown effective for the detection of ship targets [83]. However, the application of sub-THz radar maritime DBS processing using a surface maritime vessel as the antenna platform is novel. Current methods rely on imagery produced from physical apertures that mechanically rotate, and the use of azimuth refinement for stand-alone small vessels has not yet been researched. This is likely due to the non-stationary environment and non-stationary antenna making SAR like processing techniques very difficult to apply. When necessary, motion compensation techniques must be employed to SAR processing to stabilise the synthetic aperture and create focused imagery [84]. These motion compensation techniques have proven invaluable on airborne SAR, where the target dwells within the beam during the integration time and unwanted antenna motion usually from bad weather does not affect the dwell time significantly. However, at sea, the roll pitch and yaw of the platform and targets, are much more significant than airborne antenna, and therefore the dwell times of targets may be much shorter, and such motion compensation techniques need to be modified for use on maritime platforms.

Generally, the larger the area that is imaged, the better the situational awareness, and therefore the more effective the system will be at detecting and avoiding obstacles. Algorithms that stitch DBS processed image frames together have been demonstrated as an essential step for increasing situational awareness [85], and details the importance of accurately measuring the antenna kinematics.

3.1.1 Combining DBS and MIMO techniques

DBS has been investigated in some research for in automotive radar and has yielded promising results by combining it with other processing techniques to improve the resulting imagery. For example, super resolution processing coupled with DBS has shown good capability to image objects such as cars with superior resolution [86]. Another example is often, forward-looking, that is looking in the direction of motion of the vessel, multiple input multiple output (MIMO) radar and DBS processing are combined to image regions of ambiguity in DBS imagery [87]. The research for the application of DBS and SAR in forward-looking radar w.r.t the platform velocity vector is important as this region is the most likely to contain obstacles in the vessel's path, presenting danger of collision. It is also this region where the effectiveness of DBS is reduced due to Doppler ambiguity and the "blind zone", the region where the Doppler spread of stationary targets vs azimuth is less than the Doppler resolution [88]. The Doppler bandwidth is limited in the forward-looking direction, which means the synthesised cross-range resolution will be poor compared to the side-looking case. Methods to increase the Doppler bandwidth and the combination of MIMO, DBS and SAR processing has shown promise to be a good solution for these issues as outlined below.

Processing such as Unambiguous Doppler-based Forward-looking MIMO radar Beam Sharpening Scan (UDFMBSC) in [89] has been used to solve Doppler ambiguity by combining DBS processing with MIMO array processing, assuming that Doppler is symmetric about the boresight, i.e squint angle is zero, and that symmetric targets have a similar reflectivity which is unlikely in a real automotive measurement. An FFT is applied to the angle vector, and peaks of the auto-convolution were used to identify the number of targets in a range doppler cell. The method was further developed using the 'Robust Unambiguous DBS with Adaptive Threshold' (RUDAT) methodology in [90],

The FL-sparseMIMO-SAR method appears to solve the issues of the Doppler blind zone, by using sidelobe suppression and sparse MIMO, there are large physical aperture forward-looking blind-zone, resulting in fine cross-range resolutions in the forward looking region that do not solely rely on the azimuth refinement from DBS [91]. The benefit of using this method is the maintenance of the fine cross range resolution at all squint angles.

The DBS technique has found many uses besides its original purpose of azimuth resolution refinement to provide enhanced radar imagery. In the mitigation of automotive interference, where signals received by a victim radar from an interfering radar, it has shown that DBS shifts the interference beam is both shifted from its original location due to Doppler shift between interfering and victim radar and the interference is typically supressed by 10log(N) dB, as the interference has a random phase shift across the sub-beams formed in DBS processing [92], i.e, the interference spectrum is much wider than the Doppler resolution cell [93].

This literature survey has found that currently implemented sensing systems are not optimised for providing small vessels with the data required for full situational awareness in any marine environment. It also found that the research on providing autonomy in the automotive domain is mature and may hold answers into providing the same functionality in the maritime domain. Although the research into maritime DBS is in its infancy, many of the techniques discussed above for automotive DBS may be adapted for use in the maritime environment, and it is therefore important that DBS is explored for maritime situational awareness.

3.2 Doppler Beam Sharpening Image Processing Methodology

In short, DBS uses the motion of the antenna to form a synthetic aperture, where the Doppler frequency measured from the signal scattered off the target is used to estimate the azimuth angle with respect to the antenna velocity vector. Hence, DBS requires the platform to move with a known velocity which is measured relative to the 'background' reference frame, within which the target is assumed to be stationary, although the extension to moving targets will be considered later in this chapter. For practicality the 'background' reference frame is the same reference that GPS uses, known as the International Terrestrial Reference Frame (ITRF) [94]. The typical setup for DBS is seen in Figure 3.2-1.

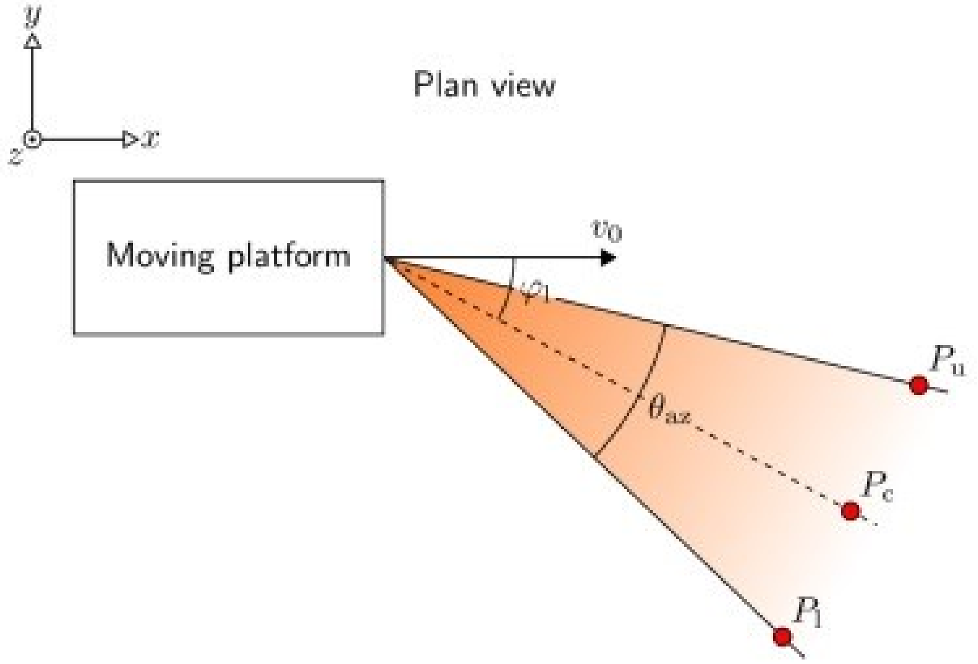

Figure 3.2-1 Doppler Beam Sharpening platform setup taken from [77].

As seen in Figure 3.2-1, the physical beam has a one-way (3dB) beamwidth of θ_{az}. The two lines denoted by P_u and P_l are the upper and lower positions in the physical beam., v_0 is the velocity vector of the moving platform. The squint angle denoted φ_1 defines the angle between the velocity vector of the platform and the boresight vector of the antenna.

A target that is stationary in the beam will be measured as having a radial velocity relative to the moving antenna, and therefore a Doppler frequency associated with it.

$$f_d^c = \frac{2v_0 f_0}{c} \cos\left(\varphi_1\right) \tag{3.2-1}$$

where $v_0 << c$ is the platform velocity, f_0 is the central carrier frequency, assuming the FMCW bandwidth is narrow, and φ_1 is the squint angle. From here, we see that faster platform velocities will achieve larger Doppler frequencies as well as higher carrier frequencies. A squint angle of ninety degrees, i.e perpendicular to the motion of the platform achieves a Doppler frequency of zero. When the squint angle approaches zero, the relative radial velocity of the point target becomes the negative of the platform speed, and for squint angles below zero degrees, the Doppler frequency becomes ambiguous with the positive valued squint angles of the same magnitude.

The width of a single Doppler bin is the inverse of the integration time, τ:

$$\Delta f_d = \frac{1}{\tau} \tag{3.2-2}$$

Within the beam, there will be a spread of Doppler frequencies depending on the positions of the various targets within the beam. To find the total spread of Doppler frequencies, point targets on the extreme sides of the beam width are considered and the difference gives the total Doppler Spread.

$$f_d^u = \frac{2v_0 f_0}{c} \cos\left(\varphi_1 - \frac{\theta_{az}}{2}\right) \tag{3.2-3}$$

$$f_d^l = \frac{2v_0 f_0}{c} \cos\left(\varphi_1 + \frac{\theta_{az}}{2}\right) \tag{3.2-4}$$

Hence the total Doppler Spread can be shown and simplified using the sum of angles trigonometric identity for the cosine function.

$$\Delta f_{d,spread} = f_d^u - f_d^l = \frac{2v_0 f_0}{c}\left(cos\left(\varphi_1 - \frac{\theta_{az}}{2}\right) - cos\left(\varphi_1 + \frac{\theta_{az}}{2}\right)\right) \tag{3.2-5}$$

$$\Delta f_{d,spread} = \frac{4v_0 f_0}{c}\sin(\varphi_1)\sin\left(\frac{\theta_{az}}{2}\right) \tag{3.2-6}$$

The spread of Doppler frequencies in the beam can be divided by the resolution of a single Doppler cell found in (3.2-2) to find the number of resolutions cells that the beam can be partitioned by. This is known as the refinement factor and defines how many times the azimuth resolution can be improved.

$$n = \frac{\Delta f_{d,spread}}{\Delta f_{bin}} = \frac{4v_0 f_0 \tau}{c}\sin(\varphi_1)\sin\left(\frac{\theta_{az}}{2}\right) \tag{3.2-7}$$

By dividing the physical antenna beam width by the resolution factor, the synthetic beam width is calculated and therefore the refined cross-range resolution.

$$\Delta\theta_{az}^r \approx \frac{\theta_{az}}{n} \tag{3.2-8}$$

$$\Delta r_{cr}^r \approx \frac{r_{cr}}{n} \tag{3.2-9}$$

Here, Δr_c^r is the new cross-range resolution, which is range dependant, and r_{cr} is the cross range resolution derived from the physical aperture. The synthetic azimuth resolution is completely described by:

$$\Delta\theta_{az}^r \approx \frac{c\theta_{az}}{4v_0 f_0 \tau \sin(\varphi_1) \sin\left(\frac{\theta_{az}}{2}\right)} \tag{3.2-10}$$

The number of Doppler bins in the physical beam is directly proportional to the sinusoid of half the physical beam width, and the azimuth resolution is proportional to the beamwidth. If $\theta_{az} < 61$ degrees, the term $\sin\left(\frac{\theta_{az}}{2}\right)$ falls within 10% of $\theta_{az}/2$, and (3.2-10) can be approximated to (3.2-11), which yields a similar result from [95], without considering the grazing angle.

$$\Delta\theta_{az}^r \approx \frac{c}{2v_0 f_0 \tau \times sin\ (\varphi_1)} \tag{3.2-11}$$

It is desirable to obtain the widest field of view possible for the best situational awareness, hence θ_{az} should be as large as possible without compromising the SNR. When calculating the azimuth resolution achieved for the surface platform, (3.2-8) is a better estimate.

To produce the DBS image, the angle needs to be related to the measured Doppler frequency which is done by re-arranging (3.2-1), where $i = 1{:}n$.

$$\varphi_i \approx \operatorname{acos}\left(\frac{cf_d^i}{2v_0 f_0}\right) = \varphi_1 + i\Delta\theta_{az}^r - \frac{\theta_{az}}{2} \tag{3.2-12}$$

3.3 Effect of Platform Velocity in Marine DBS

The platform velocity is not under control of the radar designer and is a parameter that must be measured by the navigation system to be used in the processing step. By increasing the platform velocity, the relative radial velocity of the scatterer increases, and this increases the received Doppler frequency from (3.2-1). As the range of Doppler frequencies expected in the beam increases according to (3.2-5) and the Doppler resolution remains the same as it is solely dependent on the integration time, the number of Doppler resolution cells that exist in the beam increases, hence the synthetic azimuth resolution is refined further.

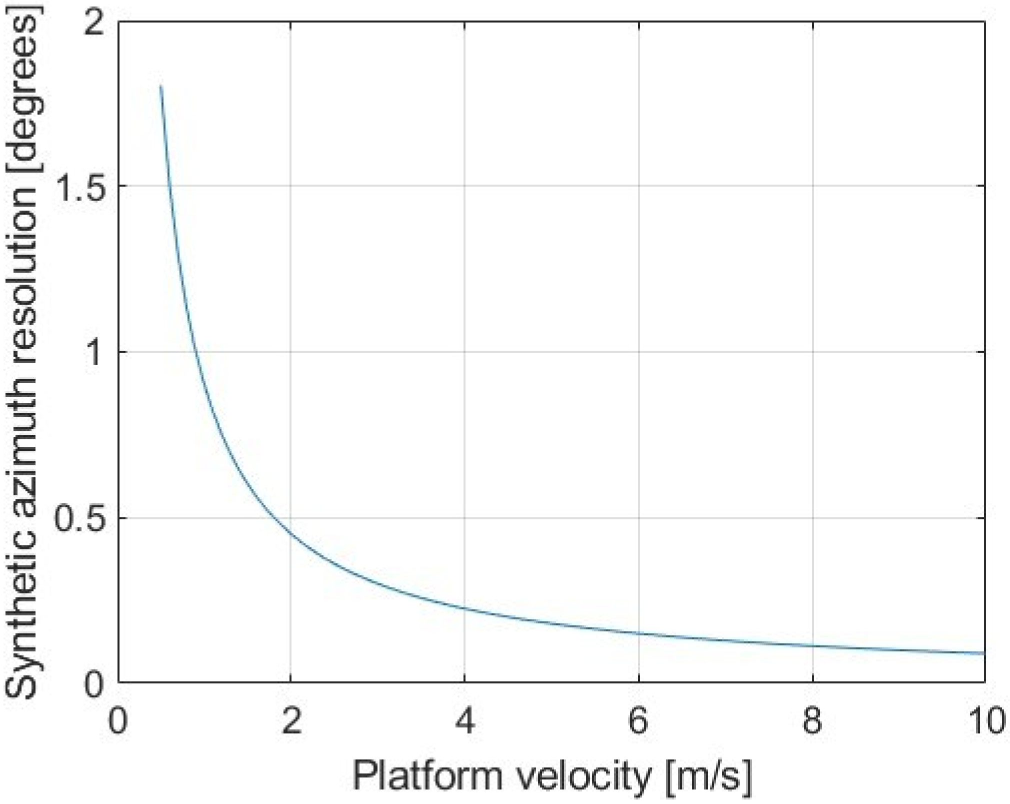

Figure 3.3-1 Synthetic azimuth resolution vs platform velocity for a 10-degree azimuth beam width physical aperture. Fixed parameters used: Integration time = 0.25 s, Squint angle = 90 degrees, Frequency = 150 GHz.

There is a limit to the speed at which the platform can travel before the received Doppler becomes ambiguous. This limit is reached when the received Doppler frequency from a scatter within the beam reaches half of the PRF, however as we know the approximate azimuth we only need the Doppler to be unambiguous across the beam. However, in cases like MIMO where the sidelobes are poor, it is beneficial to ensure Doppler is unambiguous over all angles.

$$v_{unamb} \cos\left(\varphi_{min}\right) = \frac{PRF}{2} \times \frac{c}{f_0} \tag{3.3-1}$$

The minimum look angle that is within the beam is defined as φ_{min}. At this look angle, the relative radial velocity due to the platforms motion will be at its highest. So that when platform moves with higher velocities than v_{unamb} Doppler aliasing is expected. In DBS this would be seen as incorrect azimuth placement for regions in the beam associated with higher than unambiguous Doppler. Increasing the PRF can help alleviate this problem, by increasing the maximum unambiguous Doppler allowing for faster velocities, which refines the synthetic azimuth resolution and smaller squint angles (forward looking squint).

Considering that the purpose of producing high resolution and focused DBS imagery is to use the imagery to detect targets in the platforms vicinity for scene segmentation which will lead to obstacle evasion, the velocity parameter is likely not something that can be controlled for the sole purpose of improving the imagery, and is rather something that is measured, and the signal processing will have to adapt to produce ideal imagery according to the measured velocity. For example, in the presence of an obstacle the platform will have to slow down and potentially change direction, which will reduce the synthetic azimuth resolution.

3.4 Squint angle in Marine DBS

As seen in Figure 3.2-1, the squint angle is defined as the angle between the platform velocity vector and the antenna boresight vector. In equation (3.2-1), a side-looking, i.e., ninety-degree squint angle results in small Doppler frequencies, with zero Doppler frequency for a target located at the boresight. The Doppler frequency is low because the direction between targets in the physical beam and the antenna is close to perpendicular to the platform velocity vector. Therefore, if the platform is moving at a velocity that would cause ambiguity in Doppler if the antenna is forward looking, a side looking antenna would still measure unambiguous Doppler signatures from targets within the beam, which will improve the resolution according to (3.2-10) whilst remaining below the unambiguous velocity as defined in (3.3-1).

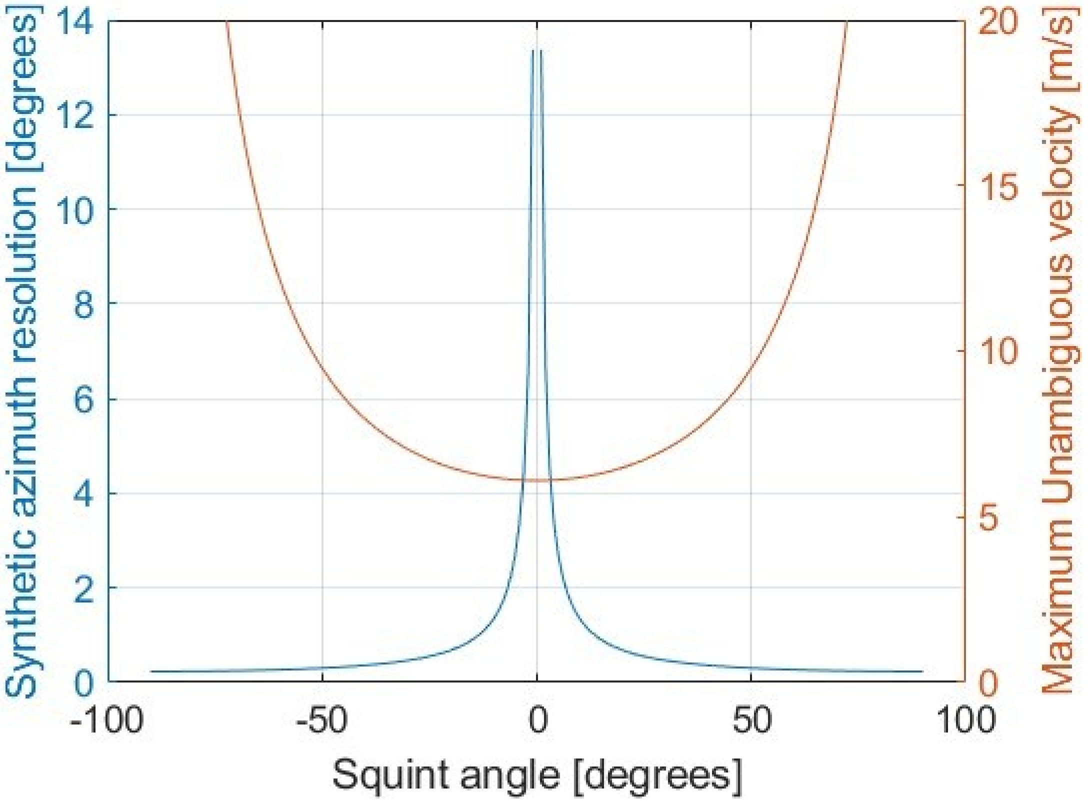

Figure 3.4-1 Relationship between the synthetic azimuth resolution and the squint angle of the radar. Fixed parameters used: Velocity = 1 m/s, Integration time = 0.25 s, carrier frequency = 150 GHz, Physical aperture beam width = 10 degrees. PRF = 6000 Hz. Overlayed is the relationship between the unambiguous velocity with squint angle.

For Squint angles at ± 90 degrees, the synthetic azimuth resolution reaches the best refinement possible. This is because the rate of change of Doppler frequency with the azimuth angle between the antenna and the target is maximised at this squint angle. As the squint angle approaches zero, the synthetic azimuth resolution begins to increase, as the change in Doppler against the azimuth angle reduces, meaning that a single Doppler resolution cell represents a larger swath in azimuth hence reducing the synthesised azimuth resolution, this is the Doppler blind-zone. The maximum unambiguous velocity is also represented which originates from the maximum unambiguous Doppler being half of the PRF, and its dependence on the squint angle. Here we see that the best setup to maximise the synthetic azimuth resolution is to have the radar set at a 90-degree squint angle, as the central Doppler frequency approaches zero, and hence the radial velocity vector will approach zero, the Maximum unambiguous velocity will be approaching infinite, or practically terms, the platform has less limitations to the maximum speed it can go. Again, approaching a squint angle of 0 degrees applies a limitation to the maximum speed of the platform.

As the Squint angle approaches zero, i.e. becomes more forward looking, the Doppler frequency of a target located at boresight increases. As soon as the physical beam passes the platform velocity vector, i.e the squint angle reduces to zero, there is a Doppler ambiguity, as the Doppler frequency for negative squint angles is the same as the Doppler frequency for positive squint angles of the same magnitude.

In the maritime environment, the platform velocity vector is loosely connected to the design of the marine platform, unlike road vehicles, where the velocity can be better estimated by the wheels/tracks position. Marine platforms may have drift velocities, especially after turning, so according to the definition of the squint angle, the squint angle may change throughout the measurement, resulting in a changing azimuth resolution. It is therefore important to measure the relative velocity and heading for each Doppler processing interval.

3.5 Integration time in DBS

The longer the duration of integration, the finer the synthesised azimuth resolution, as the Doppler resolution is the inverse of the integration time from (3.2-2), hence more Doppler cells fit exist within the beam.

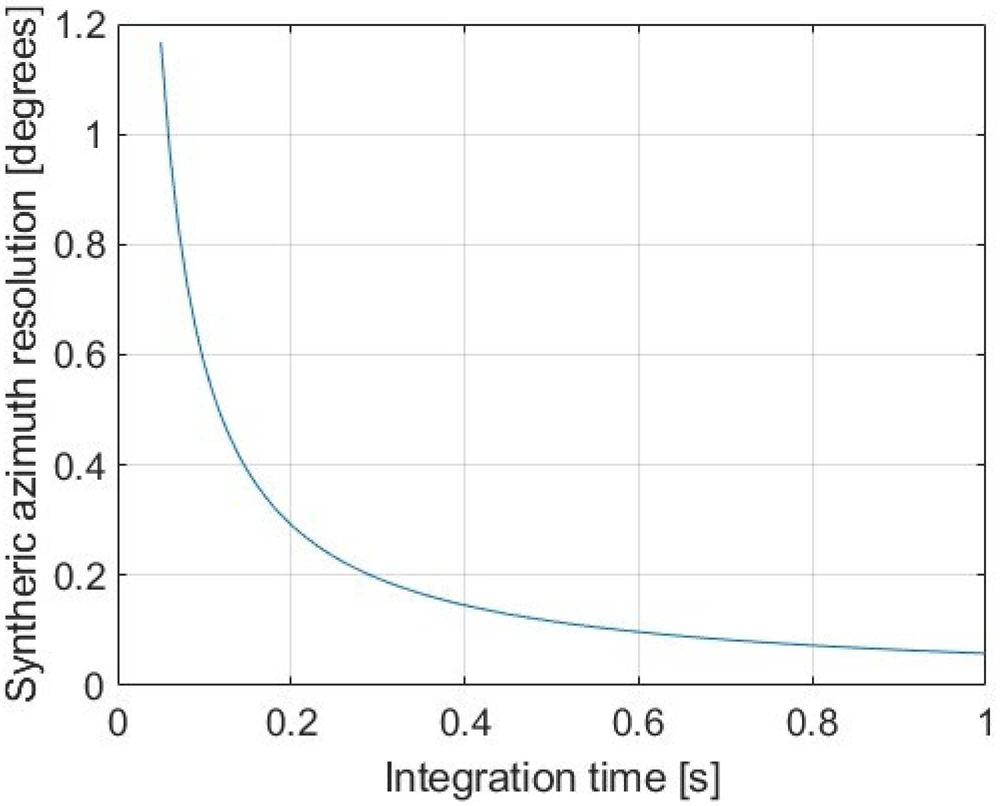

Figure 3.5-1 Relationship between the synthetic azimuth resolution and the integration time. Fixed parameters used: Velocity = 1 m/s, carrier frequency = 150 GHz, Physical aperture beam width = 10 degrees. Overlayed is the relationship between the unambiguous velocity with squint angle.

It is important to realise that during integration the platform is moving, hence the scattering points will move through the beam, where the aperture time is the time taken for the point to enter and then exit the beam. Integrating longer than the aperture time offers no real benefits whereas integrating for less produces sub-aperture imagery. So, it is important to carefully choose the integration time depending on the range, targets further away are sub-aperture for longer than closer targets due to the physical beamwidth, hence integrating for long periods may reduce the imaging potential for close targets.

3.5.1 Integration Time with the Dynamic Maritime Background and Targets

The choice of integration time used in DBS processing is important for the image quality of dynamic targets in the marine environment. By integrating for longer periods, the synthetic aperture is larger, hence the cross-range resolution is finer. However, when target motion is introduced, range-walk occurs in fast time and slow time, the RCS of the target may change as it changes orientation, and small targets can be shadowed from sections of the integration time, leading to spurious modulation of the Doppler image. Motion compensation techniques deal with deviations in the platform motion, but cannot compensate the relative motion of the targets [96]. The longer the integration time used in processing, the more likely that these effects occur and change the quality of the DBS image.

In chapter 2, Figure 2.15-1 shows the received sea clutter signal from an X-band 9.75 GHz radar with 2 m range resolution at both polarisations VV and HH. Here, the correlation times of sea clutter phenomena are illustrated, where whitecap scattering spikes have a characteristic correlation time of around 1 second, whereas specular scattering spikes have a duration of around 200 ms [76]. Therefore, in DBS imaging, the choice of integration time will affect the ability to resolve events with different correlation times. Integrating for periods less than 200 ms could mean that the wave phenomena that cause specular bursts may not decorrelate, and as result the corresponding DBS image will be heavily cluttered with specular bursts. The waves that cause whitecap scattering spikes will also not be likely to decorrelate during these integration period, so the DBS image will also be cluttered with regions cluttered with whitecap spikes. Waves that cause specular bursts will very likely decorrelate during integration periods of around one second, which means the received amplitude from the specular burst region will be comprised of amplitude from the specular burst and amplitude from other sea clutter reflections and/or noise. During an integration period of one second, the white cap scattering spikes may not decorrelate, and the amplitude from the whitecap spikes will therefore integrate, so the DBS imagery becomes cluttered with whitecap regions.

3.6 Dwell time and Doppler Cell walk

During the synthetic aperture formation, the position of the targets within the field of view changes with respect to the antenna position, except in the rare case that both target and platform have the same velocity during the integration time. As well as the change in radial position which causes range walk as explained in the previous section, the targets will also change position in azimuth. In DBS, it is interpreted as a change in Doppler frequency and if it is more significant than the Doppler resolution, this can lead to blurring in the cross-range dimension as the energy from the scatterer is spread across several Doppler resolution cells.

3.6.1 Doppler Cell Walk

It is important to consider that, as the integration time increases, the refined azimuth beamwidth becomes much smaller, and the synthetic aperture length increases, meaning the scatterers are more likely to move from one Doppler cell to the next.

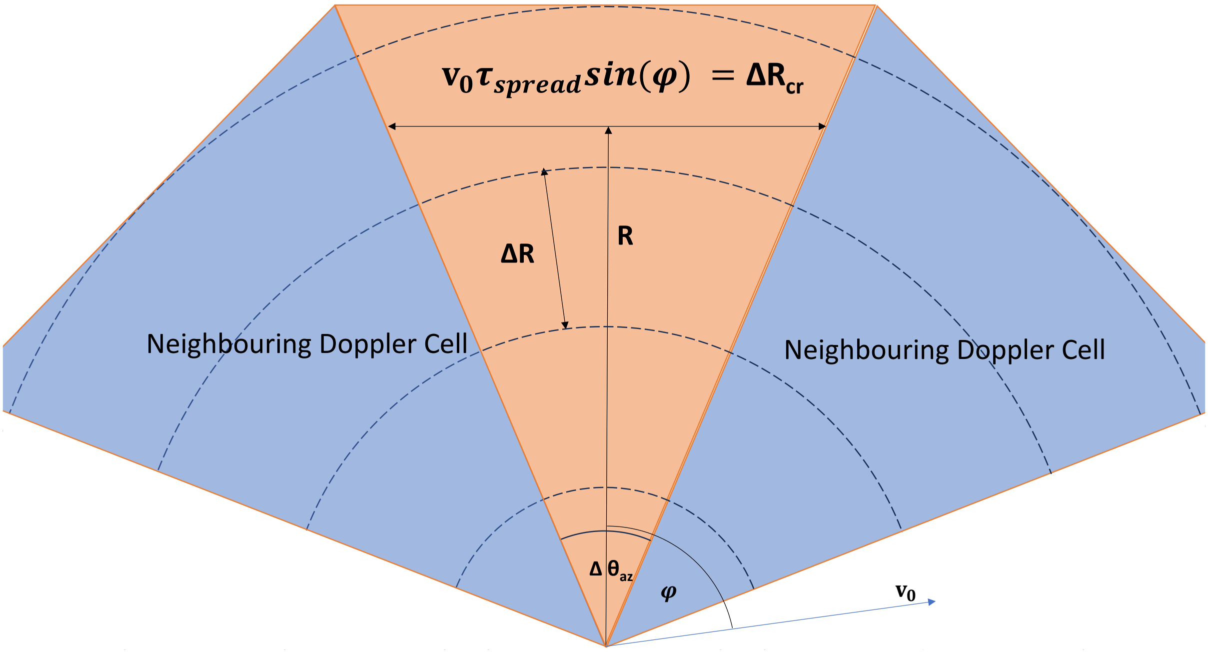

Figure 3.6-1 Physical beam that has been refined via DBS processing, showing neighbouring Doppler cells. Note that the platform is moving with a velocity v0, and the look angle of the highlighted (orange) resolution cell is denoted φ.

In Figure 3.6-1, three Doppler resolution cells are shown, which corresponds to a refined azimuth beamwidth of $\Delta\theta_{az}$, which has a look angle from the velocity vector of φ. It is important to distinguish that the squint angle φ_1, is the angle between antenna boresight and velocity vector, and that the look angle φ, is the angle between the velocity vector and any arbitrary azimuth angle in the physical beam region. Considering that the platform moves with a velocity v_0, the total distance travelled in cross range during the integration time is,

$$d = v_0 \tau \sin(\varphi) \qquad (3.6\text{-}1)$$

Therefore, if the distance travelled in cross range during the integration period is larger than the cross range between the edges of the refined beam, the scatterer will travel across Doppler resolution cells to the neighbouring Doppler cell during integration and have its energy spread, causing blurry imagery in cross range.

$$v_0 \tau \sin(\varphi) \geq 2R tan\left(\frac{\Delta\theta_{az}}{2}\right) \qquad (3.6\text{-}2)$$

As the refined azimuth should be a relatively small angle, $tan\left(\frac{\Delta\theta_{az}}{2}\right)$ can be reduced to $\frac{\Delta\theta_{az}}{2}$. Following this, using (3.2-10) to substitute $\Delta\theta_{az}$, it is possible to re-arrange (3.6-2) to find the maximum integration time possible before it is certain that the energy of a point scatter is spread between more than one Doppler resolution cell.

$$\tau_{spread} = \sqrt{\frac{cR\theta_{az}}{4v_0^2 f_0 \sin(\varphi) \sin(\varphi_1) \sin\left(\frac{\theta_{az}}{2}\right)}} \qquad (3.6\text{-}3)$$

For excessively long integration times, the scatterer may pass several Doppler resolution cells. As this happens the look angle and range of the target changes, where the shortest possible value for τ_{spread} is found at a look angle of 90 degrees. For targets that appear at the front or the rear of the boat, τ_{spread} can be very large as the Doppler remains constant.

It is important to note that although τ_{spread} calculates the maximum possible integration time required before the energy of the received signal begins to accumulate in the neighbouring Doppler bin. Integrating more pulses after this will still reduce the size of the Doppler bin according to (3.2-2), and if the amount of energy accumulated in the neighbouring Doppler cell is still insignificant, i.e below the noise floor, the resolution will still appear improved.

3.7 Range cell migration during Range and Doppler compression

The most extreme case of range walk occurs when the radial distance travelled during range compression between the antenna and target is larger than the range resolution, leading to the spreading of the target down range in the radar image.

$$\Delta R < v\cos(\varphi)\, t_{fast} \qquad (3.7\text{-}1)$$

Hence to obtain clear images, the range walk needs to be considered and its extent. For example, using a chirp duration of 0.15 ms, and a range resolution of 3 cm, which are parameters of the radar discussed in chapter 5, the radial velocity required for range walk is 200 m/s. It is well known that the case of range cell migration is insignificant during range compression, and at these velocities, range cell migration is highly unlikely in the marine environment and hence can mostly be disregarded. We therefore assume during range compression that the target position does not smear in range significantly.

During the Doppler compression processing interval, the integration time is longer than the processing time in range compression, hence range walk poses a larger problem. In the simplest case, where the processing interval is small enough to assume that the position vector between the radar and target remains the same, the range walk is:

$$\Delta R < v\cos(\varphi)\, \tau \qquad (3.7\text{-}2)$$

For example, with an integration time of 0.25 s and range resolution of 3 cm, range walk occurs for radial speeds larger than 0.12 m/s. Hence without compensation, it is expected that a point target in the marine environment will spread its energy down several range cells after Doppler compression. As the platform passes the target, range walk will become more significant the more forward or backward the target is positioned relative to the platform motion, and less significant the more side positioned the target is. In this case the exact range of the target is found before and after the processing interval, and range walk occurs when the difference between the range before and after integration is greater than the range resolution [97]. By Taylor expanding the target range after the integration interval an expression for the range walk is obtained.

$$R_{max} \cong R_0 + \frac{v_0^2 \left(\frac{\tau}{2}\right)^2}{2R_0}, R_{min} = R_0 \tag{3.7-3}$$

$$\Delta R_{walk} = R_{max} - R_{min} = \frac{(v_0 \tau)^2}{8R_0} = \frac{L_{SA}^2}{8R_0} = \frac{R_0}{8}(\Delta\theta_{az}^r)^2 = \frac{R_0 \lambda^2}{32 \Delta {r_{cr}^r}^2} < \Delta R \tag{3.7-4}$$

Here the minimum range of the target during the processing interval is denoted R_{min}, and the maximum range during the interval is denoted R_{max}. Assuming the platform has a linear velocity v_0 and the squint and is exactly 90 degrees, the range walk is presented in terms of the cross-range resolution and wavelength. For other squint angles, the velocity is multiplied by $\cos(\varphi)$, therefore the final term is multiplied by $\cos^2(\varphi)$. We see that by increasing the processing interval, and therefore increasing the cross-range resolution, we also increase the risk of range walk. As targets that are far away have a slower change in aspect as the platform passes, the change in range due to platform motion is also lower.

Range walk during Doppler compression is more of a concern for forward looking radar, where the relative radial velocity of the target is much larger than if the antennae were side looking, which is another reason why the side looking squint configuration is beneficial for DBS.

3.8 Carrier Frequency in DBS

The various advantages of moving to higher carrier frequencies were described in section 1.2 in the introduction. Increasing the carrier frequency also has an impact on the quality of image produced after DBS processing. As seen from (3.2-1), increasing the carrier frequency will also innately increase the Doppler frequency of the reflected signals, therefore the azimuth angle that is related to the Doppler frequency is smaller as seen in (3.2-12). As the Doppler resolution is solely dependent on the integration time, more Doppler resolution cells are required to form the DBS image and hence the cross-range resolution is more refined.

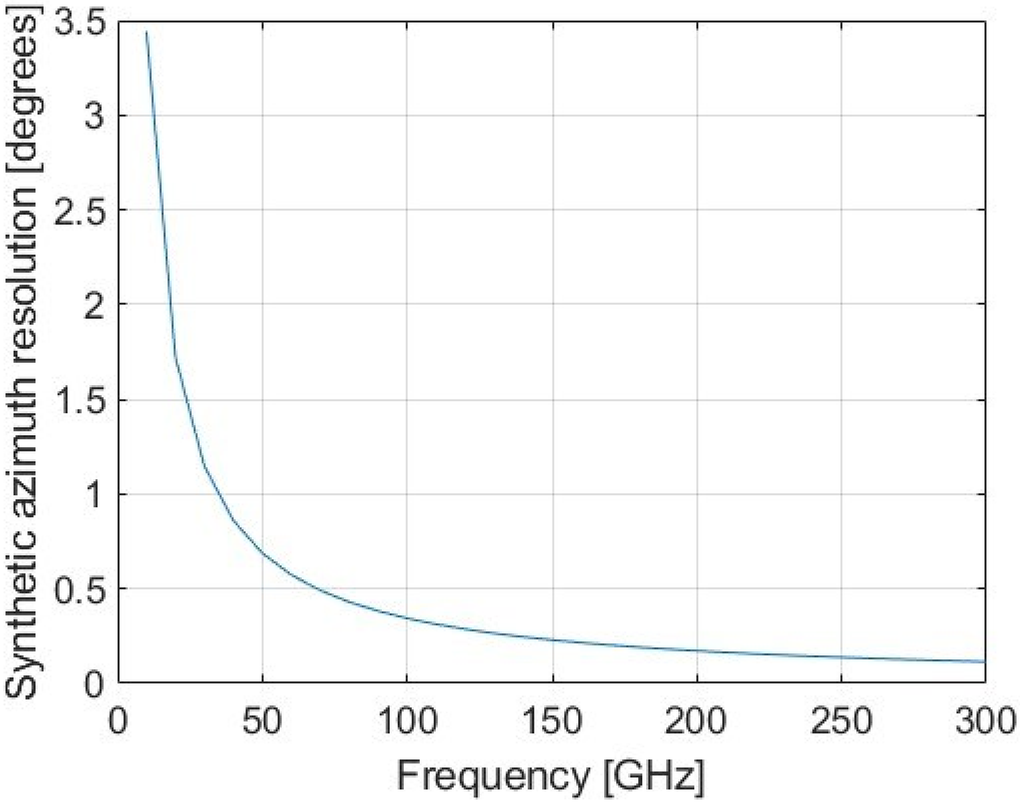

Figure 3.8-1 Relationship between the synthetic azimuth resolution and the carrier frequency of the radar. Fixed parameters used: Velocity = 1 m/s, Integration time = 0.25 s, Squint angle = 90 degrees, Physical aperture beam width = 10 degrees. Assumes that scattering is coherent throughout the integration time at all frequencies.

From Figure 3.8-1, we can visualise the effect that using a higher carrier frequency has on the synthesised azimuth resolution. From the discussions in chapter 2, the benefits of using higher carrier frequencies on image quality were discussed, that is, being able to image finer surface textures and exploit wider bandwidths to produce a fine range resolution as well as the reduced antenna size for easy installation on small autonomous vessels. Now considering the application for DBS processing, we see that the inherent increase of the Doppler frequency from a scatterer due to the increased carrier frequency enables more Doppler cells to be resolved as azimuth cells within the physical aperture beamwidth. For instance, the synthesised azimuth resolution for the 150 GHz carrier frequency, with all the same DBS processing parameters as a 300 GHz, would still be twice as large. To produce the same cross range resolution for two radars at two different frequencies, one could increase the integration time of the lower frequency radar by the ratio of the two frequencies. Therefore, it can also be mentioned that higher frequency radars are take less time to produce fine cross-range resolutions, which means higher frequency radar DBS imagery is more likely to be sensitive to scatterers with lower correlation times, such as sea spike events. It also means that non-linear target motions are less likely to blur it as the change of velocity will be smaller for shorter integration times.

3.9 Physical aperture Beam width in DBS

The refined azimuth resolution is dependent on the physical aperture beam width, although the effect azimuth beam width has on the DBS processing is nearly negligible. As the beam width increases, so does the field of view, and the range of Doppler frequencies that exist in the beam, seen in (3.2-6). Because the Doppler resolution is solely dependent on the integration time, the number of Doppler cells that exist within the physical Beam width also increases, and therefore these two effects nearly cancel each other. Using (3.2-8), the relationship between the physical aperture beam width and refined azimuth beam width is:

$$\Delta\theta_{az}^{r} \propto \frac{2}{\mathrm{sinc}\left(\frac{\theta_{az}}{2}\right)}$$

(3.9-1)

For very fine azimuth beamwidths, $\theta_{az} < 1$, $\mathrm{sinc}\left(\frac{\theta_{az}}{2}\right) \sim 1$, and hence the synthetic azimuth resolution essentially becomes independent of the beamwidth. For larger beamwidths, the dependence on $\mathrm{sinc}\left(\frac{\theta_{az}}{2}\right)$ becomes more pronounced.

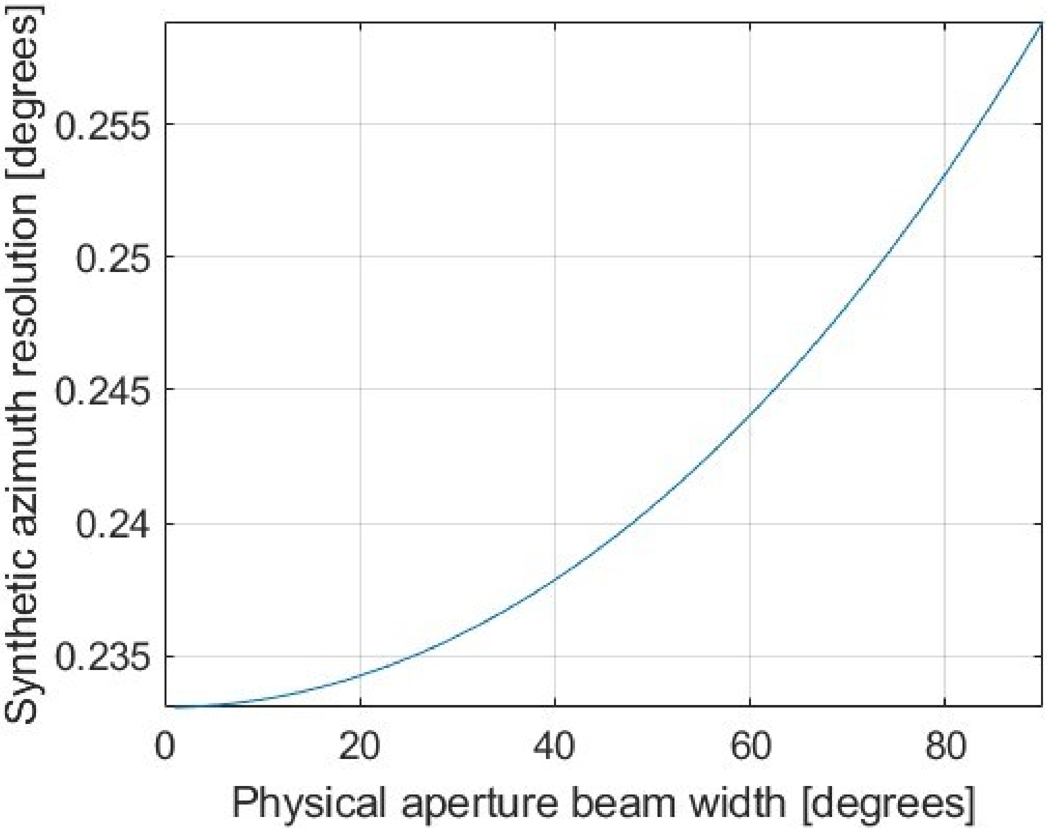

Figure 3.9-1 Relationship between the synthetic azimuth resolution, post DBS processing, against the Physical aperture beamwidth. Fixed parameters used: Velocity = 1 m/s, Integration time = 0.25 s, Squint angle = 90 degrees, Frequency = 150 GHz.

Here we can see between the physical aperture beamwidths of 0 degrees to 90 degrees, the range of synthetic azimuth resolution is near 0.02 degrees. Therefore, there is very little difference in the azimuth resolution when changing the antenna beamwidth.

When choosing the appropriate antenna for DBS measurements, it is important to consider the antenna gain, to achieve appropriate SNR and SCR for imaging, and to consider the field of view, as a narrow field of view greatly reduces dwell times, reduces maximum integration times for sub-aperture imagery and produces imagery with very small peripherals, which means targets are more likely to exist either side of the beamwidth and be missed during imaging.

3.10 The effect of target motion on DBS processing

As the platform motion is measured relative to the surface of earth, and hence the DBS processing occurs in this reference frame, any motion of the target relative to this reference frame will affect the DBS processing and change the quality of the image. In this section the DBS processing is now expressed in vector notation.

To understand the defocusing effect, the radial vector between the scatterer and antenna must first be found.

$$\boldsymbol{R} = \begin{bmatrix} x_t \\ y_t \\ z_t \end{bmatrix} - \begin{bmatrix} x_a \\ y_a \\ z_a \end{bmatrix} = \begin{bmatrix} x_t - x_a \\ y_t - y_a \\ z_t - z_a \end{bmatrix} = \begin{bmatrix} R_x \\ R_y \\ R_z \end{bmatrix} \qquad (3.10\text{-}1)$$

$$\boldsymbol{R_u} = \frac{\boldsymbol{R}}{|\boldsymbol{R}|} = \begin{bmatrix} R_x \\ R_y \\ R_z \end{bmatrix} \frac{1}{\sqrt{R_x^2 + R_y^2 + R_z^2}} \qquad (3.10\text{-}2)$$

Here, ***R*,** is the radial spatial vector between the antenna and target in *x, y* and *z* directions and $\boldsymbol{R_u}$ is the unit vector in the radial direction. The first vector defined by x_t, y_t, z_t are the cartesian co-ordinates of the target in meters. The second vector defined by x_a, y_a, z_a are the cartesian co-ordinates of the antenna. Target location is denoted t and antenna location is denoted a. The velocity vector of the scatterer and the antenna are then projected onto the normalized radial vector.

$$v_{Trad} = \boldsymbol{v_t} \cdot \boldsymbol{R_u} = \begin{bmatrix} v_{t_x} \\ v_{t_y} \\ v_{t_z} \end{bmatrix} \cdot \boldsymbol{R_u} \qquad (3.10\text{-}3)$$

$$v_{Arad} = \boldsymbol{v_a} \cdot \boldsymbol{R_u} = \begin{bmatrix} v_{a_x} \\ v_{a_y} \\ v_{a_z} \end{bmatrix} \cdot \boldsymbol{R_u} \qquad (3.10\text{-}4)$$

Here, v_{Trad} and v_{arad} are the radial speeds of the target and antenna relative to the background, derived from the velocity of the antenna v_a and the velocity of the target v_t. Finally, the difference between the velocity of the scatterer and antenna down the radial vector is computed. In this scenario, this relative radial speed, v_{rad}, replaces $v_0 cos(\varphi_1)$ in (3.2-5) to focus the DBS image on the dynamic scatterer.

$$v_{Trad} - v_{Arad} = v_{rad} \qquad (3.10\text{-}5)$$

Substituting (3.10-5) into (3.2-5) instead of using $v_0 cos(\varphi_1)$ as radial speed, and expanding it into its individual terms, the expected measured Doppler frequency in the DBS mode is expressed in (3.10-6).

$$f_d = \frac{2f_0}{c}\left[\frac{v_{t_x}R_x + v_{t_y}R_y + v_{t_z}R_z}{\sqrt{R_x^2 + R_y^2 + R_z^2}}\right] - \frac{2f_0}{c}\left[\frac{v_{a_x}R_x + v_{a_y}R_y + v_{a_z}R_z}{\sqrt{R_x^2 + R_y^2 + R_z^2}}\right] \qquad (3.10\text{-}6)$$

In the ideal case, where the scatterer is stationary, both antenna and scatterer are at the same height so $R_z = 0$, and the platform velocity only has an x-direction component, (3.10-6) collapses to (1). It becomes clear that the Doppler frequency measured by the radar is composed of 3 components. The first component is the same as (3.2-1), the 'DBS Doppler frequency'.

$$f_{d_{DBS}} = \frac{2f_0}{c}\left[\frac{v_{a_x}R_x + v_{a_y}R_y}{\sqrt{R_x^2 + R_y^2 + R_z^2}}\right] \tag{3.10-7}$$

However, (3.10-7) accounts for variation of the platform velocity in both x and y. The platform velocity and position can be measured. The only term in (3.10-7) that is approximated is Rz. For measurements at ranges beyond 10 m, it can be presumed that $R_z^2 << R_x^2 + R_y^2$ as wave heights in rough seas (sea state 5) are not typically above 4m. At close range, however, these effects may be significant. The second component due to the vertical motion of the antenna, is represented in (3.10-8).

$$f_{d_a} = \frac{2f_0}{c}\left[\frac{v_{a_z}R_z}{\sqrt{R_x^2 + R_y^2 + R_z^2}}\right] \tag{3.10-8}$$

The third component is the target velocity defocusing.

$$f_{d_t} = -\frac{2f_0}{c}\left[\frac{v_{t_x}(R_x) + v_{t_y}(R_y) + v_{t_z}(R_z)}{\sqrt{R_x^2 + R_y^2 + R_z^2}}\right] \tag{3.10-9}$$

In a real environment, the precise kinematics and position of the target cannot be known, and so more signal processing will be required to focus on the target and compensate for (3.10-8) and (3.10-9). Methods such as Inverse Synthetic Aperture Radar (ISAR) rely on the target motion to reconstruct two-dimensional images [98]. ISAR can be used to image maritime targets, where the pitch and roll motion of the target intensifies the Doppler signal, resolving superstructure forms like boat masts [99]. On less stable platforms however, it is likely that the Doppler smear in ISAR will be significant and not be of much use for small marine platform sensing. The following chapter, on Sub-THz DBS simulations, analyses the effect of target motion on DBS image quality.

3.11 Radar data processing

In a practical measurement, and what is explained in chapter 5, the ADC obtains the data as a series of consecutive intermediate frequency (IF) pulses from the output of the receiver module, each separated by the PRI, which results in a series of range profiles after the first FFT along fast time. The window, $H(t)$, is typically used to reduce the presence of sidelobes in range, so that each range profile is defined by (3.11-1):

$$R_p(r, t_{slow}) = \frac{1}{T}\sum_{t=1}^{T}\left(H(t) \times I_f(t, t_{slow})\right) e^{-\frac{2\pi i}{T}(t-1)(r-1)}$$

(3.11-1)

Where R_p is the range profile at the slow time sample number t_{slow} i.e the pulse number. Here t is the fast time sample, r is the range sample, and T is the total number of fast time samples which can be described as the ADC sample rate multiplied by the chirp duration. A N-point symmetric four-term Blackman-Harris window, denoted H, is applied to ensure most sidelobes are attenuated below the noise floor at the cost of resolution.

To process the radar data into the Range-Doppler Map, a second FFT is applied to Rp, this time down the slow time to obtain the Doppler profile at each specified range sample. In doing so the range-Doppler image is processed. The range-Doppler map is generated as described in (3.11-2).

$$RD_p(r, D) = \frac{1}{N_{int}}\sum_{t_{slow}}^{N_{int}}\left(H(N_{int}) \times R_p(r, t_{slow})\right) e^{-\frac{2\pi i}{N_{int}}(t_{slow}-1)(D-1)}$$

(3.11-2)

In (3.11-2), D is introduced as the Doppler frequency sample number and N_{int} is the maximum integration time sample, i.e the number of pulses integrated. Hence the integration time τ is equivalent to N_{int} multiplied by the PRI. Again, H is used as the windowing function to reduce the presence of Doppler sidelobes.

The instantaneous velocities are recorded by an IMU as explained in chapter 5. Once the range-Doppler has been found, the distance travelled and so the variation of velocity during the integration period will cause some image blur. The Doppler frequency is directly proportional to the relative radial velocity between the antenna and a point scatterer in the beam as seen in (3.2-1), where the platform velocity multiplied by the cosine of the squint angle defines the radial velocity, and the point scatterer in the background is assumed stationary. The point scatterer may be defined as the waves on the surface, or a target as part of the scene. As the background is dynamic, the motion of the scatterer affects the observed Doppler frequency and will therefore defocus the image.

3.12 Summary of Doppler Beam Sharpening

This chapter started briefly summarised the historical uses of the DBS processing technique and its current applications in research and how it has recently been applied to MIMO sensors for automotive sensing.

DBS was then derived from first principles under the assumption that the target was stationary, and the platform velocity was constant. From this, an investigation to the affects of each parameter on the DBS processing. The parameters of the dataset that are not controlled in post processing were the velocity off the platform, the squint angle, the physical aperture beamwidth and the carrier frequency of the radar. Faster platform speeds will increase the Doppler frequency reflected from a target as the relative radial speed is increased between antenna and target. Therefore, more of the Doppler spectrum is assigned within the physical aperture, so the refinement is greater. The squint angle was found to achieve the greatest angular refinement at 90 degrees to the motion vector, as this achieves the greatest change in Doppler frequency vs the azimuth angle. At more forward-looking squint angles, the change in Doppler spread across the aperture is less, and so only a few Doppler bins fill the physical aperture beamwidth. It was found that the angular refinement was essentially independent of the beamwidth, as wider coverage allows the detection of larger Doppler signatures at the same Doppler resolution. A higher carrier frequency inherently increases the Doppler frequency from targets, so more of the Doppler spectrum is present within the physical aperture beamwidth, hence greater refinement.

Finally, DBS is expressed in vector notation to include target motion. This is to analyse the effect of target motion. Of course, in real measurements, unless the target is co-operative, the remote sensing system will have no access to target kinematic data. However, the effect of target motion can be investigated in simulated scenes where full access to target kinematic data is available.

4 Maritime Sub-THz Scattering Simulations

The data-collection campaign required for maritime radar measurements poses many logistical challenges as well as variables beyond the researchers' control such as the weather and sea state. As mentioned in the introduction, the radar imaging technique needs to work for a variety of conditions, including higher sea states which usually comes with poor weather and difficulty to produce repeatable experiments in the field. The uncertainty with the weather means that collecting a comprehensive dataset requires many trials in the hope of encountering the necessary sea conditions from time to time. Some measurements of littoral waters can be made with the radar equipment installed on shore [100], however littoral waters tend to have different wave dynamics than the open sea and the radar must operate in both scenarios. [101]. Proving that we can detect small targets on the sea surface is one of the main goals of this research and doing this with real data and requires the placement into the water of many different targets during the measurement campaign. Some targets of interest may be very difficult to place in a practical setting, such as large containers and pallets. Some targets of interest may also be uncontrolled, such as seals and birds, and may not present themselves in the way we require for experimentation, i.e seals may be resting on the shore rather than in the water. Ideally, a method to obtain repeatable radar data of these targets under the many possible environmental conditions is required to test the robustness of radar imaging and target detection techniques.

One solution is to produce or use a real model of the problem, which can be used to obtain repeatable radar measurements through various experiments [102]. Experiments like these may accommodate targets that would otherwise be targets of opportunity in a real trial, like sea mammals [103]. Experiments are good as they are real measurements that provide real data which are reasonably repeatable, however the behaviour of phenomena such as sea waves or sea mammal behaviour may not be quite the same as in the open sea. Facilities that are specifically designed to accurately model sea wave spectra such as FloWave are a good way to measure repeatable data of sea-clutter [104]. FloWave uses a set of 168 paddles around a circular tank with a diameter of 25 m and a depth of 2 m, which produces reproducible waves of near 0.4 m high, representative of a sea state 2. These waves can be made to travel in any direction. These facilities can be used to take repeatable data with real radar equipment of sea clutter, with targets being introduced to the wave tank [105]. There are still limitations on the sea state, which size targets can be placed in the tank and the kinematic information of targets in the scene. DBS type measurements also require space to move the system, which can be limited in indoor spaces.

A solution to this issue is to electromagnetic models which can be used to simulate the radar signal reflections off a modelled environment which will be discussed in this chapter. This way, the parameters of the sea surface can be selected so it represents a specific sea state and weather condition. It also enables the insertion of targets on the surface, that can be designed to have any shape, size and motion. Furthermore, the parameters used in a simulation are known, such as target positions and dynamics, which may not be available or difficult to accurately obtain in a real trial. The knowledge of these parameters enables a more thorough analysis of processing techniques. Modern software solutions provide easy methods for CAD to produce target models.

Modern software solutions for electromagnetic simulations have the capability to use shooting bouncing ray (SBR) simulations to estimate the scattering off a model. SBR simulations work by simulating each ray and firing it at the model, where the physical trajectory of the ray and its reflection is calculated. If the simulated ray is reflected toward the antenna, the contributions to its propagation are determine and calculates, such as attenuation, reflections and divergence [106]. Each simulation estimates the returns at a single frequency. The signals which would be seen by an FMCW radar can therefore simply be created by repeating the simulation at a series of different frequencies. A pulse radar signal can, of course, be created by performing a Fourier transform on the spectrum, but the process of creating the data frequency by frequency is a good match to the fact that many sub-THz radars use FMCW modulation.

For DBS, it is required that many FMCW chirps are simulated along the platforms path to form the synthetic aperture. Hence the simulation software must be able to automate the antenna motion and pulse timing to create a full DBS measurement dataset that can be processed into DBS imagery.

This chapter presents the initial investigation into simulating large electrodynamic environments for the purpose of producing simulated data sets for signal processing. The simulation strategy developed is used to analyse the effects of dynamic target motion on the processed DBS imagery. As it is an initial investigation, more complex modelling, such as antenna motion and sea spray have not been included to ensure the analysis was straight forward but should certainly be considered for future work.

4.1 Simulating using the HFSS SBR Solver

High frequency simulation software (HFSS) developed by Ansys provides an ideal simulator for maritime radar and DBS simulations. Fundamentally, a finite element mesh is attributed to an object in the design environment, where the solutions to Maxwell's calculations according to any incident radiation on the surface mesh are solved [107]. Finding these solutions enables the computation of the backscatter properties of the object in the design environment. Like the other electromagnetic simulators such as CST, HFSS employs an SBR solver [54], i.e. an asymptotic high-frequency electromagnetic simulator which was designed to compute the RCS of electrically large objects. It uses geometrical optics to compute the currents on the surface of perfect electrical conductor (PEC) structures, and then computes the scattered field by integrating the currents using Kirchhoff's diffraction formula. An advantage of using SBR type solvers is that it can use the parallel processing in GPUs to reduce computation time [108] by simultaneously calculating the physical SBR and solving Maxwell's equations on the surface and it provides the scattering properties of many objects and many different materials valid at sub-THz, and it can be incorporated into schemes such as SAR and ISAR measurements.

The antenna forms part of the design environment, and it has a defined location, orientation, and beam pattern. To refrain from over-complication only one antenna design is considered, a parametric antenna predefined by HFSS, with a one-way beamwidth set to ten degrees. The lower and upper frequencies of the FMCW sweep are also defined with the antenna as well as the number of fast time samples. The number of samples in the sweep determines the number of samples and resolution of the IF spectrum , hence the maximum range of a simulated range profile. So, it is important that the number of samples chosen for the sweep achieves a maximum range that is not much greater than the maximum range of the simulated target, as excess samples are redundant and increase the computation time.

During the simulation of a single pulse, the environment remains stationary. To simulate the motion of the sea, many digital models of the time-evolving sea will need to be produced, of which each model is a small-time iteration ahead of the previous iteration. The time step is determined by the simulation event, for example it may be necessary for some applications to iterate the surface for each individual sample within a single FMCW chirp, or for other applications time iterations for the surface may only need to occur after each PRI. In the case for DBS measurements, it is not necessary to simulate the motion of the surface for each sample during a single FMCW pulse (fast time), as the model of the sea will not change significantly, and DBS processing is integrated over slow time. Iterating the surface for each pulse sample in fast time would also create a computational issue as there will be of the order of a thousand samples in fast time per FMCW chirp, and thousands of chirps in slow time to process a single DBS frame. Instead, to recreate the dynamic of the sea, each FMCW chirp has an associated sea surface model iteration which is evolved in time by the PRI from the previous sea model. Hence for each simulation of a chirp, the simulator is updated with the new surface model, therefore simulating the dynamic of the sea in slow time. Of course, floating targets and the antenna are also on the surface and will therefore move according to the surface dynamic too. In the simulations, target motion was considered to investigate the performance of DBS on moving targets. However, antenna motion was assumed to be linear, to ensure targets remain within the beam. Adding the non-linear motion to the antenna is scope for future work.

The advantage of using HFSS over other SBR simulators is that it allows the user to fully automate the design and simulation process by running python code which can be simply generated. The python scripts used for automating HFSS act like a set of instructions that command HFSS to do a job. For example, scripts are made to create and position an antenna, insert CAD files into the design environment, design the parametric beam and conduct a simulation. This becomes vitally important when considering a DBS simulation, where the required PRF is around 6 kHz for example, and the integration time is greater than a tenth of a second. The automation means the simulation needs to be set up once, rather than over six hundred times for each chirp in this case, and as each simulated chirp at sub-THz frequencies takes anywhere between ten minutes to an hour to solve (depending on the design environment and antenna parameters) it saves a significant amount of time as it can run in the background without being supervised.

To simulate a DBS measurement of a time-evolving surface for example, with a moving target and antenna, the following processes need to be followed.

1. Create and save a series of sea surface models to be uploaded to the design environment.
2. Load in the first iteration of the sea surface model to the design environment.
3. Load in the target, specify position and orientation.

4. Define antenna parameters, position, and orientation.
5. Define simulation process.
6. Simulate the FMCW chirp and save the data.
7. Delete the sea surface model and load in the next iteration.
8. Change the target position and orientation for the next iteration/pulse.
9. Change the antenna position and orientation for the next iteration/pulse.
10. Simulate the FMCW chirp and save the data.
11. Repeat steps six to nine, until the simulation is complete.

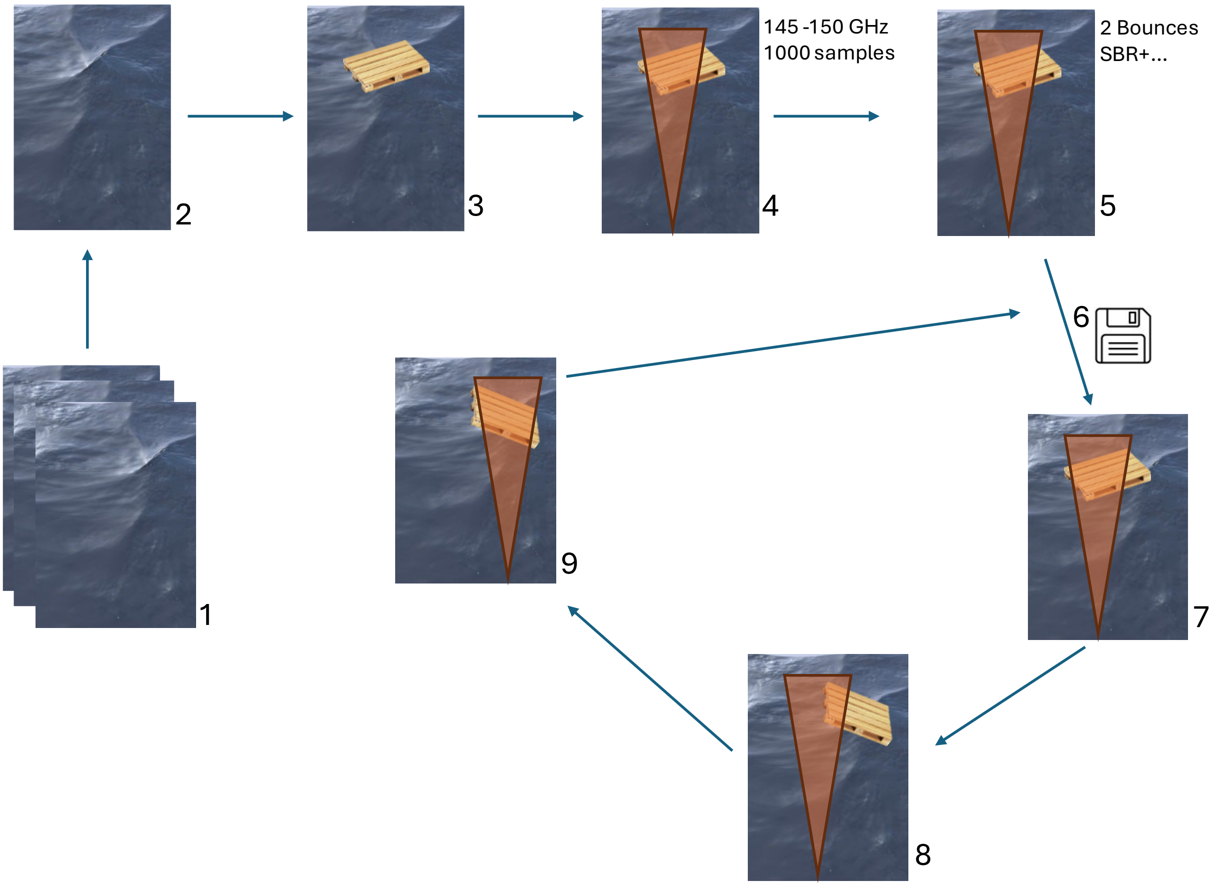

Figure 4.1-1 – Visual representation of HFSS macro simulation strategy for DBS.

4.2 Empirical sea wave spectra for sea surface simulation

The physical cartesian model of the sea surface and how it evolves over time is important as it defines the simulated scene, wave and target dynamics, and even the PRF of the simulation. To develop the physical cartesian model, the sea wave spectra, which defines the frequency distribution of waves on the sea surface, must first be considered. A series of sea wave spectra have been empirically measured and defined for specific types of sea, where these spectra define the amplitude and period of the sea waves and can be processed to obtain the wave profiles of the ocean.

4.2.1 Pierson Moskowitz

The Pierson-Moskowitz (PM) spectrum models a fully developed sea, which occurs when wind has been blowing over a fetch above 100 km, over several days [109]. The spectra were measured on the north Atlantic Ocean, which limits its uses for simulating littoral data but is useful for simulating sea data, and it was measured for various wind speeds. They constructed the Pierson-Moskowitz spectra model to fit the data.

$$S_{PM}(\omega) = \frac{\alpha g^2}{\omega^5} e^{\left[-\beta\left(\frac{g}{\omega U_{19.5}}\right)^4\right]} \qquad (4.2\text{-}1)$$

Here, S_{PM} is the ocean wave spectral density measured in m^2Hz^{-1} where $\int_{-\infty}^{\infty} S_{PM} d\omega$ is the mean square deviation of the sea surface from its mean value, α and β are empirically measured numerical constants, 0.0081 and 0.74 respectively. The acceleration due to gravity is $g = 9.81$ ms^{-2}, and the windspeed 19.5 m above the ocean surface is $U_{19.5}$. The wave frequency in radians per second is $\omega = 2\pi f$.

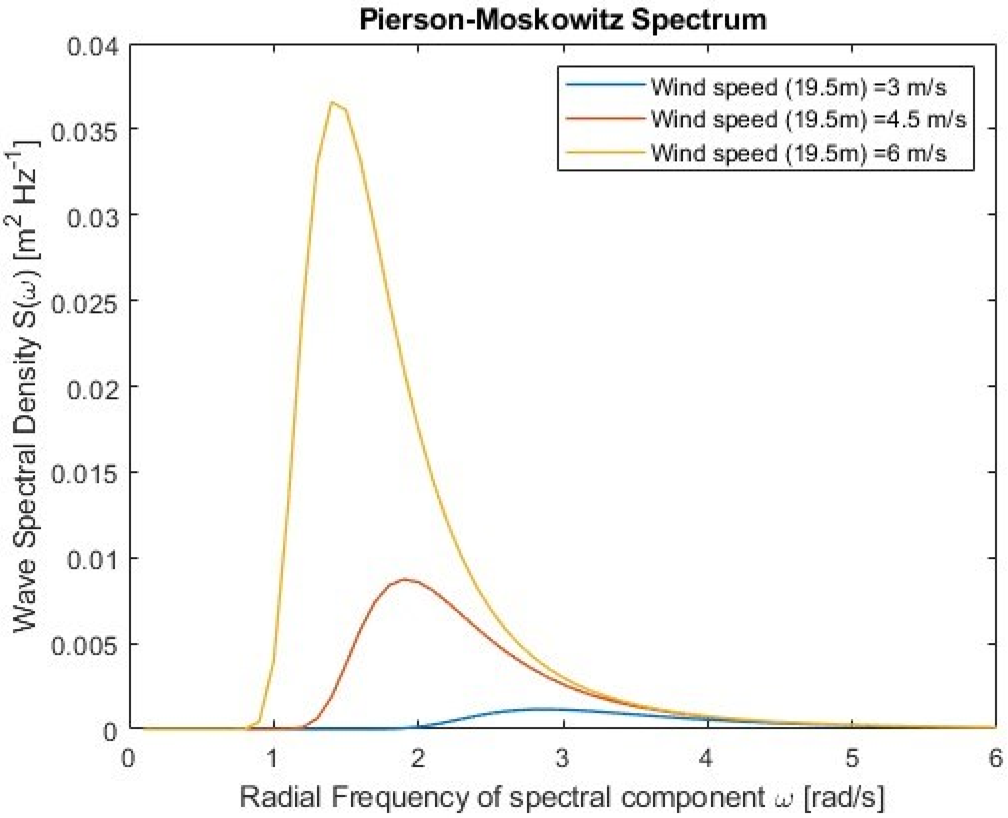

Figure 4.2-1 Pierson-Moskowitz spectra at varying wind speeds as spectral density vs Angular Frequency.

As the wind speed increases for a fully developed sea, the modal frequency decreases. This means the waves become more regular, i.e. having only one frequency with increasing wind speed. To identify the modal frequency, the frequency value at the top of the peak needs to be found which can be done by equating differential of the PM spectra in equation (4.2-1) to zero.

$$\frac{dS_{PM}(\omega = 2\pi f)}{d\omega} = ag^2\left(\frac{4\beta g^4}{U_{19.5}^4\omega^{10}} - \frac{5}{\omega^6}\right)e^{-\beta\left(\frac{g}{U_{19.5}\omega}\right)^4} \qquad (4.2\text{-}2)$$

Hence by equating (4.2-2) to zero, the equation for the modal frequency is found.

$$\omega_m = \frac{g}{U_{19.5}} \sqrt[4]{\frac{4}{5}\beta} \qquad (\, 4.2\text{-}3\,)$$

By integrating the PM spectra with respect to the angular frequency, the significant wave height can be estimated.

$$\int_0^\infty S_{PM}(\omega)d(\omega) = \frac{\alpha U_{19.5}^4}{4\beta g^2} \qquad (\, 4.2\text{-}4\,)$$

Under the assumption that the spectrum has a Rayleigh distribution, and is narrow band, it is assumed that integrating the entire wave spectrum gives the variance (second-order moment), which is the square of the standard deviation. Hence, we know that the significant wave height is four times the standard deviation, σ, of the surface height [110]. This is true for random surfaces, however, is less accurate for surfaces with regular waves, but it at least serves as a useful comparison between the PM model and sea state.

$$\frac{\alpha U_{19.5}^4}{4\beta g^2} = \sigma^2 = \left(\frac{H_{1/3}}{4}\right)^2 \qquad (\, 4.2\text{-}5\,)$$

Here, $H_{1/3}$ is defined as the significant wave height, due to its definition being the average height of the 33% of the largest waves [111]. As discussed in section 2.16, the significant wave height is used to define the sea state, and so using equation (4.2-5), it is now possible to relate the sea state to a specific wind speed which is used to define the simulated PM surface. For example, to model a Douglas sea state 3 with the PM model, where the significant wave height is between 0.5 m and 1.25 m, a PM model of $U_{19.5}^4$=4.8 m/s to 7.6 m/s can be used [112].

4.2.2 JONSWAP and other wave spectra

The PM spectrum is only one of many different sea wave spectra that can be used to model the sea waves. Other spectra such as the JONSWAP spectra can be used to create models with different sea dynamics, which is usually modelled off empirical data from different types of oceans from around the world.

JONSWAP, for example, is a spectrum that defines developing seas and that develops via non-linear interactions between the waves developing on the surface [113]. The resulting spectra is a Pierson Moskowitz spectrum multiplied by a peak enhancement factor to form the JONSWAP.

$$S_{JONSWAP}(\omega) = \frac{\alpha g^2}{\omega^5} e^{\left[-\beta\left(\frac{g}{\omega U_{19.5}}\right)^4\right]} \gamma^r \tag{4.2-6}$$

$$r = e^{-\frac{(\omega-\omega_m)^2}{2\sigma^2\omega_m^2}} \tag{4.2-7}$$

In the JONSWAP spectrum the peak frequency is directly related to the fetch, which increases over time, hence the spectrum is also time dependant. The shape parameter, γ is equal to 3.3, and σ is a constant defined as σ = 0.07 for $\omega \leq \omega_m$ and σ = 0.09 for $\omega > \omega_m$.

4.3 Directional spreading functions

The sea wave spectra define the wave profile in one direction (Usually the direction of the wind), however the input for HFSS needs to form a mesh over a 2D surface, hence directional spreading functions are required to estimate how the spectra varies against azimuth angle. Much like the various spectra that define wave profiles, there are many directional spreading functions that have been used to model how the spectra vary in azimuth. The directional spreading function gives the amplitude-squared versus the spreading angle and the wave frequency.

4.3.1 Cosine-Squared

The Cosine-Squared spreading function was defined in [114]. It is probably the simplest model and only has dependency on angle, i.e. is independent of frequency, and does not consider any other environmental parameters.

$$D(\theta) = \frac{2}{\pi}\cos^2\left(\theta_{sp} - \theta_0\right) \quad \text{for} -\frac{\pi}{2} < \theta_{sp} - \theta_0 < \frac{\pi}{2} \qquad (4.3\text{-}1)$$

Here D, corresponds to the spreading amplitude, and θ_{sp} corresponds to the spreading angle and θ_0 is the wave direction angle. To keep it simple, it is designed so the wave direction is 0 radians. The 2/π factor is required to normalise the spreading function. It ensures that the integral of the spreading function over all angles equals unity, this is to preserve the correct spectral density in the wave spectra, regardless of the angle of wave approach, and to ensure the wave heights of the final simulated surface are all correct. Although there is no dependence on frequency, the function is still represented with frequency in the x-axis as it is required when combining the spreading function with the wave spectra. As there is no frequency dependency it is likely that the spreading function is not completely realistic for real sea surfaces, however it is also unlikely that more complicated models will be much better in all sea conditions, including the littoral at sub-THz frequencies, so there seems no point in using a more complicated model.

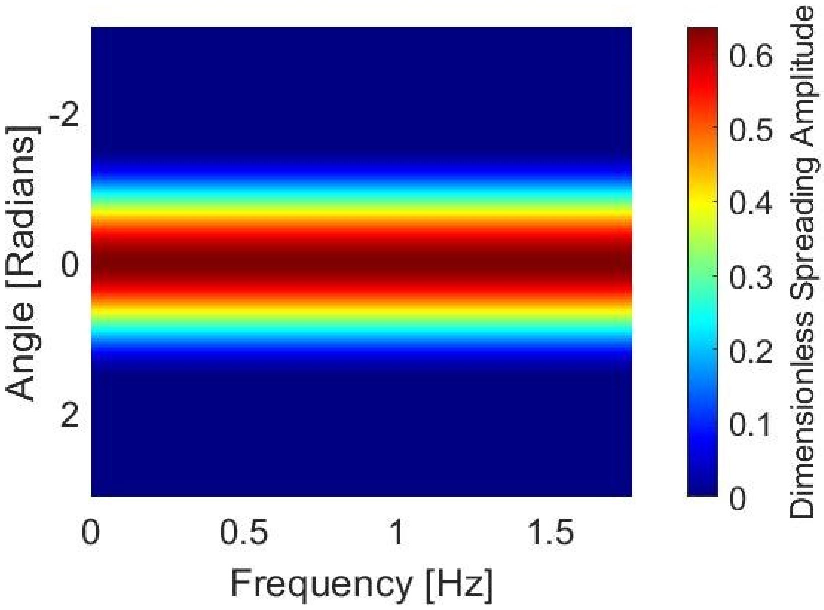

Figure 4.3-1 Cosine-Square directional spreading function

It is also worthy of note that the spreading function is symmetrical about 0 radians, as there is, as expected, no preference for the waves to spread either side of the wind vector.

4.3.2 Longuet-Higgins Directional Spreading with Mitsuyasu Spreading

The Longuet-Higgins spreading function was developed to simulate how the waves spread according to the frequency of the waves and is therefore also dependant on spectra parameters such as windspeed and fetch, depending on the chosen spectra that will be combined with the spreading function [115].

$$D(\theta, f) = \frac{2^{s-1}}{\pi}\frac{\Gamma(s+1)^2}{\Gamma(2s+1)}\left|\cos\frac{1}{2}\left(\theta_{sp} - \theta_0\right)\right|^{2s} \qquad (4.3\text{-}2)$$

Again here, D corresponds to the spreading amplitude, θ_{sp} is the spreading angle, and θ_0 is the wave direction angle. Here, Γ refers to the gamma function and s is introduced as the Mitsuyasu spreading function, which has dependency on the wave frequency and modal frequency.

$$s = \begin{cases} s_m(f/f_\mathrm{m})^5 & f \le f_\mathrm{m} \\ s_m(f/f_\mathrm{m})^{-2.5} & f > f_\mathrm{m} \end{cases} \tag{4.3-3}$$

$$s_m = 11.5(2\pi f_\mathrm{m}\,\overline{U}_{10}/g)^{-2.5} \tag{4.3-4}$$

Here $f_\mathrm{m} = \omega/2\pi$ is the modal frequency of the wave spectrum and $\overline{U}_{10}$ is the mean windspeed 10 metres above the surface. It can be shown that $U_{19.5} = 1.076 \cdot U_{10}$ under specific atmospheric conditions. This assumption can be used to ensure the windspeed used in the Mitsuyasu spreading formula, and hence in the Longuet-Higgins spreading function, remains consistient with windspeed used to determine the sea wave spectra.

4.4 Directional Wave Spectra

Now that the sea wave spectra and directional spreading functions have been defined, they can be combined to produce directional wave spectra, $E(f,\theta)$, which takes the form of wave spectral density vs, spreading angle, vs frequency. It defines the spectral density for each spreading angle.

$$E(f,\theta_{sp}) = S(f)D(f,\theta_{sp}) \tag{4.4-1}$$

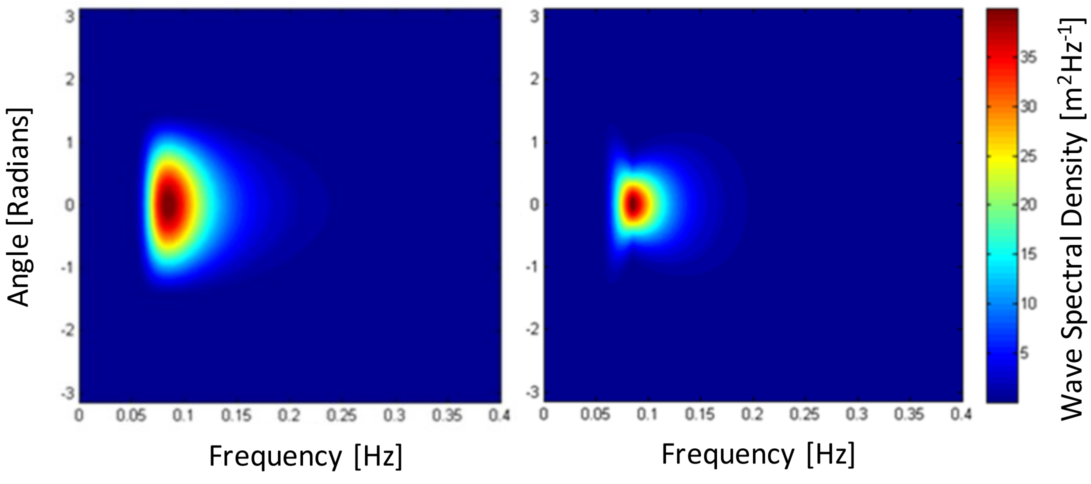

(a) (b)

Figure 4.4-1 Directional wave spectra, Pierson Moskowitz spectra with cosine squared directional spreading (a) and Mitsuyasu spreading (b).

4.4.1 Directional Wave Spectra in Spatial frequency

So far, wave spectra have been expressed in terms of temporal frequency and spreading angle, however they need to be put into a form that will enable the production of the sea surface model in Cartesian space. To start this process the dispersion relation for gravity waves, which relates the angular frequency to the wave number, k, can be used to convert the frequency vector to spatial frequency [116].

$$\omega = \sqrt{gk\tanh(kh)} \qquad (\ 4.4\text{-}2\ )$$

$$k = \frac{2\pi}{\lambda} \qquad (\ 4.4\text{-}3\ )$$

For deep seas, where $h >> \lambda$, the $tanh(kh)$ component of (4.4-2) reduces to 1, hence the dispersion relation reduces to,

$$\omega = \sqrt{gk} \qquad (\ 4.4\text{-}4\ )$$

Hence the frequency can be expressed in terms of the wave number, which is directly related to the spatial frequency, $\nu = 1/\lambda$.

$$f = \frac{1}{2\pi}\sqrt{gk} = \sqrt{\frac{g\nu}{2\pi}} \qquad (\ 4.4\text{-}5\ )$$

Now the directional wave spectra $E(f,\theta)$ from (4.4-1) can be represented in the spatial frequency domain $E(\nu,\theta)$. To preserve the wave energy in the directional wave spectra, the integrals must be equal between the different representations hence,

$$\begin{aligned} \int E(f,\theta_{sp})\,\mathrm{d}f\mathrm{d}\theta_{sp} &= \int E(\nu,\theta_{sp})\,\mathrm{d}\nu\mathrm{d}\theta_{sp} \\ &= \int E\big(f(\nu),\theta_{sp}\big)\frac{\mathrm{d}f}{\mathrm{d}\nu}\mathrm{d}\nu\mathrm{d}\theta_{sp} \end{aligned} \qquad (\ 4.4\text{-}6\ )$$

So, from (4.4-5),

$$\frac{df}{d\nu} = \frac{1}{2}\sqrt{\frac{g}{2\pi\nu}} \qquad (\ 4.4\text{-}7\ )$$

Therefore, the representation of the directional spectra using spatial frequency is,

$$E(\nu,\theta) = \frac{1}{2}\sqrt{\frac{g}{2\pi\nu}}E\big(f,\theta_{sp}\big) \qquad (\ 4.4\text{-}8\ )$$

Here (4.4-5) is used to replace f in terms of v in the original directional wave spectra formula, and the directional wave spectra is now represented in spatial frequency and angle. Currently the directional wave spectra are measured in polar co-ordinates, which can be used to form a surface, however the required model should have equally spaced resolution points in Cartesian space to ensure the simulation is the same across the entire model. Hence the conversion of polar co-ordinates to Cartesian co-ordinates is used.

$$\mathrm{d}\nu_x \mathrm{d}\nu_y = \nu \, \mathrm{d}\nu \mathrm{d}\theta_{sp} \qquad (\ 4.4\text{-}9\ )$$

Here, v_x, and v_y are the vector components of the spatial frequency in both Cartesian x and y directions respectively. Using the same argument in (4.4-6), the directional wave spectra is defined as

$$\int E(\nu_x,\nu_y)\, \mathrm{d}\nu_x \mathrm{d}\nu_y = \int E(\nu_x,\nu_y)\nu \, \mathrm{d}\nu \mathrm{d}\theta_{sp} = \int E(\nu,\theta_{sp})\, \mathrm{d}\nu \mathrm{d}\theta_{sp} \qquad (\ 4.4\text{-}10\ )$$

So finally, the conversion of the original directional wave spectra from (4.4-1) to the Cartesian spatial frequency wave spectra can be formulated as,

$$E(\nu_x,\nu_y) = \frac{1}{\nu} E(\nu,\theta_{sp}) = \frac{1}{2\nu}\sqrt{\frac{g}{2\pi\nu}} E(f,\theta_{sp}) \qquad (\ 4.4\text{-}11\ )$$

Again, ensuring that f is converted in terms of v using (4.4-5).

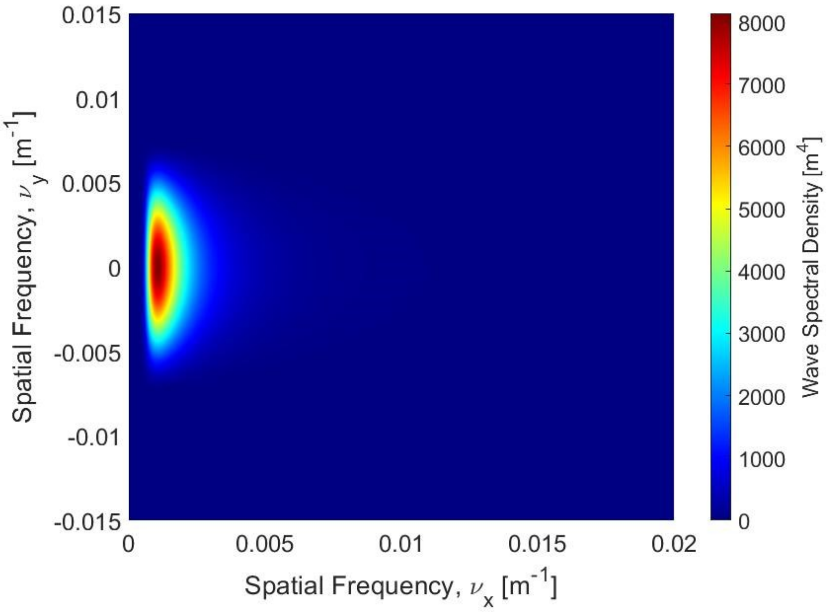

Figure 4.4-2 PM spectrum with Cosine-Squared spreading in cartesian spatial frequency.

4.5 Producing the sea surface model

The directional wave spectrum in (4.4-11) shows the amplitude-squared which can be used to define the wave energy, so taking the square root obtains the wave amplitude .

$$a_{ij} = \sqrt{2E\left(f_i, \theta_{sp}^{ij}\right)\Delta f_i \Delta\theta_{ij}} = \sqrt{2E\left(v_x^i, v_y^j\right)\Delta v_x^i \Delta v_y^j} \qquad (\ 4.5\text{-}1\ )$$

Here, a_{ij} is the complex amplitude and has been discretised using sample numbers i and j on frequency angle and spatial frequency vectors. The term Δ placed before the variable signifies the spacing of the discrete variables. Furthermore, a random phase factor, $e^{i\phi_{ij}}$, can be multiplied to each component in (4.5-1) where ϕ_{ij} is distributed uniformly between 0 and 2π. This step is important, especially when considering the time evolution of the surface which is discussed in the next section.

An IFFT is then performed on (4.5-1), which produces the sea surface in one instance of time as defined by the phase.

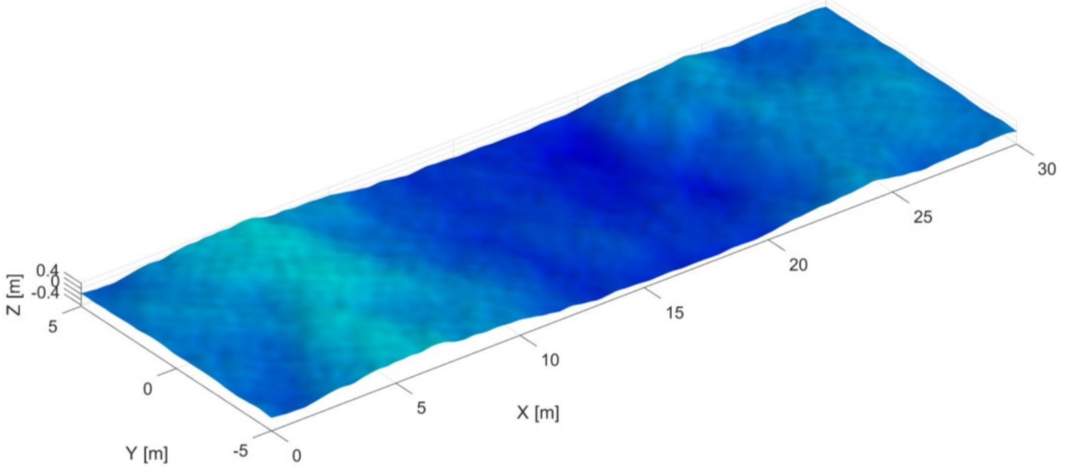

Figure 4.5-1 Simulated Sea Surface using a wind speed of 7 m/s, the cosine-squared spreading function, and PM spectrum.

It is important to note that the spatial sampling of the sea surface is defined by the maximum spatial frequency values v_x^N and v_y^N, where N is the maximum number of samples in the spectra. The size of the spacing between two adjacent discrete samples in v_x^N and v_y^N determines the maximum width and length of the plotted surface respectively.

4.5.1 Evolving the Surface Through Time

The evolution of the surface is required to simulate the dynamic of the ocean. This is done by taking the previously defined phase and progressing it to a new value according to the dispersion relation.

$$\phi_{ij}^{n+1} = \phi_{ij}^{n} + \omega_{ij}\Delta t = \phi_{ij}^{n} + \sqrt{2\pi \nu_{ij} g}\cdot \Delta t\,. \tag{4.5-2}$$

Here n is used to represent the frame number and Δt is the time interval, hence the phase of the next frame has been related to the dispersion relation and the previous surface phase values. As discussed at the beginning of this section, the time evolution of the surface dictates the PRF of the simulation, so when evolving the surface, Δt should be the intended PRI for the simulation. The result is a large dataset of sea surfaces that are all time iterated by a single PRI from the previous surface. A sea surface that is 10 m by 30 m, with a resolution of 0.0125 m produces an STL file size of 187.5 mb, so to simulate a second of data with a PRF of 6 kHz, the size of the data is over 1 Tb.

4.5.2 Uploading the surface to the HFSS design environment

The next step is to upload the produced sea surface model into the HFSS design environment. An efficient way to do this is to produce the surface as a stereolithography (STL) file, maintaining a naming convention that indicates which frame of the simulation the surface belongs to. STL files retain information on triangular facets on the geometrical surface, which means the model can be uploaded to multiple simulations with the same mesh, rather than reproducing the mesh. STL files can be easily imported to the design environment, furthermore this can be automated with the python script. For the simulation of a stationary sea surface, the environment is now ready, and the DBS measurement can be simulated on this model. Using the time evolution process for a dynamic surface, the next surface is also saved as an STL file. These STL files are ready to be imported to the HFSS design environment for simulating, as specified at the end of section 4.1. For a simulation of a dynamic surface, when the simulation has been completed for a single pulse and surface iteration, the sea surface is deleted and then the next iteration is uploaded.

4.6 Target Modelling in HFSS

The next step in producing the simulated environment is to add targets to the scene. HFSS itself enables the user to define and place basic shapes into the environment, such as spheres, cylinders, and cuboids. When defining the object, it enables the user to define size, shape, position, and orientation. For more complex targets such as pallets and buoys, it is better to import STL files into the design environment, which is the same process when importing the sea surface model. These objects can be designed using any CAD software or taken from open-source websites such as GrabCAD [117]. This thesis focuses on a pallet model, which was used for the simulations as it is typical of the flotsam which might be found in the marine environment, often in the form of flotsam, where the model was taken from GrabCAD. They float and are therefore detectable by radars on the surface of the water. They are a credible threat to the integrity of the vessel. It has a periodic structure which can be used to identify the orientation of the pallet and the scattering phenomena in a radar measurement.

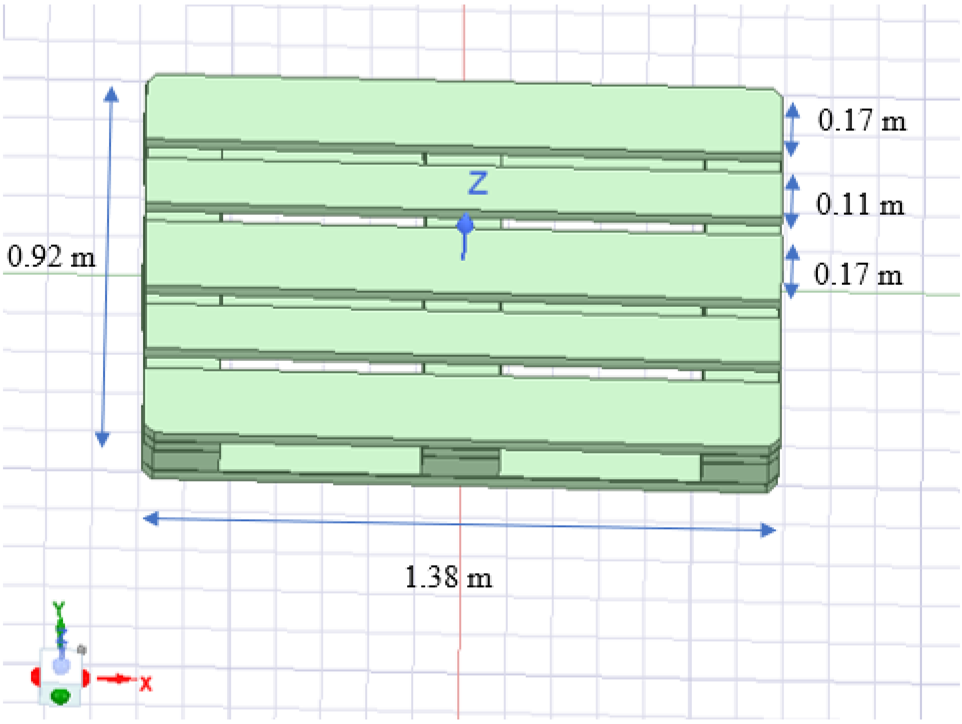

Figure 4.6-1 Pallet STL design for use in HFSS as extended target.

The gridlines are slightly sloped due to the aspect angle in HFSS. It was arbitrarily rotated so the structure underneath the pallet can be seen. It is seen that where the slats at the top of the pallet connect to the three beams in the middle, small corner structures are formed and could be regions of strong specular reflection.

4.6.1 Surface roughness for extended targets.

It will also be important to simulate rough surfaces on targets, to show how different carrier frequencies scatter off the surface. To do this, a 3D rendering software called Blender was used, as it enables the ability to model rough surfaces onto the STL file and export it for use in HFSS. Blender has many tools which can be used to achieve this, but most importantly the RMS surface roughness can also be set, which allows comparison with the Rayleigh roughness criteria [118]. In this section the pallet model was modified on Blender software to have a rough surface.

To form the rough surface on Blender, the pallet model was imported as a STL file to the Blender workspace. When editing STL models, the surface is bound by facets known as the mesh. The mesh is drawn by connecting the corners of a 2D face with a straight line to form triangles on the surface. The mesh determines the resolution of the model roughness, and so, to produce surface roughness that is close to the wavelength of the radar signal, the mesh needs to be refined. This is because Blender perturbs the vertices of the facets, so the mesh should at least be smaller than the resolution of the radar.

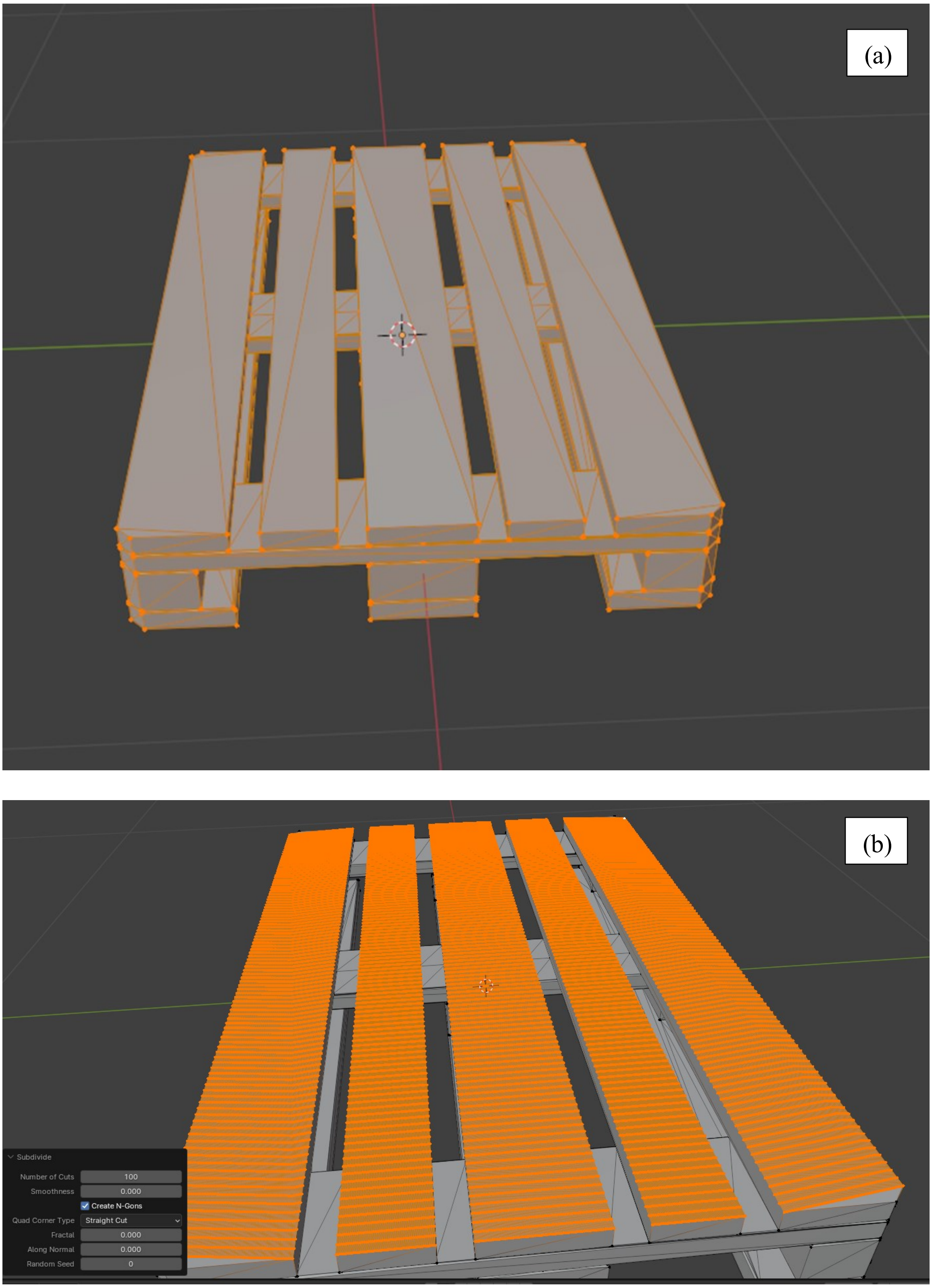

Number of Cuts: 100
Smoothness: 0.000
☑ Create N-Gons
Quad Corner Type: Straight Cut
Fractal: 0.000
Along Normal: 0.000
Random Seed: 0

Figure 4.6-2 Pallet model before mesh refinement (a) and after mesh refinement (b), where the mesh was improved over 1000 times, which allows for finer perturbation of the surface.

Using Blenders sub-divide tool, the mesh was reduced by 100 times in area, and so the mesh was formed from triangles with a base width of 1 cm and a height of 3 cm. Blender enables the user to further sub-divide the mesh, however this vastly increases the computational expenditure. Blender offers many tools to modify the models shape and size. Here, the layer tool was used to introduce surface roughness of a known height onto the surface of the pallet. The layer tool selects a small region on the model and increases its height by a set amount. By randomly assigning the regions on the surface of the pallet, random regions were raised, creating a rough texture on the pallet.

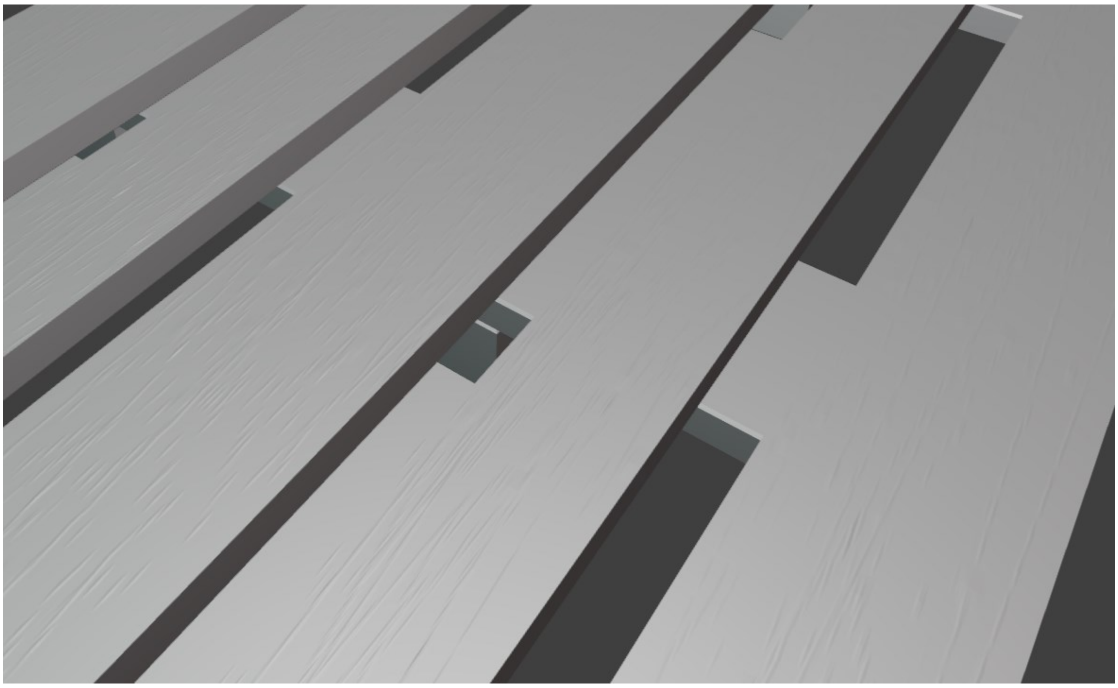

Figure 4.6-3 Pallet STL model, now with a surface roughness RMS of 2 mm.

A RMS surface roughness of 2 mm was been introduced to the pallet surface. The model is exported from Blender and imported into HFSS ready for simulation, now with its rough surface.

4.6.2 Target Dynamic for Floating Targets

For a stationary simulation with no evolving surface, the target can be placed on the sea surface with a defined position and orientation, and then the environment is ready for the simulation. For the simulation of the evolving surface, target motion can also be simulated by changing the position and orientation of the target for each new iteration of the sea surface. Target motion on the sea surface can be complicated, as it is dependent on many different factors such as target weight and shape as well as the dynamic of the surrounding sea. Hence for the purposes of simulation, only basic assumptions are made on target motion.

If assuming that the target weight is negligible, the target motion in the z axis can be assumed to be the same as the sea surface underneath it, and the cross range and range motion can remain zero. This is not directly representative of real floating target motion as it usually will have some horizontal drift velocity, which is usually in the same direction as the progression of the surface waves. A single facet on the sea surface model is taken, and the height is recorded for the same facet, resulting in the change in height against time. Using this, the target model can be moved in height according to the change in height of the sea model. Modelling how the orientation of the target changes was done by measuring the height of the surface at two separate points, 8.5 m and 9.5 m on the surface around the central position of the pallet to estimate the pitch angle.

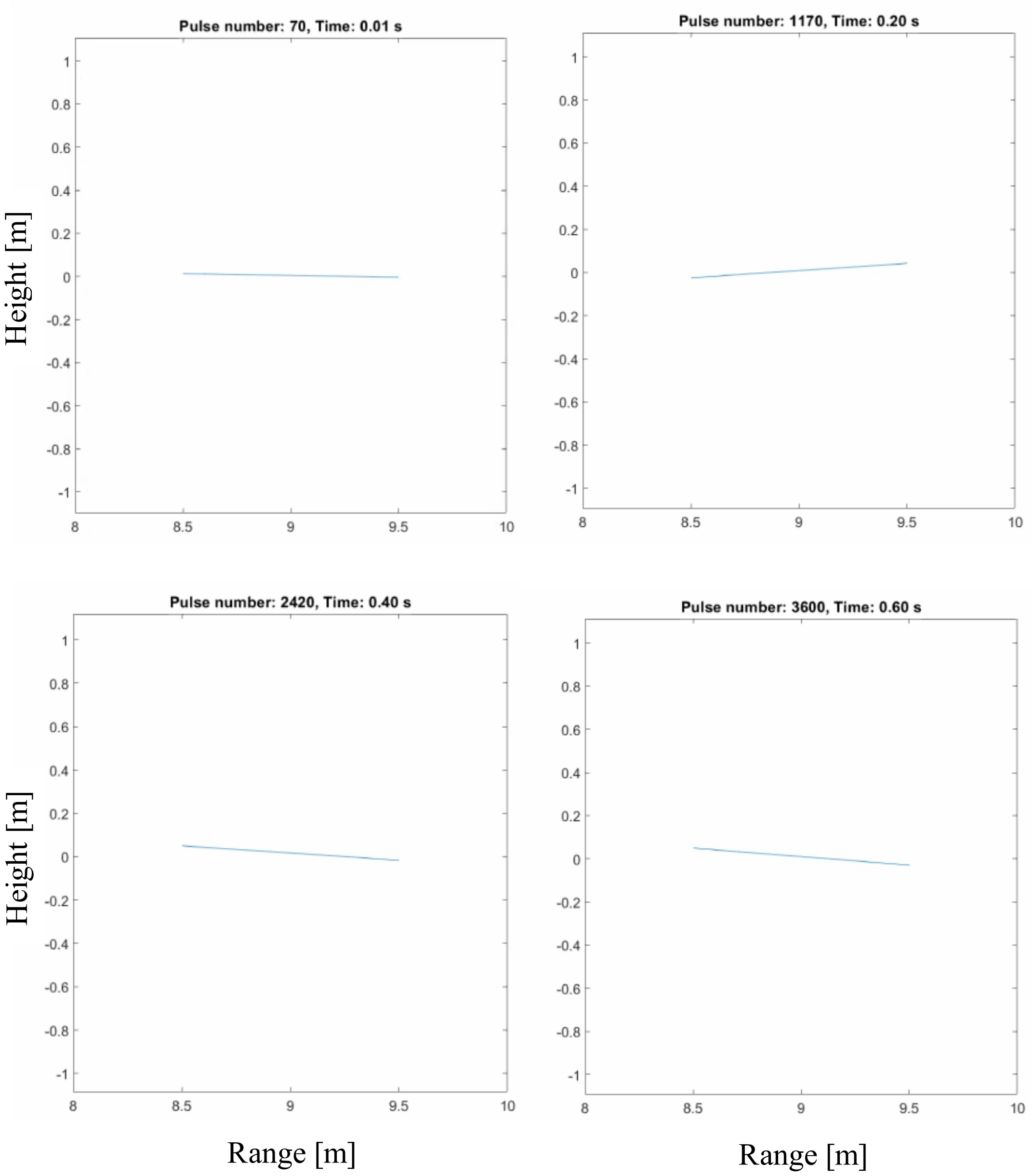

Figure 4.6-4 Pallet orientation vs time/pulse number for sea state 1 Pierson-Moskowitz and 6 KHz PRF. This data can be used in HFSS to orient the pallet for each simulated pulse.

4.7 Simulating the Antenna and Transmission in HFSS

HFSS enables the user to define a parametric antenna with a set beamwidth, and the parameters of the transmitted signal. HFSS will produce the S-parameters associated with the backscatter off the design environment. Here the S-parameters represent the linear characteristics in RF circuits and can be used to determine how much of the transmitted energy is returned to the antenna. Therefore, to use a single defined antenna as the transmitter and receiver, the S11 parameter, known as the input port reflection, is used to process the radar signal. As the power is normalised, the RCS of the target can be estimated using (2.9-5).

The user must carefully select the transmission parameters, as this will define how the simulation and results behave.

To ensure an antenna transmits, its transmission parameters must be defined, the start and stop frequency of a single sweep, as well as the number of fast time samples to simulate. An SBR simulation needs to know how many rays to emit per unit wavelength. The more rays emitted, the higher the accuracy of the simulation at the cost of computation time. The number of bounces of the SBR simulation is also defined by the user. The computation time is directly proportional to the number of samples in a sweep. For increasing frequency, the computation time also increases, as the wavelength is shorter and hence the number of rays is larger for a fixed ray density, so there are more calculations required during the SBR process. The computation time is also directly proportional to the number of bounces defined, as for each bounce, the calculations at the object boundary needs to be repeated.

Table 4.7-1 Antenna parameters for HFSS simulations

Antenna Parameter	**Value**	**Units**
Start Frequency	145	GHz
Stop Frequency	150	GHz
Horizontal Beamwidth	10	Degrees
Vertical Beamwidth	10	degrees
Sample Count	1000	N/A
Maximum Bounces	4/2	N/A
Ray density per wavelength	4	N/A

Here the bandwidth is 5 GHz which achieves a range resolution of 3 cm. As the sample count is 1000, this results in a maximum simulated range swathe of 30 m. Although large for the pallet, the SBR calculation are only completed on valid facets, and so it shouldn't complicate the simulation. The sample count determines the number of different frequencies simulated from the start frequency to stop frequency. In this case the frequency step is 5 MHz.

The more bounces in the simulation, the longer it will be. Four bounces were selected to simulate returns from corners, and surface roughness effects for target simulations. For the sea surface modelling two bounces were used to speed up the simulation, under the assumption that surface roughness was not applicable, as the PM spectrum does not model this for Sub-THz frequencies, and it is assumed no corner structures are in the sea model.

4.7.1 Simulated Linear Antenna Motion for DBS/SAR Measurements

As explained in the previous chapter, the DBS modality requires the antenna to be moving down a linear path to form the synthetic aperture. Of course, in reality, the antenna will also be subject to the surface dynamic and not move in a linear motion. To keep the analysis and simulation simple, the antenna motion was assumed linear, so the target always remains in the beam at any given time, but for future investigation the non-linear motion could be estimated and applied to the simulation. The linear motion can be simulated by defining the change in position of the antenna for each iteration of the simulation.

$$\Delta x_{ant} = \frac{v_0}{f_{chirp}} \qquad (4.7\text{-}1)$$

Where v_0 is the proposed simulated platform velocity, f_{chirp} is the PRF and the antenna spacing between each simulated pulse is Δx_{ant}. When designing the HFSS simulation, Δx_{ant} is defined by the user and hence it is important to ensure that it corresponds the correct ratio of velocity and PRF when simulating for a dynamic environment. By keeping the antenna spacing constant, it is analogous to keeping the velocity constant.

It is important to note here that, due to the stop and go nature of the simulation, for a stationary environment there is no real temporal reference. The data matrix obtained from the simulation contains the S parameters at each frequency step in the FMCW chirp against the position of the antenna along the synthetic aperture and therefore has no real time information.

Instead using (4.7-1), time information is assigned to the data by defining the PRF to be any arbitrary value, which results in a defined antenna velocity and Doppler values from the scattered signal. As a result of this, the DBS refinement factor can be defined using the input parameters of HFSS without regarding time. Firstly, the integration time used is equal to the number of pulses integrated divided by the PRF.

$$\tau = \frac{N}{f_{chirp}} = \frac{N\Delta x_{ant}}{v_0} \qquad (4.7\text{-}2)$$

Here *N* refers to the number of chirps integrated during the integration time τ. By using (4.7-1), The integration time is now seen in terms of the PRF and platform velocity. Hence by substituting (4.7-2) into (3.2-11), the resulting azimuth resolution from DBS processing is shown using the parameters that are precisely defined in the HFSS simulation.

$$\Delta\theta_{az}^{r} \approx \frac{c}{2f_0 N\Delta x_{ant} \times sin\ (\varphi_1)} \qquad (4.7\text{-}3)$$

It is clear from (4.7-3) that DBS processing on the HFSS simulated radar data is independent of time and instead is dependent on the number of pulses integrated (analogous with integration time in a real measurement) and the spacing between each pulse (analogous to velocity).

However, when introducing a dynamic environment, the dynamic may be defined by several time-influenced parameters, as in (4.5-2), which act as a ‘clock’ for the simulation. Using the example of a time evolved surface, each iteration of the surface will be time evolved by an amount *Δt*, which defines the PRF, which then can be used to define the correct antenna spacing to achieve a desired antenna velocity with (4.7-1).

4.8 Line of Sight Simulation for Verification

Once the simulation is complete, and the radar image is formed, a simple sanity check. to ensure the image shows at least what is expected from the sea surface, can be done by checking which facets on the sea surface are visible from the antenna, and therefore which facets should backscatter most of the signal toward the antenna and appear in the DBS imagery. Waves exist between the facet under test and antenna, where some waves heights are larger than the height of the line of site in the azimuth position of the wave.

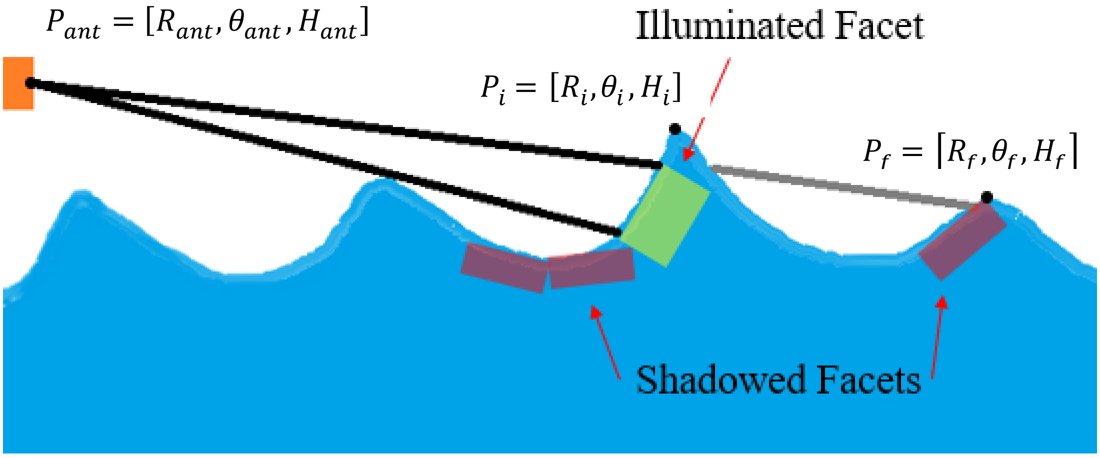

Figure 4.8-1 Antenna line of sight at sea, Illuminated facets and shadowed facets.

$$a_{LOS} = P_f - P_{ant}$$

$$a_w = P_i - P_{ant}$$

$$H_w > H_{LOS}, \quad R_{LOS} > R_w, \quad \theta_{LOS} = \theta_w \qquad (4.8\text{-}1)$$

Here, (4.8-1) outlines the criteria required for the facet under test, denoted with the subscript *f*, to be shadowed. The positions, *P*, are in cylindrical co-ordinates. P_i is a position on the sea surface that exists in front of the facet position P_f defined by the range denoted *R*, azimuth denoted θ. When H_w is greater than H_{LOS}, the facet under test is shadowed. This line-of-sight test is performed for all discrete positions that exist between the antenna and facet under test.

4.9 Point scatterer DBS HFSS simulation results.

The initial tests for the simulated DBS measurement involve a set of small spheres in the far-field of the antenna, which was used to identify the effects of Doppler smearing due to excessively long integration times. The sphere diameters were 1 cm, and can be assumed as point targets as all of the reflection comes from a small area on the surface that is normal to the inbound rays. It also serves as a sanity test to see if the RCS measured agrees with the theoretical value as well as the path loss.

4.9.1 Point Spread Function vs Integration time

A single point scatterer was used in a DBS simulation to see how the increase of integration time affects the point spread function of a single scatterer. As discussed previously, by integrating over more pulses, not only will the point scatterer move into the next Doppler cell, i.e Doppler Walk, but the size of the Doppler cell decreases. However, it is also important to note that, integrating more pulses than the minimum required for the energy to deposit into the neighbouring Doppler cell may still refine the width of the point spread function (PSF) as the resolution increases in a way that the gradient of power vs cross-range also increases.

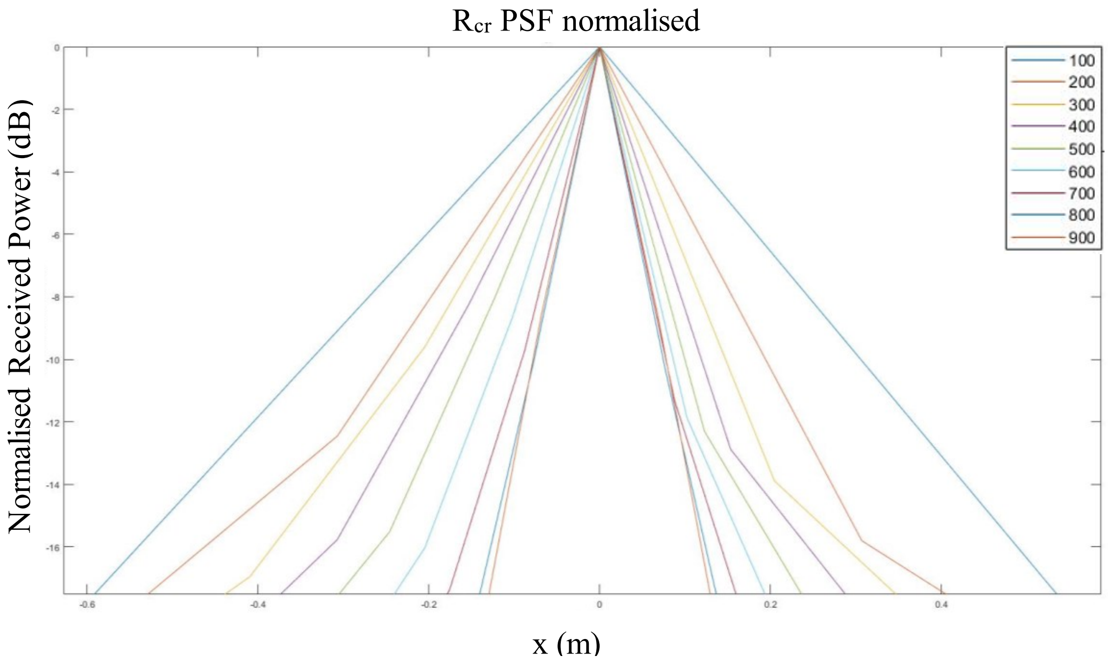

Figure 4.9-1 Point spread function of point scatterer for different numbers of integrated pulses 100 to 900.

In Figure 4.9-1 we clearly see the effect of integrating more pulses and the benefit it has on refining the PSF. However, it is noted that as the number of pulses increase, and the Doppler resolution cells reduce in frequency, the benefit of integrating more pulses begins to reduce in effectiveness. At 800 integrated pulses, we see that the PSF is nearly the same as if 900 pulses were integrated, and hence we are approaching the limit of the integration time where the PSF begins to degrade in the DBS image.

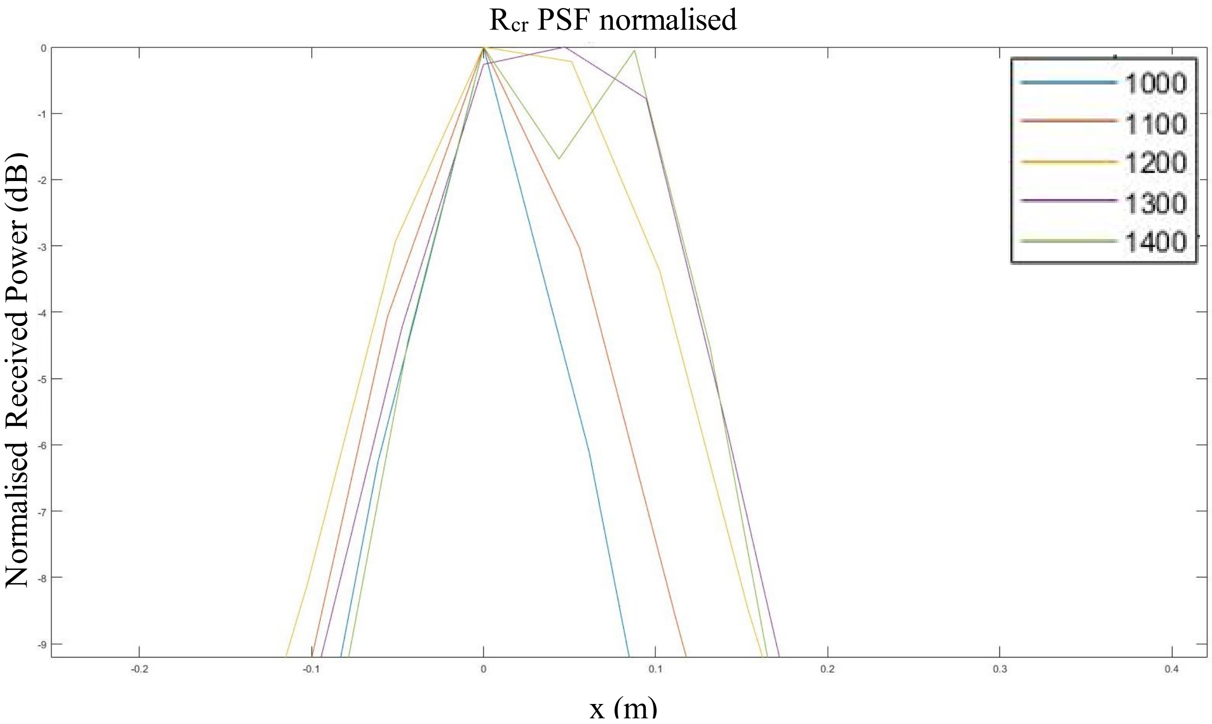

Figure 4.9-2 Point spread function of point scatterer for different numbers of integrated pulses 1000 to 1400.

In Figure 4.9-2, it becomes more obvious that the number of integrated pulses is excessive and as a result the PSF begins to widen in cross-range. At 1000 integrated pulses, the PSF appears as a single peak, which indicates that the power has mostly accumulated in a single Doppler cell. As we move closer to 1400 integrated pulses, we see that the power begins to accumulate in neighbouring Doppler cells until the power is comparable with that in the original Doppler cell.

4.10 Extended Target Simulation

Extended targets are important to simulate, as their unique structures and scattering properties may have many different effects on DBS processing. It also enables the exploration of simulating the potential diffuse scattering off the surface of the target, so that the target structure maybe be seen in the resulting DBS image by exploiting the better sensitivity to surface textures that Sub-THz frequencies can accommodate.

An important step of the modelling process is to assign a material to the target. The simplest case is to assign the model PEC properties, so that all the incident radiation energy is scattered back into the environment without any energy loss. In reality, material properties may significantly affect target RCS, however knowledge of this is limited at sub-THz frequency, so PEC was used.

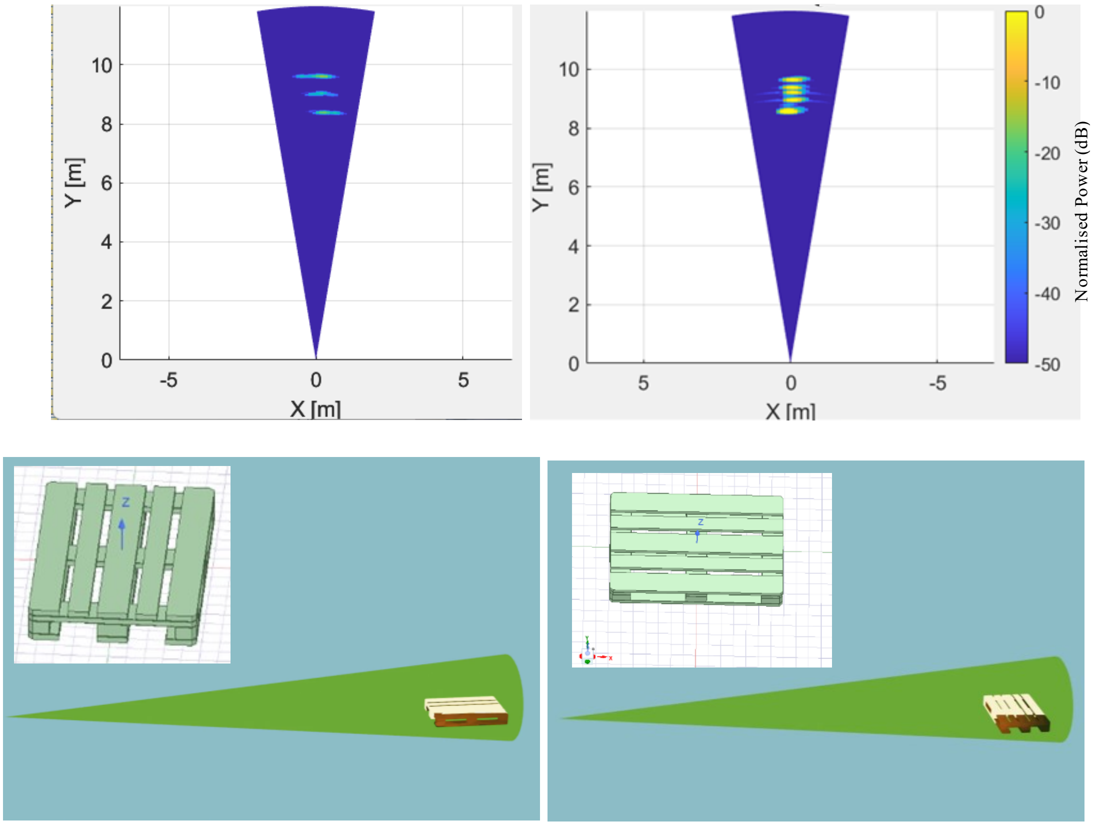

Figure 4.10-1 DBS simulation of smooth pallet (a), same simulation with pallet orientated by 90 degrees (b)

Three distinct lines appear in the DBS frame for simulation a, and the slats at the top of the pallet cannot be seen. This occurs due to the specular scattering off the three supporting beams underneath the slats. The slats of the pallet have been simulated as smooth PEC facets, and so only specular scattering is considered during the simulation.

In a wider context, this phenomenon suggests that the image formed during DBS will not always correspond directly to the optical image of the object.

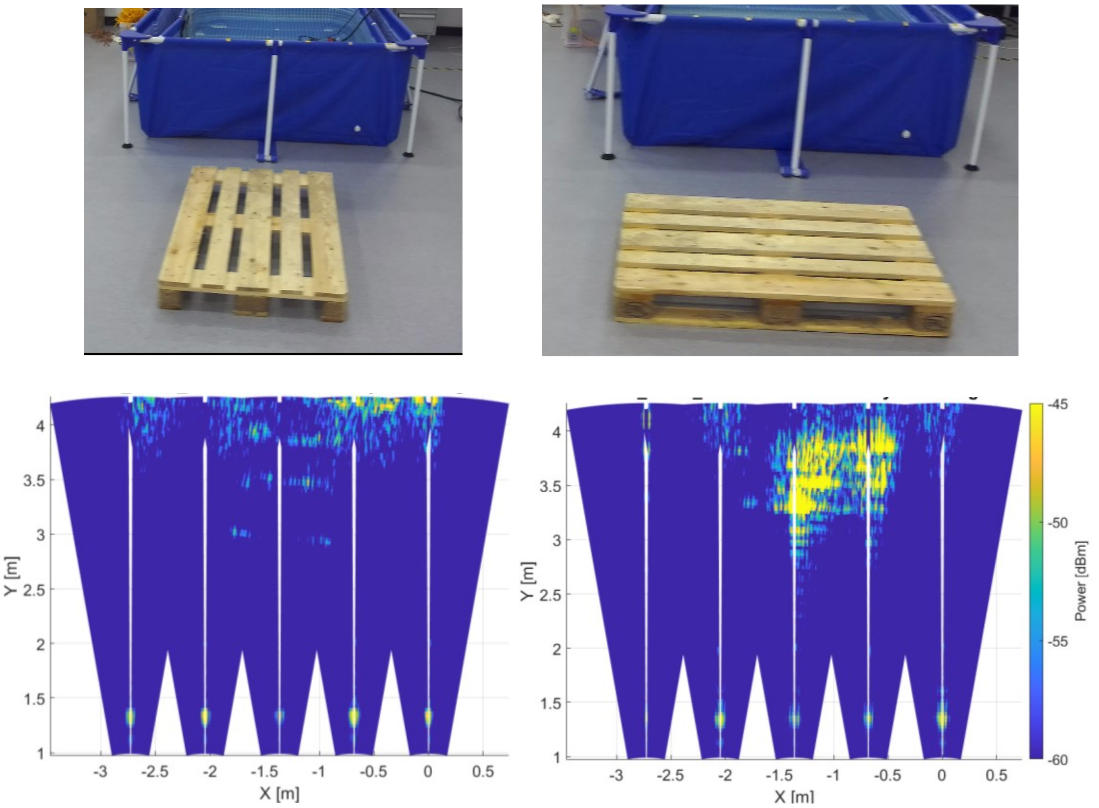

Figure 4.10-2 DBS measurements taken with a 150 GHz of the pallet at different orientations. The next chapter details the radar used, but the processed imagery appears here to validate the simulation findings.

In agreement with the results of the simulation, the image formed from the DBS processing of real data shows the same effect. For orientation a, only 3 lines are presented in the overlayed DBS image, due to the specular scattering. Although the pallet is textured and made from wood rather than PEC, it was found that the diffuse scattering off the surface was not significant in the measurements.

4.10.1 DBS rough surface target simulation results.

To investigate the capability of HFSS to measure diffuse scattering characteristics, a pallet with rough surfaces was simulated using the methodology outline in section 4.6. In this simulation a pallet with an RMS roughness of 1 cm was used to ensure that the pallet was electrically rough at the simulated grazing angle.

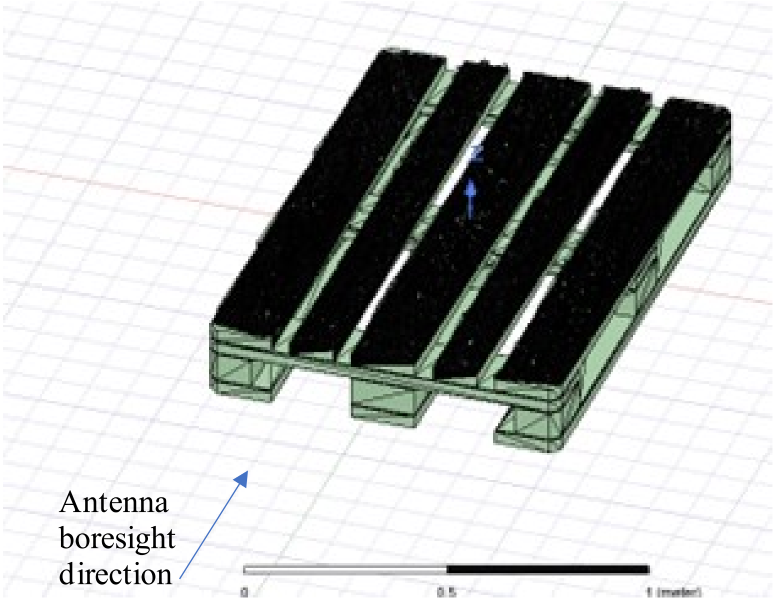

Figure 4.10-3 Pallet in HFSS design environment with antenna boresight direction.

Table 4.10-1 Extended rough target simulation parameters

Simulation Parameter	**Value**	**Units**
Antenna		
Start Frequency	145	GHz
Stop Frequency	150	GHz
Horizontal Beamwidth	10	Degrees
Vertical Beamwidth	10	degrees
Sample Count	1000	N/A
Maximum Bounces	2	N/A
Ray density per wavelength	4	N/A
Motion		
Antenna spacing/pulse	0.000167	m
Dynamic environment	No	N/A
DBS processing		
Integrated pulses	965	N/A

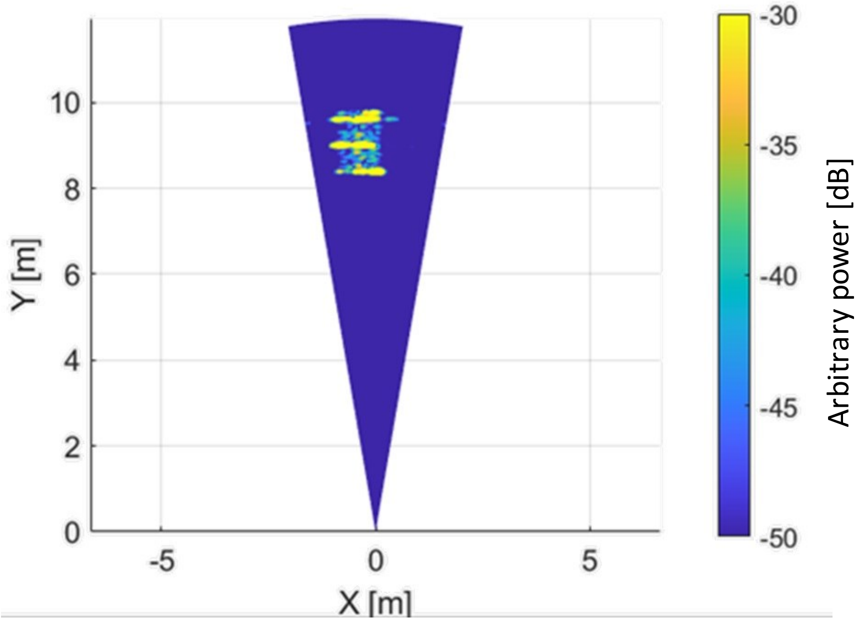

Figure 4.10-4 150 GHz DBS simulation of stationary rough pallet with RMS roughness of 1 cm.

A total of 965 pulses were integrated to form the image in Figure 4.10-4, which is near the integration limit seen from Figure 4.9-1. The resulting image is well focused, and the shape of the pallet can clearly be seen, matching the dimensions of the model. We see that the three specular regions that appeared in the smooth pallet simulation appear, as well as the diffuse scattering region between the specular regions. This scattering is not range sidelobes as they are only seen in the region occupied by the target, i. e. they do not extend up-range or down-range of the big horizontal returns. On the left side of the image, the received power begins to degrade as the pallet is still outside of the beam during part of the integration period. Now, the reflections of a stationary pallet are understood in both simulation and measurement, where the simulation agrees with the measurements, where we find the pallet is essentially smooth at 150 GHz. At low grazing angles, the surface roughness of the pallet is on the order of mm, so it is plausible that it would appear smooth and diffuse scattering would not be significant. This finding is useful as other wooden flotsam may yield similar results, and specular reflections would dominate DBS imagery of them.

4.10.2 DBS Dynamic Rough surface simulation

Now that the rough surface pallet has been imaged using DBS processing, the dynamic of the sea was added to the simulation step to investigate the effect of target motion on image quality and Doppler smear. As mentioned before, in a stationary stop and go simulation, there is no concept for timing, however, the dynamic of the pallet provides a time reference, hence the following simulation in this section is based off a 6 KHz PRF and a velocity of 1 m/s.

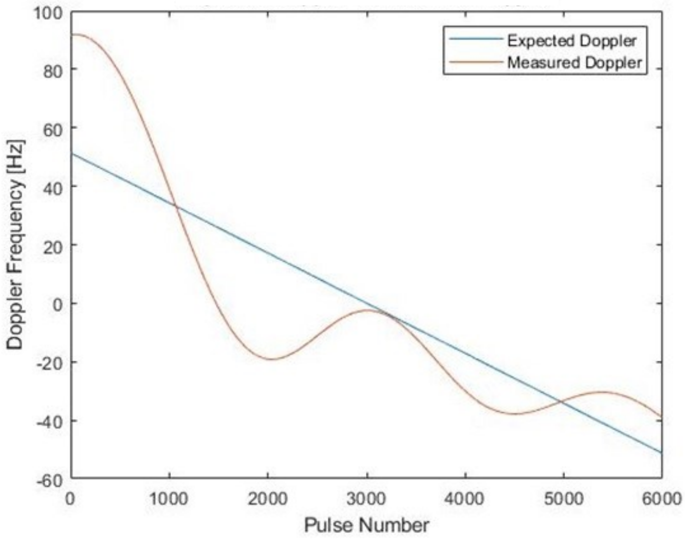

Figure 4.10-5 The expected Doppler frequency of a stationary point target at [0,9.5,0] m vs the modelled Doppler frequency of the moving pallet surface at [0,9.5,0] m where the antenna starts at [0.5, 0, 1] m.

In Figure 4.10-5, the expected Doppler frequency is the Doppler frequency a stationary target would have due to the antenna motion and what DBS assumes to form imagery. The modelled Doppler frequency is significantly different as this is the actual Doppler frequency measured from the target, which is now moving on the surface, hence the Doppler is a function of both the target motion and antenna motion. The difference between the expected Doppler and the modelled Doppler frequency will give an insight into the amount of smearing after DBS processing that is expected when measuring moving targets. This is illustrated in Figure 4.10-6.

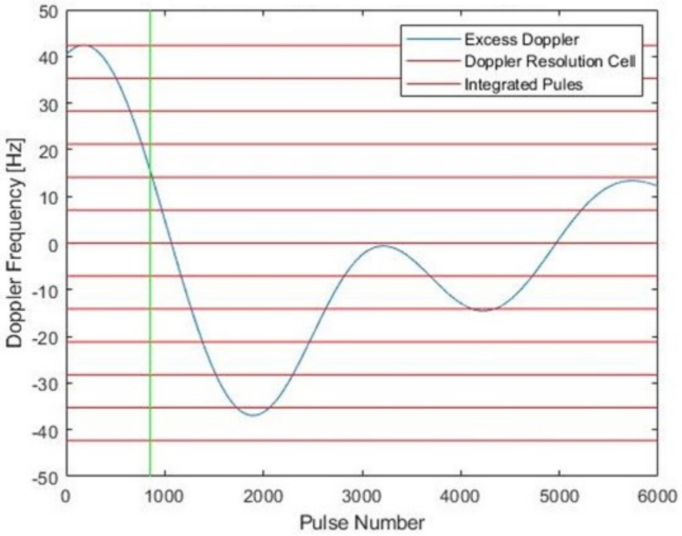

Figure 4.10-6 The difference between the modelled Doppler from a target on the sea and the Doppler expected from a stationary Doppler. Red lines indicate the boundaries of the Doppler resolution cells; Green Line indicates the number of pulses integrated. DBS in a stationary environment should yield no "excess Doppler"

Here we see that over the integration period, which is indicated by the green line 'integrated pulses', the actual Doppler frequency varies between about 40 Hz and 20 Hz more than the DBS would expect it to be, and hence the resulting imagery is displaced by 30 Hz and a point target will be spread over three Doppler bins. In terms of angles, although the centre of the pallet appears at a squint of 90 degrees, the centre will be resolved in the DBS image at an angle of 87.61 degrees. In terms of cross range, at a range of 9 m, the extra displacement is around 0.388 m which is significant with respect to the pallet size. Furthermore, during the integration period, the platform motion changes, hence the excess Doppler changes and the pallet moves through four Doppler cells, which means as well as displacement there is some Doppler smear.

Here it must be noted that, although the image is displaced in the DBS imagery, the image quality of the target may not be totally distorted.

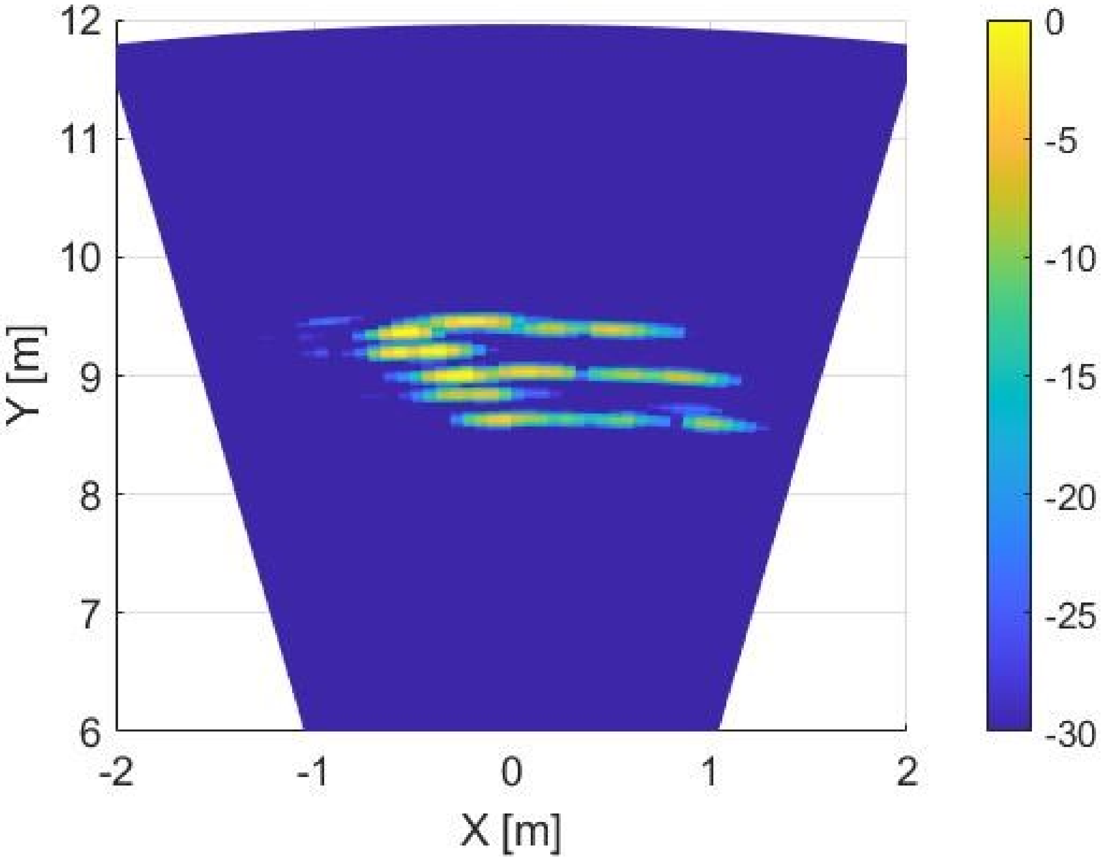

Figure 4.10-7 150 GHz DBS simulation of Dynamic rough pallet with RMS roughness of 1 cm.

The first noticeable thing about the dynamic pallet is that there is a clear distortion of the pallets shape, as it appears to be a rhomboid rather than rectangular. This distortion of shape indicates that the excess Doppler from target motion is different at the nearside than it is at the far side of the pallet. As the pallet changes orientation, i.e. the back moves up as the front moves down, the change in Doppler frequency will be different for each side. This means that the pitching motion of the pallet in the range vector will appear as yaw seen in Figure 4.10-7.

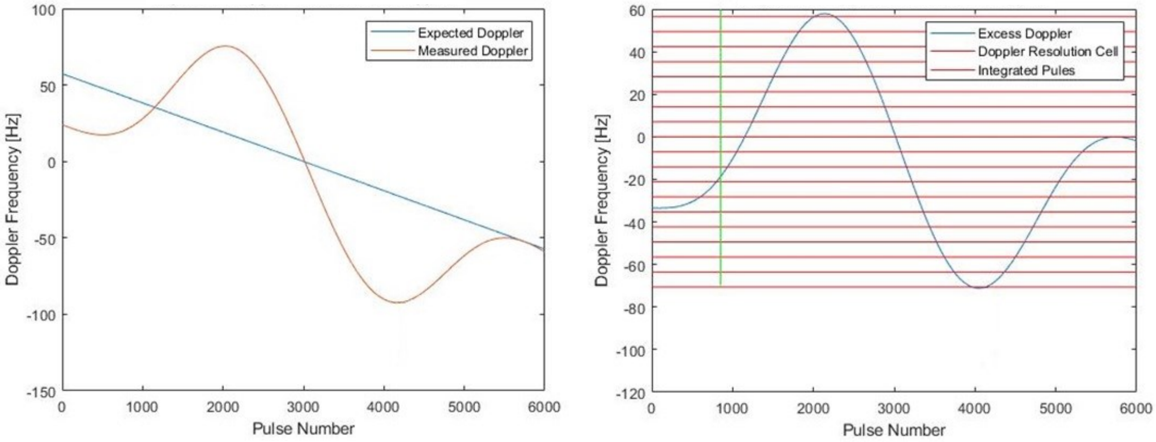

Figure 4.10-8 The expected Doppler frequency of a stationary point target at [0,8.5,0] m vs the measured/expected Doppler frequency of the moving pallet surface at [0,8.5,0] m.

Here we see that the measured Doppler frequency is around 33 Hz less than the expected Doppler for a stationary target at [0, 8.5, 0] m. In cross range, that corresponds to a cross-range difference of -0.303 m than the expected. In comparison to the Doppler frequency measured in Figure 4.10-5 and excess Doppler in Figure 4.10-6, we see that there is a 75 Hz difference between the near side and the far side of the pallet which represents a difference in cross range of 0.691 m between the front and the back of the pallet. Considering that the pallet exists down range by 1.38 m in both the DBS image and the model, and the offset between the nearside and the far side is 0.691 m, the edges of the pallet are slanted by an extra 26.6 degrees.

So, the simulation has shown that the movement of targets on the ocean's surface serve to distort the imagery produced by DBS processing. However, even with target movement, DBS processing can resolve the targets shape.

4.11 Stationary Surface Simulation

A DBS measurement is now simulated with a stationary sea surface model. This is to test the plausibility of using HFSS to image the sea surface, and to compare it to the line of sight, where we expect the returns from shadowed regions to be much less from the illuminated regions. The simulation runs similar to the process outlined in section 4.1, however the only thing that changes per simulated pulse is the antenna position, and the surface model remains the same.

The sea surface model used was based on the Pierson-Moskowitz spectrum, where the windspeed was chosen to be 3 m/s at 19.5 m above the surface. The cosine-squared spreading function was used as the directional spreading function as it ensured all waves were spread in angle equally regardless of frequency and the phase was randomly generated. Hence the sea surface model is unique. This unique structure can then be used to test if the DBS produces a focused image of the sea surface, or if any regions appear defocused due to motion.

4.11.1 Stationary Surface Only

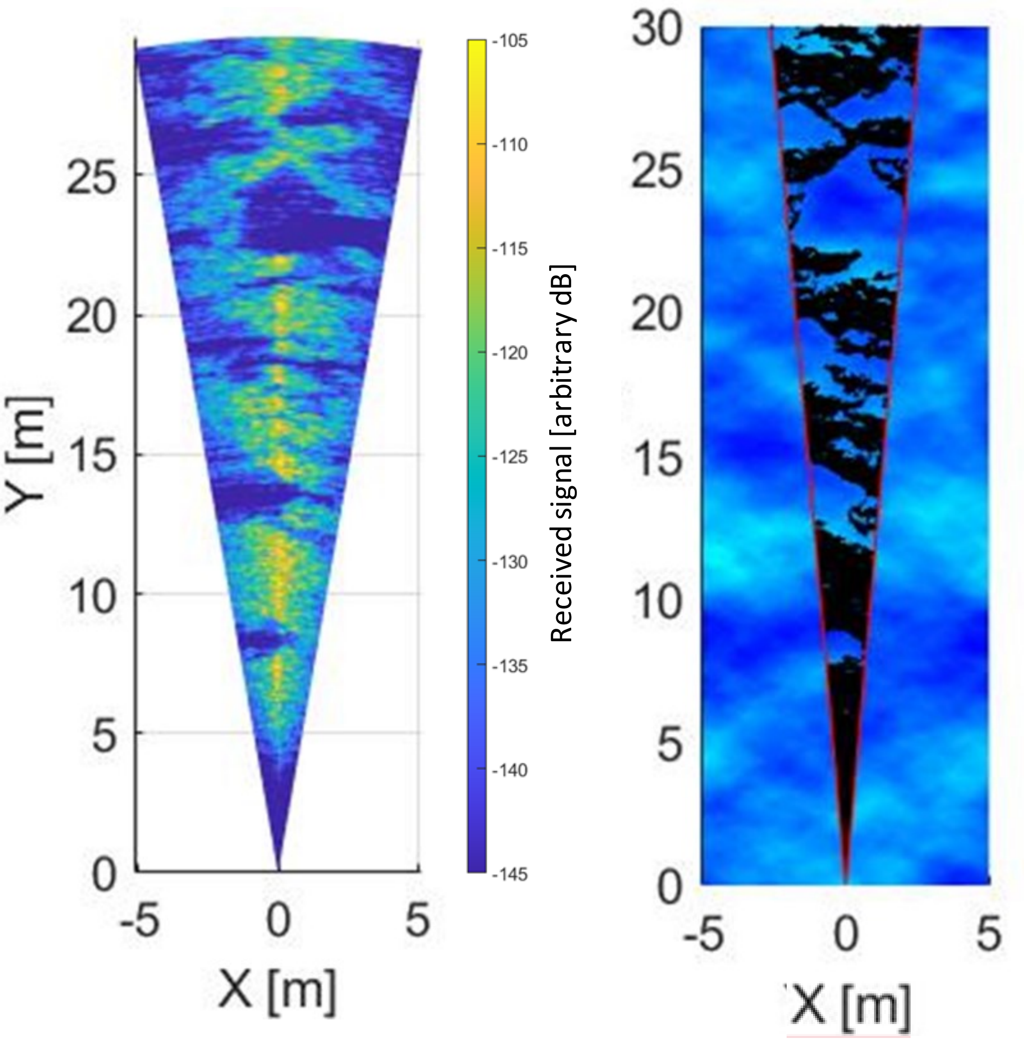

Figure 4.11-1 Stationary DBS measurement, with LoS plot to show illuminated facets. Illuminated facets appear black, whereas facets that are shadowed or out of the beam are coloured blue.

Figure 4.11-1 shows that the DBS processing works as expected for imaging the simulated marine environment. The regions that are illuminated appear in the DBS image as regions of relatively large returns. The shadowed regions are also resolved in the image as regions of relatively low returns. Furthermore, the shape of the surface facets has been resolved in the DBS image. It is noticeable that, at short ranges, there are 'illuminated facets' from the LoS perspective, but the simulated antenna pattern beam misses this region, returning low S11 parameter values in the DBS image. This can be referred to as a 'Blind-Zone' and is an effect of the antenna height and beampattern. For the purposes of vessel mounted radar, radar heights are estimated to be around 1m from the surface, and so the blind-zone should not exceed past 5 m.

5 150 GHz Radar Development for Doppler Measurements

Prior to the work presented in this thesis, the 150 GHz radar was used as an imaging radar for automotive applications [119]. The original 150 GHz architecture uses a Digital Signal Processer (DSP) to set the registers on the sweep synthesiser. The synthesiser that was used allowed for a range of chip durations from 1 – 10 ms, and a pulse repetition interval of 30 ms. The development of the 150 GHz FMCW radar was a necessary step for the DBS data collection. The PRF was upgraded to be both configurable and much higher than the previous design. The transmitter and receiver modules were mostly re-used beyond the 20 times multipliers seen in Figure 5.1-1. As discussed in section 2.14.1, the higher the PRF, the higher the unambiguous Doppler frequency, and therefore the platform can move at faster speeds and the squint angle can be reduced. It also means the Doppler frequencies measured from fast moving objects are less likely to aliase in the DBS imagery. This chapter explains the modifications made to the radar architecture and how it incorporates the old radar design to form a complete radar system for DBS measurements.

Table 4.11-1 150 GHz Radar Parameters

Parameter	**Value**	**Units**
Transmit Power	12	dBm
Minimum tested Chirp Duration	0.09	ms
Maximum tested PRF	10000	Hz
Bandwidth	5	GHz
Range resolution	3	cm
Maximum tested unambiguous velocity	± 5.17	m/s
Initial depression angle (w.r.t boat)	3	degrees

5.1 150 GHz FMCW Radar System New Design Overview

The new radar design replaces the old synthesiser with an AD9914 DDS synthesiser to produce the chirp waveform, which can be set at 530 – 780 MHz to achieve a 250 MHz bandwidth which is multiplied by 20 further in the radar architecture to achieve a 5 GHz bandwidth, and an AD5355 STALO to produce a 6720 MHz continuous waveform. These signals are up converted and passed through a power divider, which sends the signal to the transmitter and receiver sections separately. The signals are mixed by the Hittite HMC 220 mixer and the output is succeeded by an isolator and Band Pass Filter (BPF) The BPF used is the Pasternack 7.25 – 7.75 GHz, PE8741 [120], which was taken from the old design. This removes the LSB which is 5.94-6.19 GHz and keeps the USB which is 7.25-7.50 GHz as well as any leakage from the 6720 MHz LO. In the transmitter, the 7.25-7.50 GHz signal is amplified and passes through a twenty times multiplier to achieve the RF frequencies (145 -150 GHz) at the radar front end. The multiplier used is the ELVA-1 IMPATT frequency multiplier IAFM-06 [121]. The RF chirp waveform then moves to the waveguide and antenna to be transmitted as an electromagnetic wave. The LO signal that enters the receiver section is also multiplied by twenty times to achieve the RF frequency. This signal then split into two signals, namely the I and Q channels, where the Q channel is phase shifted through 90 degrees relative to the I Channel to enable quadrature down conversion. Similarly, the received RF signal travels from the waveguide and is split between the two mixers. The I and Q components of the received signal are then separately amplified and passed out of the unit via SMA cables. The IF signals from the I and Q channels are connected to the ADC via SMA to SMB cables. The ADCs convert the raw analogue signal into a digital format that can be saved and therefore analysed at any time.

The radar is controlled by a host PC which houses the ADC cards. It also communicates with the AD9914 to write the chirp waveform and with the AD5355 STALO to choose the LO frequency.

The control PC also communicates with a 10 MHz GPS defined reference signal distribution board which controls the PRF and reference clocks of the radar and the ADC cards, as explained in section 5.3. The latter emits rectangular pulses of specified frequency that feed into the AD9914 trigger ports, which causes a chirp waveform to be emitted on the rising edge of the pulse. It also feeds into the ADC trigger port which causes the data collection process to start as soon as the chirp waveform is emitted. This board also provides reference clocks which enable the exact synchronisation between all subsystems required to take measurements with the radar.

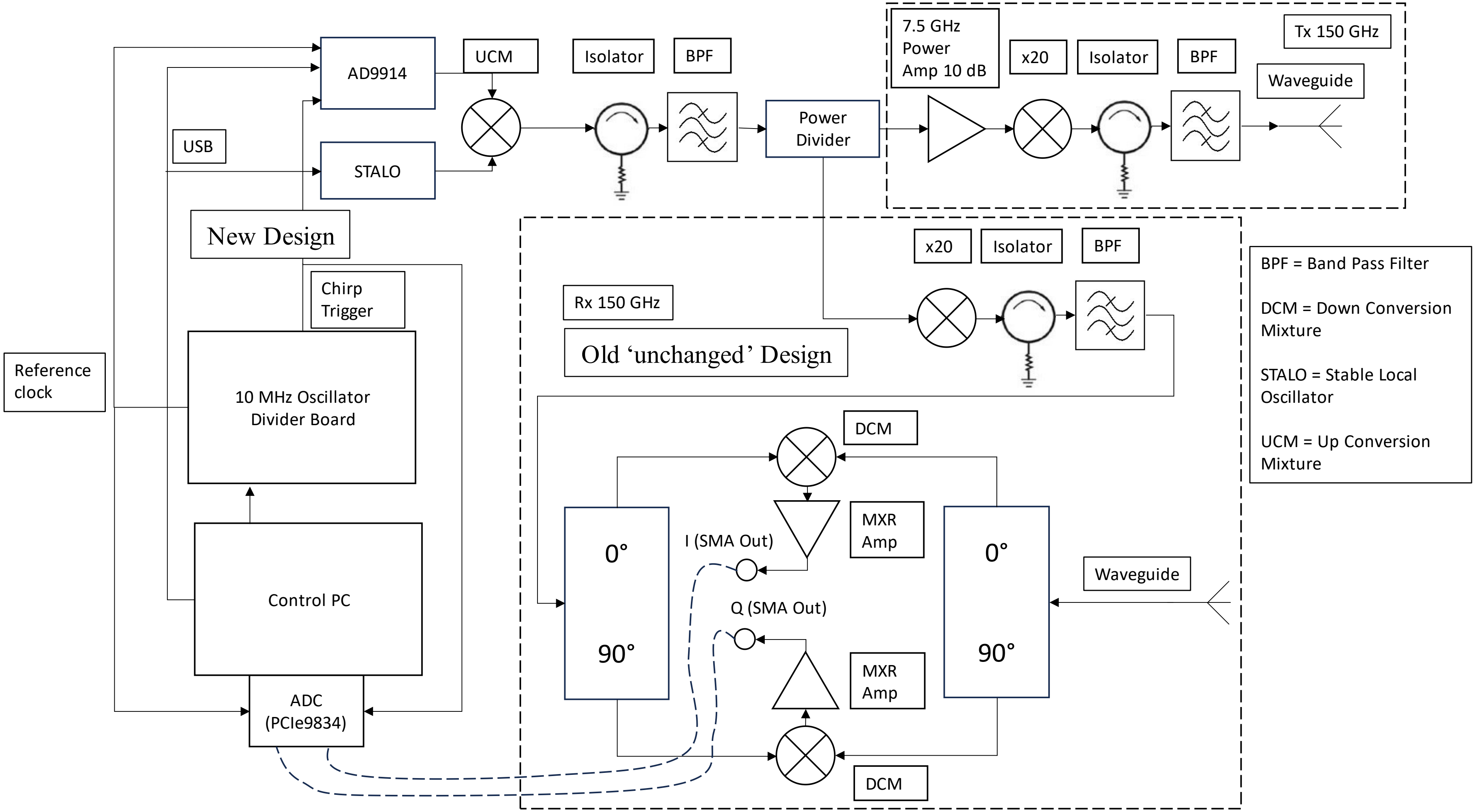

Figure 5.1-1 150 GHz FMCW Radar architecture

5.2 AD9914 DDS for Chirp Waveform Generation

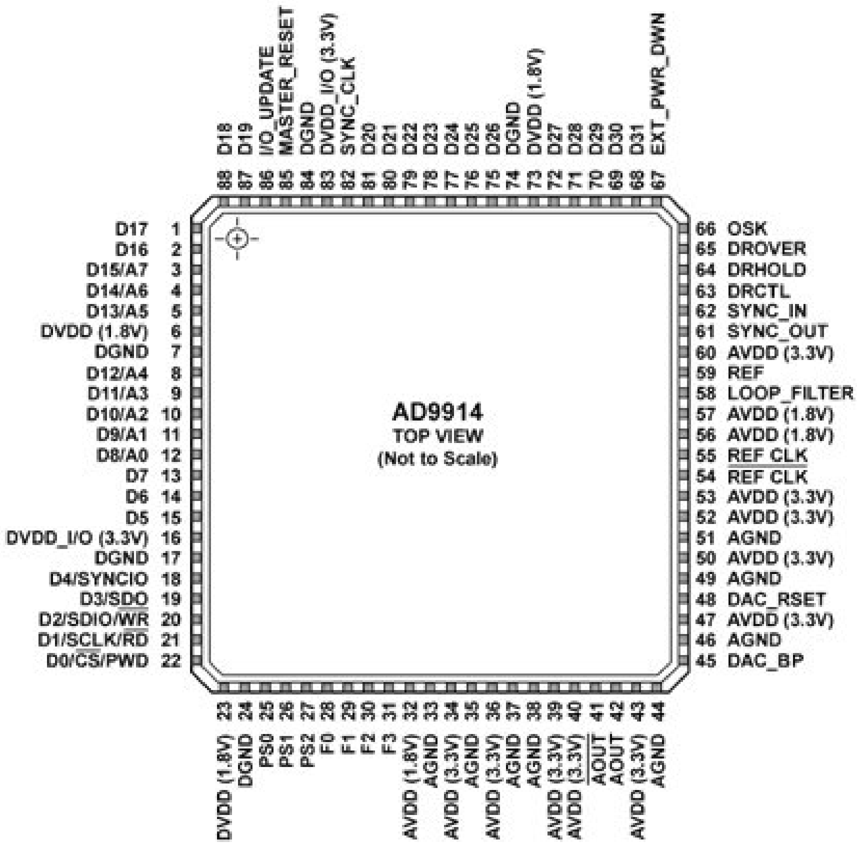

Figure 5.2-1 AD9914 Pin configuration, taken from page 10 of [122].

The AD9914 is used as a DDS to provide the digital chirp waveform that passes through the on-chip DAC, for the FMCW radar. It was supplied as an evaluation board which is also fitted with its own microcontroller that enables the host PC to communicate to the AD9914 board via its control pins seen in Figure 5.2-1. Pin 63 is the digital ramp control (DRCTL) input which takes a pulse signal and is used to trigger the chirp waveform on the rising edge and therefore to control the PRF of the radar. This pin is connected directly to the 3.3 V Square wave that is emitted from the trigger ports of the 10 MHz divider as explained in section 5.3. The analogue outputs of the DDS are connected to the next part of the radar transmitter. Pins 28 to 31, denoted F0 to F3 are function control registers than enable or disable specific functions on the evaluation board, such as the digital ramp type and the enabling of the parallel port pins denoted D. The pins that are denoted D are parallel port pins that can be used to write to the registers depending on the specific setting of the function control registers. The control registers and the parallel port are controlled via the microcontroller.

The specific waveform design is a linear chirp, equivalent to the waveform design presented in section 1.8. The 150 GHz radar mixes the DDS wave form with the signal from the local oscillator, and this signal then passes through a band pass filter to obtain a waveform at a frequency that is twenty times lower than the desired carrier frequency in the 145 GHz to 150 GHz range. This signal then passes through a twenty-times multiplier chain to produce the sub-THz frequencies, and the final multiplier stage uses an IMPATT to increase the transmission power output. So, if the linear chirp from the DDS has a start frequency of 530 MHz, and an end frequency of 780 MHz, and the local oscillator outputs a frequency of 6720 MHz, the signal after the twenty times multiplication would go from 145 GHz to 150 GHz respectively according to (5.2-1).

$$f_{out} = (f_{loc} + f_{DDS}) \times c_{multiply} \qquad (\ 5.2\text{-}1\ )$$

Here, f_{out} is the output frequency at the radar transmitter front end, f_{loc} is the frequency of the signal produced from the local oscillator, f_{DDS} is the frequency produced from the DDS and $c_{multiply}$ is the multiplication ratio of the multiplier chain. The DDS uses the system clock and the frequency tuning word (FTW) to understand what frequency to output.

$$f_{out} = \left(\frac{FTW}{2^{32}}\right) f_{sysclk} \qquad (\ 5.2\text{-}2\ )$$

Where the frequency tuning word (*FTW*) is an input for a 32-bit register, and where the value of f_{out} is the output sine-wave frequency that ranges from zero to the Nyquist frequency (half of the system clock frequency, denoted f_{sysclk}) [122]. The AD9914 was set up to be configurable, so that parameters can be changed during the measurement process depending on the application of the radar. Such configurable parameters include the chirp duration, PRF, bandwidth and starting frequency. When designing the digital ramp, the FTW for the start and stop frequencies of the chirp are found by setting f_{out} to the desired frequency and re-arranging to find FTW. There are also configurable digital ramp designs, however for the specific case of linear FMCW radar, the 'no-dwell high' ramp design was selected as its properties match the required chirp waveform design for linear FMCW radars.

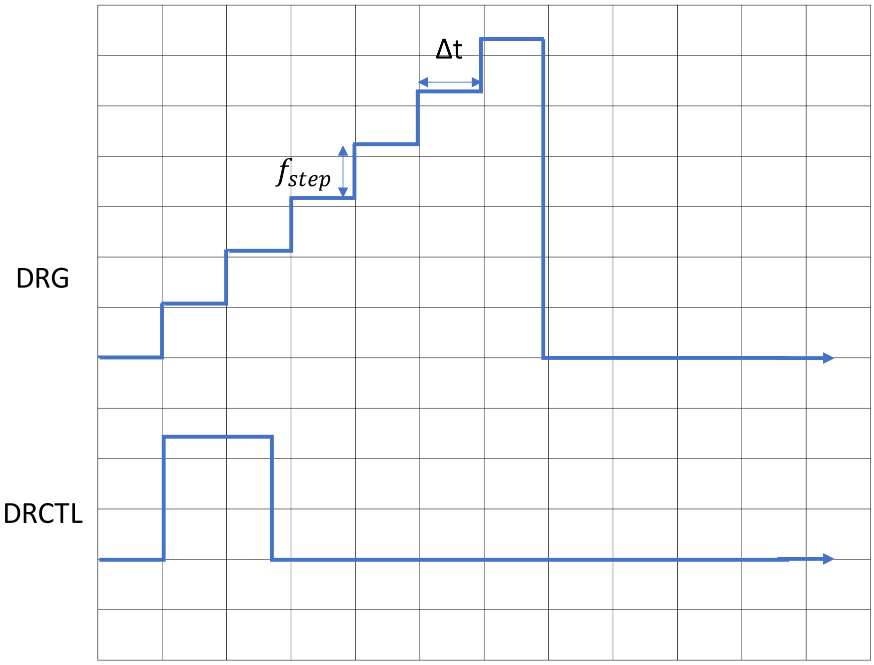

Figure 5.2-2 Digital ramp frequency output from DRG with DRCTL signal.

The digital ramp is triggered as soon as a rising edge occurs in the DRCTL pin and will continue to output the ramp signal according to the preset parameters via the AD9914 registers, until it is completed, regardless of the action of the DRCTL pin. At the end of the 'no dwell high' digital ramp, the frequency drops to the preset 'start frequency' as soon as the 'stop frequency' is reached. This means that the sweep can be re-started almost immediately after the end of the last sweep, allowing a very high duty cycle even with the relatively short sweeps used in 'Doppler modes,' such as DBS.

Currently the start and stop frequencies have been defined, but to complete the design the ramp rate, number of time steps and discrete frequency steps must also be calculated. The time steps in the digital ramp are calculated via a 16-bit register value and the DDS system clock frequency.

$$\Delta t = \frac{T_{chirp}}{n_{steps}} = \frac{24P}{f_{sysclk}} \tag{5.2-3}$$

Where P is the 16-bit digital ramp rate register and Δt is the minimum time step in the digital ramp, f_{sysclk} is the DDS clock frequency. The chirp duration is T_{chirp}, and the number of time steps in the digital ramp is n_{steps}. Ideally the digital ramp will be as smooth as possible, and as the chirp duration and bandwidth is determined by the radar operator, the rate of change of frequency of the chirp is also defined, hence the smoothest possible digital ramp occurs when Δt is minimised, hence P is set to 1. Typically, the DDS clock frequency is set to 3.36 GHz, which means for a chirp duration of 0.15 ms, there are 21000 time steps in a single chirp. In each time step, the frequency increase is also calculated.

$$f_{step} = \frac{B}{n_{steps}} = \left(\frac{M}{2^{32}}\right) f_{sysclk} \tag{5.2-4}$$

Where f_{step} is the increase in frequency for each time step, B is the bandwidth of the chirp, and M is the frequency tuning word for the register input. Once the registers that control the digital ramp has been formed, a 3.3 V rising edge, which can be obtained from a rectangular pulse signal, is required through the DRCTL pin to trigger the FMCW chirps.

5.2.1 FM Noise Levels from the Synthesizer

The fact that the sweep is a series of steps add phase noise to signal, as, indeed, does the fact that the DAC output is actually quantized. The data sheet for the AD9914 (fig 15) shows a typical single sideband FM noise level of just above -140 dBcHz^{-1} at 100kHz from carrier at a frequency of 696 MHz. The phase noise from the AD5355 STALO at the same offset and at a carrier of 3.4GHz is quoted as -116 dBcHz^{-1}, which is significantly higher.

Provided that the deviation, Δf, is much less than the modulation rate then the noise at an offset f_m from the carrier will be derived from the noise at the same modulation frequency. From [63] the single sideband (SSB) F.M. noise density at the offset will then be at an offset f_m will then be

$$P_f = \frac{\left(\frac{\Delta f}{f_m}\right)^2}{4} \tag{5.2-5}$$

Since the local oscillator frequency of 7.5 GHz is twice the 3.6 GHz reference frequency quoted in the data sheet, the FM noise would be expected to be about 6dB worse, i. e. about -110 dBcHz^{-1}. When it has been multiplied up by a factor 20 to 150 GHz the FM noise levels at a given offset will be multiplied up by a further factor of 400 (26 dB) so the noise level from the STALO at 150GHz at 100kHz from carrier is expected to be about -84 dBcHz^{-1}. This is actually very similar to the FM noise levels obtainable from millimetre-wave voltage control oscillators as used in earlier millimetre-wave FMCW radars[123], which also have FM noise levels of about -85 dBcHz^{-1}. The DDS and multiplier approach therefore does not give particularly good noise levels, but experience has shown that these levels are adequate for FMCW radars with these sorts of power levels.

It should also be noted that the discrete steps in frequency in the chirp, when compared to the ideal continuous ramp, will give a high level of FM noise at offsets which are a multiple of the step frequency, and hence lead to high levels of spurious signals at ranges separated from the true target range by multiples of a number of range cells equal to the number of frequency steps in the sweep. In the example given above where there are 21,000 steps in the chirp, the spurii will be at multiples of 21,000 range cells from the true targets. For a range resolution of 3cm (corresponding to the maximum sweep of 5GHz) this is a range separation of 630m, which is beyond the range at which any genuine targets are likely to be detected, so, any spurii will not cause a problem provided they are properly suppressed by the anti-alias filter to prevent aliasing in the ADC from folding them back into the range swathe which is of interest.

5.3 10 MHz Divider Board for Chirp Trigger Control and System Timing

As part of the refurbished 150 GHz ELVA radar, a custom clock divider circuit was designed by co-worker Scott Cassidy, based on an Atmel AVR328P microcontroller which uses a GPS disciplined 10 MHz signal as its input. The 10 MHz oscillator divider provides rectangular wave outputs of a specified frequency, which is used to trigger the radar pulses, trigger ADC data capture, as well as provide a synchronised reference clock for all sub-systems. The outputs are 3.3 V signals. It is powered with a 12 V dc power supply and is controlled via a PC through FTDI USB UART. A set of serial commands have been produced to control the device, which for ease of use, can be done through MATLAB. Furthermore, the desired PRF will be the same as the output frequency of the trigger port, and so the register values of the divider board can be calculated and written.

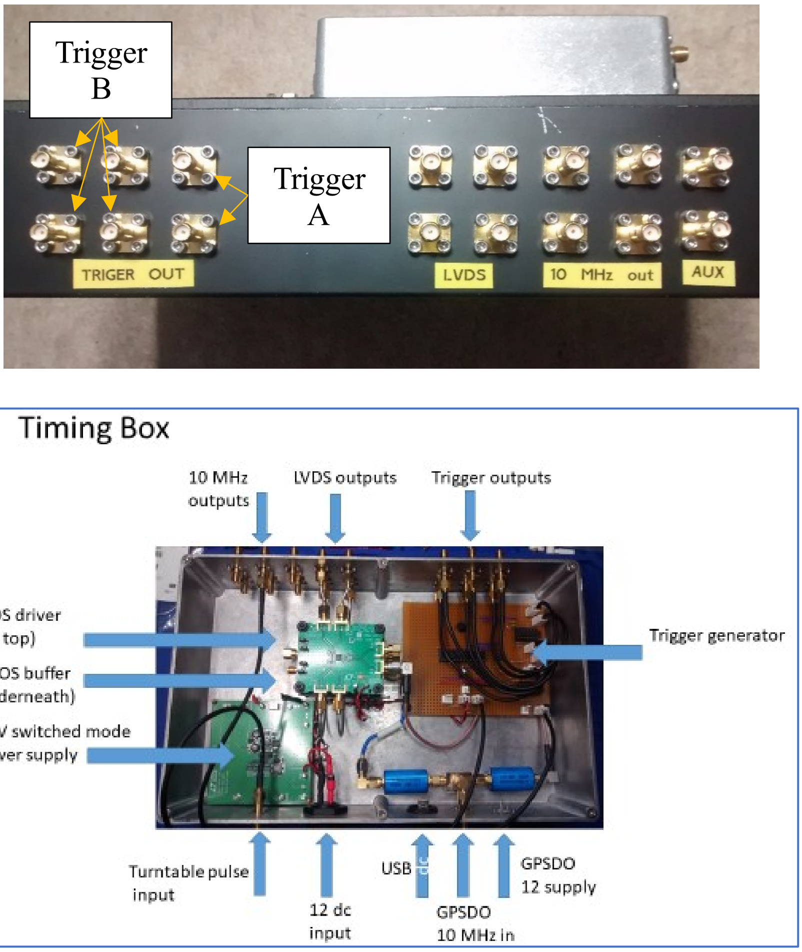

Figure 5.3-1 The 10 MHz oscillator square wave distribution board

For staring and DBS measurements, the divider board is set to ‘free burst’ mode which continually outputs the divided square wave signal. The ports denoted A and B on the trigger ports of the divider output the divided 10 MHz signal at specified frequencies. The ability to output the trigger signal at two different frequencies is useful when taking measurements with different radars. The signal from the 10 MHz oscillator is divided according to a division ratio which is defined by the user and written to register 3.

$$PRF = \frac{10000000}{2 \cdot (N + 1)} \tag{5.3-1}$$

Here, PRF refers to the frequency of the square wave trigger signal which is the same as the PRF of the radar and N refers to the division integer that the register is set to. For example, if the radar operator desires a PRF of 6000 Hz, the closest possible value of N to achieve this is 832, which yields a PRF of 6002 Hz. The square wave is set to be at a 50% duty cycle for the PRF calculated in (5.3-1).

The user must also write values to the registers ‘burst count A’ and ‘burst count B’ which defined the number of half cycles of the rectangular wave to output. By setting both values to two, both trigger ports will output a rectangular wave of the frequency defined in (5.3-1). The port with the highest burst count will always output with the PRF defined in (5.3-1), and have a duty cycle of 50%, whereas the port with the lower burst count will output a frequency which is lower by the ratio of the two burst counts. To avoid confusion in the hardware set up process, the burst count B value is set to two, which means it will output a frequency either equal or lower than the frequency at port A.

$$N_{burstA} = 2\left(\frac{f_A}{f_B}\right) \qquad (\ 5.3\text{-}2\ )$$

Here, f_A is the frequency of the square wave output from trigger port A, the same as the PRF in (5.3-1), and f_B is the frequency of the square wave from trigger port B. As the duty cycle is always 50% for the higher PRF value, the lower frequency port will output a signal with a duty cycle that is 50% divided by the ratio of the frequency of port A and the frequency of port B.

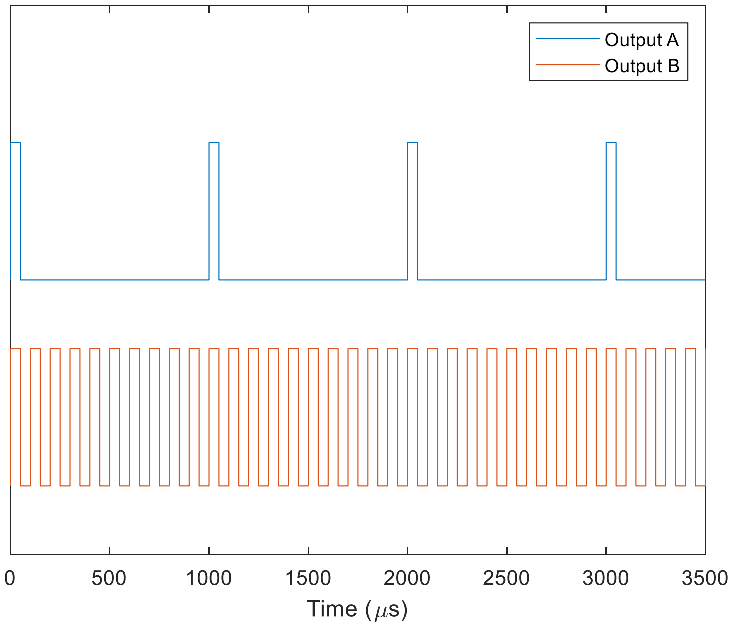

Figure 5.3-2 Trigger signal output from port A and port B.

5.4 PCIe9834 ADC cards

The PCIe9834 ADC cards are used to capture the IF data from the I and Q channels from the 150 GHz radar, converting them to digital signals. The channels are each signed 16 bits, and the voltage range is set to +/- 1 V, the input impedance is 50 ohms. It has 4 channel inputs that can be enabled via software control. Ideally, only the connected channels will be enabled, else the redundant channels will only record system noise in the PCIe9834 and take up extra disk space. The ADC has a maximum sample rate of 80 MS/s, although in this thesis, all measurements were taking with a sample rate of 40 MS/s to conserve data and remove data at ranges where the returns from any targets of interest were likely to be below noise.

The reference clock pin connects to one of the 10 MHz outputs from the 10 MHz divider board. If there is no need to time-synchronise across different sensors using the synchronised 10 MHz reference signal, the PCIe9834 has an internal reference clock of 80 MHz which can be used instead.

5.5 150 GHz antenna

The choice of antenna design for the 150 GHz radar is important when setting the system up for DBS measurement taking. As explained in section 2.6.3, typically it is desirable that an imaging radar antenna have a fine azimuth beamwidth for improved cross-range resolution and gain, however fine beamwidths will limit the FOV in DBS imagery. Furthermore, the synthetic aperture size formed during the DBS process is independent of the beamwidth of the antenna. Hence, the exchange of gain against the FOV should be considered. The two antenna types used on the 150 GHz radar are a fan beam antenna for mechanically scanned imagery, and 10-degree pyramidal horns for DBS.

5.5.1 Pyramid 10-degree horns

The available antenna chosen for the DBS measurements are 10-degree pyramidal horns, due to the adequate FOV for image formation and the adequate gain for SNR.

Figure 5.5-1 10-degree pyramidal horns for 150 GHz radar – flanges at left, apertures at right. Approximately 6 cm in length.

The pyramidal horns used with the 150 GHz radar have a beamwidth of ±5° in both the azimuth and elevation planes. They also provide a maximum gain of 24 dB. These antennas are ideal for DBS measurements as they provide a wider FOV in azimuth than the fan beam antenna and have sufficient gain to image targets. The gain is only 5 dB less than the fan beam imaging antenna described immediately below. The 10º horns are also smaller in physical size than the fan beam imaging antenna, which is a benefit to requiring a large azimuth beamwidth as the installation of the final system can be done in a small space.

5.5.2 Fan Beam Imaging antenna

As mentioned above, the ideal antenna for mechanically scanned imagery would have a very small azimuth beamwidth. It is desirable for the elevation beamwidth to be wide however, as the beam footprint will be larger, causing more scattering from the surface and therefore achieving a better image of objects on the surface, and specifically for maritime radar, dealing with the vessels roll. The antenna below has an elevation beamwidth of 15 degrees, which is below the typical maritime antenna beams.

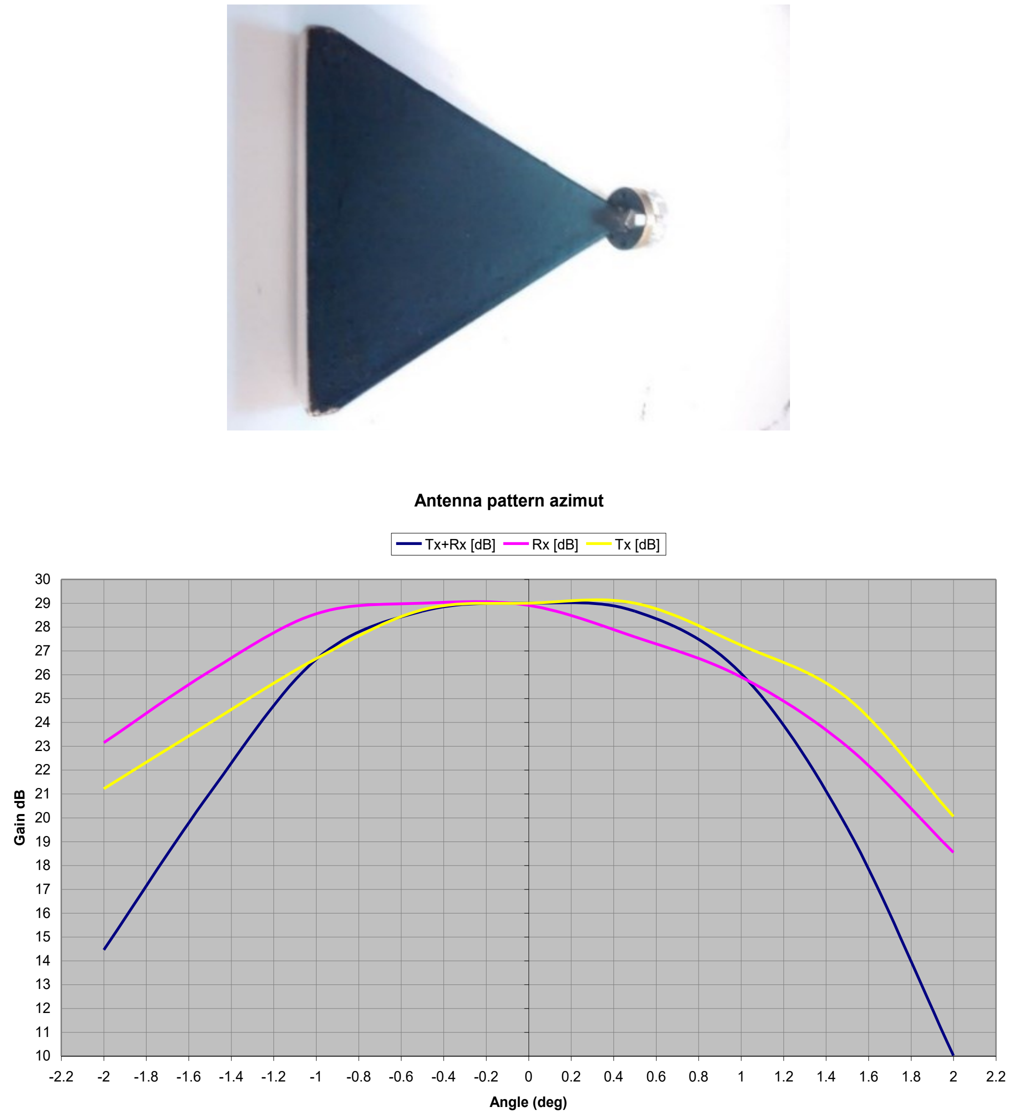

Figure 5.5-2 Fan-beam imaging antenna and azimuth antenna gain pattern

From Figure 5.5-2, there is some non-symmetry in the antenna azimuth radiation pattern, which means the antenna is misaligned. However, considering the typical ranges these antennas are used for are beyond 10 m, and the misalignment is less than 0.1 degrees, there is no significant loss due to antenna misalignment.

5.6 Macro system for DBS measurements

On top of the design of the radar, the design of the entire measurement system for DBS imaging needed to be considered. The challenge of collecting synchronised kinematic data and radar data on a portable moving platform must be addressed in order to make successful DBS measurements. Most importantly, a method of obtaining radar data that is synchronised with the kinematic data and video ground truth is required to process the DBS imagery, and then analyse the imagery.

5.6.1 Advanced Navigation IMU

The kinematic data used in the data gathering system came from an Advanced Navigation spatial FOG is a GNSS enabled IMU, which is used with the radars to provide accurate kinematics for the sensor. It provides up to 10 mm positioning accuracy using GPS, GLONASS, Galileo, and BeiDou satellites. The important bits of data required to process DBS imagery are the positions, velocities, and headings. These measurements are taken relative to the IMU, so it is vital that it remains fixed in place relative to the radar, ideally co-located with the radar antenna if possible. As the IMU uses GNSS, it is also vital that the IMU remains outside to be able to connect to the satellites. Failure to connect to the satellites may cause the inaccuracy of the measurements to increase, which would cause a position and velocity drift in the data. DBS processing of a single frame does not require information on the absolute location, however inaccuracies in the velocity measurement will cause images to be displaced from their ‘true’ location.

The velocity data is saved in a 'North, East Down' format, which is obtained through the GNSS connection. The position data is collected as latitude, longitude and height which can be converted to the North, East, Down format. The velocity data will be used to estimate the average velocity, in both magnitude and direction, of the platform during the integration period during the DBS image processing. The position data is used to estimate the central position of the antenna during the integration period, so several DBS frames can be stitched together to form an overlayed image.

The heading data is used to estimate the average look angle of the radar during the integration period. This is required when stitching several DBS frames together, as a small change in angle causes a large change in cross range for targets at large ranges. The heading is measured as the angle between the x direction according to the IMU as seen below, and true north as determined using the GNSS.

Figure 5.6-1 Advanced Navigation spatial fog directions

5.6.2 Stereolabs ZED

A Stereolabs ZED camera was used to provide a video ground truth of the scene when the radar data was collected. The ZED records with a frame rate of 30 frames per second, and records from two separate cameras that enables depth sensing. The ZED is connected to a GPU enabled PC for efficient data capture and analysis as well as timestamping so individual frames can be matched to the corresponding chirps from the radar.

Figure 5.6-2 Stereolabs ZED

5.6.3 Timestamping and data synchronisation

Synchronisation is achieved by running a time server and time client on the host PCs that control each sub-system, and records data to their respective local drives. The time server is written in C++ and used communicates using a User Datagram Protocol (UDP). The client records a local timestamp and transmits a UDP to the server. The server then records its own local time stamp and transmits its local timestamp and the clients timestamp back to the client. The client then takes a second timestamp, and the average is taken to compensate for the round trip, assuming the transmission to and from the server takes the same time. So, for each chirp from the radar, and each sample recorded from the IMU, and each frame recorded by the ZED stereo camera, a timestamp is also recorded. By matching the time stamps across each PC, the data can be synchronised by matching the closest recorded timestamps to each other, and so each chirp has a corresponding timestamp, as well as each sample from the IMU and each frame from the ZED.

To communicate the time server data, each PC in the system is given a unique IP address and is connected to a local ethernet hub via an ethernet cable, where data is streamed through parallel ports.

5.6.4 Distributed system architecture for offshore trials.

The following example was designed for measurement taking at sea, on a boat and was later used in the Gosport Sea trials. The kinematic data had to be synchronised with INRAS radar systems on the DBS trials, which are MIMO sensors that operate at 79 GHz and were used to research MIMO-DBS in the maritime environment. Although the MIMO data is not analysed in this thesis, the inclusion of these subsystems formed the design of the entire test system. A distributed system was designed which enabled all data collecting systems (IMU, radars, video cameras) to synchronise data timings, regardless of the control PC being used, and so multiple sensors could be used to obtain wide FoV sensing for situational awareness. The distributed system data analysis, however, is beyond the scope of this thesis and only the radar data from the 150 GHz FMCW is considered.

As well as the system architecture, the environmental issues had to be addressed. The maritime environment risks splashing the sensitive radar equipment with salt water which will cause corrosion; hence waterproofing is essential. As the 150 GHz signal is able to penetrate a small layer of PVC shrink wrap without any significant loss, plastic film was wrapped around the radar and sealed until presumed watertight, therefore the radar was protected from the water. The presence of water on the plastic film however will cause some attenuation of the radar signal which can be predicted using the model shown in [124], which agrees with the measured results in 0, which estimates a loss of 50dB/mm assuming the water contaminant is uniform on the film. 15 m Long cables had to be used to connect the PC and 10 MHz distribution board to the radar to enable freedom in positioning the radar and were protected using a split conduit. Power cables were connected to switch mode power supplies, so along as the cable resistance did not drop the voltage below the minimum required, around 10 V, the system should operate normally.

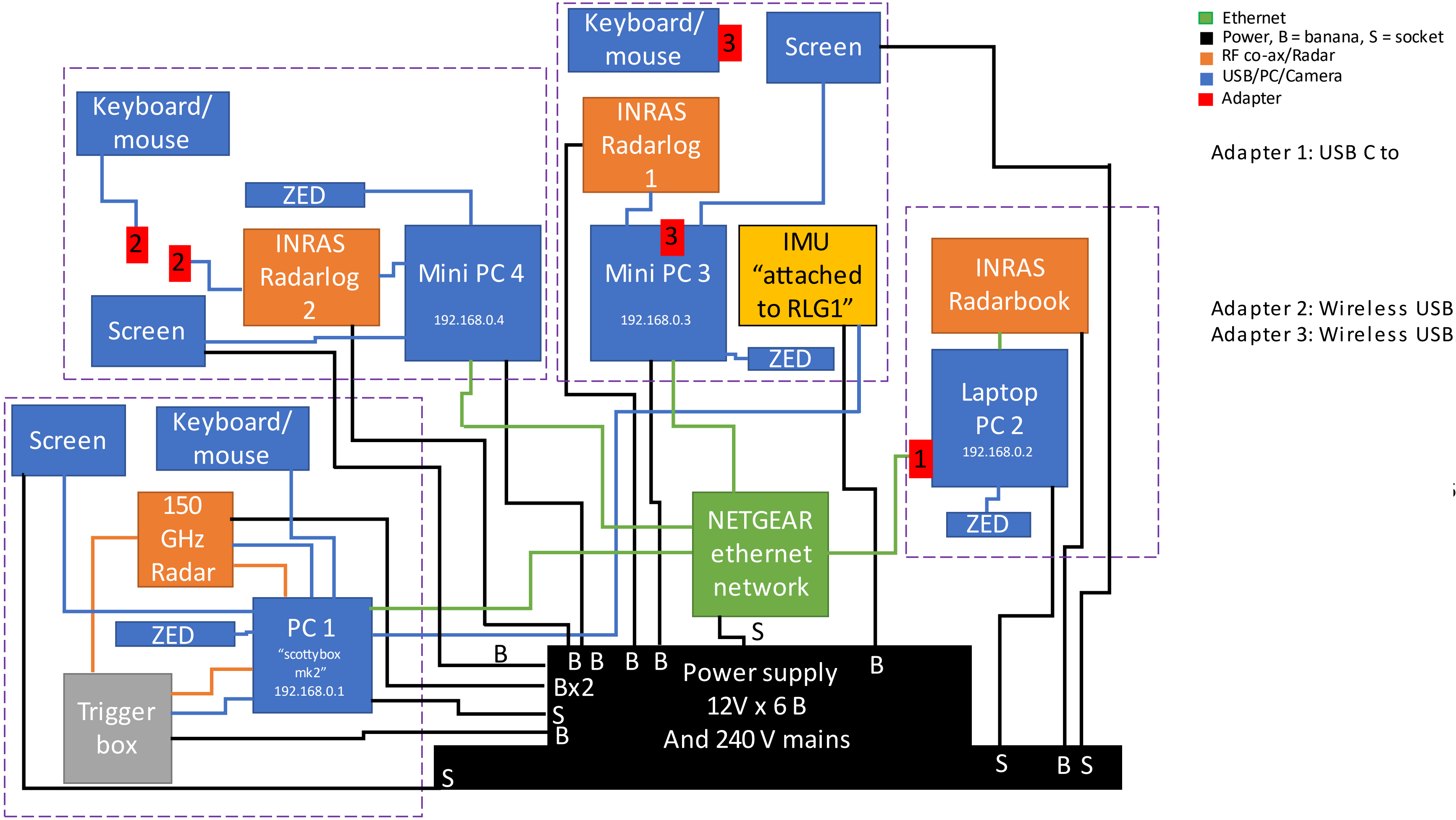

Adapter 1: USB C to

Adapter 2: Wireless USB.
Adapter 3: Wireless USB.

Figure 5.6-3 Macro level architecture for a distributed system designed for taking DBS measurements.

5.6.5 Portable power supply

The system requires several power supplies, and so it was necessary for a portable power system to be produced.

Table 5.6-1 Required power supply to run the 150 GHz radar for DBS measurements

Connection	Required voltage supply [V]
150 GHz Transmitter	12
150 GHz Receiver	12
10 GHz Divider Board	12
Advanced Navigation IMU	12
Host PC	240 (mains)
PC screen	240 (mains)
NETGEAR ethernet hub	240 (mains) – 5V converter socket connection

For an efficient and safe system setup, a single power supply that provides six dc 12 V banana cable ports, with additional local regulators as well as two 240 V mains sockets was produced. Each banana port can provide a current of up to 20 A. The system was built using three Seasonic SS500 L1U Server/P.C Power Supplies [125], of which one server is used to power a single row as seen in Figure 5.6-4 Power supply for full radar system. Figure 5.6-4. As the power servers were connected in rows, it is important for high noise 'dirty' power connections to be isolated from the radar power supply, as a dirty power supply for the radars will increase the noise floor of the radar and reduce image quality. In the DBS system setup, there were no 'dirty' power connections to be concerned with, but any setup that requires the connection of a turntable produces significant noise and needs to be considered. For the DBS system set up, the power supply would be connected to a 240 V mains power supply which would also be used to provide mains power to other components in the system.

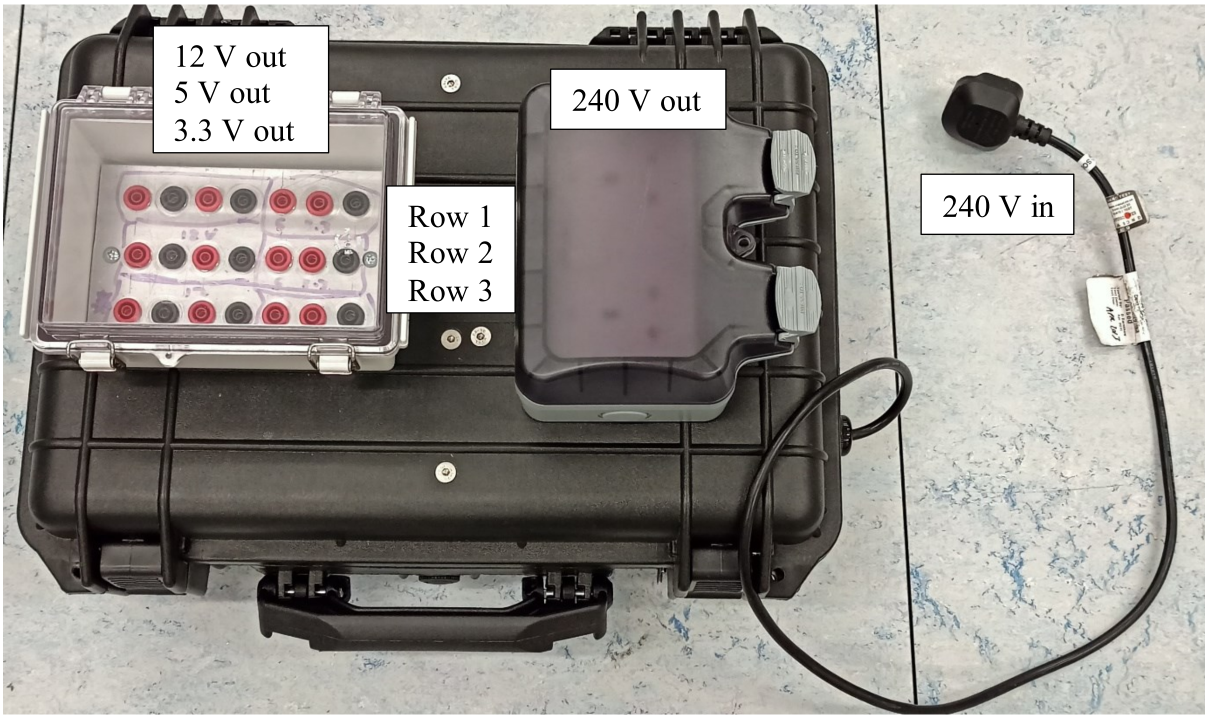

Figure 5.6-4 Power supply for full radar system.

5.7 Macro system design for scanning measurements

Along with the development of the 150 GHz radar, the development of the macro system to take mechanically scanned measurements was conducted. The scan consists of an azimuth sweep in one direction, followed by another sweep in the opposite direction for a given FoV. To form an image from a radar that is mechanically rotated around an axis, the radar will transmit a chirp at equally spaced angular intervals. Then each processed range profile will be mapped depending on the angle at which the chirp was emitted. Hence the stepper motor must communicate with the radar via the trigger port to let the radar know when to transmit. The stepper motor transmits square wave pulses for every step the motor progresses by. This square wave can be divided, much like the processes in the 10 MHz distribution board, into a square wave that can be used to trigger the radar at the desired PRF, and so a separate divider is deployed for this setup.

$$PRF = \frac{\frac{FoV}{360} \times F \times G_{ratio} \times S_{rev}}{D_{ratio}} \qquad (5.7\text{-}1)$$

Where, FoV is the field of view of the image, i.e. the maximum angle scanned for a single frame. F is the frame rate of the scanned imagery and G_{ratio} is the gearbox ratio of the motor. The motor used has a gearbox ratio of 45:1. The number of steps for an entire revolution of the motor is denoted S_{rev} and is set to 4000. D_{ratio} is the required division ratio to achieve the desired PRF and is the input for the divider. The 10 MHz distribution board has an external port 'turntable pulse input' which takes the square wave from the turntable divider as an input and distributes the same square wave among all the trigger outputs. Similar to the staring/DBS mode, the 10 MHz distribution board can also be set to divide the turntable trigger signal further, to produce two separate trigger PRFs from trigger ports A and B. It was found that the 10 MHz distribution board produced cleaner trigger signals than the turntable divider for higher PRF values, and so the desirable configuration was to set the turntable divider to transmit a trigger signal of <500 Hz, and then to sub divide further with the 10 MHz distribution board.

The following graph shows the trigger outputs when register 3 was set to 249 (20 kHz pulses), register 4 was set to 2 (divide by 3), register 5 was set to 2 (a single pulse on output A) and register 6 was set to 32 (16 pulses on output B).

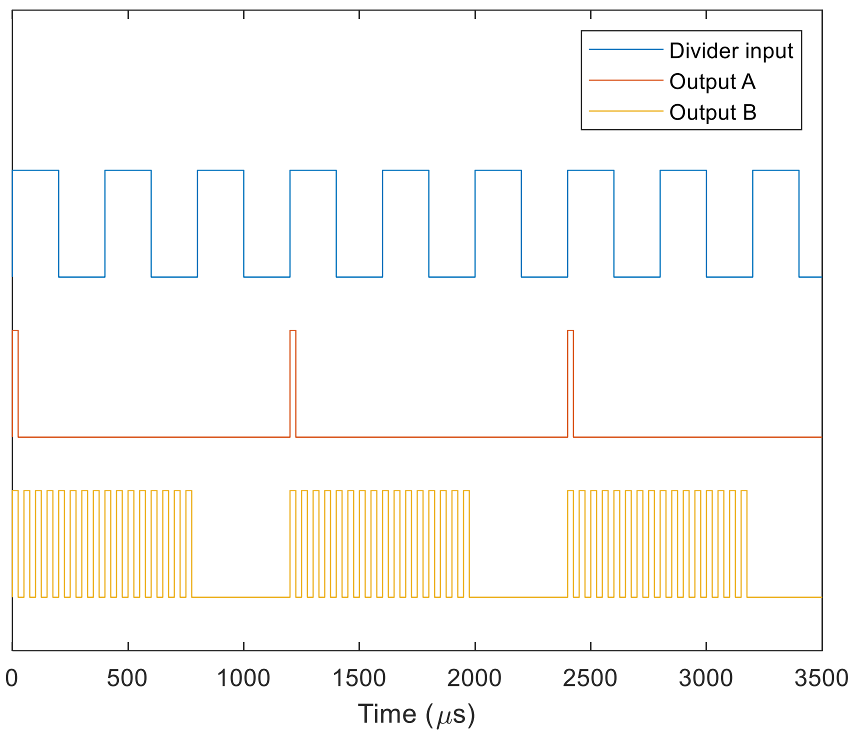

Figure 5.7-1 Trigger output pulses with external divider input of 2500 Hz

For each pulse from trigger port A, there are 16 pulses from port B, however once 16 pulses have elapsed, port B remains on standby until port A transmits again. To achieve a continuous PRF on port B, the number of pulses must be equivalent to the ratio of the PRF from port B, which is determined by register 3 using (5.3-1), and the PRF of port A which is determined by the external square wave frequency and the division ratio from register 4.

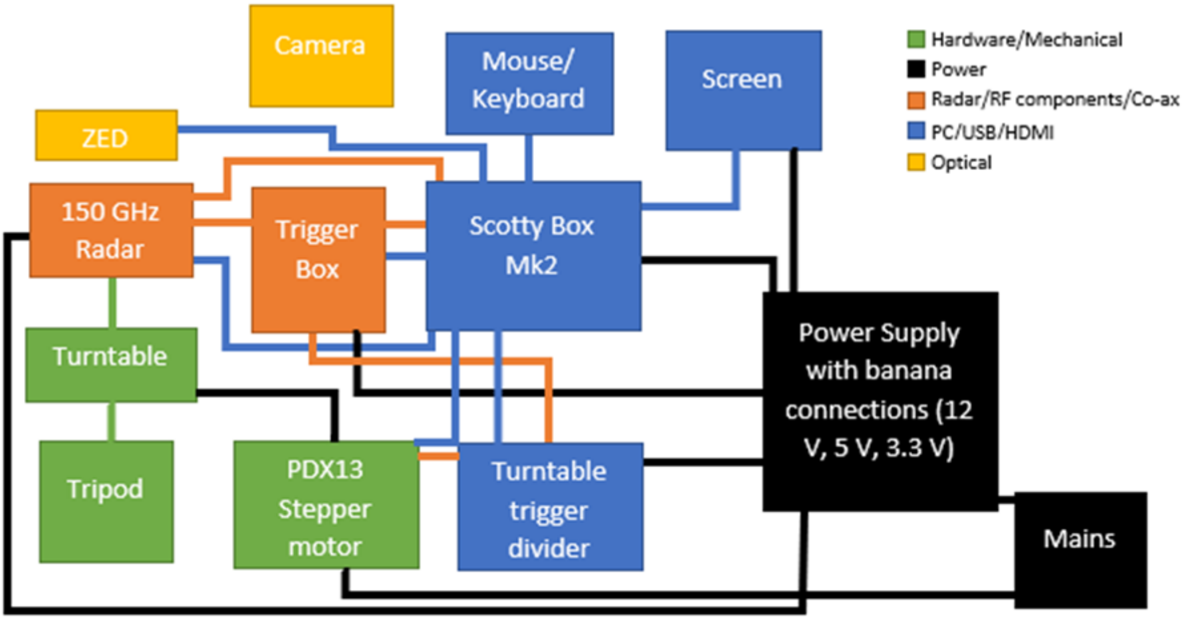

Figure 5.7-2 Schematic for scanning measurements using 150 GHz radar, from the FloWave trials for STREAM.

The 150 GHz radar is fixed to the turntable, and the turntable is fixed to a stable surface, usually a tripod, so the depression angle and the look angle can be accurately measured and set. Here, ‘Scotty Box’ is the name given to the control PC.

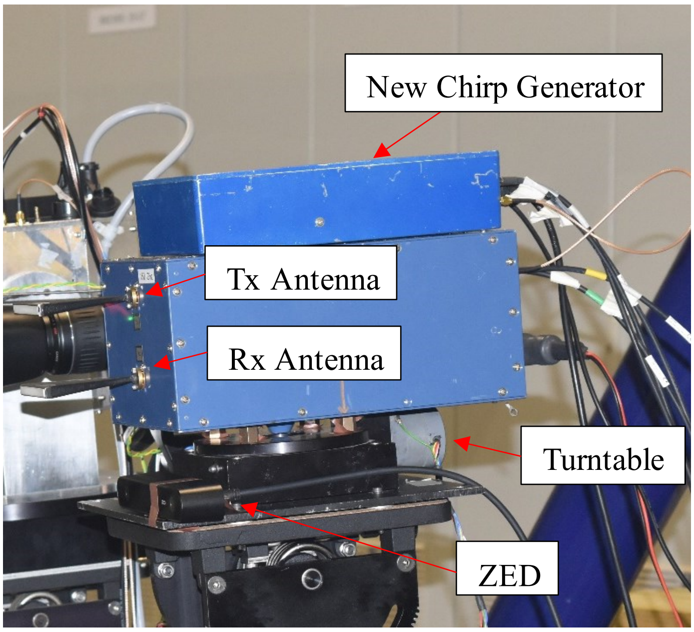

Figure 5.7-3 150 GHz radar mounted with turntable to tripod head, with optical camera and ZED. Equipped with fan beam antenna from section 5.5.2

6 Maritime Sub-THz DBS Measurement Campaigns

In this chapter the 150 GHz Radar design schematic in figure 5.6.3 was deployed to take various DBS measurements in radar test trials around the UK. The data was then processed and analysed to investigate the feasibility and effectiveness of using DBS as an imaging method for small marine craft in a variety of conditions to provide the imagery that will lead to situational awareness and path planning for autonomous marine craft.

This chapter presents the results gathered during the measurement campaigns, describing how the measurements were taken, how the signal processing effects the results, and what we learned using the DBS approach in real scenarios.

6.1 Coniston Water Initial DBS trials

The Coniston Water joint trials were a set of littoral radar measurement trials held jointly by the University of Birmingham and University of St. Andrews at Coniston Water UK, 54°20'48.8"N 3°04'32.3"W.

The trials were conducted over several days, where the main aim was to gather a large quantity of sub-THz radar data of clutter and marine target measurements. The trial location was adequate as it provided a stable area to house the radar equipment as well as a jetty which enabled the positioning of the radar offshore, and a long power extension cable provided mains power for all the equipment.

Figure 6.1-1 Birds-eye view of Coniston Water jetty, with the radar field of view and direction of motion

The jetty is a pontoon loosely attached to the shore. Hence with any movement of the equipment on it, the jetty was also moving, mainly in the vertical direction, so that the sensor platform experienced motion in 6 degrees of freedom. The radar was tilted to have a depression angle of 10° so that it pointed at the surface of the water at the range of the objects.

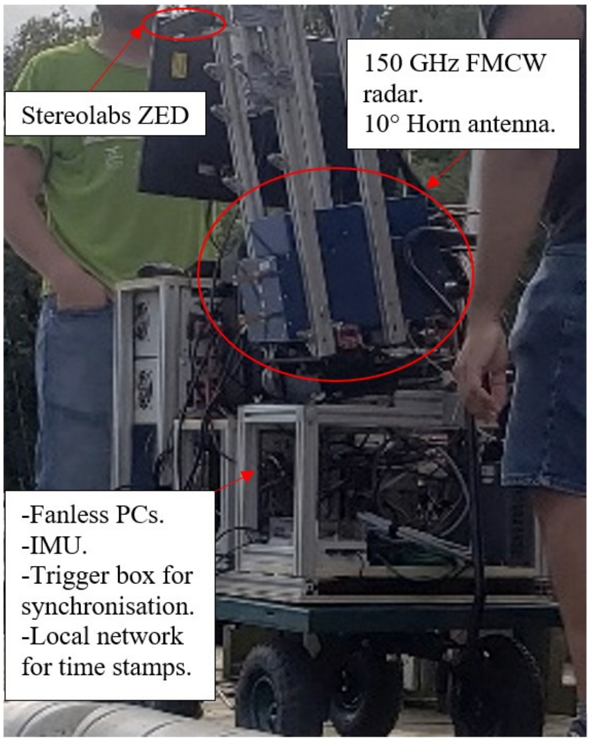

Figure 6.1-2 Compact 150 GHz FMCW radar portable system for DBS measurements, push and pulled by hand.

As mentioned in chapter 5, the 150 GHz radar is configurable, hence parameters had to be chosen before taking measurements. As the measurement requires a large enough maximum unambiguous Doppler value such that the maximum platform velocity could not be feasibly reached, and so that the Doppler signatures that exists outside the physical aperture beamwidth according to DBS processing are still unambiguous, so they do not clutter the DBS frame.

Table 6.1-1 radar and processing parameters used in Coniston DBS trials.

Parameter	Value	Units
Chirp Duration	0.15	ms
PRF	6000	Hz
Bandwidth	5	GHz
Start frequency	145	GHz
Range resolution	3	cm
Maximum unambiguous velocity	± 3.05	m/s
Beamwidth (az/el) (Fan beam)	10/10	degrees
Gain	24	dB
Initial depression angle (w.r.t shore)	10	degrees
Integration time	1	s
Squint angle	90	degrees

6.1.1 Measurement of pallet from jetty and DBS processing

A DBS measurement of a pallet was taken with the setup in Figure 6.1-2. The pallet was chosen to test the feasibility of DBS as its periodic structure would be easy to visualise in the image, its rectangular shape lets us see the orientation of the pallet in the image. The pallet was placed at a range of 9 m from the jetty and free to float on the surface. An integration time of one second was chosen to ensure that the SNR for the processed range Doppler would be high enough to see most of the returns off the pallet. The low speed of the system, as it was pulled, also ensure that the Doppler smear would not be significant. The time-synchronised velocity data from the IMU is averaged for each integration period, and from this the potential refined azimuth beamwidth can be estimated.

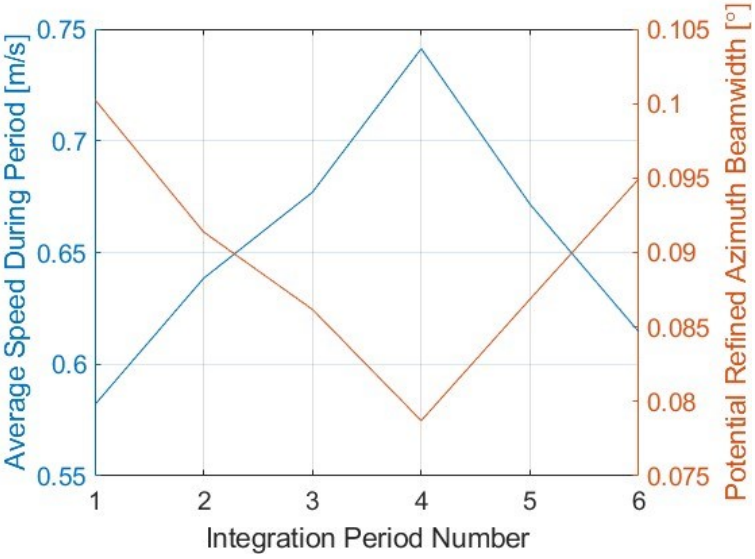

Figure 6.1-3 Measured average velocity from the IMU as the cart was pulled along the jetty during the measurement time (Blue). The maximum potential refined azimuth for each integration period/DBS frame using the measured average velocity and radar parameters. Integration time of 1 s.

Here it is important to note the wording, that the second curve shows the minimum 'potential' refined azimuth beamwidth. This assumes that the squint angle remains at 90 degrees, and that the integration time and frequency are constant for each DBS frame. However, due to any drifting motion from the jetty or platform, the squint angle may deviate from 90 degrees and therefore increase the size of the potential refined azimuth beamwidth, i.e. worsen the azimuth resolution. It also does not account for any reductions in resolution due to windowing, which is at least half due to the use of the four-term symmetric Blackman-Harris window.

The DBS frame with the highest resolution occurs at integration period number four, where the trolley is moving the fastest, achieving a potential refined azimuth beamwidth of 0.08 degrees. With the window we can assume that the resolution would be twice as large. Therefore, compared to the fan-beam antenna from section 5.5.2, the DBS processing can achieve azimuth resolutions of over ten times. Of course, this value depends on the integration time chosen and the velocity of the platform but shows that DBS has the capability to achieve imagery much sharper than using a mechanically scanned imaging antenna.

The processed Range-Doppler plot contains the unambiguous Doppler information of the scene that dwells in the beam during the integration time. However, the processed DBS frame has formed limits in the range Doppler plot that will form part of the plot . As a result, the Range-Doppler plot will have returns from moving targets and possibly any targets with a large RCS that also reflect the antenna sidelobes back to the receiver, that have Doppler signatures higher than the Doppler limits in DBS processing. In this sense, we can discuss DBS processing as an inherent form of anomaly detection that considers Doppler signatures beyond the limits formed in DBS processing as anomalies.

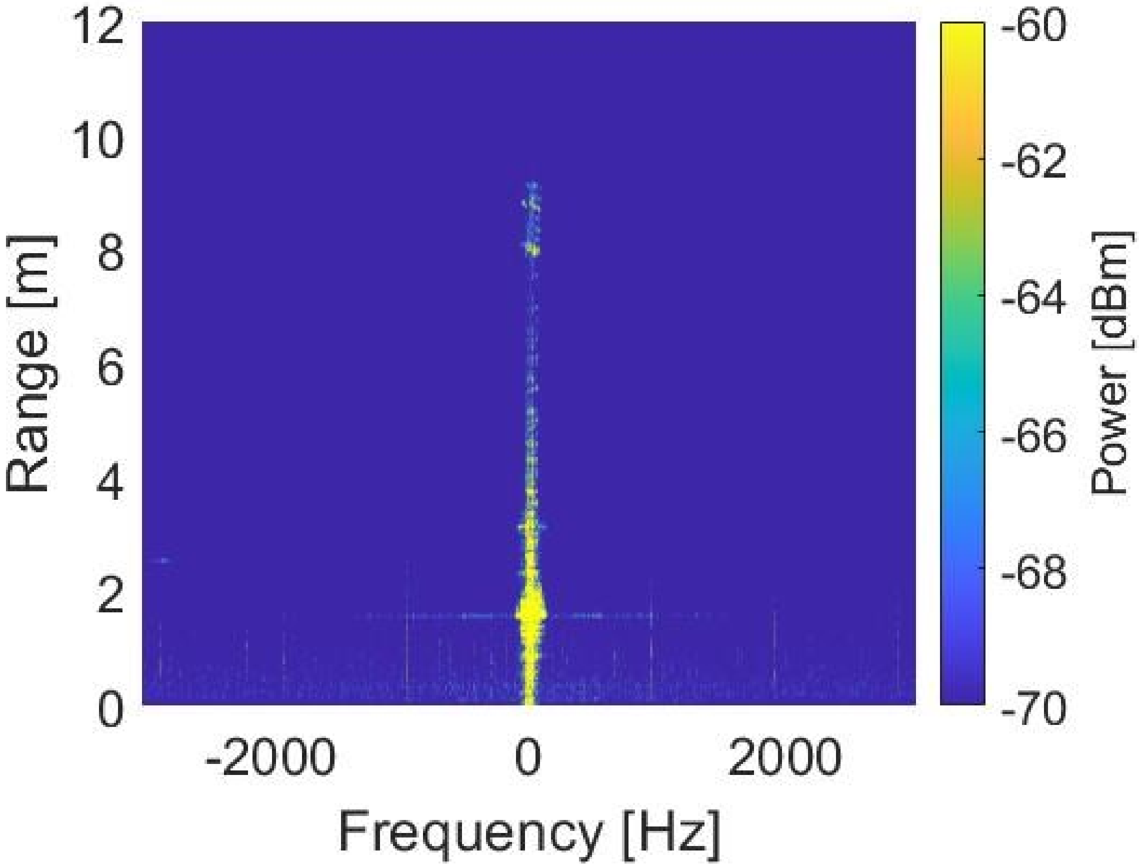

Figure 6.1-4 The 150 GHz Range-Doppler plot of a pallet which is floating on the water’s surface at around 9 m using a 1 s integration time.

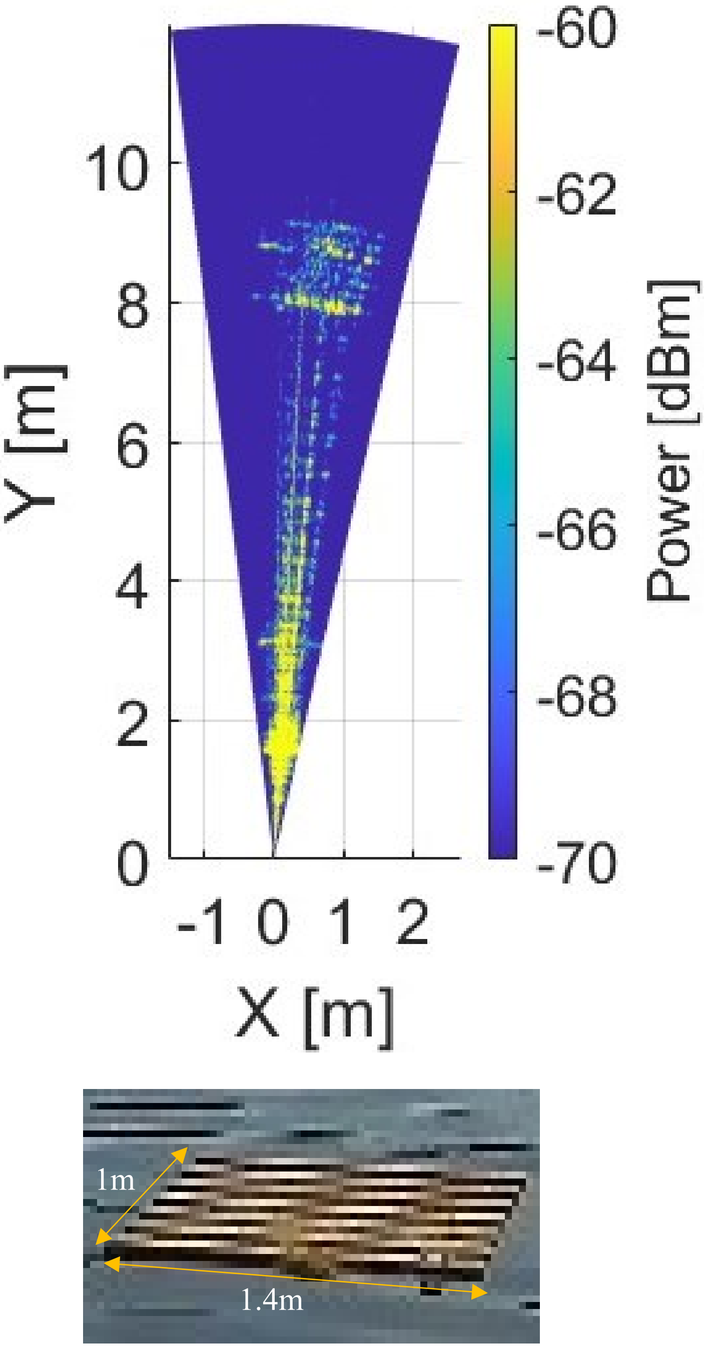

Figure 6.1-5 A single DBS frame (4th integration period number from Figure 6.1-4) after 1s of integration, of the pallet floating on the water's surface with ZED image of the pallet each slat length is ~ 75mm. Strong returns observed before 2 m are significant reflections of a moored boat on the jetty that entered the beam, and returns are smeared down range due to saturation. Both pallet shape and orientation can be observed.

The single DBS frame produced using the data collected from the 150 GHz shows a clear image of the pallet from 8 meters range to 9 metres in range. We also see that the DBS processing has the capability to image the individual slats that run horizontally across the pallet. The orientation of the pallet is also clear relative to the radar, which can be matched with the orientation seen in the optical reference image. The range-Doppler plot shows how much of the Doppler data does not appear in the DBS frame. At -3000 Hz and 3 m range, there is a small signature which does not appear in the DBS frame for example. To use more of the Doppler spectral data, the platform needs to move faster, or the antenna beamwidth would need to be larger.

The large streaks that appear down range originate from saturation from returns off a boat that is moored to the jetty around 1.5 m from the radar. As the boat appears very close, and the depression angle of the radar means there are significant reflections off the boat, the power of the signal returned from this region results in a voltage that is much higher than the voltage limit of the ADC which can be seen from the intermediate signal in Figure 6.2-6.

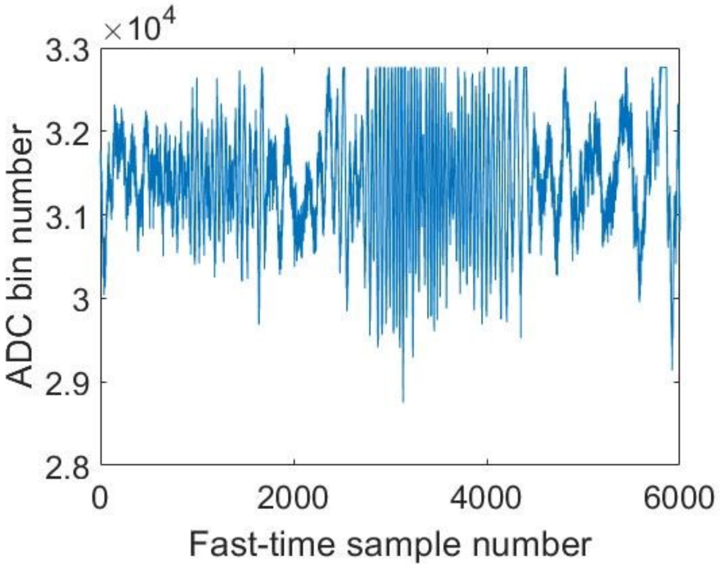

Figure 6.1-6 Single received chirp IF signal from I channel with saturation. This chirp is the 190th chirp of the 6000 integrated chirps that are processed to form Figure 6.1-5

The amplitude of the received IF signal is saturated beyond the 3000th fast time sample as the ADC bin number reaches 2^{15}, which is the largest value for a signed 16-bit register. Considering the ADC voltage gate was set to ±1 V, assuming the received signal is sinusoidal, the received power off the moored boat would have been over 10 dBm.

6.1.2 DBS over-layed frames results

The produced DBS frames can be over-layed to form a larger image using the antenna position and orientation data from the IMU. The heading data records any variation in the look angle of the boat relative to the North, East, Up vectors defined by GPS. So, when consecutive DBS frames are produced, they are translated by the distance travelled and rotated by the change in heading.

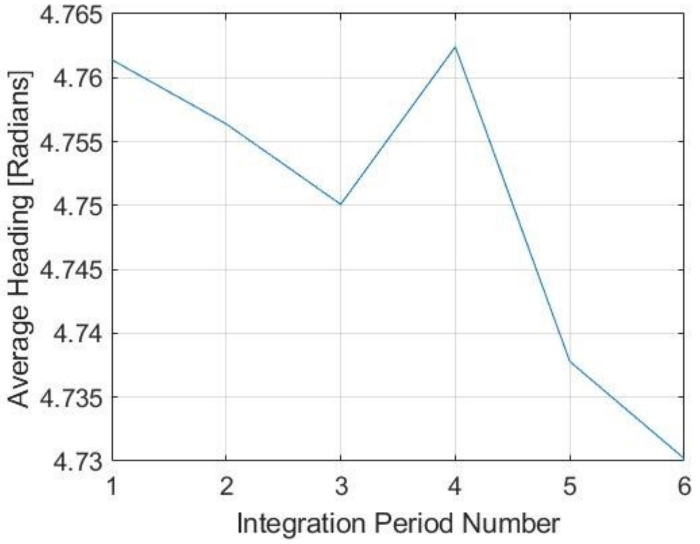

Figure 6.1-7 Average Heading Vector vs integration period number.

It can be seen from Figure 6.2-7, that the variation in heading appears small at 0.03 radians/1.72 degrees, there are no major turns whilst collecting data. However, considering the refined azimuth resolution is less than 0.1 degrees, the change of heading may also account for some significant smear during integration.

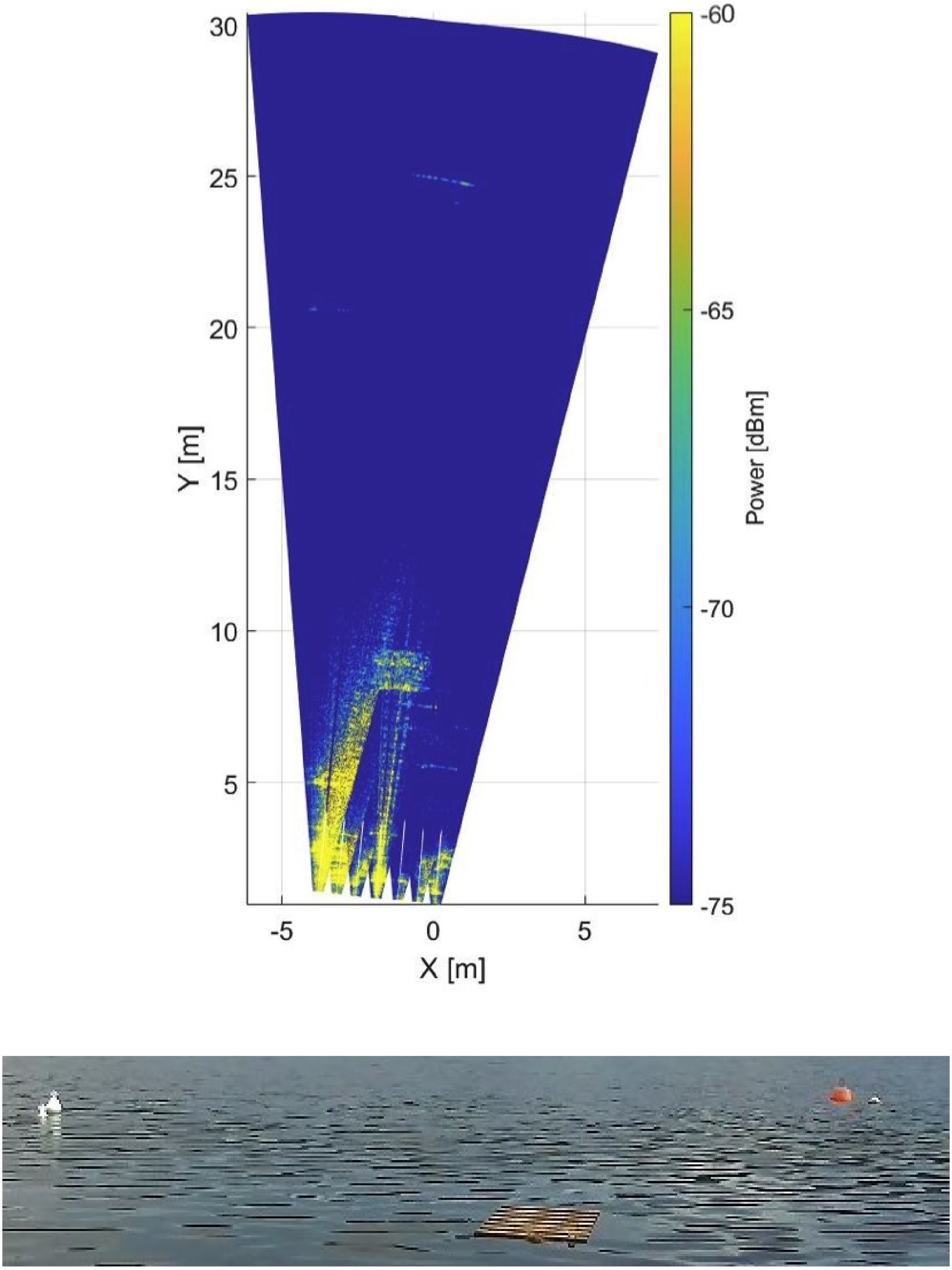

Figure 6.1-8 DBS overlayed frame stitching of 7 consecutive frames measured from the Jetty. It is produced by processing the first image frame and presenting it in cartesian space. Using the data from Figures 6.1-3 and 6.1-7, the next processed frame will be presented in cartesian space ahead of the previous frame, where any pixels that are overlapped take the highest value from the overlapping frames. This means that the highest returns from fluctuating targets are presented above, in the regions that consecutive frames overlap. The frames are produced as the cart moves along the jetty, hence the consecutive frames line up roughly in the x direction. Optical ZED image of the scene showing pallet floating freely in the middle, and 2 sets of buoys around 20 m and 25 m. Buoys are set at 21 and 25 m and the pallet is set around 9 m from the sensor.

Figure 6.1-8 shows the result of overlaying the images. Here, the ‘x’ direction was South, and the y direction East. As well as the pallet, two sets of buoys can also be seen in this image, which were not visible in Figure 6.1-5. They appear because of the change in FOV of the radar, and the fluctuation of RCS from the buoys, from frame to frame. This demonstrates the necessity to overlay multiple frames to enhance SA. The orange buoy appears to have Doppler sidelobes associated with it, which could be associated with its vertical motion on the surface as well as the smaller buoy alongside it.

6.1.3 Integration time vs image quality

Once the data has been collected, the velocity, squint angle, radar frequency and PRF are all defined in the dataset. The integration time, however, needs to be selected during the processing step. The data presented in sections 6.1.1 and 6.1.2 used an integration time of one second, the data presented here using an integration time of half of one second.

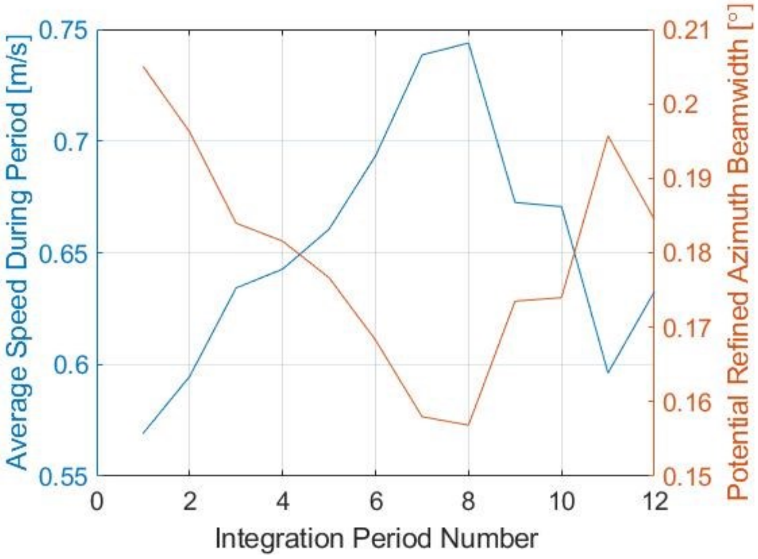

Figure 6.1-9 Measured average velocity from the IMU and the maximum potential refined azimuth for each integration period/DBS frame. Integration time of 0.5 s.

The first observation is that there are now 12 integration periods, and so the average speed used for Doppler processing is closer to the actual speed of the platform at the time. As there is now less variation of the average speed between DBS frames, it is less likely for

Doppler spreading to occur as a result, as well as there is less time for the pallet to physically drift to what would be the next Doppler cell. Using half of the integration also means that the minimum potential for the refined azimuth is now just less than 0.16 degrees.

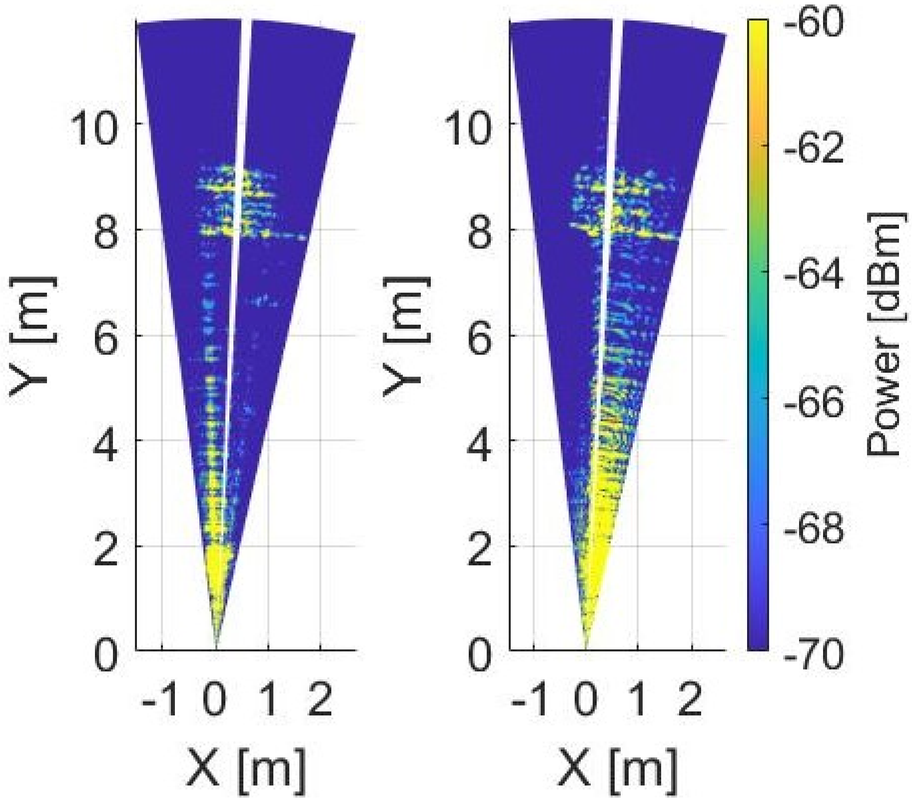

Figure 6.1-10 DBS frames number 7 and 8 after 0.5s of integration, of the pallet floating on the water's surface.

Here the centre frequency bin of the range-Doppler was removed due to the strong DC component which improves the overlayed imagery. Frame numbers 7 and 8 are produced from the same data in DBS frame 4 in section 6.1.1. One notable difference is that front of the pallet has some significant smearing at the front (8 m) which is not present in Figure 6.1-5. This indicates that the smearing originated from the motion of the pallet on the surface of the water.

6.1.4 Scanned imagery of littoral scene

As well as DBS imagery, mechanically scanned radar imagery of the pallet was taken for a 60-degree FoV, with the fan-beam antenna equipped. This used the system shown in Figure 5.7-2 which was stationed on the shore for stability.

Table 6.1-2 radar and processing parameters used in Coniston DBS trials.

Parameter	Value	Units
Chirp Duration	1	ms
PRF	200	Hz
Bandwidth	5	GHz
Start frequency	145	GHz
Range resolution	3	cm
Maximum unambiguous velocity	± 3.05	m/s
Beamwidth (az/el) (Fan beam)	2/10	degrees
Gain	29	dB
Initial depression angle (w.r.t shore)	10	degrees
Field of view	60	Degrees

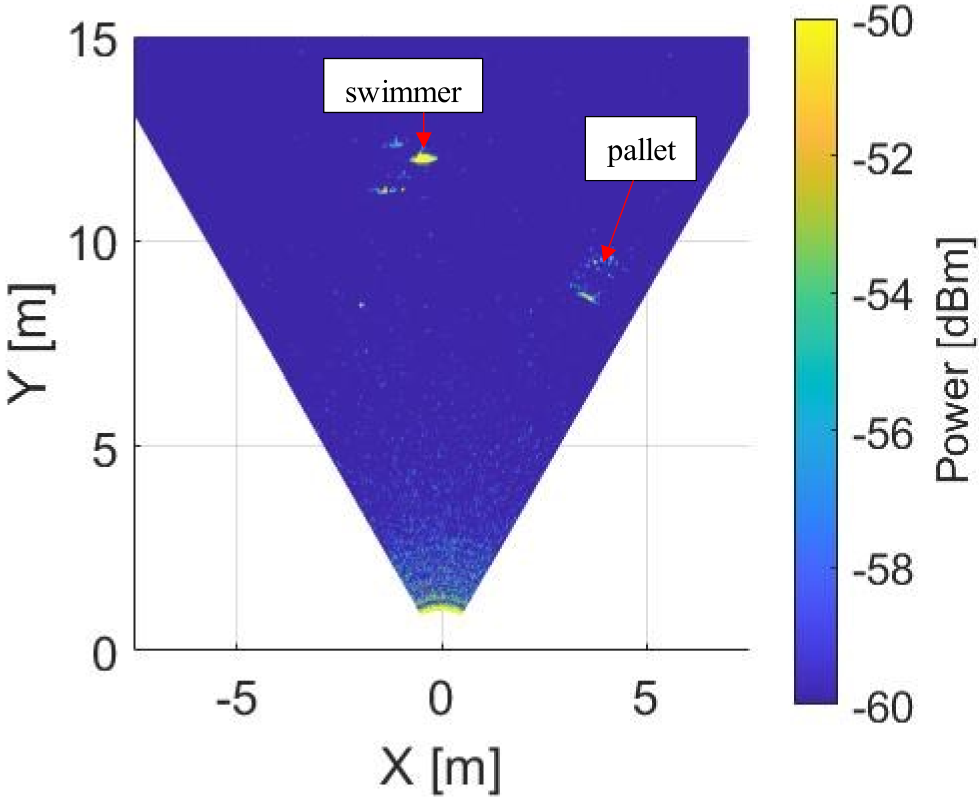

Figure 6.1-11 60 degree mechanically scanned radar image of pallet and swimmer treading water

The dynamic range is set so that the noise floor does not appear in the image. The returns off the front of the pallet appear to be 10 dB higher than what was achieved using DBS, which can be explained by using the fan beam antenna which has a gain that is 5 dB higher than the 10-degree horn antenna. The orientation of the pallet is clear in the scanned image; however, the periodic structure appears to be below the noise floor. Mechanically scanned imagery has the capability to achieve a 360-degree FoV, whereas DBS is constrained to forming frames with an azimuth FoV equal to the antenna beamwidth and overlaying subsequent frames. To increase the azimuth coverage for a DBS based sensing system, a distributed system will be required where each antenna covers a different swath of the azimuth.

6.2 Gosport Marina offshore DBS trial

The Gosport Marina Trial was held on April 14th, 2023, and was conducted between Gosport Marina, UK, and the Isle of wight, around latitude: 50.7526 degrees north, longitude -0.0216 degrees east. It comprised of a series of repeated offshore measurements with 77 GHz automotive MIMO radars and the 150 GHz FMCW radar. The trial had several objectives as listed below:

- Take repeated DBS mode measurements in real sea conditions from a medium size vessel to prove capability of DBS to produce imagery of the maritime scene and targets.
- Test the setup of the distributed system as seen in chapter 5.
- Test the resilience of the hardware in maritime conditions.

On the trial day, the weather was particularly poor, windy and rainy, with an estimated Douglas Sea state 3.

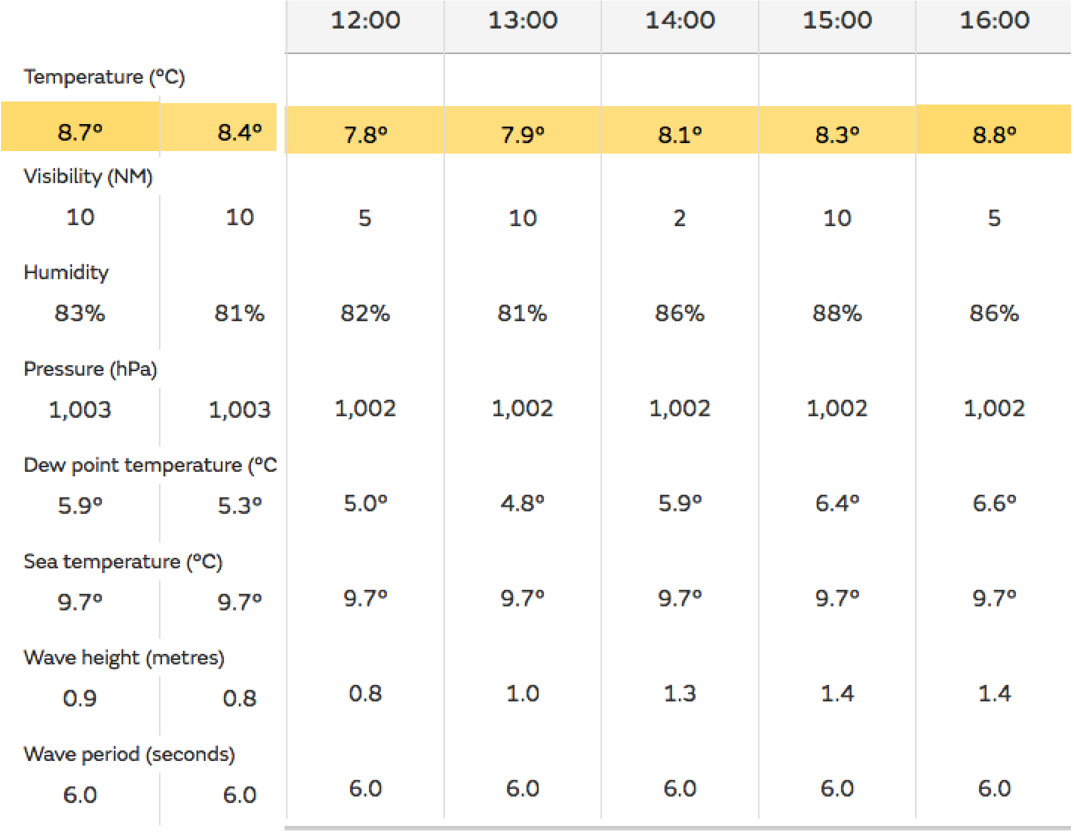

			12:00	13:00	14:00	15:00	16:00
Temperature (°C)	8.7°	8.4°	7.8°	7.9°	8.1°	8.3°	8.8°
Visibility (NM)	10	10	5	10	2	10	5
Humidity	83%	81%	82%	81%	86%	88%	86%
Pressure (hPa)	1,003	1,003	1,002	1,002	1,002	1,002	1,002
Dew point temperature (°C	5.9°	5.3°	5.0°	4.8°	5.9°	6.4°	6.6°
Sea temperature (°C)	9.7°	9.7°	9.7°	9.7°	9.7°	9.7°	9.7°
Wave height (metres)	0.9	0.8	0.8	1.0	1.3	1.4	1.4
Wave period (seconds)	6.0	6.0	6.0	6.0	6.0	6.0	6.0

Figure 6.2-1 Sea wave profile and weather data from Greenwich Light Vessel, table taken from [126].

The equipment outlined in Figure 5.6-3 was installed onto a small fishing vessel (catamaran), and it was taken to Isle of Wight, where several floating targets were placed on the surface to take DBS/SAR mode measurements, as well as the measurement of targets of opportunity.

Figure 6.2-2 150 GHz radar installed on Catamaran for DBS/SAR mode measurements.

6.2.1 Gosport Marina Results

The 150 GHz radar parameters were set before it was installed on the side of the boat and remained the same throughout the entire Gosport Marina measurement campaign.

Parameter	Value	Units
Chirp Duration	0.15	ms
PRF	6000	Hz
Bandwidth	5	GHz
Range resolution	3	cm
Maximum unambiguous velocity	+/- 3.05	m/s
Beamwidth (az/el)	10/10	degrees
Gain	24	dB
Initial depression angle (w.r.t boat)	3	degrees
Squint angle	90	degrees
Integration time	0.25	s

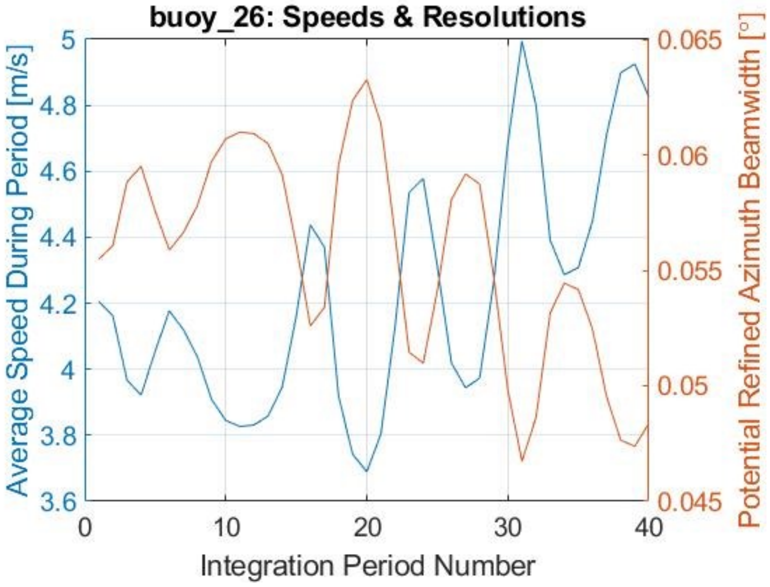

Figure 6.2-3 Measured average velocity from the IMU and the maximum potential refined azimuth for each integration period/DBS frame. Integration time of 0.25 s.

Unlike the setup in section 6.1, the velocity and the motion dynamic in these measurements exactly represent a small vessel, and so the potential refined azimuth beamwidth is also representative of what can be achieved at sea. Again, although the value oscillates near 0.055 degrees, this does not factor in windowing, and changes in velocity. Even with the strong windowing it achieves azimuth resolutions better than 20 times more refined that the fan beam antenna.

Figure 6.2-4 The Peel Wreck Buoy, around 25 m from the radar. The size of the buoy was around 3.5 m tall and a 3 m diameter. The top of the buoy was likely deliberately shaped to form a corner reflector so that it would show as a bright reflector on the radars of passing ships.

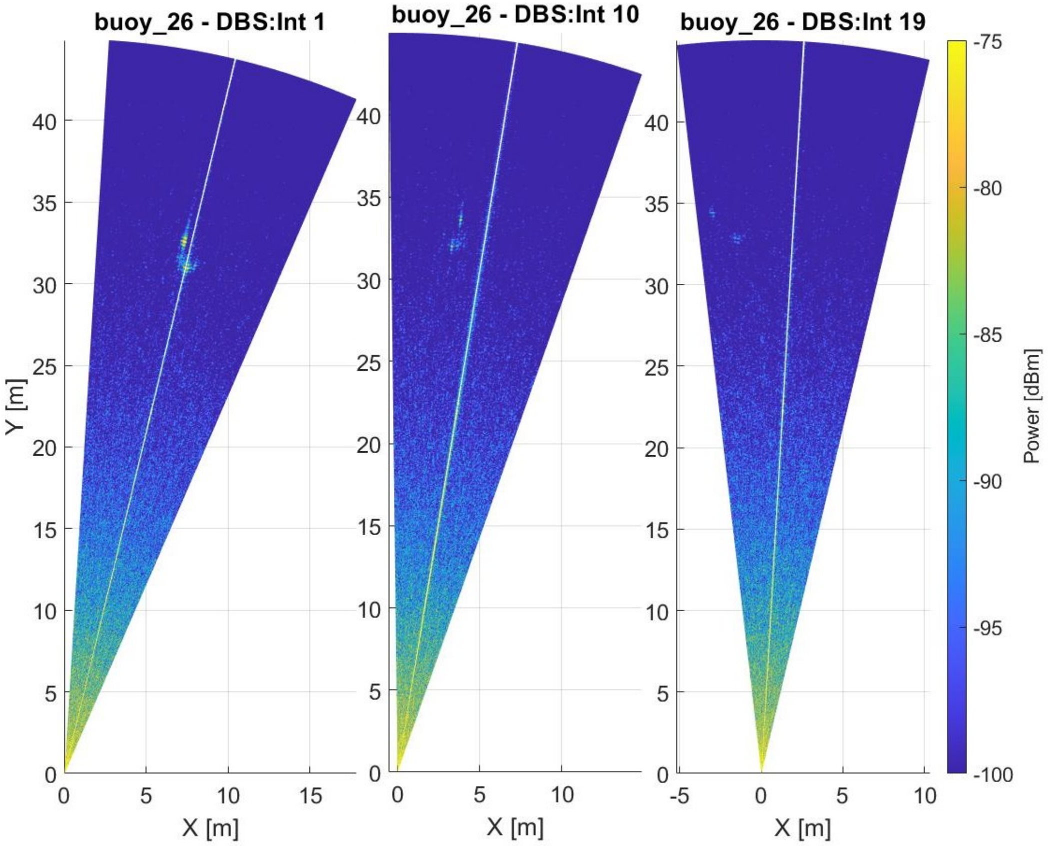

Figure 6.2-5 Three 150 GHz DBS frames of the Peel Wreck Buoy integration time of 0.25 s, the 'int' number refers to the integration period/DBS frame. In this case the first frame is processed after 0.25 s, the middle frame is after 2.25 s and the final frame is at 4.25 s. The buoy is floating on the surface at just over 30 m and the periodic motion/defocusing of the buoy is observed throughout the frames.

Here the peel wreck buoy appears in the DBS frames at 30 m range from the boat. There two regions of that appear in the image, which are specular reflections of the base of the buoy, and the top of the buoy which forms a corner like target, hence the high RCS. The most intriguing result is that we can now successfully obtain DBS images in realistic sea states using the basic processing outlined in chapter 3. Even though the synthetic aperture is perturbed by the non-linear motion of the vessel, the Doppler signature is strong enough to form imagery.

As the integration time is 0.25 s, the frame rate is 4 Hz. The buoy is anchored to the peel wreck, but it is floating on the surface and therefore sways with a similar dynamic to surface waves. This can be seen in the DBS frames, as the corner region moves from the left in frame 1, to the right in frame 10 and back to the left at frame 19. The buoy was no longer in dwell after frame 19, which is a dwell time of 4.75 s, however it would be of interest to keep the buoy in dwell to see if the wave period of 6 seconds could be estimated from the DBS imagery, which may provide information if the target is floating like the buoy, or fixed to the floor, like a metal sign post.

The boat also oscillated in the lateral direction, meaning that the antenna would sometimes face downwards towards the water, and in some instances face the sky. In the instance where the boat faced the water, the returns from the buoy would diminish, and the returns from the clutter would increase.

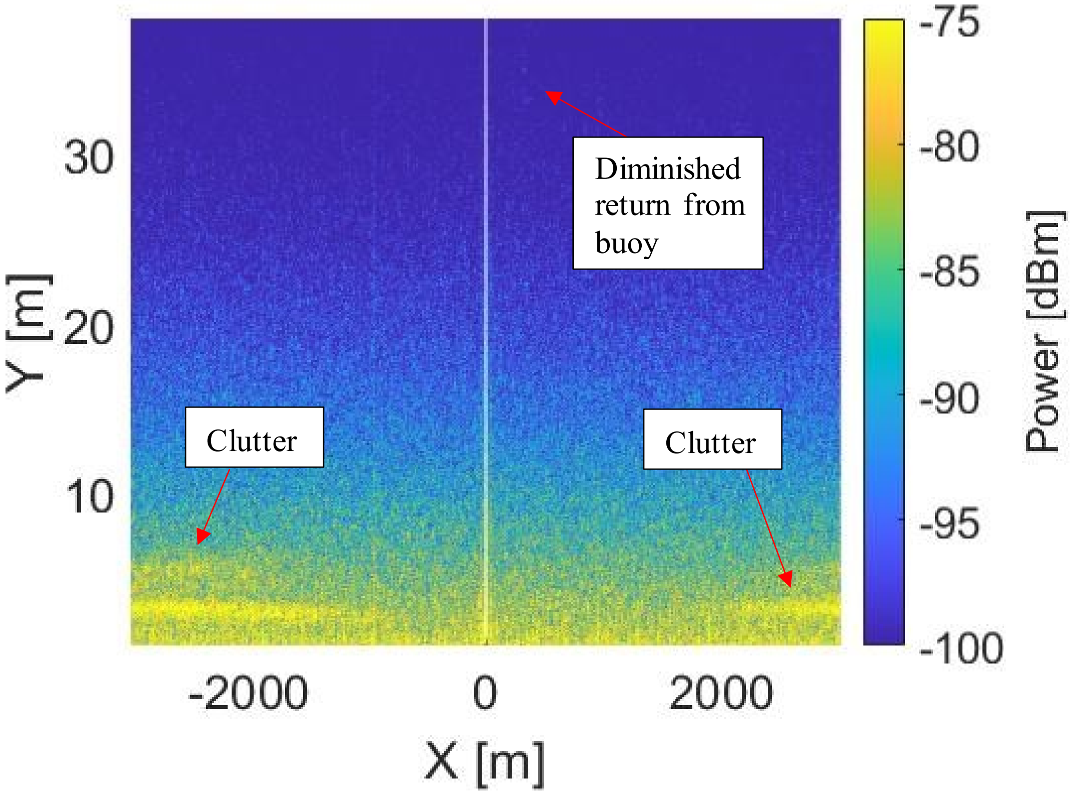

Figure 6.2-6 Range-Doppler plot of frame where boat was tilted towards the ocean.

In this particular frame, the returns off the buoy are around -95 dBm, which is close to the noise floor of the radar. The measured sea clutter had an ambiguous doppler signature that had a Doppler spread of over 2000 Hz. As the velocity recorded for this frame was ~ 4.2 m/s, and assuming that the squint angle remains at 90 degrees, the DBS frame is formed using the data between ± 360 Hz. Any data with a greater magnitude of Doppler than this does not form part of the DBS frame. Therefore, this is an example of how DBS processing alone can be used as a form of anomaly detection, where the energy from the clutter is omitted by its spread in Doppler.

A metal spherical target of diameter 48 cm was placed on the surface to replicate a creature in the sea [105]. The RCS of the metal sphere is -7.4 dBsm, although part of the sphere is submerged, it is assumed that most of the reflections occur on a small section of the sphere that faces the antenna boresight. Compared to the RCS of a human torso, it is an overestimate of the RCS, but the measurements and applicability of detecting swimmers is another complicated issue, we are interested to see if they can be imaged for now. DBS measurements were taken and the data processed.

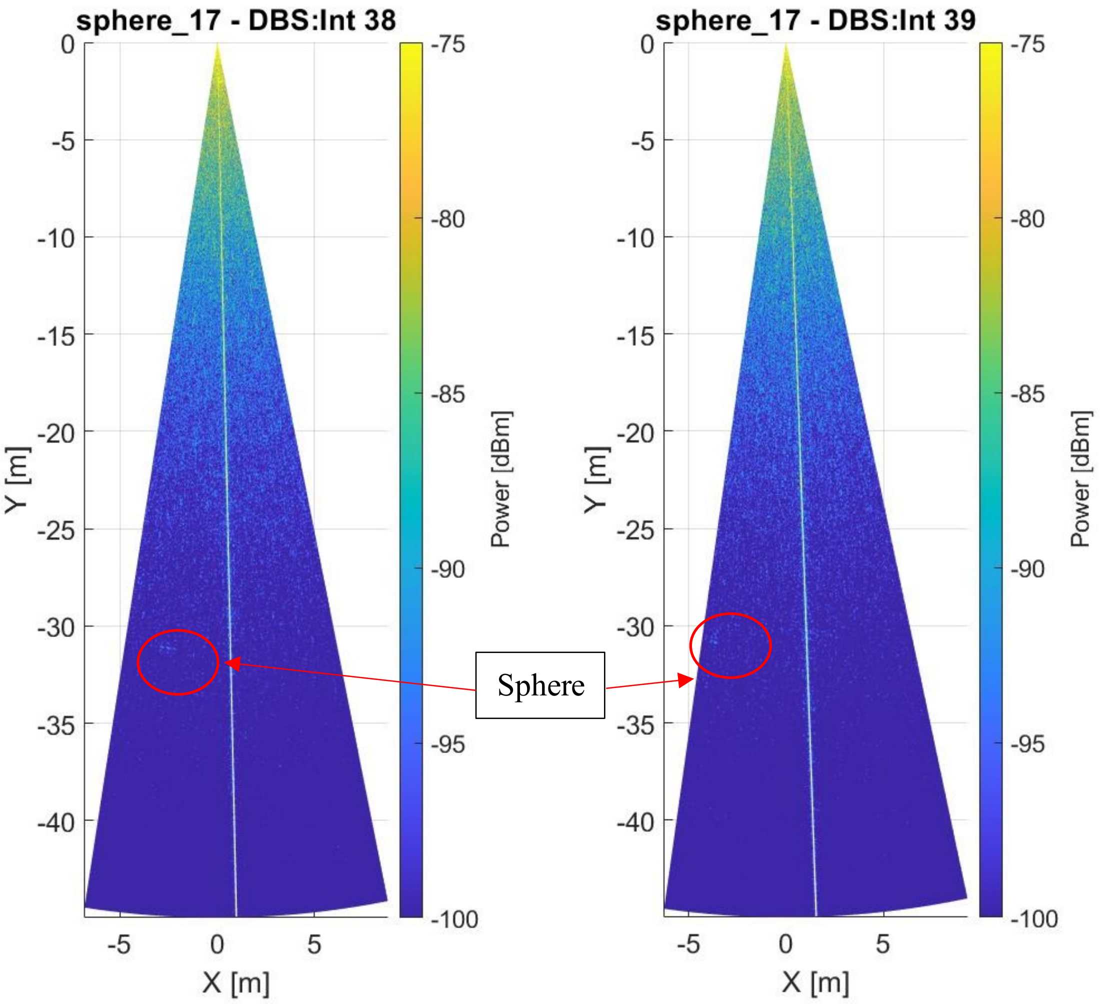

Figure 6.2-7 Consecutive DBS frame of the sphere at just over 30 m integration time of 0.25 seconds.

The consecutive DBS frames appear to be upside down as the GPS heading was used to position the images in the GPS reference frame. The estimated peak power received from the spheres in this image was -95 dBm, by assuming IF waveform was sinusoidal the power was calculated from the ADC input, so does not account for any losses in the radar. The calculated estimate from (2.9-6) is -93 dBm, so we can assume that this is the sphere. Furthermore, the sphere remains present in several frames, and so there is potential to use frame to frame correlation techniques to help identify and track the target.

6.3 Radar design meeting requirements for offshore DBS measurements

Table 6.3-1 Comparison of Gosport and Coniston trial parameters

Parameter	Coniston Value	Gosport Value	Units
Chirp Duration	0.15	0.15	ms
PRF	6000	6000	Hz
Range resolution	3	3	cm
Minimum azimuth resolution	0.08	0.05	degrees
Maximum unambiguous velocity	± 3.05	± 3.05	m/s
Minimum Squint angle	0	52	degrees
Initial depression angle (w.r.t shore)	10	5	degrees
Integration time	1	0.25	s
Squint angle	90	90	degrees

We see from table 6.2-1 that the Gosport trial provides a limitation on the squint angle due to the Doppler ambiguity. To resolve this, the PRF should be increased to 10 KHz, which is possible to do with the current set up, and will allow DBS processing to be unambiguous across all possible squint angles. It is also found that longer integration times are viable for the

Coniston trial where the velocity was much slower, as the Doppler smear would be less, whereas in the Gosport trial, excessive integration times would defocus targets and were therefore limited to integration times of 0.25 s.

6.4 Repeatable wave measurements

An experiment was designed to provide repeatable wave measurements using the radar systems from chapter 5. It consists of a wave tank that is partially filled with water, and a mechanical wave generator which uses a DC motor and paddle. The wave tank can replicate sea waves at different states, that is fully controllable, repeatable, and fundamentally real. The data that is collected from this experiment is used to test anomaly detection techniques as well as provide validation to the simulated data.

Figure 6.4-1Wave tank experiment setup for controlled experimentation.

To obtain data for the verification of the HFSS simulation strategy, the radar was left in staring mode, and the paddle was set to generate waves at a frequency of 1.77 Hz and an amplitude of 9 m. It is worth noting that the resistance from the water may reduce the paddle frequency. The radar was set to a PRF of 200 Hz and a chirp duration of 1 ms, with a range resolution of 3 cm, and a depression angle of 10 degrees. These results parallel the simulation results in section 4.10 and lay the groundwork for future quantitative analysis.

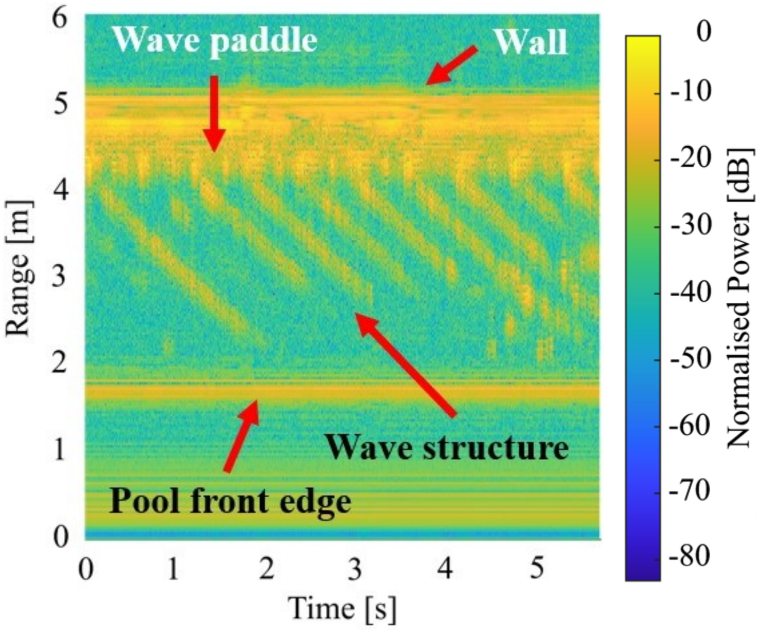

Figure 6.4-2 Range profiles augmented in time on repeatable wave data generated in lab.

The wave structure can clearly be seen in the radar data, as the waves progress down the pool from the paddle with an average normalised power of -10 dB and appear to have a near constant velocity. At 5 seconds, the waves begin to reflect off the front edge which forms a standing wave and effects the wave structure and hence the returns off the surface. To verify the simulation, a clear wave structure is needed, so only the first 4 seconds of data will be fit for verification purposes. A potential method to mitigate the standing wave issue would be to use a wave breaker.

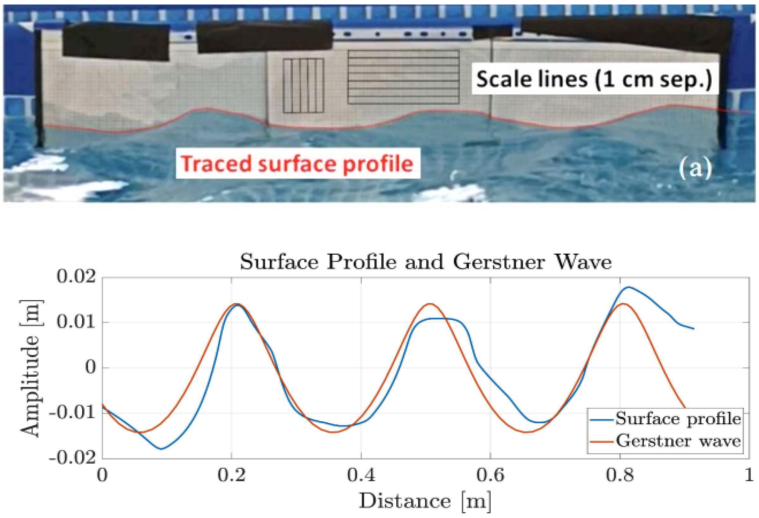

Figure 6.4-3 Traced surface profile using video data and graph paper (top), The trace and fitted Gerstner profile (bottom).

Using the data in Figure 6.4-3 Traced surface profile using video data and graph paper (top), The trace and fitted Gerstner profile (bottom)Figure 6.4-3, a Gerstner wave with an amplitude of 1.5 m and a wavelength of 0.3 m fit the surface wave profile [127]. an estimate of the surface profile of the pool can be produced in a HFSS and the simulation can be run, replicating the radar parameters and situation that was seen in the experiment.

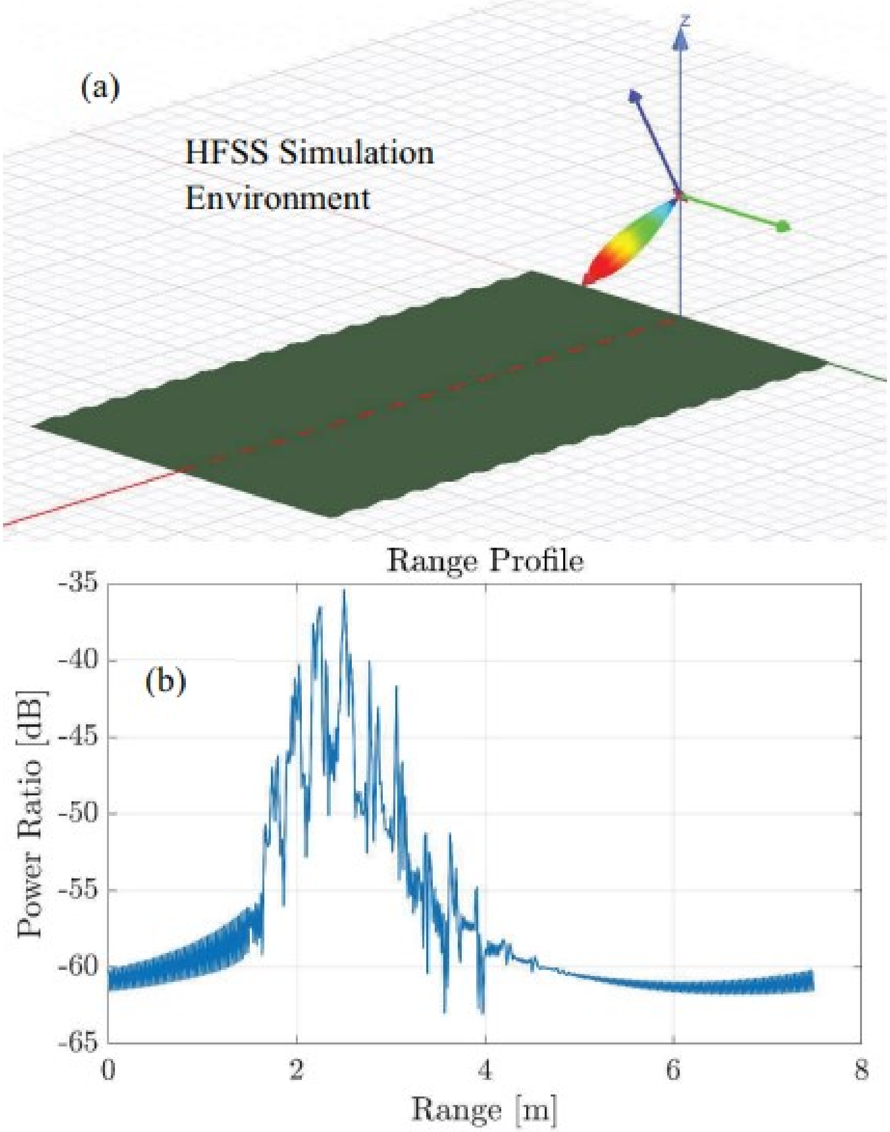

Figure 6.4-4 Simulated wave pool set up using Gerstner wave profile to approximate the surface (a), corresponding simulated range profile at 150 GHz (b), taken from [128]. The purpose of the simulation is to compare to the data measured in the pool to verify the simulation technique.

Although still in its early stages, the next steps are to simulate enough range profiles to form a complete time series data set for a direct comparison to the data from Figure 6.4-2. It is worth noting that by simulating the entire surface as a Gerstner wave, the simulation assumes that the waves generated from the paddle have already reached the front end of the wave tank, hence the range profile generated in Figure 6.4-4 is more akin to the range profiles generate after 4 s but before 5 s in Figure 6.4-2. To improve the simulation, the development of the waves in the tank may also be simulated, which will help verify simulated Doppler data and be more representative of what is seen from the wave tank experiment.

6.5 Summary of the Measurement Campaigns Data and Processing

This chapter has presented a selection of results taken from a measurement campaign to gather target and sea clutter data for Maritime DBS and scanned imagery as well as staring data at Sub-THz frequencies. The novelty of gathering DBS/SAR mode data in the maritime environment at frequencies >100 GHz is stressed here. The large amount of data gathered during this project has been primarily analysed for DBS processing, although the intention is to use the data for further investigation of DBS processing and the DBS measurement system.

It was found that DBS processing of radar data is feasible in medium sea conditions for small vessels, and the achievable refined azimuth beamwidths are near 0.1 degrees for integration times of 0.25 s. It was also found that the returns of clutter have a large Doppler spread, and the DBS processing removes the majority the clutter energy from the image. Of course, the most intriguing result is that we can obtain refined imagery of target on the surface despite the non-linear movements of the platform.

As well as DBS processing the measurement campaign for repeatable wave data has been presented as a tool to verify the HFSS simulation and a solution to obtaining repeatable wave data. Different targets can be placed in the wave tank under the same wave conditions which provides a method to test anomaly detection techniques. A comparison between data that contains waves only, and waves plus a target can be directly compared. This work has laid the groundwork for future quantitative analysis, where the accuracy of the simulation can be quantitatively defined.

7 Summary, Conclusion and Discussion of Future Work

7.1 Summary

This thesis is dedicated to the research of DBS in the context of imaging the marine environment for the use of marine target measurements, target detection with the ultimate goal of providing the data required to achieve full autonomy for the vessel. The DBS/SAR modality requires the sensor to move in a linear path, where SAR processing has been extensively research but DBS processing less so. The application of DBS processing to the maritime environment is a novel concept which takes advantage of the fact that the non-linear platform and target motions which devastate the effectiveness of SAR image processing have small, quantifiable changes in the DBS image processing. The study has involved a range of research activity, including the development of the sensing system for DBS measurements, the creation of DBS modality sub-THz simulations using HFSS, an extensive measurement campaign using the sensing system at sea, and initial data analysis.

The thesis starts by explaining the problems faced with providing autonomy to small vessels and how DBS will be used to provide some of the data required for situational awareness. Of course, with modern trends in sensor fusion and the availability of many different sensors, the autonomy of the vessel will be achieved by using many sensors, and the radar system along with DBS sensing will be used to image the surrounding scene through adverse weather. Chapter 2 introduces the basic radar principles that are required to understand the operation of the radars and data collection.

DBS is then introduced from its conception to its uses in modern day research. The parameters are each defined, and an exploration into how each parameter needs to be considered when processing the DBS image done. Finally, the DBS equation is adapted for use in the maritime environment, where the motion of the target is also considered, and the effect of defocussing is described.

In section 4, the simulation of the sea surface, targets and the radar antenna and signal using HFSS was described and the results from the simulation were analysed. The simulation used the Pierson-Moskowitz due to its well-defined periodic structure, which helps the validation of the simulation. The PM Sea spectra was made angular dependant using a cosine squared spreading function, and the spectra was converted to a sea surface model with a defined time dependant phase, allowing for the production of several time evolved sea surfaces. The sea surface model was compared to a line-of-sight model for verification, and it was used to define the motion of targets on its surface. A pallet model was also simulated for DBS measurements, to better understand how the DBS image is formed, and to explain its appearance in the image.

Section 5 describes the developmental process of the 150 GHz sub-THz radar to ensure that it was enabled to take Doppler measurements. It explains how the new DDS and local oscillator was integrated into the pre-existing radar architecture, and how the improved PRF enables a large enough unambiguous Doppler for DBS measurement. The 150 GHz radar was then implemented into a new bespoke sensing system that used a stereo camera for optical truth, an IMU to measure the kinematics of the boat, and a time server, to keep all the data time synchronised, so it could be used to automatically produce DBS imagery.

Section 6 presents the measurement campaign for using Sub-THz radar at sea, and how the initial tests at Coniston water identified the feasibility of taking DBS measurements to produce high resolution imagery of targets. The result present in this thesis is that of a floating pallet, which can be compared to the simulation work. The image of the pallet is also compared to a scanned image using the same radar equipped with imaging antenna. The solution for taking repeatable wave measurements was also presented in this section, and its uses for validating the simulation work and testing anomaly detection work is shown.

Finally, in section 7, a short review on the anomaly detection techniques that will hold relevance for the DBS data was presented. The initial development of using invertible transforms as a method of resolving anomalies was explained, and techniques found in literature to be useful for maritime radar small target detection, which is applicable to radar imagery was explored.

7.2 Conclusions

The work towards the production of this thesis initiated a series of measurement campaigns where the development of the distributed system for maritime sensing was the key aim, where the measurements taken are primarily in the DBS/SAR modality. The initial tests at Coniston Water were done to show the feasibility of using the sub-THz radar for maritime target detection was practically feasible. The Gosport marina trial further confirmed the feasibility of maritime DBS as the exact conditions which the processing was intended for were met on that trial. The author has collected a large quantity of datasets for DBS measurements taken at sea at 150 GHz, and further plans to take more measurements at different sub-THz frequencies in the future.

The simulation strategy that was devised to simulate maritime radar data successfully produced valid results at 150 GHz. The smooth pallet simulation identified that, without surface roughness, only specular reflections would be received. Furthermore, the limitation on the number of allowed bounces made it so the returns in the simulated DBS imagery originated from regions of the pallet that formed corner like targets. When adding vertical and rolling motion to the pallet, the DBS processing forms an image where the pallet appears to have yawed. Using the DBS processing outlined in chapter 3, it was seen that the difference in Doppler between the back and front of the pallet was ten resolution cells, hence the skewed appearance of the pallet. Although this result means we understand how images defocus, efforts to compensate for target motion are yet to be considered, although MIMO radars show great promise combining MIMO with DBS to focus on moving targets. The simulation also has the capability to image a large swath of ocean as a model, and the line-of-sight simulation validates the result. Shadowed regions have a much lower nRCS than illuminated facets, and so the structure of the ocean can be identified in the processed DBS image.

One of the aims of the research presented in this thesis was to upgrade the 150 GHz sub-THz radar so it could achieve the required pulse repetition frequencies needed for DBS measurements and the integration of the radar into the entire DBS system to enable DBS measurements to be conducted. These aims were achieved as outlined in chapter 5, as the radar can now chirp at rate of 10 KHz, which is its maximum tested PRF. Beyond this, the PRF is limited by the latency of the ADC. The subsequent testing of the system in chapter 6 showed that the system performed well in tough conditions. Although the sensitivity of the radar is not the strongest, post DBS processing results show that the returns off the small spherical target at a range of 30 m had enough SNR to be identified in the data. The range Doppler data also indicates that the clutter was processed out of the DBS image, and that the roll of the boat had a significant effect on target visibility. It was found that the refined cross range resolution of DBS images taken from the boat were over ten times better than the resolution achievable when using the fan-beam imaging antenna. It was also found that the DBS imagery seems to specifically resolve the signals from corners, such as the corner on top of the Peel wreck buoy, and the corners formed in the structure of the pallet. The image of the pallet in Coniston matches what was expected from the simulation, and the high quality of the image, as well as the accuracy of the frame to frame positioning of the pallet in the image means that the DBS data should be very useful as an input when using anomaly detection techniques that require some form of frame to frame analysis, or, like traditional optical classifiers, the size and shape of the pallet image.

Currently, no anomaly detection techniques have been applied to the DBS data as this is the next stage of the research process. Efforts to understand anomaly detection techniques are currently being researched by applying them to radar data taken during the extensive measurement campaign ran throughout the STREAM project. Some of the anomaly detection techniques being considered have been presented in this thesis from their basic principles, however the next steps will require the analysis of target and clutter data, in particular understanding the distributions, which will be used to measure for the presence of anomalies. It was found that using invertible transforms, in its most basic form could be used to resolve anomalies in the radar data, and this idea needs to be explored further, as both the Radon transform and 2D-FFT don't require statistical knowledge to function.

7.3 Limitations

As with any novel work, there are limitations that restrict the use of maritime DBS and the simulation strategy.

The strategy proposed for full scene sub-THz simulation is computationally expensive, and the production of a simulated dataset for DBS when using a full multi-faceted sea surface model will take a long while to produce, pending the computer does not crash. In the interest of reducing computational expenditure, the simulation is limited to stop and go, where the model remains stationary during the sweep. This means the unambiguous Doppler is limited to the simulated time step, and if a large range of Doppler is required, more samples are required to be simulated. As with all simulations, assumptions were made to make an idealistic case. In sea environments we can expect sea spray and other artefacts to appear, which requires much more detailed modelling as proposed in this thesis, but the result would be a more realistic simulation.

The radar hardware proposed in this thesis also imposes limitations on the measured data for DBS processing. One major limitation is that, by increasing the PRF, and reducing the chirp duration, the noise bandwidth increases, which results in poor sensitivity. At sub-THz frequencies, transmit power is already quite low, and as a result current DBS processing will struggle to image low SNR targets. As well as this, DBS benefits from using wide-beam antenna, which results in less gain, so stronger sub-THz amplifiers are required. The hardware is also limited by the buffer time of the PC and ADCs which limits the PRF, as triggering the ADC too quickly can cause system crashes. The highest tested in this work was 10 KHz. As a result, for faster platforms, this limits the squint angle as in the forward-looking direction, the Doppler will become unambiguous.

7.4 Future Work

This research provides the first important steps into the use of azimuth refinement of radar imagery taken from a small vessel mounted Sub-THz radar as an input for anomaly detection and scene segmentation.

One important area of future research will be the motion compensation of the vessel, and the compensation for the irregular motion of the targets, and the application of these techniques to focus the imagery. As discussed in chapter 3, there is already interest in using MIMO DBS which inherently focuses the imagery by convolving the DBS processing with the MIMO processing to find the correct adjustment factor for the platform velocity.

The simulation work shown in chapter 4 is still in its infancy. The work shown in this thesis is certainly not the most efficient method of simulating on HFSS, and future work into finding the most efficient simulations to yield results, without compromising on the quality, is worth some attention. However, with the simulation strategy being well defined, the application of DBS processing for many different models can be investigated. One simulation which is being considered is to use a different time-iterated model of the sea surface for each pulse, to see how the received clutter structure appears in DBS. Although the method of simulation remains the same, due to the large sea surface models, the simulation is not efficient enough to complete in a reasonable time, hence the requirement for better efficiency. The simulated data from the pool and the real data measured in the repeatable wave experiment needs quantitative analysis which is the next step now the foundations of the work have been made. Another way to make the simulation more representative of a real maritime platform would be to introduce antenna motion in 6 degrees of freedom, where we hope to see the effects of changing grazing angle due to the rolling of the ship, where clutter power should increase and decrease.

The 150 GHz radar was upgraded to achieve the high PRF required to ensure the maximum unambiguous Doppler was high enough, that either the vessel could move faster to achieve greater refinement of the cross-range resolution, and that the squint angle could be reduced so that the radar can be used in the forward-looking direction. However, the MISL laboratory also boasts experimental 79 GHz and 300 GHz FMCW radars that are currently undergoing the same chirp generator upgrade, so we can take DBS measurements at different sub-THz frequencies. Currently the chirp generators have been produced for these radars and require integration before they can be used for experiments. A direct comparison of the DBS processing at three different Sub-THz frequencies will be a valuable contribution to knowledge, as it is expected to show that higher frequencies are more sensitive to surface textures and can achieve the same azimuth resolution refinement using shorter integration times, which in theory, should make the imaging more sensitive to events that have a correlation time that is less than the integration time. The DBS system that was tested is also in its early phase. The advanced navigation IMU was excessive for the purpose of the experiments, as it was only required for positioning data and the average velocity between integration time.

Finally, a thought to the future of this work in general. DBS has shown great promise to produce high resolution imagery in the maritime environment. The issues of Doppler ambiguity for low squint angles, and defocussing due to target motion have been addressed, but are not solved using the single Tx and Rx radars. MIMO radars can solve these issues through MIMO-DBS where MIMO has good resolution in the low squint direction, but the large sidelobes limit the azimuth resolution, and DBS reduces the sidelobes. Analysing the PSF of a moving target in the MIMO and DBS data separately and aligning the peaks by introducing a 'velocity factor' can be used to focus on moving targets. Again, single Tx and Rx radars do not have the azimuth reference to do this, so without any information of the target, it is difficult to account for target motion.

Now DBS has been shown as an effective technique for producing high resolution imagery at sea, the next stage is to resolve and detect targets as anomalies in the imagery. Anomaly detection is a fundamental area of research with applications in fraud detection, cyber security, surveillance and more. Across these topics, the definition of anomaly detection can be broadly expressed as "The identification of an occurrence in data that does not conform to what the data is expected to be according to a background model" [129]. It is also said that an anomaly is an event of low probability with respect to normal behaviour of the input data [130]. A full exploration of the anomaly detection techniques that originate from both radar and optical data needs to be done using the high-resolution imagery obtained from DBS as its input. In general, many different techniques exist in literature to improve the contrast between the background of sea clutter and the targets as anomalies [131]. One example which has been applied to sea radar data is using the fractal dimension to separate sea clutter from target returns. [132], [133]. Once contrast has been achieved, a suitable anomaly detector will have to be selected, where a threshold will be chosen to minimise the number of false alarms or missed detections. An example of this would be to use the multi-variate gaussian anomaly detection, which can be used to form image segmentation [134].

The current fascination with neural networks and artificial intelligence (AI) has sparked major interest across all fields, and the author believes in the future, that AI techniques will begin to dominate all forms of digital processing, including the detection and classification of targets in Sub-THz radar, as it is already being used for image and pattern recognition in the optical domain.

References

[1] F. Norouzian, E. G. Hoare, E. Marchetti, M. Cherniakov and M. Gashinova, "Next Generation, Low-THz Automotive Radar – the potential for frequencies above 100 GHz," 2019 20th International Radar Symposium (IRS), Ulm, Germany, 2019, pp. 1-7, doi: 10.23919/IRS.2019.8767461.

[2] L. Daniel and M. Gashinova, "Sub-THz Radar Imagery for Automotive Application," 2022 19th European Radar Conference (EuRAD), Milan, Italy, 2022, pp. 261-264, doi: 10.23919/EuRAD54643.2022.9924931.

[3] G.Rutkowski. "Determining Ship's Safe Speed and Best Possible Speed for Sea Voyage Legs" in TransNav, International Journal on Marine Navigation and Safety of Sea Transportation, vol. 10, pp425-430, 2016, doi: 10.12716/1001.10.03.07.

[4] Jeong-Bin Yim, Deuk-Jin Park, "Modeling evasive action to be implemented at the minimum distance for collision avoidance in a give-way situation" in Ocean Engineering, Volume 263, 2022, 112210, ISSN 0029 8018. https://doi.org/10.1016/j.oceaneng.2022.112210. Available from https://www.sciencedirect.com/science/article/pii/S0029801822015232.

[5] Jung Sik Jeong, "Maritime traffic characteristics in waterway with time variant CPA" in Annual of Navigation. May 2013. DOI: 10.2478/aon-2013-0004.

[6] Sea Cleaners, "WATCH: Unique clean-up ship wins AiP", Maritime Journal, 2022. Last accessed 2024. Available: https://www.maritimejournal.com/industry-news/watch-unique-clean-up-ship-wins-aip/1474337.article

[7] Katie Maggs, "Keeping Seals Safe", The Outdoor Swimming Society. Available https://www.outdoorswimmingsociety.com/seal-swimming.

[8] Institute of mathematics, "Danger: Rogue Waves", 2010. Last accessed 2024. Available: https://ima.org.uk/731/danger-rogue-waves/

[9] Australian Maritime Safety Authority. "Collisions between vessels and marine fauna". Australian Government 2023. Available from https://www.amsa.gov.au/collisions-between-vessels-and-marine-fauna [last accessed May 2024].

[10] National Oceanic and Atmospheric Attenuation. "Waves". US Department of Commerce. 2023. Available from https://www.noaa.gov/jetstream/ocean/waves [last accessed May 2024].

[11] K. Konstantinidis et al., "A THz dielectric lens antenna," 2016 IEEE International Symposium on Antennas and Propagation (APSURSI), Fajardo, PR, USA, 2016, pp. 1493-1494, doi: 10.1109/APS.2016.7696453.

[12] M.I.Skolnik, "Introduction to radar systems". Editorial: New York: Mcgraw-Hill, 1980.

[13] V. S. Chernyak and I. Y. Immoreev, "A Brief History of Radar," in IEEE Aerospace and Electronic Systems Magazine, vol. 24, no. 9, pp. B1-B32, Sept. 2009, doi: 10.1109/MAES.2009.5282288.

[14] Swords, S. S., "Technical History of the Beginnings of Radar,"London, 2008, IET iSBN 978-0-86341-043-7

[15] Burns, R. W., (Ed.) "Radar Development to 1945," London, 1988, Peter Peregrinus, ISBN 0 86341 139 8

[16] K. B. Cooper, R. J. Dengler, N. Llombart, B. Thomas, G. Chattopadhyay and P. H. Siegel, "THz Imaging Radar for Standoff Personnel Screening," in IEEE Transactions on Terahertz Science and Technology, vol. 1, no. 1, pp. 169-182, Sept. 2011, doi: 10.1109/TTHZ.2011.2159556.

[17] D. R. Vizard, M. Gashinova, E. G. Hoare and M. Cherniakov, "Portable low THz imaging radars for automotive applications," 2015 40th International Conference on Infrared, Millimeter, and Terahertz waves (IRMMW-THz), Hong Kong, China, 2015, pp. 1-2, doi: 10.1109/IRMMW-THz.2015.7327711.

[18] D. Phippen et al., "Height Estimation for 3-D Automotive Scene Reconstruction Using 300-GHz Multireceiver Radar," in IEEE Transactions on Aerospace and Electronic Systems, vol. 58, no. 3, pp. 2339-2351, June 2022, doi: 10.1109/TAES.2021.3133339.

[19] A. Pirkani, D. Kumar, M. Cherniakov and M. Gashinova, "Distributed Automotive Radar Multi-Modal Sensing," 2023 20th European Radar Conference (EuRAD), Berlin, Germany, 2023, pp. 319-322, doi: 10.23919/EuRAD58043.2023.10289419.

[20] L. Daniel, Y. Xiao, E. Hoare, M. Cherniakov and M. Gashinova, "Statistical Image Segmentation and Region Classification Approaches for Automotive Radar," 2020 17th European Radar Conference (EuRAD), Utrecht, Netherlands, 2021, pp. 124-127, doi: 10.1109/EuRAD48048.2021.00042.

[21] D. Jasteh, E. G. Hoare, M. Cherniakov and M. Gashinova, "Experimental Low-Terahertz Radar Image Analysis for Automotive Terrain Sensing," in IEEE Geoscience and Remote Sensing Letters, vol. 13, no. 4, pp. 490-494, April 2016, doi: 10.1109/LGRS.2016.2518579.

[22] M. Kiyoto, T. Kondoh, K. Ban, and K. Shirahata, “Radar sensor for automobiles,” in Proc. IEEE Int. Solid-State Circuits Conf., 1974, pp. 438–442.

[23] D. Grimes and T. Jones, “Automotive radar: A brief review,” Proc. IEEE, vol. 62, no. 6, pp. 804–822, 1974.

[24] C. Waldschmidt, J. Hasch and W. Menzel, "Automotive Radar — From First Efforts to Future Systems," in IEEE Journal of Microwaves, vol. 1, no. 1, pp. 135-148, Jan. 2021, doi: 10.1109/JMW.2020.3033616.

[25] NXP “SAF86xx RFCMOS AUTOMOTIVE RADAR SoC” Revision 1, Dec. 2023.

[26] M. Schneider, "Automotive radar–status and trends," in German microwave conference, 2005, pp. 144-147.

[27] E. Yurtsever, J. Lambert, A. Carballo and K. Takeda, "A Survey of Autonomous Driving: Common Practices and Emerging Technologies," in IEEE Access, vol. 8, pp. 58443-58469, 2020, doi: 10.1109/ACCESS.2020.2983149.

[28] Köhler M, Hasch J, Blöcher HL, Schmidt L-P. Feasibility of automotive radar at frequencies beyond 100 GHz. International Journal of Microwave and Wireless Technologies. 2013;5(1):49-54. doi:10.1017/S175907871200075X

[29] Howse, D., & Gregory, R. (1997). Radar at Sea: The Royal Navy in World War 2. Naval Institute Press.

[30] Rosenberg, Luke Watts, Simon. (2022). Radar Sea Clutter - Modelling and Target Detection - 1.2 Maritime Surveillance Radars. (pp. 1). Institution of Engineering and Technology (The IET). Retrieved from https://app.knovel.com/hotlink/pdf/id:kt012WI8BG/radar-sea-clutter-modelling/maritime-surveillance.

[31] Moir, Ian Seabridge, Allan Jukes, Malcolm. (2013). Civil Avionics Systems (2nd Edition) - 13.3.4 Maritime Patrol. (pp.522). John Wiley & Sons. Retrieved from https://app.knovel.com/hotlink/toc/id:kpCASE0001/civil-avionics-systems/civil-avionics-systems

[32] Martino, Gerardo Di Iodice, Antonio. (2021). Maritime Surveillance with Synthetic Aperture Radar - 1.2.1 SAR Principles and Main SAR Missions. (pp. 3). Institution of Engineering and Technology (The IET). Retrieved from https://app.knovel.com/hotlink/pdf/id:kt012GYAIN/maritime-surveillance/sar-principles-main-sar

[33] European Maritime Safety Agency (EMSA). Cleanseanet [online] 2023. Available from http://www.emsa.europa.eu/csn-menu.html [Accessed May 2024].

[34] M. Martorella, D. Pastina, F. Berizzi and P. Lombardo, "Spaceborne Radar Imaging of Maritime Moving Targets With the Cosmo-SkyMed SAR System," in IEEE Journal of Selected Topics in Applied Earth Observations and Remote Sensing, vol. 7, no. 7, pp. 2797-2810, July 2014, doi: 10.1109/JSTARS.2014.2321708.

[35] H. Ma et al., "Maritime target detection using GNSS-based radar: Experimental proof of concept," 2017 IEEE Radar Conference (RadarConf), Seattle, WA, USA, 2017, pp. 0464-0469, doi: 10.1109/RADAR.2017.7944248.

[36] Martino, Gerardo Di Iodice, Antonio. (2021). Maritime Surveillance with Synthetic Aperture Radar - 1.1 Maritime Surveillance. (pp. 1). Institution of Engineering and Technology (The IET). Retrieved from https://app.knovel.com/hotlink/pdf/id:kt012GYAG2/maritime-surveillance/introducti-maritime-surveillance.

[37] A. De Luca, L. Daniel, K. Kabakchiev, E. Hoare, M. Gashinova and M. Cherniakov, "Maritime FSR with moving receiver for small target detection," 2015 16th International Radar Symposium (IRS), Dresden, Germany, 2015, pp. 834-839, doi: 10.1109/IRS.2015.7226340.

[38] Raymarine, ‘Quantum’, 2024. https://www.raymarine.com/en-gb/our-products/marine-radar/quantum

[39] Aziz, Hafizah & Hazwan, M.Y. & RASHID, NUR EMILEEN & raja abdullah, raja syamsul azmir & Othman, Kama & Salah, Asem. (2015). RCS analysis on different targets and bistatic angles using LTE frequency. Int. J. Ind. Electron. Electr. Eng.. 3. 658-663. 10.1109/IRS.2015.7226397.

[40] Balanis, Constantine A. (2016). Antenna Theory - Analysis and Design (4th Edition). John Wiley & Sons. Page 32. Retrieved from https://app.knovel.com/hotlink/toc/id:kpATADE01N/antenna-theory-analysis/antenna-theory-analysis

[41] M. Born and E. Wolf, Principles of Optics: Electromagnetic Theory of Propagation, Interference and Diffraction of Light, 7th ed. Cambridge University Press, 1999.

[42] K. T. Selvan and R. Janaswamy, "Fraunhofer and Fresnel Distances: Unified derivation for aperture antennas," in IEEE Antennas and Propagation Magazine, vol. 59, no. 4, pp. 12-15, Aug. 2017, doi: 10.1109/MAP.2017.2706648.

[43] Fujimoto, Kyohei Morishita, Hisashi. (2013). Modern Small Antennas - 9.3.3 Efficiency Measurement. (pp. 385). Cambridge University Press. Retrieved from https://app.knovel.com/hotlink/pdf/id:kt00TY2HE2/modern-small-antennas/efficiency-measurement

[44] D. K. Barton, Modern Radar System Analysis, 1st ed. Artech House Inc., 1988.

[45] Cisco, “Antenna patterns and their meaning”. White paper, 2007. Last accessed July 2024. https://www.industrialnetworking.com/pdf/Antenna-Patterns.pdf

[46] M. I. Skolnik, Introduction to radar systems, 2nd ed. ed. New York ; London: McGraw-Hill, 1980, page 225.

[47] Radiocommunication Sector of International Telecommunication Union. Recommendation ITU-R P.676-10: Attenuation by atmospheric gases 2013.

[48] The MathWorks, Inc. “gaspl” (2024). MATLAB version: 9.13.0 (R2024a). Accessed: April 01, 2024. Available: https://uk.mathworks.com/help/phased/ref/gaspl.html.

[49] Radiocommunication Sector of International Telecommunication Union. Recommendation ITU-R P.840-2: Attenuation due to clouds and fog 2013.

[50] F. Norouzian et al., "Signal reduction due to radome contamination in low-THz automotive radar," 2016 IEEE Radar Conference (RadarConf), Philadelphia, PA, USA, 2016, pp. 1-4, doi: 10.1109/RADAR.2016.7485217.

[51] Y. Xiao, L. Daniel and M. Gashinova, "The End-to-End Segmentation on Automotive Radar Imagery," 2021 18th European Radar Conference (EuRAD), London, United Kingdom, 2022, pp. 265-268, doi: 10.23919/EuRAD50154.2022.9784524.

[52] E. Marchetti, L. Daniel, E. G. Hoare, F. Norouzian, M. Cherniakov and M. Gashinova, "Radar Reflectivity of a Passenger Car at 300 GHz," 2018 19th International Radar Symposium (IRS), Bonn, Germany, 2018, pp. 1-7, doi: 10.23919/IRS.2018.8448009.

[53] Dassault Systemes, “CST Studio Suite, High Frequency Simulation, Workflow & Solver Overview”. 2019. Accessed 2024. Available: https://space.mit.edu/RADIO/Documentation.

[54] ANSYS, “ANSYS HFSS SBR+” 2018, available: https://www.ansys.com/content/dam/resource-center/application-brief/ansys-sbr-plus.pdf.

[55] Melvin, William L. Scheer, James A. (2014). Principles of Modern Radar, Volume 3 - Radar Applications - 13.3.4 Raindrop-Scattering Cross Sections. (pp. 601). Institution of Engineering and Technology (The IET). Retrieved from https://app.knovel.com/hotlink/pdf/id:kt00U54SR2/principles-modern-radar/raindrop-scattering-cross

[56] Sen, A. K. Bhattacharya, A. B. (2019). Radar Systems and Radio Aids to Navigation - 4.3 Back Scatter Cross Section. (pp. 110). Mercury Learning and Information. Retrieved from https://app.knovel.com/hotlink/pdf/id:kt011QC381/radar-systems-radio-aids/back-scatter-cross-section

[57] The MathWorks, Inc. “rcssphere” (2024). MATLAB version: 9.13.0 (R2024a). Accessed: April 01, 2024. Available: https://uk.mathworks.com/help/radar/ref/rcssphere.html.

[58] Mahafza, Bassem. Radar Systems Analysis and Design Using MATLAB, 2nd Ed. Boca Raton, FL: Chapman & Hall/CRC, 2005.

[59] Brooker, Graham. (2009). Introduction to Sensors for Ranging and Imaging - 8.4.4 Other Simple Calibration Reflectors. (pp. 304). SciTech Publishing. Retrieved from https://app.knovel.com/hotlink/pdf/id:kt008RFAD1/introduction-sensors/other-simple-calibration

[60] M. I. Skolnik, Introduction to radar systems, 2nd ed. ed. New York ; London: McGraw-Hill, 1980, page 18.

[61] Bullock, Scott R. (2018). Transceiver and System Design for Digital Communications (5th Edition) - 1.4.10 Noise Figure. (pp. 24). Institution of Engineering and Technology (The IET). Retrieved from https://app.knovel.com/hotlink/pdf/id:kt011FD5M6/transceiver-system-design/noise-figure

[62] Galati, Gaspare. (1993). Advanced Radar Techniques and Systems - 1.5 Continuous-time Optimum Filtering. Institution of Engineering and Technology (The IET). Retrieved from https://app.knovel.com/hotlink/pdf/id:kt003TADA2/advanced-radar-techniques/continuous-time-optimum

[63] Stove, A.G.: 'Linear FMCW radar techniques', IEE Proceedings F (Radar and Signal Processing), 1992, 139, (5), p. 343-350, DOI: 10.1049/ip-f-2.1992.0048 IET Digital Library, https://digital-library.theiet.org/content/journals/10.1049/ip-f-2.1992.0048

[64] Middleton, R. J. C.,”Dechirp-on-Receive Linearly Frequency Modulated Radar as a Matched-Filter Detector,” IEEE Trans. AeES 48, pp 2716-8, (3) 7/12

[65] Brooker, Graham. (2022). Sensors for Ranging and Imaging (2nd Edition) - 11.2.1 Range Resolution. (pp. 497). Institution of Engineering and Technology (The IET). Retrieved from https://app.knovel.com/hotlink/pdf/id:kt012WBRT1/sensors-ranging-imaging/sensors-ra-range-resolution

[66] Rees, Gareth. (1999). Remote Sensing Data Book - Nyquist Frequency. (pp. 139). Cambridge University Press. Retrieved from https://app.knovel.com/hotlink/pdf/id:kt006R5DF3/remote-sensing-data-book/nyquist-frequency

[67] C. L. Dolph, ‘A current distribution for broadside arrays which optimizes the relationship between beamwidth and side-lobe level'' Proceedings of the IRE, vol. 34, pp. 335-348, 1946.

[68] National Instruments. ‘Understanding FFTs and Windowing’. 2022. Last accessed June 2024: https://download.ni.com/evaluation/pxi/Understanding%20FFTs%20and%20Windowing.pdf

[69] A. G. Stove, D. A. Robertson and D. G. Macfarlane, "Littoral sea clutter returns at 94GHz," 2014 International Radar Conference, Lille, France, 2014, pp. 1-6, doi: 10.1109/RADAR.2014.7060308.

[70] Bell, P. S., Williams, J. 1., Clark, S., Morris, B. D. and Vila-Concejo, A., 'Nested Radar Systems for Remote Coastal Observations,' J. Coastal Research, Special Issue 39, 2004

[71] J. A. Richards, Remote Sensing with Imaging Radar, 1st ed., Heidelberg: Springer, 2009.

[72] J. W. Strutt, "Resolving or separating power of optical instruments", Phil. Mag., vol. VIII, pp. 261-274, 1879.

[73] Toffoli, A. and Bitner-Gregersen, E.M. (2017). Types of Ocean Surface Waves, Wave Classification. In Encyclopedia of Maritime and Offshore Engineering (eds J. Carlton, P. Jukes and Y.S. Choo). https://doi.org/10.1002/9781118476406.emoe077

[74] Ward, Keith Tough, Robert Watts, Simon. (2013). Sea Clutter - Scattering, the K Distribution and Radar Performance (2nd Edition) - 2.2 The Sea Surface. (pp. 19). Institution of Engineering and Technology (The IET). Retrieved from https://app.knovel.com/hotlink/pdf/id:kt00BRYHM6/sea-clutter-scattering/the-sea-surface

[75] Fred.E Nathanson. “Radar Design Principles: Signal Processing and the Environment Hardcover – 1 Jan. 1991” Jan 1991.

[76] Ward, Keith Tough, Robert Watts, Simon. (2013). Sea Clutter - Scattering, the K Distribution and Radar Performance (2nd Edition) - 2.8 Clutter Spikes and Modulations. (pp. 34). Institution of Engineering and Technology (The IET). Retrieved from https://app.knovel.com/hotlink/pdf/id:kt00BRYHT1/sea-clutter-scattering/clutter-spikes-modulations

[77] L. Daniel, A. Stove, E. Hoare, D. Phippen, M. Cherniakov, B. Mulgrew, M. Gashinova. (2018). Application of Doppler Beam Sharpening for Azimuth Refinement in Prospective Low-THz Automotive Radars. IET Radar, Sonar & Navigation. 12. 10.1049/iet-rsn.2018.5024.

[78] C. A. Wiley, "Synthetic Aperture Radars," in IEEE Transactions on Aerospace and Electronic Systems, vol. AES-21, no. 3, pp. 440-443, May 1985, doi: 10.1109/TAES.1985.310578.

[79] M. E. Radant, "The evolution of digital signal processing for airborne radar," in IEEE Transactions on Aerospace and Electronic Systems, vol. 38, no. 2, pp. 723-733, April 2002, doi: 10.1109/TAES.2002.1009002.

[80] L. Daniel and M. Gashinova, "Sub-THz Radar Imagery for Automotive Application," 2022 19th European Radar Conference (EuRAD), Milan, Italy, 2022, pp. 261-264, doi: 10.23919/EuRAD54643.2022.9924931.

[81] Y. Xiao, L. Daniel and M. Gashinova, "The End-to-End Segmentation on Automotive Radar Imagery," 2021 18th European Radar Conference (EuRAD), London, United Kingdom, 2022, pp. 265-268, doi: 10.23919/EuRAD50154.2022.9784524.

[82] D. Mao, Y. Zhang, Y. Zhang, C. Li, Y. Huang and J. Yang, "Doppler Centroid Estimation for Doppler Beam Sharpening Imaging Based on the Morphological Edge Detection Method," IGARSS 2018 - 2018

IEEE International Geoscience and Remote Sensing Symposium, Valencia, Spain, 2018, pp. 8925-8928, doi: 10.1109/IGARSS.2018.8519560.

[83] K. H. Kim, S. G. Kim and J. W. Yi, "Detection of ship targets near coastline by using Doppler Beam Sharpening technique," 2011 3rd International Asia-Pacific Conference on Synthetic Aperture Radar (APSAR), Seoul, Korea (South), 2011, pp. 1-4.

[84] J. C. Kirk, "Motion Compensation for Synthetic Aperture Radar," in IEEE Transactions on Aerospace and Electronic Systems, vol. AES-11, no. 3, pp. 338-348, May 1975, doi: 10.1109/TAES.1975.308083.

[85] G. Wang, L. Feng, J. Li, T. Xing, C. Ma and C. Kang, "A Robust Image Stitching and Geometric Correction Method for Doppler Beam Sharpening Imaging," 2019 6th Asia-Pacific Conference on Synthetic Aperture Radar (APSAR), Xiamen, China, 2019, pp. 1-4, doi: 10.1109/APSAR46974.2019.9048367.

[86] H. -Y. Lei, J. -T. Xiong, S. -J. Wei, X. -Y. Lou and T. Zhang, "Millimetre-Wave Automotive Radar Imaging Enhancement via Doppler Beam Sharpening," IGARSS 2023 - 2023 IEEE International Geoscience and Remote Sensing Symposium, Pasadena, CA, USA, 2023, pp. 4403-4406, doi: 10.1109/IGARSS52108.2023.10282601.

[87] S. L. Cassidy, S. Pooni, M. Cherniakov, E. G. Hoare and M. S. Gashinova, "High-Resolution Automotive Imaging Using MIMO Radar and Doppler Beam Sharpening," in IEEE Transactions on Aerospace and Electronic Systems, vol. 59, no. 2, pp. 1495-1505, April 2023, doi: 10.1109/TAES.2022.3203953.

[88] V. P. Fedosov, R. R. Ibadov, S. R. Ibadov and V. V. Voronin, "Restoration of the Blind Zone of the Image of the Underlying Surface for Radar Systems with Doppler Beam Sharpening," 2019 Radiation and Scattering of Electromagnetic Waves (RSEMW), Divnomorskoe, Russia, 2019, pp. 424-427, doi: 10.1109/RSEMW.2019.8792685.

[89] S. Yuan, P. Aubry, F. Fioranelli and A. G. Yarovoy, "A Novel Approach to Unambiguous Doppler Beam Sharpening for Forward-Looking MIMO Radar," in IEEE Sensors Journal, vol. 22, no. 23, pp. 23494-23506, 1 Dec.1, 2022, doi: 10.1109/JSEN.2022.3215862.

[90] S. Yuan, F. Fioranelli and A. Yarovoy, "An adaptive threshold-based unambiguous robust Doppler beam sharpening algorithm for forward-looking MIMO Radar," 2023 20th European Radar Conference (EuRAD), Berlin, Germany, 2023, pp. 65-68, doi: 10.23919/EuRAD58043.2023.10288626.

[91] A. Albaba, M. Bauduin, T. Verbelen, H. Sahli and A. Bourdoux, "Forward-Looking MIMO-SAR for Enhanced Radar Imaging in Autonomous Mobile Robots," in IEEE Access, vol. 11, pp. 66934-66948, 2023, doi: 10.1109/ACCESS.2023.3291611.

[92] A. Pirkani, S. Cassidy, F. Norouzian, M. Gashinova and M. Cherniakov, "Doppler Beam Sharpening for Enhanced MIMO Imagery in the Presence of Automotive Interference," 2021 18th European Radar Conference (EuRAD), London, United Kingdom, 2022, pp. 417-420, doi: 10.23919/EuRAD50154.2022.9784499.

[93] A. Pirkani, F. Norouzian, E. Hoare, M. Gashinova and M. Cherniakov, "Statistical Analysis of Automotive Radar Interference," 2020 IEEE Radar Conference (RadarConf20), Florence, Italy, 2020, pp. 1-6, doi: 10.1109/RadarConf2043947.2020.9266653.

[94] D.Angermann et al. “Terrestrial Reference Frame”. Global Geodetic Observing System (GGOS). https://ggos.org/item/terrestrial-reference-frame/ Last accessed: 01/04/2024.

[95] Bassem R. “Radar Systems Analysis and Design Using MATLAB” – 4th edition, 12.4 SAR Design Considerations. Published: Chapman & Hall/CRC 2022. ISBN: 9780367507930.

[96] R. Wang, Y. -H. Luo, Y. -K. Deng, Z. -M. Zhang and Y. Liu, "Motion Compensation for High-Resolution Automobile FMCW SAR," in *IEEE Geoscience and Remote Sensing Letters*, vol. 10, no. 5, pp. 1157-1161, Sept. 2013, doi: 10.1109/LGRS.2012.2234435.

[97] S. Wang, Z. Su and R. Wu, "Modified Range-Doppler imaging method for the high squint SAR," 2010 IEEE Radar Conference, Arlington, VA, USA, 2010, pp. 1450-1453, doi: 10.1109/RADAR.2010.5494388.

[98] E. Marchetti, A. Stove, E. Hoare, M. Cherniakov and M. Gashinova, "Images of satellite elements with a space-borne Sub-THz ISAR system," *2021 18th European Radar Conference (EuRAD)*, London, United Kingdom, 2022, pp. 425-428, doi: 10.23919/EuRAD50154.2022.9784477.

[99] P. L. Cross, "Maritime automated targets recognition algorithm test bed for high resolution ISAR imagery," *2013 IEEE International Conference on Technologies for Homeland Security (HST)*, Waltham, MA, USA, 2013, pp. 369-374, doi: 10.1109/THS.2013.6699032.

[100] D. Kumar et al., "150 GHz Radar Imagery using Doppler Beam Sharpening for Marine Sensing," 2023 24th International Radar Symposium (IRS), Berlin, Germany, 2023, pp. 1-10, doi: 10.23919/IRS57608.2023.10172456.

[101] Watts, S., Rosenberg, L.: Challenges in radar sea clutter modelling. IET Radar Sonar Navig. 16(9), 1403–1414 (2022). https://doi.org/10.1049/rsn2.12272

[102] D. Kumar et al., "Repeatable Wave Data for Sub-THz Radar Marine Target Detection Experiments," 2023 20th European Radar Conference (EuRAD), Berlin, Germany, 2023, pp. 148-151, doi: 10.23919/EuRAD58043.2023.10289628.

[103] Rahman, S., Vattulainen, A. B., Robertson, D. A. & Milne, R, “Millimetre wave radar signatures of sea lions”, 7 Feb 2023, International conference on radar systems (RADAR 2022). Stevenage, UK: IET digital library, p. 14-19 6 p. 10038919

[104] Draycott, S.; Davey, T.; Ingram, D.M. “Simulating Extreme Directional Wave Conditions.” Energies 2017, 10, 1731. https://doi.org/10.3390/en10111731

[105] A.Stove, et al. “Radar Cross Sections of Flotsam at Sub-THz Frequencies” submitted and accepted to 21st European Radar Conference (EuRAD), September, Paris, France 2024.

[106] T. Savides and B. Dwolatzky, "Radar simulation using the shooting and bouncing ray technique," CCECE 2003 - Canadian Conference on Electrical and Computer Engineering. Toward a Caring and Humane Technology (Cat. No.03CH37436), Montreal, QC, Canada, 2003, pp. 307-310 vol.1, doi: 10.1109/CCECE.2003.1226402.

[107] Z. Cendes, "The development of HFSS," 2016 USNC-URSI Radio Science Meeting, Fajardo, PR, USA, 2016, pp. 39-40, doi: 10.1109/USNC-URSI.2016.7588501.

[108] NVIDIA, “Accelerating Ansys HFSS Ray-Tracing (SBR+) Simulations With NVIDIA GPUs” Last accessed 2024. ”https://www.nvidia.com/en-us/on-demand/session/gtc24-p63183/

[109] W. J. Pierson and L. Moskowitz, “A Proposed Spectral Form for Fully Developed Wind Seas Based on the Similarity Theory of S. A. Kitaigorodskii,” J. Geophys. Res., vol. 69, no. 24, pp. 5181–5190, Dec. 1964.

[110] M. K. Ochi, "Ocean Waves - The Stochastic Approach," 1st ed. Cambridge University Press, 1998.

[111] A.Saulter, A.Leonard-Williams, “Assessment of significant wave height in UK coastal waters – 2011 update” 2011.

[112] J.L.Whitrow, “A Model of Low Grazing Angle Sea Clutter for Coherent Radar Perdormance Analysis” Australian Government, Department of Defence. DSTO-TR-2864. June 2013.

[113] Hasselmann K., et al. “Measurements of wind-wave growth and swell decay during the Joint North Sea Wave Project (JONSWAP)” Ergnzungsheft zur Deutschen Hydrographischen Zeitschrift Reihe, A(8) (Nr. 12), p.95, 1973.

[114] W. J. Pierson, G. Neumann, and R. W. James, “Practical methods for observing and forecasting ocean waves by means of wave spectra and statistics,” 1955.

[115] M. S. Longuet-Higgins, “Observation of the directional spectrum of sea waves using the motion of a floating buoy,” in Ocean Wave Spectra, 1st ed., Prentice-Hall Inc., 1963, pp. 111–136.

[116] Dingemans, M.W, “Water wave propagation over uneven bottoms”. 1997. Advanced Series on Ocean Engineering, vol. 13, World Scientific, p. 25769, ISBN 978-981-02-0427-3, OCLC 36126836, 2 Parts, 967 pages.

[117] GRABCAD, “GRABCAD community” https://grabcad.com/library last accessed 01/04/2024.

[118] Arijan Belec, Blender 3D Incredible Models: A comprehensive guide to hard-surface modeling, procedural texturing, and rendering, Packt Publishing, 2022.

[119] D. Jasteh, E. G. Hoare, M. Cherniakov and M. Gashinova, "Experimental Low-Terahertz Radar Image Analysis for Automotive Terrain Sensing," in IEEE Geoscience and Remote Sensing Letters, vol. 13, no. 4, pp. 490-494, April 2016, doi: 10.1109/LGRS.2016.2518579.

[120] Pasternack, “8 Section Bandpass Filter With SMA Female Connectors Operating From 7.25 GHz to 7.75 GHz With a 500 MHz Passband”, last accessed 2024. https://www.pasternack.com/8-section-band-pass-filter-7.25-7.75-ghz-passband-500-mhz-pe8741-p.aspx

[121] ELVA-1, “IMPATT Active Frequency Multipliers 26-180 GHz”. Last accessed 2024. https://elva-1.com/products/a40027

[122] Analog Devices. (2014, 14 June). Available: https://www.analog.com/media/en/technical-documentation/data-sheets/ad9914.pdf

[123] Stove, A. G., “Measurement of Oscillator Phase and Amplitude Noise at W-Band” Proc. ARMMS Conf. April 2008.

[124] A. Arage, G. Kuehnle and R. Jakoby, "Measurement of wet antenna effects on millimetre wave propagation," 2006 IEEE Conference on Radar, Verona, NY, USA, 2006, pp. 5 pp.-, doi: 10.1109/RADAR.2006.1631796.

[125] Seasonic. (Accessed 2023, 20 December) Available: https://seasonic.com/l1u

[126] Met Office, “Marine observations – Greenwich Light Vessel”, 2023. Last accessed 2024. https://www.metoffice.gov.uk/weather/specialist-forecasts/coast-and-sea/observations/162305

[127] Craik, ADD 2004, 'The origins of water wave theory', Annual Review of Fluid Mechanics, vol. 36, pp. 1-28. https://doi.org/10.1146/annurev.fluid.36.050802.122118

[128] L. Daniel et al., "Millimetre-wave and sub-THz maritime radar scene simulation," International Conference on Radar Systems (RADAR 2022), Hybrid Conference, Edinburgh, UK, 2022, pp. 581-586, doi: 10.1049/icp.2023.1297.

[129] M. H. Bhuyan, D. K. Bhattacharyya and J. K. Kalita, "Network Anomaly Detection: Methods, Systems and Tools," in IEEE Communications Surveys & Tutorials, vol. 16, no. 1, pp. 303-336, First Quarter 2014, doi: 10.1109/SURV.2013.052213.00046.

[130] W. V. N. V. Mahadevan, “Anomaly detection in crowded scenes,” in 2010, IEEE Computer Society Conference on Computer Vision and Pattern Recognition.

[131] T. Gu, W. Xu and X. Hu, "A Novel Small Target Detection Method for Marine Radar," 2019 IEEE 3rd Advanced Information Management, Communicates, Electronic and Automation Control Conference (IMCEC), 2019, pp. 1490-1495, doi: 10.1109/IMCEC46724.2019.8984027.

[132] T. Lo, H. Leung, J. Litva, and S. Haykin, ‘Fractal characterisation of sea-scattered signals and detection of sea-surface targets’, IEE Proceedings F - Radar and Signal Processing, vol. 140, no. 4, pp. 243–250, Aug. 1993, doi: 10.1049/ip-f-2.1993.0034

[133] F. Berizzi and E. Dalle-Mese, “Fractal analysis of the signal scattered from the sea surface,” in IEEE Transactions on Antennas and Propagation, 1999.

[134] Y. Xiao, L. Daniel and M. Gashinova, "Image Segmentation and Region Classification in Automotive High-Resolution Radar Imagery," in IEEE Sensors Journal, vol. 21, no. 5, pp. 6698-6711, 1 March1, 2021, doi: 10.1109/JSEN.2020.3043586.

APPENDIX A. Publications

Authored

[A] D. Kumar et al., "150 GHz Radar Imagery using Doppler Beam Sharpening for Marine Sensing," 2023 24th International Radar Symposium (IRS), Berlin, Germany, 2023, pp. 1-10, doi: 10.23919/IRS57608.2023.10172456.

Won the "Young Scientist Award" at IRS 2023. Main author, and took measurements at Coniston Water UK. Developed parts of the 150 GHz radar and system architecture.

[B] D. Kumar et al., " Repeatable Wave Data for Sub-THz Radar Marine Target Detection Experiments" 2023 20th European Microwave Week, European Radar (EuRad), Berlin, Germany, 2023.

Co-Authored

[C] A.Stove, et al. "Radar Cross Sections of Flotsam at Sub-THz Frequencies" submitted and accepted to 21st European Radar Conference (EuRAD), September, Paris, France 2024.

Designed the turntable/tripod setup for scanning measurements, planned scanning measurements and operated the radar during the experiment.

[D] A. Pirkani, A. G. Stove, D. Kumar, M. Cherniakov and M. S. Gashinova, "77 GHz FMCW Imaging Radar for Low Observable and Small Marine Target Detection in Dynamic Sea Conditions Based on Combined MIMO and DBS," in *IEEE Transactions on Radar Systems*, vol. 2, pp. 517-534, 2024, doi: 10.1109/TRS.2024.3400694.

[E] A. Pirkani, D. Kumar, M. Cherniakov and M. Gashinova, "Distributed Automotive Radar Multi-Modal Sensing," 2023 20th European Radar Conference (EuRAD), Berlin, Germany, 2023, pp. 319-322, doi: 10.23919/EuRAD58043.2023.10289419.

[F] A. Pirkani, D. Kumar, L. Daniel, E. Hoare, M. Cherniakov and M. Gashinova, "Dynamic Multi-Target Detection and Focus in Maritime Conditions," 2023 20th European Radar Conference (EuRAD), Berlin, Germany, 2023, pp. 510-513, doi: 10.23919/EuRAD58043.2023.10289505.

Won the "Best paper prize" at EuRad 2023. Implemented the use of IMU and timestamping with INRAS Radar for measurements on Coniston Water. Helped with interpretation of IMU data.

[G] A. Pirkani et al., "Doppler Beam Sharpening for MIMO and Real Aperture Radars at mm-wave and Sub-THz Maritime Sensing," 2023 24th International Radar Symposium (IRS), Berlin, Germany, 2023, pp. 1-10, doi: 10.23919/IRS57608.2023.10172423.

Developed 150 GHz radar upgrades and took measurements at Coniston Water UK. Identified use of IMU with INRAS Radarbook for DBS measurements and help set up the system during measurement campaign.

[H] A. G. Stove, L. Daniel, M. Gashinova, E. Hoare and D. Kumar, "Finding Anomalies in Radar Sea Clutter Using Radon Transforms," 2021 18th European Radar Conference (EuRAD), London, United Kingdom, 2022, pp. 421-424, doi: 10.23919/EuRAD50154.2022.9784544.

Discussion on use of Radon Transform on Clutter and Target data, and preliminary application of Radon transform on data taken from Hayling Island, Portsmouth UK. Data collection and provision of data to main author.

[K] Liam Daniel* , Emidio Marchetti, Dillon Kumar, Andrew Stove, Edward Hoare, Marina Gashinova and Mikhail Cherniakov. “Millimetre-Wave and Sub-THz Maritime Radar Scene Simulation” Radar 2022.

APPENDIX B. 150 GHz Noise Measurements

The 150 GHz receiver was fitted with a 50-ohm load and the signal from the receive channel was recorded to measure the noise spectrogram.

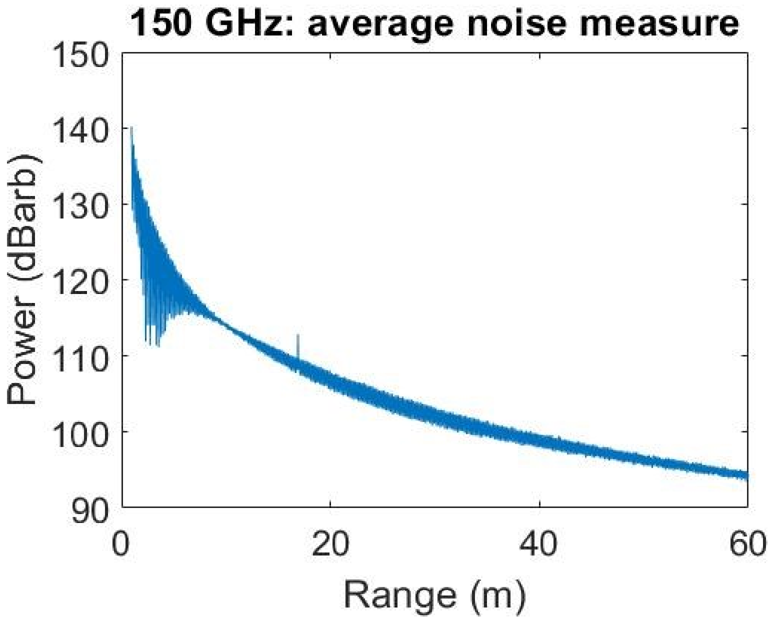

Figure B.1 Receiver output of the 150 GHZ with 50 ohm load attached, presumed to be noise. Formatted as a range profile.

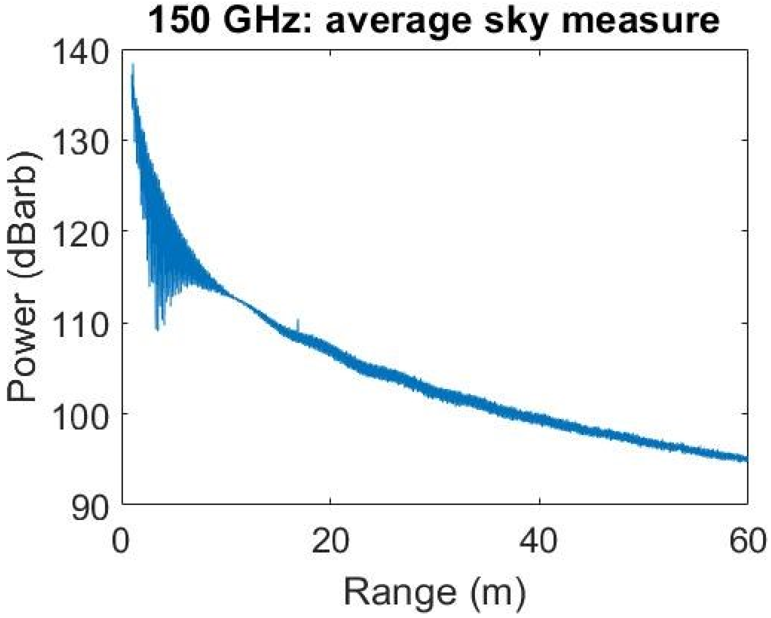

Figure B.2 Receiver output of the 150 GHz when antenna is pointed towards open sky, with fan beam imaging antenna equipped.

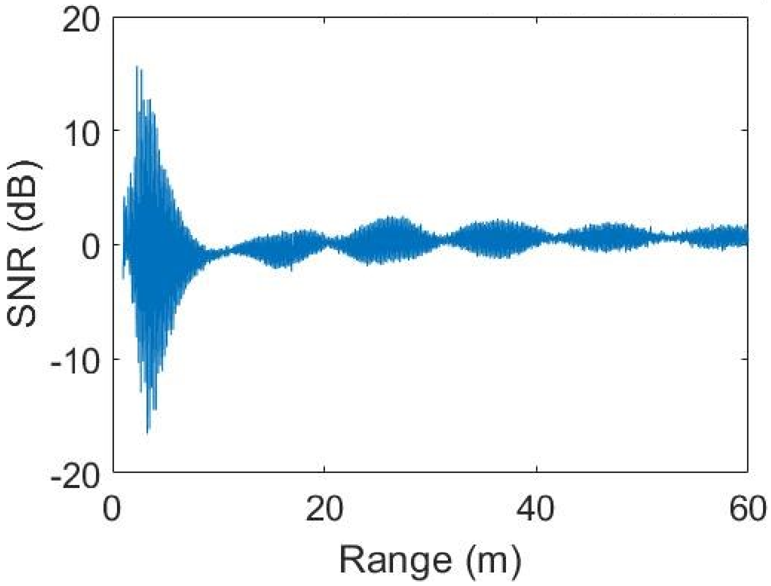

Figure B.3 Ratio of figure B.2 and figure B.1, which gives the ratio of the signal measured from the sky, to the noise plot figure.

There is a spurious signal around 18 m, which is 3 dB above noise, which is enough to be seen in the range profile and hence the radar imagery.

The leakage to noise ratio stays centred around 0 dB which is ideal and indicates that the transmitter has not directly leaked into the receiver components, however at close range the Leakage to noise ratio indicates ±15 dB's above the noise floor. This is not a problem when measuring objects beyond 5m of the antenna.

APPENDIX C. FloWave trial data

The FloWave trial conducted by UoB and UStA STREAM participants at FloWave, Edinburgh on 21st July 2023. My responsibilities for this trial were to produce a single radar scanning system for use with a tripod.

The purpose of the FloWave trial was to collect repeatable staring and scanning measurements at 4 different carrier frequencies, different grazing angles, wave heights and wave directions.

The trial was conducted at FloWave, Edinburgh, UK. It is a large circular wave tank, diameter of 25m and depth of 2m, capable of producing sea waves with defined sea surface spectra and patterns (regular or irregular waves etc).

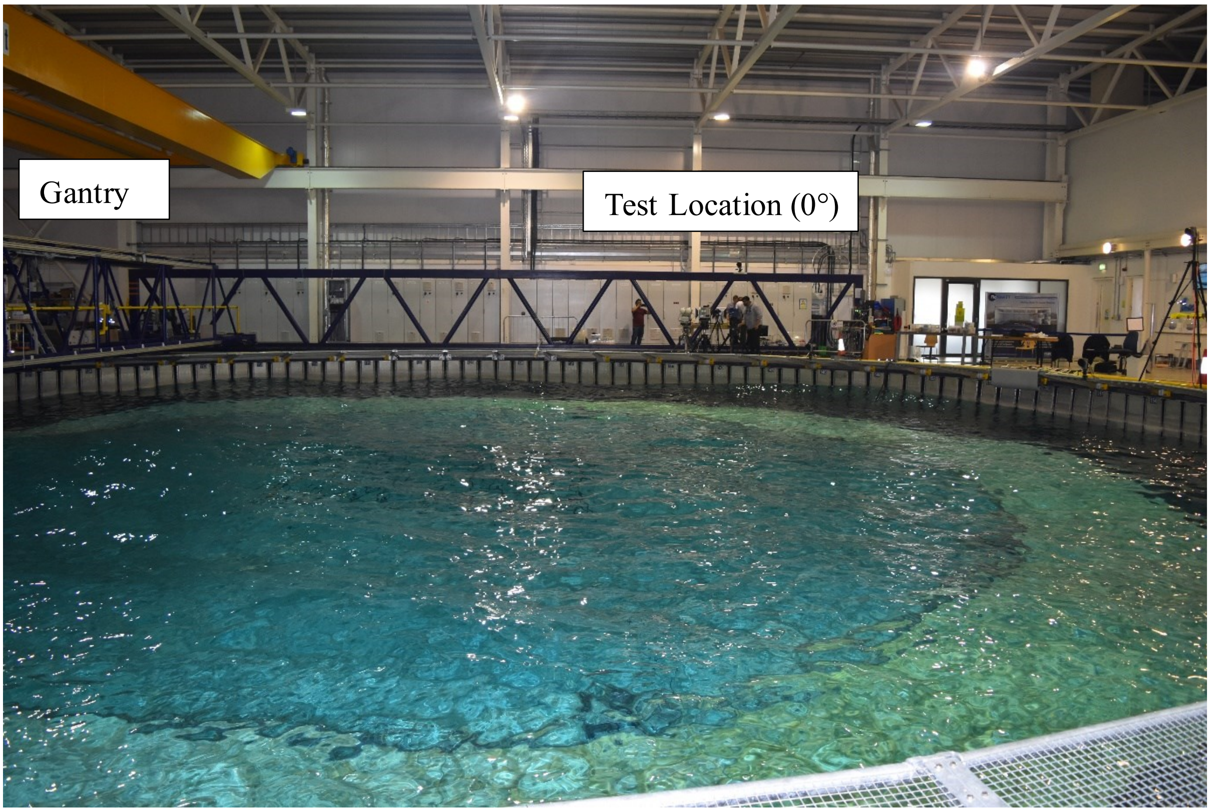

Figure C.1 FloWave circular wave tank environment with electronic paddles bordering the water.

The radars were set to a height of 1.3m, from the floor to the radar baseline. The azimuth was set to 0 degrees, and the depression angle was an independent variable that was set as either 3,5,7 or 10 degrees depending on the measurement.

For each dataset recording, stereo optical imagery from the ZED camera was taken, as well as imagery from the professional camera, ground truth of the control desk (from UStA). The professional camera imagery can be linked with the corresponding dataset on the filing system, and can be synchronised by matching the frames with the timestamped ZED imagery. Each file outputs recorded parameters used during the recording, and this is recalled during analysis.

All waves produced were Pierson-Moskowitz spectra, with a cosine-squared spreading function. So, the spectra can be modelled using the wave height setting and compared to the simulation results in chapter 4.

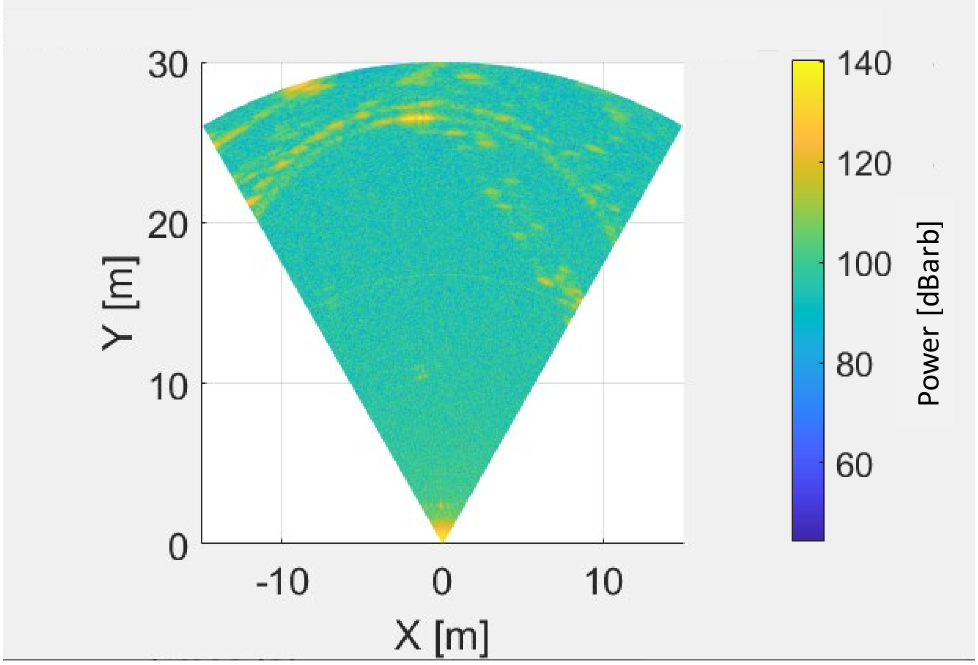

Figure C.2 FloWave Scanned imagery at 150 GHz. Gantry visible at [5,15] m. Paddles structure can be seen in image.

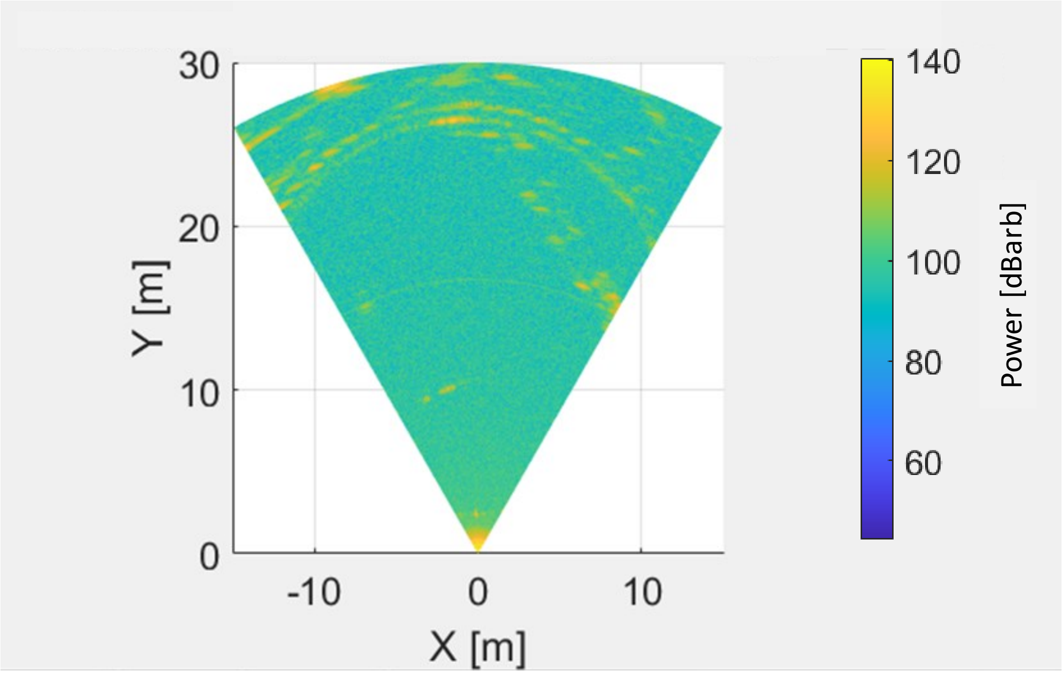

Figure C.3 Flow wave imagery with a sphere being towed across the wave tank surface.

The goal of the measurement in Figure C.3 was to image the small sphere, as it was of a similar shape of a human head. The RCS of the wet rope was also large enough to be detected, which is promising for the argument that sub-THz radars are sensitive to the rough surface of the rope, and could therefore be used to measure flotsam of a similar shape. These results have since been replicated in the lab wave tank experiment for more analysis, for future work.